UA
United Aircraft Research Laboratories

A WEAK INTERACTION STUDY OF THE
VISCOUS FLOW ABOUT OSCILLATING AIRFOILS

By S. J. Shamroth and J. P. Kreskovsky

A WEAK INTERACTION STUDY OF THE
VISCOUS FLOW ABOUT OSCILLATING AIRFOILS*

S. J. Shamroth and J. P. Kreskovsky
United Aircraft Research Laboratories

SUMMARY

This investigation combines an incompressible inviscid and a viscous flow calculation procedure by assuming the viscous correction to the inviscid flow pressure distribution is small (weak interaction) to predict the flow about airfoils oscillating in pitch and heave. The calculations made in the investigation predict the detailed viscous flow regions including transition and separation phenomena and provide a detailed analysis of leading edge separation, transition, and reattachment. Results from the calculation show the leading edge viscous flow field to be quasi-steady although the imposed inviscid pressure distribution shows significant unsteady effects. Although unable to predict the flow field about a stalled airfoil, the indications are that the present procedure can indicate the onset of catastrophic flow separation.

INTRODUCTION

The phenomenon of dynamic stall, which is largely controlled by the viscous boundary layer in direct contact with the airfoil surface, plays an important role in the successful design and operation of helicopter rotor blades. Under high-speed flight conditions the retreating rotor blades are subject to a diminished dynamic pressure and, as a result, high blade performance requires large lift coefficients to be present in the retreating portion of the rotor disc. These large lift coefficients are generated through large incidence angles often exceeding the maximum angle for which the boundary layer can remain completely attached to the airfoil surface even under dynamic conditions. When a significant amount of boundary layer separation appears, the airfoil experiences a deterioration in performance which is termed stall. Stall is most easily described in terms of a lift coefficient-incidence

angle relation. At low incidence angles no significant amount of boundary layer separation is present and the lift coefficient varies linearly with incidence, as is predicted by inviscid flow theory. At some given incidence the lift coefficient-incidence curve becomes nonlinear as the lift increases less quickly than incidence; this decrease in the lift-incidence slope is accompanied by a thickening of the viscous boundary layer and perhaps even by boundary layer separation which causes the lift to vary from its inviscid value. Further increases in incidence lead to larger decrements in the lift coefficient from the linear lift-incidence relation of potential flow and eventually an incidence corresponding to a maximum lift coefficient is reached; after this maximum is reached any further increase in incidence is accompanied by a decrease in lift. At these higher incidence angles the viscous flow about the airfoil is characterized by large separated regions along the suction side of the airfoil and in the airfoil wake, clearly indicating a relationship between boundary layer separation and airfoil stall. In addition to the behavior of the lift coefficient during stall, the moment coefficient about the quarter chord point shows a large change from its nearly zero value characteristic of unstalled flow, indicating a significant shift in the center of pressure.

The performance of the airfoil during dynamic stall plays an important role in determining the overall helicopter performance. Obviously, the lift is highly-dependent upon airfoil performance during stall and, furthermore, blade fatigue stress, blade flutter, and aircraft vibration are significantly affected by the periodic aerodynamic loading and unloading as the blade proceeds about the rotor disc. Thus, an accurate procedure for predicting the unsteady flow about an airfoil during dynamic stall would represent a significant input to a rotor design system.

McCullough and Gault (ref. 1) have postulated three types of stall for airfoils in steady flow; these are leading-edge stall, trailing-edge stall, and thin-airfoil stall. The first of these, leading-edge stall, is supposedly related to the formation of a separation bubble in the vicinity of the airfoil leading edge. For leading-edge stall it is conjectured by McCullough and Gault (ref. 1) that as incidence increases the bubble moves upstream until an incidence is reached at which the bubble suddenly bursts and the flow separates from the airfoil surface. The bursting process is accompanied by a sudden loss in lift and decrease in airfoil performance. In contrast to leading-edge stall, which is supposedly associated with separation at the leading edge of the airfoil, trailing-edge stall, which usually occurs on relatively thick airfoils, is associated with the separation of the boundary layer on the aft portion of the airfoil. Under most operating conditions, trailing-edge stall is associated with the separation of a turbulent rather than a laminar boundary layer. At low incidence no trailing-edge separation occurs. However, at some given incidence the boundary layer separates in the vicinity of the

2

trailing edge and, if the incidence continues to increase, the separation point moves forward causing a gradual decrement in airfoil performance. The effects associated with trailing-edge stall are considerably more gradual than those associated with leading-edge stall. The final type of stall conjectured by McCullough and Gault (ref. 1) is thin-airfoil stall, which, as the name implies, occurs on thin airfoils. Like leading-edge stall, thin-airfoil stall is associated with a separation bubble in the vicinity of the leading edge. However, ref. 1 suggests that in the case of thin-airfoil stall the bubble grows with increasing incidence angle, whereas for leading-edge stall the bubble moves upstream and can even shorten with increasing incidence angle.

The three different types of stall discussed in ref. 1 appear to be associated with three different types of viscous separation. However, boundary layer separation is an extremely sensitive phenomenon, the nature of which can be significantly altered by changes in the applied pressure distribution, free-stream turbulence level, Reynolds number, etc., and, therefore, it is not unreasonable to expect an airfoil which exhibits one type of stall under a given set of conditions to exhibit a different type of stall under different conditions. It may even be possible for an airfoil to be subject to leading-edge and trailing-edge stall simultaneously. Obviously, since stall is heavily dependent upon the extremely sensitive viscous separation mechanism, it is questionable how well mechanisms of stall deduced from any specific set of data correspond to the mechanisms of stall under different operating conditions.

Although the suggestions of McCullough and Gault (ref. 1) apply to static stall, it seems reasonable to suppose that some of these same mechanisms are present in dynamic stall. However, important differences do exist between the static and dynamic cases (e.g., refs. 2 and 3). First of all, the maximum incidence angle which the airfoil can tolerate before the linear lift coefficient-incidence angle relation breaks down is significantly higher in the dynamic case than in the static case, indicating that a delay in stall is obtained through dynamic phenomena. The maximum lift coefficient obtained under dynamic conditions in general is significantly greater than that obtained under static conditions. In addition, under dynamic conditions, stall shows a definite hystersis effect under which the aerodynamic coefficients are not uniquely dependent upon the instantaneous incidence angle but rather depend upon the time history of the airfoil motion. These differences between static and dynamic stall indicate that even though static and dynamic stall may have similar mechanisms, theories which employ static stall data to predict dynamic stall phenomena cannot be expected to be accurate. Accurate theoretical predictions of the airfoil loading during dynamic stall require a theory which recognizes the time-dependent nature of the dynamic stall problem.

Several theories of various degrees of sophistication have been proposed to predict airfoil loading during dynamic stall. One such theory, due to Ham (ref. 4), is based upon an inviscid flow analysis which ignores any direct effect of boundary layer separation upon stall phenomena. The theory models dynamic stall by the shedding of vortices from the airfoil leading edge. Although the theory has predicted both the maximum lift and moment coefficients for an airfoil undergoing dynamic stall, it has not yet predicted the coefficients through an entire loop. In addition to Ham's inviscid theory, semiempirical dynamic stall theories are also available. A semiempirical method used by Carta, Commerford, and Carlson (ref. 5) is based upon a correlation of existing experimental data. However, it is not clear how far the method can be extended to either other airfoils or other types of motion. Similar procedures could be developed for airfoils undergoing other types of motion, however, each class of airfoil and motion may require a different body of experimental data. The procedure of Ericsson and Reding (refs. 6 and 7) is based upon assuming an effective camber and an effective incidence which change as the hysteresis loop develops. When these effective quantities are used in conjunction with a semiempirical lag time, the force and moment coefficients during dynamic stall are predicted. However, the method is highly-empirical and does not predict stall from basic boundary layer separation considerations.

In contrast to the analyses of refs. 4 through 7, which are semiempirical, there is the more fundamental analysis developed by Crimi and Reeves (ref. 8). The Crimi-Reeves analysis is based upon a solution of the fluid dynamic equations in the neighborhood of an airfoil in arbitrary motion. In brief, the analysis of ref. 8 combines the solution of the linearized potential flow equations with the boundary layer momentum equations to predict the flow field behavior. Although the procedure produces qualitative agreement with the basic features of dynamic stall, its theoretical predictions are in quantitative disagreement with experimental data. An examination of the Crimi-Reeves analysis indicates assumptions are made that may lead to the observed quantitative differences between theory and experiment. In particular, the Crimi-Reeves analysis is based upon simplified treatments of separated regions, the transition process, and the nominally inviscid flow field. Although the method of ref. 8 uses a finite-difference solution to the boundary layer equations in regions of attached flow, it uses an integral boundary layer solution in regions of separated flow. The integral solution requires an assumption of a velocity profile family and this assumption restricts the validity of the solution. Secondly, the procedure uses an empirical transition model and, finally, the procedure uses a linearized potential flow theory to represent the outer inviscid flow.

4

The present report describes the development of a weak-interaction solution for the dynamic stall of helicopter rotor blades using an approach similar to that of Crimi and Reeves (ref. 8), but with an improved treatment of the separated flow regions, transition phenomena, and the potential flow regions. By definition, the weak-interaction solution ignores the effect of viscous displacement upon the nominally inviscid outer solution. The weak-interaction assumption is valid as long as the viscous displacement thickness remains small compared to the airfoil thickness. However, when the displacement thickness becomes large and significantly modifies the inviscid pressure distribution, such as in regions of significant boundary layer separation, the theory is invalid. In order to obtain accurate predictions of the flow field when a significant separation region is present, it is necessary to use a strong-interaction theory which recognizes the mutual interaction between the viscous inner and nominally inviscid outer flow fields. Such a strong-interaction calculation procedure could be developed by an extension of a successful weak-interaction procedure in which an inner solution such as the the viscous solution of the present report is coupled to an inviscid outer solution. The coupling would require continuity of flow angle along the line joining these solutions. Alternatively, the entire flow field could be solved by the Navier-Stokes equations thus avoiding the problem of coupling two different solutions in two regions of the flow. Such a solution has recently been obtained for internal duct flow problems by Briley and McDonald (ref. 9).

Although the present weak-interaction solution is limited in applicability to flow situations in which the viscous displacement thickness does not significantly affect the inviscid pressure distribution, the present effort can accurately predict the flow field under conditions for which the boundary layer does not significantly affect the pressure distribution. In this regard, as is shown subsequently, the procedure is capable of analyzing the detailed viscous flow mechanisms including those mechanisms governing the leading edge separation bubble and the method is also capable of predicting conditions for incipient stall. In addition, the procedure may be regarded as a first step in the development of strong-interaction solution to the isolated airfoil dynamic stall problem, or a solution for the dynamic stall problem based upon a single set of equations representing the flow field in the entire solution domain.

5

LIST OF SYMBOLS

a_1, a_2, a_3	structural coefficients
c	chord
c_f	skin friction coefficient
$\mathcal{D}_1$	sublayer damping function
$\mathcal{D}_2$	low Reynolds number correction function
E	turbulence source terms
k	curvature, or reduced frequency
ℓ	mixing length
L	dissipation length
P	pressure
$\overline{q^2}$	turbulence kinetic energy
R_τ	turbulence Reynolds number
S	turbulence source terms
s	surface coordinate
s_s	surface coordinate of stagnation point
t	time
u	streamwise velocity component
v	transverse velocity component
x	streamwise coordinate, or chordwise location
y	transverse coordinate
α	incidence angle

6

δ	boundary layer thickness, or calculation layer thickness
δ_s	sublayer thickness
δ^*	displacement thickness
ϵ	turbulence dissipation
η	dimensionless transverse coordinate
θ	momentum thickness
κ	von-Karman constant
ν	kinematic viscosity
ν_t	kinematic eddy viscosity
ξ	vorticity
ρ	density
ρ_i	acceleration parameter
τ	shear stress or relaxation time
$\phi_1, \phi_2, \phi_3, \phi_4$	integral functions (see Eqs. (35) through (38))
ψ	stream function

THEORY

General

The airfoil flow field calculations described in the present r~p .t ~. obtained by dividing the flow field into several distinct regions ε solviι. the appropriate equations in each region. In this manner results obtained in one region serve as boundary conditions for other regions and the entire flow field about the airfoil is constructed. The major flow field division is the separation between the relatively th n viscous layer near the airfoil surface and the nominally inviscid outer flow. The calculations are initiated by obtaining the nonlinear, incompressible, inviscid solution about an airfoil in arbitrary motion using the procedure of Giesing (ref. 10). The Giesing procedure predicts an inviscid velocity distribution about the airfoil as a function of time and this inviscid velocity distribution serves as a time-dependent outer edge boundary condition for the viscous flow calculation. The viscous flow region is divided into several subregions, as shown in Fig. 1. The stagnation region is specified in the vicinity of the airfoil leading edge. This is followed on the su tion surface by the region where a leading edge separation bubble is anticipated and by a fully-turbulent region which may exhibit a trailing edge separation bubble. The fully-turbulent region may, for convenience, be divided into two or more subregions. The stagnation region is followed on the pressure side by a transition region where boundary layer transition is likely to occur and then by a fully-turbulent region which again may be divided into two or more subregions.

The viscous calculation is initiated in the stagnation region using the inviscid flow solution as an outer edge boundary condition. The necessary boundary conditions at the junction between the stagnation and transition region and the stagnation and possible separated region are specified by assuming that at these boundaries the second derivatives in the streamwise direction are zero. When the viscous flow field is divided into several distinct subregions, a significant advantage is gained in terms of the required computer storage. Obviously, for a given grid resolution the storage required by the subregion approach is much less than that which would be required if the entire viscous flow were done in a single calculation. However, if a large enough core capacity were available, the subregion approach would not be necessary. The subregion approach has the disadvantage of limiting the amoun, of upstream influence. Since the upstream boundary conditions for each region (except for the stagnation region) are determined by the flow field of the previous region, it is obvious that upstream influence cannot propagate through a subregion boundary. This constraint upon upstream influence can lead to a constraint on the upstream propagation of a separated flow region as demonstrated in the airfoil calculation discussed subsequently.

8

After a solution is obtained for the stagnation region, solutions are
found for the separated and transition regions. In each case the upstream
boundary condition is obtained from the stagnation region solution; at the
upstream boundary vorticity and stream function are continuous. The outer
edge boundary condition is imposed by the inviscid flow solution and the
downstream boundary condition is set using the assumption that second
derivatives with respect to the streamwise coordinate are zero. The solutions
in the fully-turbulent region are then obtained in a similar manner.

The Potential Flow Solution

The outer nominally inviscid, potential flow field is obtained using the
computer code developed by Giesing (ref. 10). The Giesing procedure calculates
the incompressible, inviscid flow field about a two-dimensional airfoil in
arbitrary unsteady motion. The basic technique used by the procedure is to
divide the airfoil body surface into a series of elements and then to apply a
source distribution around the body, one at each element. The source distri-
bution is adjusted until the velocity normal to the airfoil surface is zero.
In addition to the airfoil source distribution, the airfoil contains a bound
circulation which is adjusted to satisfy the Kutta condition at the airfoil
trailing edge. The vortex wake shed by the airfoil is carried by the fluid
particles to which it is attached and changes in space and time. A complete,
detailed description of the procedure and comparisons with experimental data
and other analyses can be found in refs. 10 and 11.

The Viscous Flow Solution

General. - The viscous calculation procedure used in the present report
was originally developed by Briley and McDonald (ref. 12) in a study of
transitional separation bubbles. The procedure solves the vorticity-stream
function incompressible Navier-Stokes equations in either their full or
reduced form. When the full vorticity-stream function form of the equations
is used, the time-dependent vorticity equation is solved with a Douglas-Gunn
(ref. 13) perturbation of the Crank-Nicholson differencing scheme which
generates an alternating-direction-implicit (ADI) method. In the reduced form,
a Douglas-Gunn (ref. 13) perturbation of the backward difference scheme is
used for the vorticity transport equation while an approximate stream function
equation, not requiring a full ADI sweep, is used. In both the full and
approximate form of the governing equations the resulting ADI procedure
advances the vorticity equation in time through a two-step calculation
procedure. ADI procedures present an extremely efficient way of solving multi-
dimensional problems, and in the past a major obstacle in the routine solution
of such problems has been the large amount of computer time required to obtain

9

a solution. In explicit methods such as those of ref. 14 the governing equations are subject to one or more stability restrictions on the size of the time step relative to the spatial mesh size. These stability limits usually correspond to a limit arising from convective considerations or to a limit arising from diffusive considerations. In typical incompressible boundary layer type flows the viscous limit is expected to dominate the problem.

While explicit stability restrictions may not be a serious disadvantage for inviscid flow calculations in situations for which a laminar boundary layer must be resolved the limitation in time step specified by the explicit procedure stability limits may be a serious disadvantage. In the case of a turbulent boundary layer the extreme resolution required in the sublayer region obviously magnifies the problem. Thus, explicit methods inherently contain the key disadvantage that the maximum step size is fixed by the spatial step size rather than the physical time scale. One way out of the sublayer dilema with an explicit procedure is simply to assume a form for the appropriate variable within the sublayer. In the present problem of flow separation it is obviously very limiting to suggest such a profile as an artifice to eliminate grid points, particularly in a flow where the temporal behavior close to separation is of interest.

In contrast to explicit methods, implicit methods tend to be stable for large time steps and so have the allowable time step set by physical consider-ations rather than by the computational mesh and, therefore, offer the prospect of substantial increases in computational efficiency if the computa-tional effort per time step is competitive with that of explicit methods. In the calculations of the present report the viscous stability limit would be expected to determine the maximum time step limitation of an explicit solution method, however, due to the use of an implicit method, time steps on the order of 1000 times the viscous stability limit were not uncommon.

The governing equations. - The calculations presented in the present report are based upon a solution of the Navier-Stokes equations written in vorticity-stream function form. The equations are written in an airfoil coordinate system for airfoil sections subjected to two-dimensional flows. Within these two-dimensional boundary layers Coriolis and centripetal effects due to the pitching motion of the airfoil are expected to be small compared to the viscous and usual boundary layer convective effects and, therefore, they are neglected. It should be noted that at the leading edge stagnation point Coriolis effects may be important, however, these effects became negligible very quickly. For example, if the leading edge region of the NACA 0012 air-foil is approximated by a circular cylinder, a reduced frequency of 0.2 and a chord Reynolds number of 10^7 is assumed, and for the purpose of estimation of transverse velocity gradients, a steady flow calculation is used to approimate

the viscous flow near the front stagnation point then the Coriolis force becomes negligible compared to the convective momentum transfer well within one degree of the stagnation point along the cylinder surface. As shown by many authors (e.g., ref. 15), the vorticity transport equation can be written in Cartesian coordinates as

$$\frac{\partial \xi}{\partial t} + u\frac{\partial \xi}{\partial x} + v\frac{\partial \xi}{\partial y} = \nu\left[\frac{\partial^2 \xi}{\partial x^2} + \frac{\partial^2 \xi}{\partial y^2}\right] \tag{1}$$

where ξ is the vorticity given by

$$\xi = \frac{\partial u}{\partial y} - \frac{\partial v}{\partial x} \tag{2}$$

t is time, x and y are the Cartesian coordinates, u and v are velocity components in the x and y directions, respectively, and ν is the kinematic viscosity. A stream function ψ is defined by

$$u = \frac{\partial \psi}{\partial y} \; , \; v = -\frac{\partial \psi}{\partial x} \tag{3}$$

which leads to the relation

$$\frac{\partial^2 \psi}{\partial x^2} + \frac{\partial^2 \psi}{\partial y^2} = \xi \tag{4}$$

Equations (1) and (4) form the set of equations to be solved for laminar flow. For turbulent flow the equations are written in the form of conservation of momentum in the x- and y-coordinate directions as

$$\frac{\partial u}{\partial t} + u\frac{\partial u}{\partial x} + v\frac{\partial u}{\partial y} = -\frac{1}{\rho}\frac{\partial p}{\partial x} + \nu\left[\frac{\partial^2 u}{\partial x^2} + \frac{\partial^2 u}{\partial y^2}\right] \tag{5}$$

11

$$\frac{\partial v}{\partial t} + u\frac{\partial v}{\partial x} + v\frac{\partial v}{\partial y} = -\frac{1}{\rho}\frac{\partial p}{\partial y} + \nu\left[\frac{\partial^2 v}{\partial x^2} + \frac{\partial^2 v}{\partial y^2}\right] \qquad (6)$$

The velocity components u and v are divided into mean and fluctuating parts

$$u = \bar{u} + u' \qquad (7)$$

$$v = \bar{v} + v' \qquad (8)$$

where the overbar indicates mean quantities and the prime indicates fluctuating quantities. Substituting Eqs. (7) and (8) into Eqs. (5) and (6) and averaging leads to

$$\frac{\partial \bar{u}}{\partial t} + \bar{u}\frac{\partial \bar{u}}{\partial x} + \bar{v}\frac{\partial \bar{u}}{\partial y} = -\frac{1}{\rho}\frac{\partial \bar{p}}{\partial x} + \nu\left[\frac{\partial^2 \bar{u}}{\partial x^2} + \frac{\partial^2 \bar{u}}{\partial y^2}\right] + \frac{1}{\rho}\left[\frac{\partial \sigma_x}{\partial x} + \frac{\partial \tau_{xy}}{\partial y}\right] \qquad (9)$$

$$\frac{\partial \bar{v}}{\partial t} + \bar{u}\frac{\partial \bar{v}}{\partial x} + \bar{v}\frac{\partial \bar{v}}{\partial y} = -\frac{1}{\rho}\frac{\partial \bar{p}}{\partial y} + \nu\left[\frac{\partial^2 \bar{v}}{\partial x^2} + \frac{\partial^2 \bar{v}}{\partial y^2}\right] + \frac{1}{\rho}\left[\frac{\partial \tau_{xy}}{\partial x} + \frac{\partial \sigma_y}{\partial y}\right] \qquad (10)$$

where

$$\begin{bmatrix} \sigma_x & \tau_{xy} \\ \tau_{xy} & \sigma_y \end{bmatrix} = -\rho\begin{bmatrix} \overline{u'^2} & \overline{u'v'} \\ \overline{u'v'} & \overline{v'^2} \end{bmatrix} \qquad (11)$$

The stress-strain relations are assumed to be given by

$$\begin{bmatrix} \sigma_x & \tau_{xy} \\ \tau_{xy} & \sigma_y \end{bmatrix} = \rho \nu_t \begin{bmatrix} a(u_y + v_x) & u_y + v_x \\ u_y + v_x & b(u_y + v_x) \end{bmatrix} \tag{12}$$

where ν_t is the kinematic eddy viscosity and the subscripts x and y indicate partial differentiation with respect to x and y, respectively. When Eq. (12) is substituted into Eqs. (9) and (10), use is made of the relation

$$\xi = \frac{\partial u}{\partial y} - \frac{\partial v}{\partial x} \tag{13}$$

and the pressure is eliminated from the equations, the resulting turbulent vorticity transport equation is

$$\frac{\partial \bar{\xi}}{\partial t} + \bar{u}\frac{\partial \bar{\xi}}{\partial x} + \bar{v}\frac{\partial \bar{\xi}}{\partial y} = \nu \left[\frac{\partial^2 \bar{\xi}}{\partial x^2} + \frac{\partial^2 \bar{\xi}}{\partial y^2} \right] + S \tag{14}$$

where S is the turbulent dissipative contribution given by

$$S = \nu_t \left[\bar{\xi}_{yy} - 3\bar{\xi}_{xx} - 4\bar{v}_{xxx} \right] + (\nu_{t_{yy}} - \nu_{t_{xx}})(\bar{\xi} + 2\bar{v}_x)$$

$$+ 2\nu_{t_y}(\bar{\xi}_y - 2\bar{u}_{xx}) - 2\nu_{t_x}(\bar{\xi}_x + 2\bar{v}_{xx}) + \nu_t(a-b)(\bar{\xi} + 2\bar{v}_x)_{xy} \tag{15}$$

$$+ \nu_{t_y}(a-b)(\bar{\xi} + 2\bar{v}_x)_x + \nu_{t_x}(a-b)(\bar{\xi} + 2\bar{v}_x)_y + \nu_{t_{xy}}(a-b)(\bar{\xi} + 2\bar{v}_x)$$

In the calculations made in the present report, the viscous flow fields are basically boundary layer type flows in which the length scale and velocity in the streamwise direction are at least an order of magnitude larger than the length scale and velocity in the transverse direction. If the x-coordinate is associated with the streamwise direction, this implies that

$$u \gg v$$

$$\frac{\partial}{\partial y} \gg \frac{\partial}{\partial x} \tag{16}$$

so that

$$S = \nu_t \, \bar{\xi}_{yy} + \nu_{tyy} \, \bar{\xi} + 2 \, \nu_{ty} \, \bar{\xi}_y \tag{17}$$

For turbulent flow Eqs. (4), (14), and (17) determine the flow field.

Equations (1) and (4) for laminar flow or Eqs. (4), (14), and (17) for turbulent flow represent the full Navier-Stokes equations (with the approximation to turbulence dissipation) in stream function-vorticity form. If the flow field being investigated is a boundary layer type flow in which the streamwise velocity, u, is much larger than the transverse velocity, v, and derivatives with respect to the transverse coordinate, y, are much larger than derivatives with respect to the streamwise coordinate, x, then

$$\frac{\partial v}{\partial x} \ll \frac{\partial u}{\partial y} \tag{18}$$

and the stream function equation, Eq. (4), may be approximated by

$$\frac{\partial^2 \psi}{\partial y^2} = \xi = u_y \tag{19}$$

For these flows Eq. (19) replaces Eq. (4). When Eq. (19) replaces Eq. (4), the set of equations is termed the reduced set of equations. It should be noted that the reduced set of equations is equivalent to a set of boundary layer equations with the addition of a streamwise diffusion of vorticity term (ref. 12). In most of the calculations presented in the present report the streamwise diffusion term does not contribute significantly to the vorticity equation balance.

14

The preceding equations represent the equations written in a Cartesian system; however, for purposes of the calculations in the present report, a coordinate transformation was performed to allow for airfoil curvature and so as to better represent the change in shear layer width along the streamwise direction. The curvature of the body, k, is accounted for by assuming a coordinate system for curved walls in which the streamwise distance, x, is taken along the body surface and the transverse distance, y, is taken normal to the body surface. The curvature of the body, k, is a specified function of x. The curved-wall coordinate system is discussed in detail in ref. 15. In the curved-wall body coordinate system the vorticity equation becomes

$$\frac{\partial \xi}{\partial t} + \frac{u}{1+ky} \frac{\partial \xi}{\partial x} + v \frac{\partial \xi}{\partial y} = \frac{\nu}{[1+ky]^2} \frac{\partial^2 \xi}{\partial x^2} - \frac{\nu}{[1+ky]^3} y \frac{dk}{dx} \frac{\partial \xi}{\partial x}$$

$$+ \nu \frac{\partial^2 \xi}{\partial y^2} + \frac{\nu k}{[1+ky]} \frac{\partial \xi}{\partial y} \qquad (20)$$

where ξ is vorticity, u and v are velocities in the x and y directions, respectively, and ν is kinematic viscosity. The vorticity-stream function relation remains

$$\nabla^2 \psi = \xi \qquad (21)$$

which in the curved-wall coordinate system is written as

$$\frac{1}{(1+ky)^2} \frac{\partial^2 \psi}{\partial x^2} - \frac{y}{(1+ky)^3} \frac{dk}{dx} \frac{\partial \psi}{\partial x} + \frac{\partial^2 \psi}{\partial y^2} + \frac{k}{(1+ky)} \frac{\partial \psi}{\partial y} = \xi \, (22)$$

The velocities are related to the stream function by

$$u = \frac{\partial \psi}{\partial y} \qquad (23)$$

15

$$v = \frac{-1}{1+ky} \; \frac{\partial \psi}{\partial x} \tag{24}$$

For turbulent flow the momentum conservation equations in the x- and y-directions are written in the curvilinear coordinate system and the velocity is divided into mean and fluctuating parts. After the usual averaging procedure is performed, the pressure is eliminated by cross differentiation and an order of magnitude argument is applied to the apparent shear stress. The procedure is analogous to that of Eqs. (5) through (15), and leads to the result

$$\frac{\partial \bar{\xi}}{\partial t} + \frac{\bar{u}}{1+ky} \frac{\partial \bar{\xi}}{\partial x} + \bar{v} \frac{\partial \bar{\xi}}{\partial y} = \frac{\nu}{(1+ky)^2} \frac{\partial^2 \bar{\xi}}{\partial x^2} + \frac{\partial^2}{\partial y^2} \left[(\nu + \epsilon)\xi \right]$$
$$- \frac{\nu}{(1+ky)^3} y \frac{dk}{dx} \frac{\partial \bar{\xi}}{\partial x} + \frac{k}{(1+ky)} \frac{\partial}{\partial y} \left[(\nu + 3\epsilon)\bar{\xi} \right] \tag{25}$$

The derivation of Eq. (25) is given in APPENDIX A. Equations (22) and (25) represent the Navier-Stokes equations in curvilinear coordinates. In order to always keep the grid within the viscous layer a further transformation is introduced whereby

$$x = x \tag{26}$$

$$\eta = y/\delta \tag{27}$$

16

The vorticity transport equation becomes

$$\xi_t + \frac{u}{K}\, \xi_x + \left[\frac{v}{\delta} - \frac{u}{K}\,\frac{\eta\delta_x}{\delta}\right]\xi_\eta$$

$$= \frac{\eta}{\delta}\,\delta_t\,\xi_\eta + \frac{\nu}{K^2}\left[\xi_{xx} - 2\eta\,\frac{\delta_x}{\delta}\,\xi_{x\eta} + 2\eta\,\frac{(\delta_x)^2}{\delta^2}\,\xi_\eta\right.$$

$$\left. - \frac{\eta}{\delta}\,\delta_{xx}\,\xi_\eta + \frac{\eta^2}{\delta^2}\,(\delta_x)^2\,\xi_{\eta\eta}\right] + \frac{1}{\delta^2}\left\{\left[\nu + \epsilon\right]\xi\right\}_{\eta\eta} \qquad (28)$$

$$- \frac{\nu}{K^3}\,\eta\delta k_x\left[\xi_x - \frac{\eta}{\delta}\,\delta_x\xi_\eta\right] + \frac{k}{K\delta}\left\{\left[\nu + 3\epsilon\right]\xi\right\}_\eta$$

where subscripts indicate differentiation and

$$K = 1 + k\eta\delta \qquad (29)$$

The stream function equation becomes

$$\frac{1}{K^2}\left\{\psi_{xx} - 2\eta\,\frac{\delta_x}{\delta}\,\psi_{x\eta} + 2\eta\,\frac{\delta_x^2}{\delta^2}\,\psi_\eta - \eta\,\frac{\delta_{xx}}{\delta}\,\psi_\eta + \frac{\eta^2}{\delta^2}\,\delta_x^2\,\psi_{\eta\eta}\right\}$$

$$- \frac{\eta\delta}{K^3}\left[\psi_x - \eta\,\frac{\delta_x}{\delta}\,\psi_\eta\right] + \frac{1}{\delta^2}\,\psi_{\eta\eta} + \frac{k}{K}\,\frac{1}{\delta}\,\psi_\eta = \xi \qquad (30)$$

It should be noted that the final form of the equations allows the grid to adjust naturally to both spatial and temporal changes in the boundary layer thickness.

17

The Turbulence and Transition Models

The turbulence model. - In laminar flows the stress is composed solely of the molecular stress which is determined uniquely by the molecular viscosity (a property of the fluid) and the local velocity field. However, as shown in Eqs. (9) and (10), in turbulent or transitional flow where the flow field is composed of a mean and fluctuating part the averaging procedure gives rise to additional terms which appear to act as stress terms in the momentum conservation equations and which generally are called turbulent stress terms. These additional terms in the momentum equation lead to additional terms in the vorticity transport equation and calculations in the turbulent and transitional regime require a mathematical model to represent these terms. Since, under normal conditions, airfoils operate in the regime where laminar, transitional, and turbulent viscous flow regions are present, any calculation procedure attempting to predict the viscous flow field about an airfoil must contain both a turbulence model and a transition model.

Insofar as the turbulent flow is concerned a large variety of models have been developed for fully-turbulent flows (e.g., ref. 16). These models can be divided into two broad categories, equilibrium turbulence models and historical turbulence models. Equilibrium turbulence models assume that the turbulent stress is determined uniquely by the local mean velocity field. These equilibrium procedures usually hypothesize an eddy viscosity or mixing length determined solely be mean flow conditions. Although equilibrium turbulence models are adequate for the prediction of many turbulent boundary layers, their basic assumption relating the turbulent shear stress to local flow conditions is clearly in error for flow situations in which rapid changes in the mean flow field occur (e.g., refs. 17 and 18); in rapidly developing flows the turbulent stress is not determined by local conditions but rather by the history (both upstream spatial history and temporal history) of the flow and in these cases the theory is improved if a model which includes the flow history is used. A large number of such models for steady-state turbulent flows are discussed in ref. 16. In addition to the steady-state historical turbulence models of ref. 16, a time-dependent historical model has been developed by Patel and Nash (ref. 19) and applied to a variety of flows by Nash, Carr, and Singleton (ref. 20).

In the present calculations the turbulence model used is that developed by McDonald and Camarata (ref. 21) which solves an integral form of the turbulence kinetic energy equation. In brief, the turbulence kinetic energy equation is a conservation equation derived from the Navier-Stokes equations by writing the instantaneous quantities as a sum of mean and fluctuating parts. The ith Navier-Stokes momentum conservation equation ($i = 1,2,3$ referring to the three coordinate directions) is multiplied by the ith component of fluctuating velocity and the average of the resulting three equations is taken.

18

The three averaged equations are summed to obtain the turbulence kinetic energy equation. The derivation of the turbulence kinetic energy equation has been given by Favre (ref. 22) for the general case of a compressible fluid and approximated by Bradshaw and Ferris (ref. 23) to boundary layer flows. For incompressible flow the derivation has been given by many authors (e.g., ref. 24).

In the case of incompressible flow, the boundary layer approximation to the turbulent kinetic energy equation can be written as

$$\underbrace{\frac{\partial}{\partial t}\left(\overline{q^2}/2\right)}_{\text{temporal change}} + \underbrace{\frac{\partial}{\partial x}\left(U\overline{q^2}/2\right) + \frac{\partial}{\partial y}\left(V\overline{q^2}/2\right)}_{\text{advection}} = \underbrace{- \overline{u'v'}\,\frac{\partial U}{\partial y}}_{\text{production}}$$

$$+ \underbrace{\frac{\partial}{\partial y}\left(\frac{\overline{p'v'}}{\rho} + \frac{\overline{v'q^2}}{2}\right)}_{\text{diffusion}} - \underbrace{\epsilon}_{\text{dissipation}} \underbrace{- \left(\overline{u'^2} - \overline{v'^2}\right)\frac{\partial U}{\partial x}}_{\text{normal stress production}}$$

(31)

where $\overline{q^2}$ is the turbulence kinetic energy.

$$\overline{q^2} = \overline{u'^2} + \overline{v'^2} + \overline{w'^2}$$

(32)

It should be noted that in the turbulent flow calculations of the present report the boundary layer approximations are expected to be valid and thus the boundary layer form of the turbulence kinetic energy equation is appropriate.

Following Townsend (ref. 25) and Bradshaw and Ferris (ref. 23), McDonald and Camarata (ref. 21) introduce structural coefficients a_n and L, together with a mixing length ℓ; these scales are defined as

$$-\overline{u'v'} = a_1 \overline{q^2}\ ,\quad \overline{u'^2} = a_2 \overline{q^2}\ ,\quad \overline{v'^2} = a_3 \overline{q^2}\ ,$$

(33)

$$\epsilon = \overline{(-u'v')}^{3/2}/L\quad \overline{(-u'v')}^{1/2} = \ell\,\frac{\partial U}{\partial y}$$

19

and a_1, a_2, and a_3 are assumed to have values 0.15, 0.50, and 0.20, respectively. The turbulence kinetic energy equation is then integrated between the wall and the edge of the boundary layer at $y = \delta$ to obtain the equation

$$\frac{\partial \phi_1}{\partial t} + \frac{\partial \phi_2}{\partial x} = \phi_3 - \phi_4 + E \tag{34}$$

where

$$\phi_1 = \frac{2}{a_1} \int_0^{\eta_{b.l.}} l^2 \left(\frac{\partial \bar{u}}{\partial y}\right)^2 d\eta \tag{35}$$

$$\phi_2 = \frac{2}{a_1} \int_0^{\eta_{b.l.}} l^2 \, \bar{u} \left(\frac{\partial \bar{u}}{\partial y}\right)^2 d\eta \tag{36}$$

$$\phi_3 = 2\delta \int_0^{\eta_{b.l.}} l^2 \left[1 - \eta_L\right] \left|\frac{\partial \bar{u}}{\partial y}\right|^3 d\eta \tag{37}$$

$$\phi_4 = 2\delta \int_0^{\eta_{b.l.}} \frac{a_2 a_3}{a_1} \, l^2 \left|\frac{\partial \bar{u}}{\partial y}\right|^2 \left[\frac{\partial \bar{u}}{\partial x} - \eta \, \delta_x \frac{\partial \bar{u}}{\partial y}\right] d\eta \tag{38}$$

$$E = \left[q_e \frac{l_e}{l_\infty}\right]^2 \left[\frac{\partial \bar{u}}{\partial t} + \bar{u} \frac{\partial \bar{u}}{\partial x} - \bar{v}\right]_e \tag{39}$$

20

$$\eta = Y/\delta \tag{40}$$

The term containing ϕ_1 represents the temporal rate of change of turbulence kinetic energy, the term containing ϕ_2 represents the streamwise rate of change of turbulence kinetic energy, the term containing ϕ_3 represents the integral of turbulence production minus dissipation, and the term containing ϕ_4 represents the normal stress production. The terms designated by E represent turbulent source terms resulting from disturbances imposed upon the viscous layer by the free stream. It should be noted that the turbulence kinetic energy at the edge of the boundary layer, q^2_e is damped by the factor $(\ell_e/\ell_\infty)^2$ where ℓ_e is the value of the mixing length at the boundary layer edge and ℓ_∞ is the "wake" value of mixing length; i.e., the value far from the wall. In most regions of the flow $\ell_e/\ell_\infty = 1.0$ and thus no damping of the entrained turbulence energy occurs. However, near the stagnation point, ℓ_e is initially considerably smaller than ℓ_∞ due to the extremely thin highly viscous layer present near the stagnation point and the entrainment is damped heavily in this region. As the flow proceeds away from the stagnation point ℓ_e quickly rises to the value of ℓ_∞ and no damping of the entrained turbulence occurs.

The dissipation length is given by

$$L = 0.18 \tanh \left[\kappa y / (0.18) \right] \mathcal{D}_1 \mathcal{D}_2 \tag{41}$$

where κ is the von Karman constant taken as 0.41, $\mathcal{D}_1$ is a sublayer damping factor, and $\mathcal{D}_2$ is a low Reynolds number correction. In the original McDonald-Camarata model the sublayer damping was assumed to be given by the van Driest damping model and no low Reynolds number correction was made. However, following a later work by McDonald and Fish (ref. 26), the sublayer damping is assumed to distribute normally about a mean height $y^+(y^+ = y\sqrt{\tau/\rho}/\nu)$ with a standard deviation σ leading to the equation

$$\mathcal{D}_1 = P^{1/2} \left\{ \left(y^+ - \bar{y}^+ \right) / \sigma \right\} \tag{42}$$

where P is the normal probability function; $\bar{y}^+$ is taken as 23, and σ as 8.

21

The low Reynolds number correction is based upon the work of McDonald (ref. 27) which relates the correction factor, $\mathcal{D}_2$, to a turbulence Reynolds number, R_T, given by

$$R_T = \frac{1}{\delta} \int_0^{\delta} \nu_t \, dy \Big/ \frac{1}{\delta_s} \int_0^{\delta_s} \nu \, dy \tag{43}$$

where δ is the viscous layer thickness, δ_s is the sublayer thickness defined as the location at which the laminar stress has fallen to 4 percent of the total stress, ν_t is the turbulent kinematic viscosity defined as

$$\nu_t = (-\overline{u'v'})/(\partial \bar{u}/\partial y) \tag{44}$$

and ν is the laminar kinematic viscosity. The correction factor $\mathcal{D}_2$ is given by

$$\mathcal{D}_2 = \left[1.0 + \exp\left(-1.63 \ln f_T + 9.7\right) \right] \tag{45}$$

where

$$f_T = 68.1 \, R_T + 614.3 \qquad R_T > 40 \tag{46}$$

$$f_T = 100 \, R_T^{-22} \qquad\qquad R_T \leq 1 \tag{47}$$

and for $1 < R_T \leq 40$, f_T is fitted between Eqs. (46) and (47) by a cubic constructed to match the function and slope at the join points.

Finally, a one-parameter mixing length profile, ℓ_∞, is introduced where

$$l = \ell_\infty \, \mathcal{D}_1 \, \tanh\left[\kappa y / \ell_\infty\right] \tag{48}$$

Introduction of Eqs. (41) and (48) into Eq. (34) yields a differential equation for the wake value of the mixing length, ℓ_∞, which is solved in conjunction with the mean flow equations to determine both the mean flow field and the shear stress development. A detailed derivation and discussion of the turbulence model as well as the transition model (to be discussed subsequently) is given by Shamroth and McDonald (ref. 28).

The transition model. - Althougn the McDonald-Camara·· ·· ·bulence model, as previously described, is a well-proven turbulence model for fully-turbulent flows, it is still necessary to include a model to predict the flows in the transitional regime. Such a model based upon a solution of the turbulence kinetic energy equation has been developed by McDonald and Fish (ref. 26) and has been verified through comparisons with a large body of experimental data by McDonald and Fish (ref. 26), Shamroth and McDonald (ref. 28), and Kreskovsky, Shamroth, and McDonald (ref. 29). It should be noted that this transition model is based upon a rigorous conservation equation rather than semiempirical data correlations, as is the case with most other transition models (see, ref. 30). The model has successfully predicted the behavior of a large variety of transitional boundary layers from the incompressible to the low hypersonic Mach number regime subject to various heat transfer rates, pressure gradients, and wall roughness heights (refs. 26, 28, and 29). In brief, the transition model is identical to the turbulence model with the exception that the structural coefficient, a_1, becomes a function of the turbulence Reynolds number of the form

$$a_1 = a_0 \left[f_\tau / f_{\tau_0}\right] \Big/ \left\{1 + 666\, a_0 \left[\left(f_\tau / f_{\tau_0}\right) - 1\right]\right\} \tag{49}$$

where f_τ is given by Eqs. (46), (47), and the cubic fit with $f_{\tau_0} = 100$. The variable a_0 is a function of the wall-to-free-stream temperature ratio (ref. 28) and for the case of wall temperature equal to free stream temperature a_0 is equal to 0.0115. Thus the turbulence kinetic energy equation is always solved in conjunction with the governing mean flow equations. If the calculated mixing length is very small, the flow is laminar; however, the mixing length may increase causing the turbulent transport to be comparable to the

laminar transport and, in this case, the flow is transitional. Finally, the mixing length may reach a fully-turbulent value leading to a fully-turbulent flow.

Solution of the Equations

Solution of the full set of equations. - When the full set of vorticity-stream function equations are used, an iterative solution is required between the vorticity transport equation, Eq. (1), and the vorticity-stream function relation, Eq. (4). The set of equations are subject to the boundary conditions at the wall and at the boundary layer outer edge as follows:

$$\text{at } y = 0$$

$$\psi = 0 \tag{50}$$

$$\partial \psi / \partial y = 0$$

$$\text{at } y = \delta$$

$$\partial \psi / \partial y = u_e \tag{51}$$

$$\xi = 0$$

Briley and McDonald (ref. 12) solve the set by first assuming a wall vorticity distribution and then solving the vorticity transport equation by a Douglas-Gunn ADI procedure. In the Douglas-Gunn procedure the vorticity transport equation is written in the general form

$$\phi_t = A\phi_{xx} + B\phi_x + C\phi_{yy} + D\phi_y + E \tag{52}$$

where ϕ is a dependent variable (in this case, vorticity), A, B, C, D, and E are coefficients, and subscripts indicate derivatives. A two-step calculation procedure is used to advance the calculation in time from t_o to $t_o + \Delta t$. In this procedure ϕ^b is the dependent variable at the known time step, t_o, ϕ^* is the dependent variable at the first step of the calculation procedure, and ϕ^{**} is the dependent variable at the second step of the calculation (or at time = $t_o + \Delta t$).

24

In the first step of the procedure derivatives with respect to y are treated implicitly using Crank-Nicholson differencing and those with respect to x are treated explicitly leading to the equation

$$\frac{\phi^*}{\Delta t} - \frac{C}{2}\phi^*_{yy} - \frac{D}{2}\phi^*_y = \frac{\phi^b}{\Delta t} + A\phi^b_{xx} + B\phi^b_x + \frac{C}{2}\phi^b_{yy} + \frac{D}{2}\phi^b_y + E \quad (53)$$

which is solved for ϕ^* by inverting a tridiagonal matrix. In the second step of the procedure derivatives with respect to x are treated implicitly while those with respect to y are treated explicitly leading to the equation

$$\frac{\phi^{**}}{\Delta t} - \frac{A}{2}\phi^{**}_x - \frac{B}{2}\phi^{**}_x - \frac{C}{2}\phi^*_{yy} - \frac{D}{2}\phi^*_y = \frac{\phi^b}{\Delta t}$$
$$+ \frac{A}{2}\phi^b_{xx} + \frac{B}{2}\phi^b_x + \frac{C}{2}\phi^b_{yy} + \frac{D}{2}\phi^b_y + E \quad (54)$$

Equation (53) is subtracted from Eq. (54) leading to the simpler equation for ϕ^{**}

$$\frac{\phi^{**}}{\Delta t} - \frac{A}{2}\phi^{**}_{xx} - \frac{B}{2}\phi^{**}_x = \frac{\phi^*}{\Delta t} - \frac{A}{2}\phi^b_{xx} - \frac{B}{2}\phi^b_x \quad (55)$$

After the vorticity transport equation is solved, the stream function equation is solved with the wall and edge boundary conditions

$$\psi = 0 \text{ at } y = 0$$
$$\partial\psi/\partial y = u_e \text{ at } y = \delta \quad (56)$$

by a Peaceman-Rachford ADI procedure for elliptic equations (ref. 31). The Peaceman-Rachford procedure introduces a series of acceleration parameters, ρ_i, and then solves the stream function equation by an iteration process. For each choice of acceleration parameter, ρ_i, two sweeps are made. In the first sweep the iteration is advanced from solution ψ^i to $\psi^{i+\frac{1}{2}}$ by treating x-derivatives

as explicit and y-derivatives as implicit. In the second sweep the x-derivatives are treated implicitly and the y-derivatives explicitly and the solution is advanced to ψ^{i+1}. Thus, the procedure advances as

$$\psi_{yy}^{i+1/2} + \rho_i \psi^{i+1/2} = \zeta - \psi_{xx}^{i} + \rho_i \psi^{i}$$

(57)

$$\psi_{xx}^{i+1} + \rho_i \psi^{i+1} = \zeta - \psi_{yy}^{i+1/2} + \rho_i \psi^{i+1/2}$$

If ψ^{i+1} agrees with ψ^i within a specified tolerance, the equation is considered solved; if not, the procedure is repeated for the next acceleration parameter. It should be noted that, if the acceleration parameter, ρ_i, is taken as the inverse of a time step $1/\Delta t_i$, the Peaceman-Rachford procedure is analogous to the Douglas-Gunn procedure.

After the stream function equation has been converged the streamwise velocity component at the wall consistent with the stream function solution is computed. If the wall velocity is zero within a specified tolerance, the set of equations is considered solved at the given time step; if not, a new wall vorticity distribution is assumed using a secant extrapolation and the entire procedure consisting of the solution of the vorticity transport equation and the stream function-vorticity relation is repeated.

Solution of the reduced set of equations. - As can be summarized from the preceding discussion, the iterative solution to the full set of equations can be a relatively time consuming process. The computer time required by the reduced equations is less by an order of magnitude than that required by the full set of equations; therefore, the reduced set represented by Eqs. (1) and (19) have been utilized whenever possible. When the reduced set of equations are used, the vorticity transport equation and the reduced stream function equation are solved as a coupled set by the Douglas-Gunn ADI perturbation of the backward difference procedure using the boundary conditions represented by Eqs. (50) and (51). When the reduced set of equations are solved, the equations are first integrated with the x-derivatives taken as implicit and the y-derivatives as explicit. Since the reduced stream function-vorticity relation contains no derivatives with respect to x, the integration is performed only for the vorticity transport equation and is similar to that for the full set of equations. The equations are then integrated with y-derivatives taken as implicit and x-derivatives as explicit. During these integrations a coupled set of equations is solved in which the coefficient matrix takes the form of a block tridiagonal matrix, each block being a 2 x 2 submatrix. The fact that the system can now be solved in a coupled manner eliminates the

26

previously required iteration on wall vorticity. The reduction in the stream function equation eliminates the Peaceman-Rachford iterative ADI solution required when using the full stream function equation.

RESULTS

Verification of the Calculation Procedure

General. - Before predictions were made for the flow field about oscillating isolated airfoils, it was deemed necessary to verify the calculation procedure. Since the potential flow computer code used in the present effort was extensively checked out by its originator (refs. 10 and 11), little effort was expended in verifying this code. The major verification effort concentrated on the viscous flow calculation procedure. Verification of the viscous flow calculation procedure requires verification of the mathematical models used in the procedure and verification of the finite-difference procedure itself. The finite-difference procedure was verified by comparing predicted results and available analytical solutions for a wide variety of laminar flows. These comparisons between numerical solutions of the present procedure and analytical solutions for laminar flows assess how well the finite-difference solutions correspond to solutions of the original differential equations. In addition, calculations for transitional boundary layers made with the present procedure were compared with calculations made with the well-established UARL boundary layer prediction deck.

Insofar as the mathematical models are concerned, the only mathematical models present other than that implied by representing the flow field by the Navier-Stokes equations, are the turbulence and transition models. These models have been verified for steady-state, unseparated boundary layer type flows through a large number of comparisons between theoretical predictions and experimental data (refs. 26, 28, 29, and 32). In addition, successful predictions of experimentally measured transitional separation bubbles have been made by Briley and McDonald (ref. 12). Thus, the turbulence and transition models are well-established for steady-state viscous flows.

The major unresolved question centers upon how well the turbulence and transition models represent time-dependent flow fields. Since the basic equation used to predict the turbulent shear stress development is the turbulent kinetic energy equation, an equation derived directly from the Navier-Stokes equations, there can be little argument regarding the governing equation itself, Eq. (31). The major uncertainty resides in the turbulence model, Eqs. (33) and (41) through (48); however, some such model must be hypothesized in order to solve the turbulence kinetic energy equation. If

27

unsteady calculations are to be valid, then the turbulence model should be valid for the flows under consideration. In general, the characteristic frequency of turbulence is given by

$$\omega_t = \frac{u}{\delta} \qquad (58)$$

and for helicopter applications the characteristic frequency of the airfoil is at most

$$\omega_a = \frac{2u}{c} \qquad (59)$$

where δ is the boundary layer thickness, u is the free stream velocity, and c is the airfoil chord. The ratio of the frequency of the turbulence to that of the airfoil motion is

$$\frac{\omega_t}{\omega_a} = \frac{c}{2\delta} >> 1 \qquad (60)$$

Therefore, the turbulence frequency is expected to be much greater than the airfoil frequency and the turbulence structure should be unaffected by the time-dependent mean motion at least in the absence of large separated regions. Thus, the turbulence model is expected to be valid.

Potential flow calculation. - As previously discussed, the potential flow calculation procedure is a well accepted procedure, the results of which have been verified by its author (refs. 10 and 11). An additional comparison was made under the present effort between theoretically predicted lift and moment coefficients with the data of Carta, Commerford, Carlson, and Blackwell (ref. 33). The results of this comparison, shown in Fig. 2, are considered to be good. The experimental data have been corrected for finite span effects by a correction factor obtained from comparison of the low incidence experimentally determined lift-incidence slope with the theoretical value.

28

Laminar viscous flow calculations. - One suitable test case for assessing
the present calculation procedure is the flat plate stagnation point laminar
flow field termed Hiemenz flow (ref. 15). The inviscid flow solution at large
distances from the plate is given by

$$u = ax$$
$$v = -ay$$

(61)

The analytical viscous solution is a similarity solution in which the
dimensionless velocity, u/ue, is a function of the dimensionless transverse
coordinate, $y/\sqrt{v/a}$, where u_e is the inviscid flow velocity in the streamwise
direction, and v is the kinematic viscosity. A comparison between the
solution predicted by the numerical procedure and the analytical solution as
given by ref. 15 is presented in Fig. 3. As can be seen, the comparison is
excellent.

A second steady-state laminar solution which serves as a good test case
for the calculation procedure is that of flow about a circular cylinder, since
such a flow provides an additional feature not present in the Hiemenz flow.
In particular, flow about a circular cylinder provides a geometry having a
finite-radius of curvature and thus the calculation serves as a check on the
radius of curvature effect in the present calculation procedure. A comparison
between the numerical solution of the present analysis and that obtained
analytically from the Blasius series solution to the boundary layer equations
(ref. 15) is presented in Fig. 4. The agreement between the numerical and
analytical solutions, shown in Fig. 4, at three different angular locations
($\theta = 0$ being the front stagnation point) is excellent. In Fig. 4, u_e is the
local free-stream velocity, u_∞ is the approach velocity, and R is the
cylinder radius.

The viscous flow calculation procedure was also used to predict the flow
along a flat plate oscillating sinusoidally in its own plane to assess the
accuracy of the procedure in predicting time-dependent flows. The numerical
solution was run using both the full set of Navier-Stokes equations and the
reduced set of equations; no significant differences in the results were
apparent. The velocity profiles calculated by the numerical procedure through
one half a cycle are compared to the analytical solution of ref. 15 in Fig. 5.
The analytical solution is given by

$$u(y, t) = u_0 \left[\cos(\omega t) - e^{-ky} \cos(\omega t - ky) \right] \qquad (62)$$

$$k = \sqrt{\frac{\omega}{2\nu}} \qquad (63)$$

In Fig. 5 the open circles represent the solutions obtained from both the reduced and full Navier-Stokes equations for an oscillation frequency of 100 radians/sec. It should be noted that in the numerical calculation the plate was assumed stationary and the inviscid flow field oscillated, whereas in ref. 15 the plate was assumed to oscillate in a quiescent fluid; however, as discussed by Lighthill (ref. 34), the two problems are equivalent. As can be seen, agreement is excellent. A comparison between the wall vorticity, $\partial u/\partial y$, predicted by the numerical procedure and that given by the analytical solution is presented in Fig. 6. The wall vorticity, being proportional to the skin friction, is a very sensitive indicator of the accuracy of the numerical procedure. The agreement is again excellent. It should be noted that the reduced equations were used successfully for the oscillating plate problem even though regions of reversed flow are present in the flow field.

In addition to these laminar viscous flow calculations made in the presence of a solid wall, calculations were made for the wake behind a flat plate and these results are compared to the results obtained by Goldstein and Luckert as given by Rosenhead and Simpson (ref. 35) in Fig. 7. Since Goldstein's solution was numerical and Luckert's graphical, Goldstein's solution is regarded as the more reliable of the two. Agreement between the present solution and that of Goldstein is good.

Transitional viscous flow calculations. - The results of Figs. 3 through 7 demonstrate the ability of the present numerical procedure to predict boundary layer, stagnation point, and wake flows in the laminar regime including unsteady effects and the effects of a finite radius of curvature. The procedure's ability to predict transitional flows was verified by comparing the results of the present procedure with the results of a well-established transitional boundary layer calculation procedure previously verified by an extensive comparison between theoretical predictions and experimental data (refs. 26, 28, 29, and 32). A comparison between steady-state transitional results of the present procedure, using the reduced set of

30

equations, and the results of the boundary layer procedure are presented in Fig. 8. As can be seen, the results are nearly identical. The transition model utilized was virtually identical in both cases.

Turbulent viscous flow calculations. - An additional comparison was made between the present procedure and the data of Karlsson (ref. 36) to assess the procedure's applicability to time-dependent turbulent flows. In ref. 36 Karlsson investigated a boundary layer developing under an oscillating free-stream velocity given by

$$u_\infty\left(x,t\right) = u_0\left(x\right) + u_\infty^{(1)} \cos\omega t \tag{64}$$

Karlsson represented the velocity field within the boundary layer by the series expansion

$$u\left(x,y,t\right) = \bar{u}\left(x,y\right) + u^{(1)}\cos\phi\cos\omega t - u^{(1)}\sin\phi\sin\omega t + r \tag{65}$$

and measured $u(x,y)$, $u^{(1)} \cos\phi$ and $u^{(1)}\sin\phi$. In Eq. (65) r represents the higher order harmonics. Calculations corresponding to Karlsson's data for the conditions

$$\omega/2\pi = 1.0 \text{ cycles/sec}$$

$$u_\infty^{(1)}/u_0 = 0.35 \tag{66}$$

were carried out under two different sets of assumptions. The first calculation assumed the boundary layer at time zero to be independent of the stream-wise coordinate, x; this is termed the similarity solution. The second calculation assumed that at an upstream station, the velocity satisfied an equilibrium turbulent boundary layer profile; i.e.,

$$u\left(y,t\right) = u_e\left(y\right)\left(1 + \frac{u_\infty^{(1)}}{u_0} \cos\omega t\right) \tag{67}$$

31

where $u_e(y)$ is the steady-state turbulent boundary layer profile. This time-dependent initial value solution was then allowed to develop as the flow proceeded downstream. The results of both calculations are presented in Fig. 9 where $u^{(1)}\cos\phi$ is represented by $u_i^{(1)}$ and $u^{(1)}\sin\phi$ is represented by $u_o^{(1)}$. The agreement is moderately good. In both calculations the predicted mean velocity profile agrees well with data and the predicted first harmonics agree qualitatively with the data. Both calculations predict the rapid rise of the in-phase harmonic with distance from the wall and, although both calculations predict a velocity overshoot for the in-phase component, both disagree with Karlsson's measurements as to the magnitude and location of the overshoot. Similarly, agreement between theory and experiment for the out-of-phase component is good in the wall region but disagreement exists in the outer region. However, considering the present limits of the theoretical predictions, which either assume a similarity solution or a set of initial conditions at a given streamwise station in which no overshoot of the first in-phase harmonic is present and in which no first out-of-phase harmonic exists (see Eq. (67)), the agreement between theory and experiment seems satisfactory.

Comparison between the full and reduced sets of equations. - As previously discussed, there are two options available within the viscous calculation procedure used in the present report, the option using the full stream function-vorticity relation, Eq. (4), and the option using the reduced stream function-vorticity relation, Eq. (19). The full relation represents an exact equation with no approximation to the original Navier-Stokes equations, whereas the reduced equation requires the approximation

$$\frac{\partial v}{\partial x} << \frac{\partial u}{\partial y} \tag{68}$$

where x is associated with the streamwise direction, y with the transverse direction, and u and v are velocity components in the x and y directions, respectively. The approximation obviously is valid in attached boundary layer type flows and, as shown by the calculations of Briley and McDonald (ref. 12), the approximation appears to be valid in relatively thin separation bubbles; however, at the initiation of the present study it was not obvious if the reduced set of equations leads to valid solutions in the stagnation region of the airfoil. Since the reduced set of equations are much more efficient to solve than the full set, they are used whenever possible and, therefore, a test comparison between the results of the full set and the reduced set was made for steady flow in the vicinity of an airfoil front stagnation point.

A comparison between the two results for a modified NACA 0012 airfoil at
2.5 deg angle of attack is shown in Fig. 10. The Reynolds number for the
calculation was 0.26 x 10^7 and a free-stream turbulence level of 0.01 was
assumed. In Fig. 10 the normal distance and surface coordinate are normalized
by the chord length. The normalized surface coordinate, s/c, is zero at the
trailing edge and increases along the pressure surface to a value of 1.015 at
the leading edge. The surface coordinate then continues to increase along the
suction surface ʻ ɔ the trailing edge. The stagnation point is located well on
the pressure side of the leading edge at s/c = 1.00.

As shown in Fig. 10, the only significant difference in the results is
reflected in the momentum thickness in the vicinity of the stagnation point.
The full Navier-Stokes solution indicates a sharp increase in momentum
thickness in the immediate area of the stagnation point due to the presence
of a velocity overshoot, whereas the reduced Navier-Stokes equations solution
gives a smooth variation of momentum thickness in the same region. The
comparison indicates the validity of the solution from the reduced equations
in the vicinity of the front stagnation point and, therefore, in subsequent
viscous calculations the reduced set of equations was used exclusively.

Predictions for Flow About Oscillating Airfoils

General. - Weak-interaction predictions were made for the flow field
about a modified NACA 0012 airfoil for three different types of motion. The
first calculation was for the flow about an airfoil oscillating in pitch
about the quarter chord point. The flow conditions were based upon experi-
mental data which showed that the airfoil did not encounter stall. The
second calculation was made for the flow about an airfoil once again
oscillating in pitch, however, in this second case the data showed the air-
foil to be stalled over a large portion of the cycle. Finally, a third calcu-
lation was made for an airfoil oscillating sinusoidally in heave; in this third
case, the airfoil was stalled over a significant portion of the cycle. In all
three cases the calculation was made by first predicting the inviscid flow
field via the Giesing calculation procedure (ref. 10). This inviscid calcula-
tion then serves as an outer edge boundary condition for the viscous flow
calculation. The viscous flow itself is divided into subregions, as shown in
Fig. 1. The viscous calculation has been described previously; in brief, the
stagnation region is solved first and the results from the stagnation region
serve as upstream boundary conditions for the next downstream region on both
the suction and pressure surface. In this manner, the solution for each
viscous region serves as a boundary condition for the next region. The mean
spacing in each region varied to allow adequate resolution of the local flow
field. Typically, the streamwise mesh spacing is smallest in the leading
edge separated region where $\Delta x/c$ is of the order of 0.0025. The largest

33

streamwise mesh spacing is used in the pressure side fully-turbulent region where $\Delta x/c$ is roughly 0.0177. The distribution and number of grid points normal to the airfoil surface also vary from region to region so that optimum resolution of laminar boundary layers, transitional regions, and turbulent boundary layer sublayers is obtained. As an example of the total number of grid points used, the distribution grid points for each segment of the Case II airfoil are given below:

Stagnation region	30 x points by 24 y points
Pressure side transition region	34 x points by 26 y points
Pressure side fully-turbulent region	34 x points by 33 y points
Suction side separated region	30 x points by 26 y points
Suction side fully-turbulent region	34 x points by 30 y points
Suction side fully-turbulent trailing edge region	34 x points by 23 y points
Total number of grid points	5648

Case I - unstalled airfoil oscillating in pitch. - The first time-dependent airfoil flow field calculation is for a modified NACA 0012 airfoil oscillating sinusoidally in pitch. The airfoil and motion chosen correspond to test point 3184.2 of ref. 3 for which the mean angle of attack is 7.76 deg, the amplitude of the sinusoidal oscillation is 5.24 deg, the dimensionless frequency, k, is 0.252, and the Reynolds number based upon chord length is 0.26×10^7. The free-stream turbulence level is assumed to be one percent. Under static conditions, maximum lift for the modified airfoil at a chord Reynolds number of 0.26×10^7 occurs at 12.9 deg and the nonlinear portion of the lift-incidence curve begins at approximately 9 deg. Thus the airfoil is being investigated at conditions which slightly exceed the limit of static stall; however, from observation, the airfoil does not undergo any dynamic stall. The variation of the experimentally determined lift and moment coefficients compared with the theoretical predictions using the computer code of ref. 10 is presented in Fig. 11. The comparison between theory and experiment is considered good.

A comparison between differential pressure coefficients, as predicted by the theory (ref. 10) and measured by experiment (ref. 3), is presented in Figs. 12 through 14 and the surface pressure coefficient at several incidence angles is shown in Fig. 15. As shown in Figs. 12 and 13, the theoretical predictions are in good agreement with the data as might be expected for an unstalled airfoil. However, as shown in Fig. 14, a large discrepancy does exist between theory and experiment at $x/c = 0.91$. The modified NACA 0012 airfoil has a trailing edge tab (see Fig. 1) and at the junction of this tab

and the airfoil skin there is a rapid change in surface curvature. This rapid change in curvature causes the potential flow program to seek a stagnation point and give a physically unrealistic pressure maximum at the tab location. For example, at an incidence of 7.5 deg the predicted pressure coefficients on the suction side trailing edge are as follows:

x/c	C_p
0.67	-0.18
0.75	-0.09
0.82	+0.06
0.88	+0.33
0.93	+0.06

The severe local maximum at the 88 percent chord location is physically unrealistic and is due to the sharp curvature in the airfoil surface at the juncture of the tab and the airfoil skin. In reality such a sharp maximum would not exist since the boundary layer displacement thickness would be expected to smooth the pressure distribution. Before the inviscid flow field calculated by the Giesing procedure is input to the viscous flow calculation, a three-point least-squares smoothing in time and a five-point least-squares smoothing in space is performed to insure a smooth variation of the outer edge viscous flow boundary conditions. However, additional smoothing was required in the region of the unrealistic pressure maximum. Prior to performing a least-squares smoothing of the inviscid velocity field, the local C_p maximum (velocity minimum) is relieved somewhat through a two-point central averaging procedure. The averaging procedure consists of first obtaining the velocity at the 88 percent chord location as the average of the velocities just upstream and downstream of this location. The velocity at points upstream and downstream of the 88 percent chord point are then evaluated by marching both upstream and downstream away from the 88 percent location using the formula

$$v_j = 0.5 \left(v_{j+1} + v_{j-1} \right) \tag{69}$$

Considering j to be increasing in the direction of marching, it is noted that V_{j-1} is a previously averaged velocity. Equation (69) is used to smooth the velocity field between $x/c = 0.80$ and $x/c = 0.98$; with this central averaging the only portion of the flow significantly modified is that in the immediate region of the 88 percent chord location.

35

The viscous flow field is initiated in the stagnation region using the reduced Navier-Stokes equations. As previously demonstrated, use of the reduced equations is quite justified on the basis of the comparisons with solutions to the complete Navier-Stokes equations and results in a considerable reduction in computer run time. Use of the reduced equations still permits separation bubbles to appear as demanded by the physical constraints of the problem. The results predicted at both ends of this stagnation region are used as upstream conditions for two further segments, one on the suction surface and one on the pressure surface. The segment downstream of the stagnation region on the suction side of the airfoil contains the region where the leading edge separation bubble appears. This segment is then followed by the suction side fully-turbulent region which in itself may be divided into two or more segments. On the pressure side of the airfoil the stagnation region is followed by the segment where boundary layer transition usually takes place. This region is then followed by the pressure side fully-turbulent region.

Results of the calculations in the stagnation region are presented in Figs. 16 through 22. The calculation in this region is made assuming quasi-steady flow and the results are monitored to verify the validity of this approximation. Quasi-steady calculations are made in the stagnation region at discrete instants of time by using the instantaneous velocity distribution from the Giesing time-dependent inviscid flow procedure as a steady outer-edge boundary condition. The viscous calculation is carried out by assuming an initial viscous flow field and then letting the calculation march to a steady-state holding the outer edge velocity constant. The stagnation region calculation is first made at a time t_1 in the cycle assuming the initial flow field to have a quadratic velocity profile. After this initial solution is converged, the next viscous calculation is made at a time t_2 in the cycle using the inviscid flow velocity distribution at time t_2 and assuming as an initial guess that the viscous flow field at time t_2 is a scaled version of the viscous flow field at time t_1. The scaled flow field gives the initial conditions for the viscous flow field and the calculation procedure is then allowed to march in time to a steady-state while holding the outer edge velocity constant. Thus the stagnation region is calculated as a series of quasi-steady solutions at selected points in the cycle by impulsively changing the outer edge inviscid flow velocity distribution and allowing the scaled viscous region to adjust to this new outer edge boundary condition. The time increment $(t_{n+1} - t_n)$ is typically 0.1 for the cycle. If the time required to adjust to this new condition is τ (the relaxation time), the ratio of $\tau/(t_{n+1} - t_n)$ is typically of the order of 0.04. If ϕ_1 is the solution at t_1 and ϕ_2 is the solution at t_2 then τ is typically taken to be the time required for $(\phi - \phi_1) = 0.88 \ (\phi_2 - \phi_1)$. Thus, since the solution approaches ϕ_2 in a somewhat asymptotic manner, τ can be regarded as two time constants of

36

an exponential decay from ϕ_1 to ϕ_2 or from the first steady solution to the second. For the purpose of these calculations the vorticity at each point in the flow field was monitored. The time constant, τ, was defined as the time required for the vorticity at all points in the flow field to satisfy the criteria $(\omega - \omega_1) = 0.88 \ (\omega_2 - \omega_1)$ where ω is the vorticity. Since the time required by the viscous layer to adjust to a new inviscid flow is so much smaller than the time required to change the inviscid flow, the viscous flow may be properly regarded as quasi-steady in the stagnation region. This quasi-steady nature of the viscous leading edge region has also been hypothesized by McCroskey (ref. 37) and Patay (ref. 38), based upon boundary layer calculations.

The location of the stagnation point as a function of the incidence angle is presented in Fig. 16. The surface coordinate, s, is zero at the trailing edge and increases as the coordinate travels along the pressure surface to the leading edge and then along the suction surface back to the trailing edge. The leading edge is located at $s/c = 1.015$ where c is the chord length. Although the viscous flow may be considered quasi-steady, Fig. 16 shows that the inviscid flow is certainly not quasi-steady since the front stagnation point location is not solely determined by the incidence angle but depends upon the flow time history. Predictions of skin friction coefficient in the stagnation region at selected incidence angles are presented in Fig. 17 where the distributions are presented such that time increases from the bottom of the figure to the top. Prediction of momentum thickness and displacement thickness are presented in Figs. 18 and 19; the location of the stagnation point is indicated by a circle. It should be noted that the displacement thickness, δ^*, and the momentum thickness, θ, are defined by

$$\delta^* = \int_0^\delta \left(1 - \frac{u}{u_e}\right) dy \tag{70}$$

$$\theta = \int_0^\delta \frac{u}{u_e} \left(1 - \frac{u}{u_e}\right) dy \tag{71}$$

Since both edge velocity, u_e, and the local velocity, u, are zero at the stagnation point, the integrands are indeterminate; however, the integrals are not necessarily zero. It should be noted that a grid point was not located at the stagnation point in any calculation. As the flow proceeds away from the stagnation point in both the pressure and suction segments the integral thicknesses tend to increase due to the influence of skin friction and tend to

decrease due to the influence of the very strong favorable pressure gradient. The results show the pressure gradient effect to be dominant on the suction side of the stagnation point and the skin friction effect to be dominant on the pressure side of the airfoil. It should be pointed out that the favorable pressure gradient on the suction side of the airfoil is greater than that on the pressure side and, therefore, the results obtained are not at all unreasonable. The variation of mixing length in the stagnation region is presented in Fig. 20. Near the stagnation point the mixing length grows due to the large amount of entrainment of free-stream turbulence which acts as a source term on the turbulence kinetic energy equation, however, in this region the eddy viscosity is small compared to the molecular viscosity due to the relatively small transverse velocity gradients and the large viscous wall damping effect. Elsewhere in the stagnation region the mixing length is negligible.

Predictions of velocity profiles in the stagnation region are presented in Figs. 21 and 22. Predictions of the profile at various incidence angles for a given location on the pressure side of the stagnation point are shown in F 5. 21 and on the suction side of the stagnation point in Fig. 22 where u_∞ is the free-stream approach velocity. When the incidence is at its maximum value, $\alpha = 13$ deg, the stagnation point moves far down on the pressure side of the airfoil as demonstrated by the velocity plots. The profiles on the suction side of the airfoil are fuller than those on the pressure side reflecting the stronger favorable pressure gradients present on the suction surface. It should be noted that all profiles appear to be laminar.

The viscous flow in the pressure side segment containing the transition region is presented in Figs. 23 through 27. The variation of skin friction coefficient is presented in Fig. 23, where the skin friction coefficients at upstream locations in this region indicate laminar flow. As the flow progresses downstream it undergoes transition. As the incidence angle increases the transition is delayed due to the increased favorable pressure gradient and the movement of the stagnation point rearward on the pressure side. At the higher incidence angles transition is delayed until near the end of this segment. Predictions of momentum and displacement thickness for the pressure side transition segment are presented in Figs. 24 and 25. The characteristic sharp increase in slope of the integral quantities as a function of distance at the start of the transition zone is evident at the lower angles of attack. The variation of mixing length is presented in Fig. 26. The pressure side transition region also is calculated assuming a quasi-steady viscous flow field and in this region the ratio of viscous relaxation time to the inviscid flow change time is of the order of 0.15, again indicating quasi-steady viscous flow. Predictions of velocity profiles at a constant stream-wise station in the pressure side transition region are shown in Fig. 27. The

streamwise station was chosen to be near the end of the segment and the velocity profiles show the fully-turbulent, transitional, and laminar character of the flow as the transition zone moves rearward and then forward as the incidence angle increases and decreases, respectively. The results on the fully-turbulent pressure segment are presented in Figs. 28 through 32 which again show skin friction coefficient, displacement thickness, momentum thickness, mixing length distributions, and velocity profiles at specified angles of attack. However, in this segment the quasi-steady approximation is not valid and the flow in this region was predicted as time-dependent and viscous.

The predictions of the flow field for the segment containing the separated region on the suction side of the airfoil are presented in Figs. 33 through 38. At lower incidence angles no bubble is present, however, as the incidence angle increases a bubble does appear. The position of the bubble and the resulting streamline pattern at seven specified incidence angles are presented in Fig. 33. No bubble is present at $\alpha = 2.5$ deg. The theory predicts a bubble to appear in the vicinity of the leading edge of the airfoil by the time the incidence is equal to 6.11 deg. As the incidence angle increases the bubble increases in size and moves upstream. A further increase in incidence leads to a further upstream movement and contraction of the bubble. As the incidence angle is decreased the bubble moves backward on the airfoil, increases in size, then decreases in size, and finally disappears. The bubble behavior predicted by the theory corresponds to experimental observation for hover tests of Velkoff, Blaser, and Jones (ref. 39) and was hypothesized by Ham (ref. 4) based upon various steady-state data and the time-dependent data of Isogai (ref. 40). Ham attributed the dealy in stall under dynamic conditions to the retardation of the bubble reattachment point with incidence angle under dynamic conditions. In the present study the separated viscous flow region was calculated under the viscous quasi-steady assumptions. The ratio of viscous relaxation time to inviscid flow change time was of the order of 0.15, thus indicating that the quasi-steady viscous flow assumption is valid. Therefore, the present results indicate that, if Ham's hypothesis is to be believed, the delay in the movement of the reattachment point is due to the time-dependent nature of the inviscid flow. Distributions of skin friction, momentum thickness, and displacement thickness for the segment containing the separated region are presented in Figs. 34 through 36. The skin friction plot indicates clearly the length of the separated region. The streamwise variation of mixing length for this segment is presented in Fig. 37. The turbulence kinetic energy model has been used to predict transition and the turbulence field in this region. As shown in Fig. 37, the predicted bubbles are transitional. At any given instant the bubble behavior predicted by the present theory and presented in Figs. 33 through 37 is in qualitative agreement with McCullough and Gault's (ref. 1) description of steady-state leading edge bubbles.

The velocity profiles in the suction side separated region at selected instantaneous incidence angles are shown in Fig. 38 at a fixed streamwise location. Moving from left to right, the initial profile, $\alpha = 2.5$ deg, shows that the flow is approaching separation, however, at the low incidence no leading edge separation occurs. The second profile, $\alpha = 6.11$ deg, shows the initiation of flow separation as the bubble appears on the airfoil (see Fig. 33). The third profile, $\alpha = 9.35$ deg, clearly reflects the forward motion of the bubble as the profile shows a larger reversed flow region than the previous profile. As the angle of attack continues to increase, the separation bubble becomes smaller and moves even further forward on the airfoil. The fourth profile shown in Fig. 38 at $\alpha = 13$ deg shows that at this point in the cycle the entire separation bubble has moved upstream of $s/c = 1.057$. The shape of the profile indicates the transitional behavior of the boundary layer in the area of flow reattachment. The last three profiles shown in Fig. 38 then show the rearward movement, growth, and final disappearance of the separation bubble as the incidence returns to its minimum value.

An examination of the suction side inviscid velocity distribution predicted by the Giesing calculation procedure shows a strong adverse pressure distribution followed by a strong favorable pressure distribution in the region of the tab which is located at the trailing edge of the airfoil (see Fig. 1). Even after the smoothing procedure of Eq. (69) was carried out it was felt that adequate resolution in the vicinity of the tab would require more grid points than could be accommodated in core storage if the entire suction fully-turbulent region were done simultaneously and, therefore, the suction side fully-turbulent region itself was divided into two regions both of which were calculated as unsteady regions. The first region is between the 10 percent chord station and the 80 percent chord station and the second region is between the 80 percent chord station and the trailing edge. Calculations in the first of these regions are shown at specified angles of attack in Figs. 39 through 42. The calculations on the aft section of the airfoil are presented in Figs. 43 through 46. Although the suction side trailing edge region appears to approach separation (defined as the appearance of a region of reversed flow), separation is never reached. As shown in Figs. 42 and 46, the flow remains turbulent in these regions. Velocity profiles in both fully-turbulent regions are shown in Fig. 47.

Case II - the stalled airfoil oscillating in pitch. - The second set of calculations made are again for an airfoil oscillating in pitch. This case corresponds to test point 3171.4 of ref. 3 for which the mean incidence is 12.53 deg, the amplitude of oscillation is 5.39 deg, the reduced frequency, k, is 0.242, and the Reynolds number based upon chord is 0.47×10^7. Under static conditions, the maximum lift for a Reynolds number of 0.47×10^7 occurs at 9.5 deg, therefore, the airfoil is operating well above the static stall limit over most of its cycle.

A comparison between theoretical ; predicted and experimentally measured lift and moment coefficients is prese d in Fig. 48. As can be seen, serious disagreement exists between theory and experiment, particularly for the moment coefficient at high incidence. Throughout the entire cycle the predicted lift coefficient is considerably higher than that measured. This comparison indicates that in contrast to Case I which is not in stall, the Case II airfoil is in stall. The differential pressure coefficients, shown in Figs. 49 through 51, also indicate the airfoil is experiencing a more extensive stall at the higher angles of attack. Surface pressure coefficients are shown in Fig. 52. A comparison between Figs. 50 and 51 for theoretical predictions at $x/c = 0.88$ and 0.91 indicates the very poor local prediction at the tab. As in the previous calculations, the velocity distribution in the region of the locally predicted pressure maximum was smoothed using the averaging procedure outlined in Eq. (69). This distribution was then least-squared and input into the viscous flow calculation procedure.

The viscous calculations for the Case II airfoil divide the viscous flow into six regions, including a stagnation region, a pressure side transition region, a pressure side fully-turbulent region, and a suction side separation region, as shown in Fig. 1. In addition, the airfoil suction side fully-turbulent region is divided into two subregions. As for the Case I airfoil the coordinate, s, represents the distance along the surface. Results for the stagnation region are presented in Figs. 53 through 57. As in Case I, it was found that the stagnation region, the pressure side transition region, and the suction side separated region are quasi-steady. In these regions the time required for a viscous solution to adjust from a set of outer boundary conditions at time, t_1, to a new set of outer boundary conditions at a time, $t_1 + \Delta t$, is much less than Δt. The fact that the calculated viscous response time scale is much smaller than the outer flow inviscid time scale demonstrates that the flow in these regions is quasi-steady.

The location of the stagnation point as a function of the incidence angle, shown in Fig. 53, indicates that the stagnation point moves between $s/c = 0.926$ and $s/c = 0.983$. Since the airfoil nose is at $s/c = 1.015$, the stagnation point is always on the underside of the airfoil. The variations of skin friction in the stagnation region at various instantaneous incidence angles are shown in Fig. 54. In this region the skin friction coefficient shows its expected high value in the vicinity of the stagnation point and then rapidly decreases. The variation in momentum thickness and displacement thickness at various instantaneous angles of attack is presented in Figs. 55 and 56. The location of the stagnation point is denoted in Figs. 55 and 56 by an open circle. The predicted mixing length distribution, ℓ_∞/δ, at several incidence angles is presented in Fig. 57. In the region of the stagnation point the mixing length is fairly large due to a large amount of entrainment of free stream turbulence. However, in the immediate vicinity of the stagnation point

the transverse velocity gradients are small and the viscous damping is large leading to the eddy viscosity being much smaller than the laminar viscosity. Thus the flow acts laminar. As the flow proceeds away from the stagnation point, the mixing length decreases but eventually may increase depending on the turbulent energy balance.

Predictions of the flow in the pressure side transition region are presented in Figs. 58 through 61. The skin friction distributions of Fig. 58 and the mixing length distributions of Fig. 61 show the flow to be undergoing transition from the laminar to turbulent state. The transitional nature of the viscous flow is also indicated by the change in slope of the momentum thickness and displacement thickness plots of Figs. 59 and 60. The solutions for the fully-turbulent pressure side region are presented in Figs. 62 through 65. In this region the flow is unsteady and no quasi-steady assumption is used. The flow remains fully-turbulent here as demonstrated by the mixing length distributions presented in Fig. 65.

The segment downstream of the stagnation segment on the suction side of the airfoil is termed the separation region. In this small region extending over 6 percent chord, there is a large adverse pressure gradient and at high incidence angles a leading edge separation bubble is likely to exist. The viscous flow predictions in the separated region are presented in Figs. 66 through 70. A plot of the streamlines at various instantaneous incidence angles is presented in Fig. 66. The results show that a leading edge separation bubble is present through all of the cycle. The cycle proceeds from $\alpha = 7.17$, 11.92, 15.43, 17.92, 15.27, 11.74, and 7.17 in Fig. 66. Although not shown, there does exist a small portion of the cycle for α larger than its minimum value when no bubble is present. As shown in Fig. 66, the bubble demonstrates the expected behavior of appearing as a relatively large bubble, moving forward as incidence angle increases and moving aft as incidence angle decreases. There is also a tendency for the bubble to shorten at the highest incidence angles.

As previously discussed, this predicted behavior is confirmed by experimental evidence (refs 1, 38 through 40). Predictions of skin friction coefficients are presented in Fig. 67 and of momentum and displacement thickness in Figs. 68 and 69. The predicted mixing length distributions of Fig. 70 indicate that the bubbles are transitional as the predicted mixing length is beginning to increase at stations at which the bubble exists. It should be noted that, although the experimental evidence indicates the airfoil is in stall through much of its cycle (Figs. 48 through 50), the predicted leading edge bubble behavior is not significantly different from that predicted in the unstalled airfoil, Case I. The major difference in the leading edge bubble region is that for the Case I airfoil the bubble is present over only approximately one-half the cycle, whereas for the present Case II airfoil the bubble

is present over nearly all of the cycle. However, as will be shown subsequently, in the second suction side fully-turbulent region significant differences between the Case I and Case II calculations appear.

The suction side fully-turbulent region is divided into two segments, the first extending from the 5 percent chord station to the 30 percent chord station, and the second extending from the 30 percent chord station to the trailing edge. The predicted results in the first suction side fully-turbulent region are presented in Figs. 71 through 74. As can be seen, the flow appears to be well-behaved in this segment.

Although the first segment of the suction side Case II fully-turbulent region gives predictions similar to the predictions of the Case I airfoil, the second segment shows a very much different behavior between the Case II and Case I airfoils. It should be recalled that the Case I airfoil was determined experimentally not to 'e in stall, whereas the experimental data shows the Case II airfoil to be in stall through a significant portion of its cycle. As shown in Figs. 43 through 46, which present the suction side trailing-edge region for the Case I airfoil, the viscous flow approaches separation in the vicinity of the trailing edge but trailing edge separation does not occur. It may be expected that for an airfoil at higher incidence angle, such as the Case II airfoil, separation would occur in the trailing edge region. In order to understand the results presented for the Case II trailing edge region, it is helpful to review how the calculation in this region is made.

The trailing edge region is a region in which time-dependent effects are important and, therefore, a time-dependent solution of the reduced Navier-Stokes equations is obtained. Since the segment is solved as a time-dependent flow field, it is necessary to specify an initial flow field at time t_o. This initial flow field is set by assuming that at the upstream boundary of the segment being calculated the flow variables are identical to those at the downstream boundary of the previous upstream segment at the same time t_o. The flow field is then assumed similar in the streamwise coordinate so that at any streamwise station at the initial time, t_o, the flow variables are scaled distributions of the upstream flow variables. The distributions are scaled so as to match the outer edge velocity imposed by the time-dependent inviscid flow calculation procedure. The flow field in the segment being investigated is then calculated by letting the assumed initial flow field develop in time according to the governing equations. At each time, t_n, the upstream boundary conditions are set equal to the conditions calculated at the downstream boundary of the previous segment at time, t_n; the outer edge boundary conditions correspond to the conditions calculated at time t_n by the inviscid flow calculation procedure. Therefore, in summary, an initial flow field is assumed, time-dependent upstream and outer edge boundary conditions obtained from other calculations are imposed and the governing equations are solved.

43

Since the outer flow is cyclic, the effect of the initial conditions in general should disappear and a cyclic viscous solution ought to be calculated. For previous calculations the initial conditions in the viscous region disappear within less than one-quarter of a cycle; that is, the viscous flow solution became cyclic within one and one-quarter cycles of time integration. This was confirmed by carrying out calculations of the time-dependent region over approximately one and one-half cycles.

Calculations for the second segment of the Case II fully-turbulent region are presented in Figs. 75 through 77. In contrast to the Case I calculations in which a cyclic nonseparated viscous region was calculated, the Case II calculations show a large separation bubble to appear. This behavior is demonstrated in Fig. 75 which shows skin friction coefficient at various incidence angles. The coefficient for the initial profile is shown at the bottom of Fig. 75 for an incidence of 7.17 deg. As shown in the remaining plots of Fig. 75, the skin friction in the trailing edge region drops rapidly as time and angle of incidence increase until at $\alpha = 17.92$ deg a significant separation region (indicated by negative skin friction) is present. The separated region continues to increase in extent even after the incidence reaches a maximum and decreases. For example, at 15.27 deg the separated region extends over approximately 50 percent of the suction side of the airfoil. The calculation was continued back to the minimum angle of attack and no tendency for the bubble to disappear was noted. Prediction of momentum thickness and displacement thickness are presented in Figs. 76 and 77, and predicted streamlines are shown in Fig. 78. An examination of the results of Figs. 75 through 77 clearly indicates that the bubble is being prevented from moving upstream only by the upstream initial condition being imposed upon the segment. The dimensionless mixing length originally remained at about 0.09 but as time increased grew to a value of approximately 0.40 in the separated flow regime. In addition, the bubble has, of course, grown to such an extent that the weak-interaction assumption of the viscous layer not affecting the pressure distribution is being violated. The effect of the bubble growth would relax the pressure gradient and in a strong-interaction solution which includes the mutual interaction between the viscous and inviscid flow fields an equilibrium may be reached and the bubble may stop growing. Within the limits of weak-interaction theory the indication is that the leading edge bubbles in the Case I unstalled and Case II stalled airfoils behave very similarly; no dramatic flow phenomena in the leading edge region are predicted in the stalled case. However, the trailing edge regions behave quite differently. In the unstalled case, Case I, the flow remains attached; in the stalled case, Case II, a trailing edge bubble is formed which moves rapidly upstream and separates the flow over a significant portion of the airfoil suction surface. This behavior suggests a possible stall mechanism for this

type of airfoil in which a trailing edge bubble is formed and then rapidly moves toward the leading edge as incidence is increased until a·large portion of the airfoil is separated and stall occurs.

Case III - the stalled airfoil oscillating in heave. - The final set of oscillating airfoil calculations are for an airfoil oscillating sinusoidally in heave. The airfoil and motion originally chosen correspond to test point 3090.2 of ref. 3 for which the incidence angle in absence of vertical motion is equal to 12.36 deg, the magnitude of the vertical oscillation is 0.306 based on the semichord, the reduced frequency, k, is 0.242, and the Reynolds number based upon chord is 0.26×10^7. Under static conditions, the maximum lift for a Reynolds number of 0.26×10^7 occurs at 12.9 deg and the nonlinear portion of the lift-incidence curve begins at approximately 9 deg. Thus the airfoil is being investigated at conditions which exceed the limits of static stall.

Theoretical prediction of the lift and moment coefficients made using the theory of Giesing (ref. 10) are compared with the experimentally measured values of ref. 3, in Fig. 79. The predictions are indicated by the chain line and termed Run A. As can be seen, there is considerable discrepancy between theory and experiment, particularly for the moment coefficient at large negative values of normalized transverse location. The predicted lift coefficient is higher than the measured value throughout the entire cycle. However, some discrepancies do appear between the data of Liiva (see ref. 41) and that of Halfman, Johnson, and Haley (ref. 42) and Rainey (ref. 43). In all three cited references experimental investigations were made for airfoils oscillating in heave. The data of both refs. 42 and 43 showed that the airfoil dissipates work to the surrounding air and, therefore, the airfoil is stable in the bending mode. The data of Liiva (refs. 3 and 41) on the other hand disagrees and shows regions of bending mode instability to exist under the influence of heave (ref. 41). Although this stability discrepancy is a discrepancy in the aeroelastic response, it may result from a discrepancy in the flow fields present about the airfoils. In view of these discrepancies between the Liiva data (ref. 41) and that of Halfman (ref. 42) and Rainey (ref. 43) and the fact that the airfoil under the stated conditions only appeared to be stalled at the high negative values of the transverse coordinate, a second inviscid calculation, Run B, was made in which all motion parameters remained the same except the vertical oscillation was set at 0.612 based on semichord. In this second case, Run B, the maximum instantaneous incidence angle is approximately 20 deg as opposed to a maximum of 16 deg in the original case and thus the second case, Run B, is a case in which the airfoil is much more likely to be in the region of stall over a significant portion of the motion cycle. Since it was desired to calculate the viscous flow field under conditions for which stall does occur and since the heave data of refs. 3 and 41 showed discrepancies with that of refs. 42 and 43,

the second inviscid run was used for the viscous calculations to insure calculation of a stalled airfoil. Theoretical predictions of lift and moment coefficient made using the Giesing procedure (ref. 10) are shown by the solid line for Run B in Fig. 79. The differential pressure coefficients are shown in Figs. 80 through 82. Surface pressure coefficients for Run B are presented in Fig. 83. A comparison between Figs. 81 and 82 for theoretical predictions at $x/c = 0.88$ and 0.91 indicate the very poor local prediction at the airfoil tab which was also present for both the Case I and Case II airfoils. As in the previous calculations, the velocity distribution in the region of the locally predicted pressure maximum was smoothed using the averaging procedure of Eq. (69). This distribution was then least-squares smoothed and input into the viscous flow calculation procedure.

The viscous calculations for the Case III airfoil divide the viscous flow field into only five regions instead of the six regions used for the Case I and Case II airfoils. The division is as follows: a stagnation region, a pressure side transition region, a pressure side fully-turbulent region, a suction side separation region, and a suction side fully-turbulent region. In the calculations made for the Case I and Case II airfoils, the suction side fully-turbulent region was further divided into two segments. However, due to the results of the calculations for the Case II airfoil in which a large trailing edge separation bubble was prevented from moving forward due to the location of the segment boundary, the suction side fully-turbulent region was treated as a single segment for the Case III airfoil. As in Case I and Case II, it was again found that the stagnation region, the pressure side transition region, and the suction side separated region were quasi-steady. Thus the flow in these regions was calculated using the quasi-steady viscous flow assumption although the imposed outer edge velocity distribution was that obtained from the time-dependent inviscid flow computation.

The results of the calculation for the stagnation region are presented in Figs. 84 through 88. The variation of skin friction in the stagnation region at various instantaneous transverse positions is shown in Fig. 85. In this region the skin friction coefficient shows its expected high value in the vicinity of the stagnation point and then rapidly decreases. The variation in momentum thickness and displacement thickness at various instantaneous transverse positions is presented in Figs. 86 and 87. The stagnation point is indicated by an open circle. The predicted mixing length distribution, ℓ_∞/δ, at several transverse positions is presented in Fig. 88.

Predictions of the flow in the pressure side transition region are presented in Figs. 89 through 92. The skin friction distributions of Fig. 89 and the mixing length distributions of Fig. 92 show the flow to be undergoing transition at all but two transverse positions. The transitional nature of the viscous flow field is also indicated by the change in slope of the

46

momentum thickness and displacement thickness plots of Figs. 90 and 91. The solutions for the fully-turbulent pressure side region are presented in Figs. 93 through 96. In this region the flow is unsteady and no quasi-steady assumption is used. The flow remains fully-turbulent here, as demonstrated by the mixing length distributions presented in Fig. 96.

The Case III separation region extends over 7 percent chord where there is a large adverse pressure gradient and due to the high incidence angle (recall that the geometric incidence angle is constant for this case) a leading edge separation bubble is likely to exist. The viscous flow predictions in the separated region are presented in Figs. 97 through 101. A plot of the streamlines at various instantaneous transverse locations is presented in Fig. 97. The results show that a leading edge separation bubble is present through the complete cycle. The cycle proceeds from Y/Y_{max} = -1.0, -0.309, +0.309, +1.0, +0.309, -0.309, and -1.0 in Fig. 97 with time increasing from bottom to top. Note that initially the airfoil is in its lowest position and the separation bubble has moved forward on the airfoil. Then, as the airfoil moves upward, the bubble moves back and grows in size. As the airfoil begins to move downward, the separation bubble becomes shorter and moves forward again. This behavior is explained by considering the relative incidence angle of the airfoil. Although the incidence angle (measured with respect to a constant reference direction) is constant, as the airfoil moves upward its velocity is added in a vector sense to the velocity of the free stream and the resultant velocity yields a lower effective incidence angle. Likewise, when the airfoil moves downward, the effective incidence angle is increased. With this behavior in mind, the predicted results appear to be in agreement with what is observed experimentally for airfoils oscillating in pitch (refs. 1, and 38 through 40). Predictions of skin friction coefficients are presented in Fig. 98 and of momentum and displacement thickness in Figs. 99 and 100. The predicted mixing length distributions of Fig. 101 indicate that the bubbles are transitional as the predicted mixing length is beginning to increase at stations in which the bubble exists.

The suction side fully-turbulent region of the Case III airfoil was treated as one segment rather than the two used for the Case I and Case II airfoils. This was accomplished by using variable mesh spacing in the streamwise direction. The streamwise mesh spacing varied so that a relatively tight mesh was used at the upstream boundary of the segment. The mesh spacing then increased until the region of the tab was approached. Near the tab the spacing was again decreased. The calculation was performed in this manner so that any separation bubble which appeared would have a segment of nearly 90 percent of the airfoil chord over which it could grow without encountering the upstream boundary of the segment as it did in the Case II calculation. The results for this segment are shown in Figs. 102 through 104. As in the Case

II calculation, a cold start initial condition is shown at the bottom of Figs. 102 through 104. As discussed previously, this cold start initial condition is obtained by specifying the stream function and vorticity profiles at the upstream boundary and then scaling these profiles at each streamwise station to match the edge velocity. As the calculation progresses in time a large separation bubble appears almost immediately and continues to grow. This is shown in the plots of skin friction (Fig. 102) where, for example, when the airfoil is at a transverse position of +1.00 the separated region is almost 50 percent of the chord in length. When the airfoil begins to move downward and the effective incidence angle becomes greater, the separated region grows rapidly until at $Y/Y_{max} = +0.8$ it covers nearly 70 percent of the airfoil, as indicated by the top plot of skin friction coefficient shown in Fig. 102, at which time the calculation was terminated. The momentum thickness and displacement thickness are shown in Figs. 103 and 104. Figure 103 shows that the displacement thickness at the termination of the run is extremely large and the assumption of weak-interaction is severely violated. For this reason and due to the similar behavior of the Case II calculation, no attempt was made to carry out the computation for the remainder of the cycle, although the calculation was still numerically stable.

DISCUSSION AND CONCLUSIONS

A weak-interaction solution for the problem of the flow field about an airfoil in arbitrary unsteady motion has been developed by combining an unsteady nonlinear potential flow computer code (ref. 10) with a finite-difference viscous flow computer code (ref. 12). The potential flow procedure serves to predict an inviscid flow field about the airfoil and this inviscid flow field is input into the viscous procedure as an outer edge boundary condition for the viscous layer. The viscous development is then predicted under the influence of the applied inviscid flow field using the weak-interaction assumption that the viscous flow does not significantly influence the outer inviscid flow field. The weak-interaction assumption is valid as long as the viscous displacement thickness remains small compared to the airfoil thickness. However, when the displacement thickness becomes large and significantly modifies the inviscid pressure distribution, such as in a region of significant boundary layer separation, the weak-interaction theory is invalid and accurate predictions of the flow field under these conditions requires a theory which recognizes the mutual interaction between the viscous inner and nominally inviscid outer flow fields. Such a strong-interaction calculation procedure could be developed by an extension of a successful weak-interaction procedure in which an inner viscous solution such as the viscous solution of the present report is coupled to an inviscid outer solution. The coupling would require continuity of flow angle along the line

joining these solutions. Alternatively, the entire flow field could be
solved by the Navier-Stokes equations thus avoiding the problem of coupling
two different solutions in two regions of the flow.

Although a weak-interaction solution is limited in applicability to flow
situations in which the viscous displacement thickness does not significantly
affect the inviscid pressure distribution, weak-interaction solutions should
accurately predict airfoil flow fields if no significant regions of separation
are present. In this regard the weak-interaction solution can give a
quantitative picture of viscous flow phenomena such as demonstrated by the
separation bubble calculation presented previously. In addition, the procedure
should be able to predict incipient stall since when incipient stall occurs
the separated region is still small enough to allow the weak-interaction
assumption to be valid. It should be noted that in their study of transitional
separation bubbles Briley and McDonald (ref. 12) included a strong-interaction
viscous correction to the inviscid pressure field. However, this was a
linearized correction and is only valid for thin separated regions. Therefore,
it could not be validly applied to the thick trailing edge separated regions
computed in the present effort.

Three airfoil calculations have been presented; the first of these,
Case I, corresponds to an airfoil experimentally found not to exhibit any
characteristics of stall, and the second and third calculations, Case II and
III, were for airfoils which are in stall over a significant portion of the
motion cycle. The viscous calculations in the first unstalled case differed
considerably from the calculations in the second and third stalled cases. In
the unstalled case a well-behaved viscous flow was found to exist over the
entire airfoil, whereas in the stalled cases significant separated regions
appeared along the trailing section of the airfoil. Leading edge separation
appears on the suction surface in all cases; however, in both the stalled and
unstalled calculations the flow in the leading edge separation region soon
undergoes transition, reattaches, and forms a well-behaved bubble. Thus, no
qualitative differences in the leading edge separation bubbles are predicted
between the experimentally observed unstalled and stalled airfoils.

The predicted leading edge bubble behavior indicates a possible mechanism
of leading edge stall. As the airfoil increases in incidence, a bubble
appears in the leading edge region. In each case the boundary layer is laminar
at the leading edge bubble separation point and undergoes transition to the
turbulent state. The calculations show an increase in incidence to be
accompanied by a forward movement and a shortening of the bubble, as has been
deduced from experimental data by Velkhoff, Blaser, and Jones (ref. 39),
Isogai (ref. 40), and McCullough and Gault (ref. 1). In each case the forward

movement of the separation point with increasing incidence angle is
accompanied by a forward movement in transition location and, hence, a
subsequent forward movement in reattachment. The net result being a predicted
shortening of the separation bubble as incidence increases.

Whether or not the bubble undergoes transition is determined by both the
applied pressure gradient and the free-stream disturbance level. If the
bubble does not undergo transition, it is expected that the bubble would not
reattach and leading edge stall would occur. Within the limits of weak-
interaction theory this would correspond to a viscous solution in which the
leading-edge bubble were to grow very rapidly leading to a large separated
region. In the present calculations transition always occured soon after
separation; however, transition is a strong function of the free-stream
turbulence level (ref. 26) and, if a low enough turbulence level were assumed,
transition would be expected to be delayed and the leading edge bubble could,
depending on local conditions, grow rapidly leading to eventual leading edge
stall.

The major difference in the visccus calculations between the stalled and
unstalled airfoils occurs in the trailing edge suction side region. In Case I,
the calculation for the air foil which has been determined experimentally not
to be in stall, the suction side trailing edge segment is a well-behaved
viscous flow region. The viscous layer approaches separation at the junction
of the airfoil skin and the trailing edge tab but separation does not occur.
In Case II and Case III, both of which have been determined experimentally to
be in stall, a large separated region does appear along the suction side
trailing segment. Due to the absence of a strong-interaction mechanism for
alleviating the pressure distribution, the separated region grows uncontrolled.
In Case II the trailing edge separated region encompasses over 50 percent of
the airfoil suction surface and is prevented from becoming larger only by the
location of the segment boundary. In Case III the trailing edge separated
region grew to 70 percent of the airfoil surface and the displacement thick-
ness reached approximately 25 percent of the airfoil chord when the calcula-
tion was terminated. The appearance of this large separated region is
interpreted as indicative of stall. Thus the viscous behavior in the
unstalled and stalled cases is significantly different. In the unstalled
case, Case I, the flow remains attached in the trailing edge region, whereas
in the stalled cases, Case II and Case III, a trailing edge bubble is formed
which moves rapidly upstream and separates the flow over a significant portion
of the airfoil suction surface. This behavior suggests a possible stall
mechanism for this type of airfoil and motion in which a trailing edge bubble
is formed and then rapidly moves toward the leading edge until a large portion
of the airfoil is separated and stall occurs. This mechanism could cause
trailing edge stall or could modify the overall pressure distribution about
the airfoil in such a manner as to cause the leading edge bubble to fail to

reattach; this failure of the leading edge bubble to reattach would cause the airfoil to go into leading edge stall. In regard to the problem of whether the NACA 0012 airfoil actually undergoes leading edge or trailing edge stall, it has been pointed out by Ericsson and Reding (ref. 6) that under steady conditions the NACA 0012 airfoil is a prime candidate for transition between stall types with variation in chord Reynolds number; according to ref. 6, the stall shifts from the leading edge type to the trailing edge type at a Reynolds number based upon chord of approximately 0.6×10^7. Therefore, the NACA 0012 airfoil could be expected to exhibit either leading edge or trailing edge stall or even a combination of the two.

The viscous flow calculation procedure divides the entire viscous region into several subregions and an examination of the results in each of these subregions indicates the degree of sophistication required in each portion of the viscous flow field. The calculations indicate the leading edge region to be quasi-steady; i.e., the viscous shear layer adjusts to changes to the outer edge boundary conditions in a time scale much shorter than the time scale of the outer flow. This quasi-steady conclusion has also been reached by McCroskey (ref. 37) and Patay (ref. 38) based upon boundary layer calculations. When the leading edge region is quasi-steady and when no viscous flow separation appears, the viscous region can (and should) be calculated through a finite-difference steady-state boundary layer procedure. In general, finite-difference, steady-state boundary layer procedures would be expected to be considerably more rapid in terms of computer time than a solution of the full Navier-Stokes equations or than the solution of the 'reduced' Navier-Stokes equations used in the present effort. It should be pointed out that the reduced Navier-Stokes equations are equivalent to a set of time-dependent boundary layer equations with the addition of a streamwise diffusion term and solve the steady-state problem by assuming an initial flow field and then allowing the flow field to develop in time under steady-state boundary conditions. However, the present procedure for solving the reduced equations is highly competitive with the more usual time-dependent boundary layer codes.

The pressure side of the airfoil downstream of the stagnation region consists of a transition region and a fully-turbulent region. The transition region has been found to be quasi-steady for the airfoils investigated under the present effort. Therefore, as for the stagnation region, a steady-state boundary layer procedure may be preferable to the asymptotic time solution of the reduced set of equations used in the present study. However, the best available transition model must be embodied in any computation procedure for the pressure side transition region. The fully-turbulent pressure side region was found to be unsteady and it is felt that the procedure which was used (i.e., the solution of the reduced set of equations) was competitive with any presently available alternative procedure.

On the suction surface the stagnation region is followed by the region where a leading edge separation bubble is expected to appear. This region contains a very complex flow field which exhibits both eparation and transition. Any procedure used in this region should be capable of accurately predicting both phenomena. As has been shown by the predicted separation bubble behavior, the present procedure appears to predict the experimentally observed physical behavior of leading edge separation bubbles. Based upon the excellent qualitative predictions of the present procedure and the extreme complexity of the flow field in this region, it does not appear that any simplified analysis should be used to predict the leading edge separation bubble behavior. The leading edge separation region is followed by a suction side unsteady, fully-turbulent flow region. Once again it is felt that the procedure for solving the reduced set of equations, which was used in this region, should be competitive with any pre ently available alternate procedure.

In summary, the major modifications to the current procedure which would be recommended in a weak-interaction solution are in the stagnation region and the pressure side transition region. In both regions a savings in computer running time could be gained by replacing the present solution procedure with a steady-state finite-difference boundary layer procedure using the best available transition model. In all other regions the procedures used in the present effort appear to contain a necessary and sufficient amount of sophistication to obtain weak-interaction solutions.

APPENDIX A

THE TURBULENT VORTICITY TRANSPORT EQUATION
INCLUDING CURVATURE EFFECTS

For flow over a curved wall a curvilinear coordinate system is introduced in which the x-axis is along the wall and the y-axis perpendicular to the wall. The coordinate system, therefore, consists of a set of curves parallel to the wall and a set of straight lines perpendicular to the wall. As shown by ref. 15, if the curvature is denoted by k the streamwise and transverse momentum equations become

$$\frac{\partial u}{\partial t} + \frac{u}{1+ky} \frac{\partial u}{\partial x} + v \frac{\partial u}{\partial y} + \frac{uvk}{1+ky} = \frac{-1}{1+ky} \frac{1}{\rho} \frac{\partial p}{\partial x} + \text{viscous terms} \quad \text{(A-1)}$$

$$\frac{\partial v}{\partial t} + \frac{u}{1+ky} \frac{\partial v}{\partial x} + v \frac{\partial v}{\partial y} - \frac{ku^2}{1+ky} = - \frac{1}{\rho} \frac{\partial p}{\partial y} + \text{viscous terms} \quad \text{(A-2)}$$

In the curvilinear coordinate system the vorticity, $\vec{\omega}$, is given by

$$\vec{\omega} = \nabla \times \vec{v} = \frac{\vec{e}_3}{1+ky} \left\{ \frac{\partial v}{\partial x} - \frac{\partial}{\partial y} \left[(1+ky) u \right] \right\} \quad \text{(A-3)}$$

where $\vec{e}_3$ is the unit vector perpendicular to the x-y plane. The vorticity transport equation is obtained by subtracting Eq. (A-1) multiplied by (1+ky) from Eq. (A-2) to obtain a transport equation for $\vec{\omega}$. In the present effort

$$\xi = - \omega \quad \text{(A-4)}$$

As in the case of Cartesian coordinates, the additional turbulence stress terms are obtained by dividing u and v into mean and fluctuating parts, averaging, and then combining the equations. Since all extra turbulence stress terms result from the nonlinear convective terms, the nonlinear convective terms are now examined in detail. Before dividing the nonlinear convective terms into mean and fluctuating parts, the streamwise and transverse momentum equations, Eqs. (A-1) and (A-2), are modified through the continuity equation

$$\frac{1}{1+ky}\ \frac{\partial u}{\partial x} + \frac{\partial v}{\partial y} + \frac{ky}{1+ky} = 0 \tag{A-5}$$

Use of Eq. (A-5) lets the nonlinear convective term in the streamwise and transverse equations, C_{T_1} and C_{T_2}, be expressed as

$$
\begin{aligned}
C_{T_1} &= \frac{u}{1+ky}\ \frac{\partial u}{\partial x} + v\frac{\partial u}{\partial y} + \frac{kuv}{1+ky} \\
&= \frac{1}{1+ky}\ \frac{\partial u^2}{\partial x} + \frac{\partial uv}{\partial y} + 2\frac{kuv}{1+ky} - \frac{1}{1+ky}\ \frac{u\partial v}{\partial x} - \frac{u\partial v}{\partial y} - \frac{kuv}{1+ky} \\
&= \frac{1}{1+ky}\ \frac{\partial u^2}{\partial x} + \frac{\partial uv}{\partial y} + \frac{2kuv}{1+ky}
\end{aligned} \tag{A-6}
$$

$$
\begin{aligned}
C_{T_2} &= \frac{u}{1+ky}\ \frac{\partial v}{\partial x} + \frac{v\partial v}{\partial y} - \frac{u^2}{1+ky} \\
&= \frac{1}{1+ky}\ \frac{\partial uv}{\partial x} + \frac{\partial v^2}{\partial y} + \frac{k(u^2-v^2)}{1+ky} - \frac{1}{1+ky}\ \frac{v\partial u}{\partial y} - \frac{v\partial v}{\partial y} - \frac{kv^2}{1+ky} \\
&= \frac{1}{1+ky}\ \frac{\partial uv}{\partial x} + \frac{\partial v^2}{\partial y} - \frac{k(u^2-v^2)}{1+ky}
\end{aligned} \tag{A-7}
$$

When the velocities are divided into mean and fluctuating parts and the mean continuity equation is applied the results are

54

$$C_{T_1} = \frac{1}{1+ky}\frac{\partial(\overline{u}^2+\overline{u'^2})}{\partial x} + \frac{\partial(\overline{u}\,\overline{v}+\overline{u'v'})}{\partial y} + \frac{2k(\overline{u}\,\overline{v}+\overline{u'v'})}{1+ky}$$

$$= \frac{1}{1+ky}\,\overline{u}\frac{\partial\overline{u}}{\partial x} + \overline{v}\frac{\partial\overline{u}}{\partial y} + \frac{k\overline{u}\,\overline{v}}{1+ky} + \frac{1}{1+ky}\frac{\partial\overline{u'^2}}{\partial x} + \frac{\partial\overline{u'v'}}{\partial y} + \frac{2k\overline{u'v'}}{1+ky} \tag{A-8}$$

$$C_{T_2} = \frac{1}{1+ky}\frac{\partial(\overline{u}\,\overline{v}+\overline{u'v'})}{\partial x} \quad \frac{\partial(\overline{v}^2+\overline{v'^2})}{\partial y} - \frac{k\left[(\overline{u}^2-\overline{v}^2)-(\overline{u'^2}-\overline{v'^2})\right]}{1+ky}$$

$$= \frac{1}{1+ky}\,\overline{u}\frac{\partial\overline{v}}{\partial x} + \overline{v}\frac{\partial\overline{v}}{\partial y} - \frac{k\overline{u}^2}{1+ky} \tag{A-9}$$

$$+ \frac{1}{1+ky}\frac{\partial(\overline{u'v'})}{\partial x} + \frac{\partial\overline{v'^2}}{\partial y} + \frac{k(\overline{v'^2}-\overline{u'^2})}{1+ky}$$

The fluctuating averaged terms in Eqs. (A-8) and (A-9) contribute to the turbulence stresses. The contribution of the fluctuating terms to the vorticity equation is obtained by bringing the terms to the right-hand side of the equations, taking the derivative with respect to y of Eq. (A-8) multiplied by (1+ky), and subtracting this from the derivative with respect to x of Eq. (A-9) which gives the contribution C_{T_3}

$$C_{T_3} = \frac{\partial}{\partial x}\left\{ + \frac{1}{1+ky}\frac{\partial(-\overline{u'v'})}{\partial x} - \frac{\partial\overline{v'^2}}{\partial y} - \frac{k(\overline{v'^2}-\overline{u'^2})}{1+ky}\right\}$$

$$- \frac{\partial}{\partial y}\left\{ -\frac{\partial\overline{u'^2}}{\partial x} + (1+ky)\left[\frac{\partial(-\overline{u'v'})}{\partial y} + \frac{2(-\overline{u'v'})}{1+ky}k\right]\right\} \tag{A-10}$$

When the usual boundary layer type assumption is made that derivatives with respect to y are much large than those with respect to x, this reduces to

$$C_{T_3} = -\frac{\partial}{\partial y} \left\{ (1 + ky) \left[\frac{\partial(-\overline{u'v'})}{\partial y} + 2\frac{(-\overline{u'v'})}{1 + ky} \kappa \right] \right\} \tag{A-11}$$

By analogy to the procedure for two-dimensional flow $(-\overline{u'v'})$ is related to the mean flow field through an eddy viscosity, ν_t. It should be noted that in the present calculations ν_t is not solely dependent on local mean flow conditions but rather is dependent upon the flow history through the turbulence kinetic energy equation. The relation between $-\overline{u'v'}$ and ν_t is given by

$$-\overline{u'v'} = -\nu_t \omega \tag{A-12}$$

Therefore,

$$C_{T_3} = (1 + ky) \frac{\partial^2(\nu_t \omega)}{\partial y^2} + 3k \frac{\partial}{\partial y}(\nu_t \omega) \tag{A-13}$$

It should be noted that the relationship between $-\overline{u'v'}$ and ν_t given in Eq. (A-12) is somewhat different than the usual formulation

$$-\overline{u'v'} = \nu_t \frac{\partial \overline{U}}{\partial y} \tag{A-14}$$

However, examining Eq. (A-3), with the assumption that $\partial v/\partial x$ is small it is found that

$$\omega = -\frac{\partial \overline{U}}{\partial y} - \frac{uk}{1 + ky} \tag{A-15}$$

and, thus, Eq. (A-12) may be written

56

$$-\overline{u'v'} = \nu_t \, \frac{\partial \bar{u}}{\partial y} + \frac{uk}{1+ky} \qquad\qquad (A-16)$$

Thus it is evident that the formulation of Eq. (A-12) differs from the usual formulation of Eq. (A-14) only in regions of significant curvature, or only in the region of the leading edge of the airfoil where the flow is expected to remain laminar and ν_t is negligible. In other regions of the airfoil, where the curvature is negligible, the two formulations are equivalent.

REFERENCES

1. McCullough, G. B. and Gault, D. E.: Examples of Three Representative
    Types of Airfoil Section Stall at Low Speed. NACA TN 2502,
    September 1951.

2. Carta, F. O.: Analysis of Oscillatory Pressure Data Including Dynamic
    Stall Effects. NASA CR- to be published.

3. Gray, L. and Liiva, J.: Two-Dimensional Tests of Airfoils Oscillating
    Near Stall, Vol. II, Data Report. USAAVLABS Technial Report 68-13B,
    April 1968.

4. Ham, N. D.: Aerodynamic Loading on Two-Dimensional Airfoil During
    Dynamic Stall. AIAA Journal, Vol. 6, No. 10, 1968, pp. 1927-1934.

5. Carta, F. O., Commerford, G. L. and Carlson, R. G.: Determination of
    Airfoil and Rotor Blade Dynamic Stall Response. Journal of the American
    Helicopter Society, Vol. 18, No. 2, 1973, pp. 31-39.

6. Ericsson, L. E. and Reding, J. P.: Unsteady Airfoil Stall.
    NASA CR-66787, 1969.

7. Ericsson, L. E. and Reding, J. P.: Analytic Predictions of Dynamic Stall
    Characteristics. Preprint No. 72-682, AIAA, 1972.

8. Crimi, P. and Reeves, B. L.: A Method for Analyzing Dynamic Stall of
    Helicopter Rotor Blades. NASA CR-2009, May 1972.

9. Briley, W. R. and McDonald, H.: An Implicit Numerical Method for the
    Multidimensional Compressible Navier-Stokes Equations. United Aircraft
    Research Laboratories Report M911363-6, November 1973.

10. Giesing, J. P.: Unsteady Two-Dimensional Potential Flow With Lift.
    Douglas Aircraft Company Report No. LB (32144), March 19...

11. Giesing, J. P.: Nonlinear Two-Dimensional Unsteady Potential Flow With
    Lift. Preprint No. 66-968, AIAA, 1966.

12. Briley, W. R. and McDonald, H.: Numerical Prediction of Incompressible
    Separation Bubbles. United Aircraft Research Laboratories Report
    N110887-3, June 1974.

13. Douglas, J. and Gunn, J. E.: A General Formulation of Alternating Direction Methods. Numerische Math., Vol. 6, 1964, pp. 428-453.

14. Liu, D. C. S. and Chen, C. F.: Numerical Experiments in Time-Dependent Rotational Couette Flow. Journal of Fluid Mechanics, Vol. 59, Part 1, 1973, pp. 77-95.

15. Schlichting, H.: Boundary Layer Theory, Fourth Edition. McGraw-Hill Book Co., Inc., New York, 1960.

16. Kline, S. J., Morkovin, M. V., Sovran, G., and Cockrell, D. J., Ed.: Proceedings: Computation of Turbulent Boundary Layers - 1968 AFOSR-IFr-Stanford Conference, Vol. I, December 1968.

17. Mueller, T. M. and Robertson, J. M.: A Study of the Mean Motion and Turbulence Downstream of a Roughness Element. Modern Developments in Theoretical and Applied Mechanics, Vol 1, Plenum Press, New York, 1963.

18. Goldberg, P.: Upstream History and Apparent Stress in Turbulent Boundary Layers. M.I.T. Turbine Laboratory Report No. 85, 1966.

19. Patel, V. C. and Nash, J. F.: Some Solutions of the Unsteady Turbulent Boundary Layer Equations. IUTAM Symposium on Unsteady Boundary Layers, Quebec, Canada, 1971.

20. Nash, J. F., Carr, L. W., and Singleton, R. E.: Unsteady Turbulent Boundary Layers in Two-Dimensional Incompressible Flow. Preprint No. 73-650, AIAA, July 1973.

21. McDonald, H. and Camarata, F. J.: An Extended Mixing Length Approach for Computing the Turbulent Boundary Layer Development. Proceedings of the AFOSR-IFP-Stanford Conference on Boundary Layer Prediction (Stanford, California), December 1968.

22. Favre, A. J.: The Equations of Compressible Turbulent Gases. Annual Summary Report No. 1, Institute de Mechanique Statistique de la Turbulence, January 1965.

23. Bradshaw, P. and Ferris, D. H.: Calculation of Boundary Layer Development Using the Turbulent Kinetic Energy Equation: Compressible Flow on Adiabatic Walls. Journal of Fluid Mechanics, Vol. 46, 1971, pp. 83-110.

24. Hinze, J. O.: Turbulence. McGraw-Hill Book Co., Inc., New York, 1959.

25. Townsend, A. A.: Equilibrium Layers and Wall Turbulence. Journal of Fluid Mechanics, Vol. 11, 1961, pp. 97-120.

26. McDonald, H. and Fish, R. W.: Practical Calculations of Transitional Boundary Layers. International Journal of Heat and Mass Transfer, Vol. 16, No. 9, 1973, pp. 1729-1744.

27. McDonald, H.: Mixing Length and Kinematic Eddy Viscosity in a Low Reynolds Number Boundary Layer. United Aircraft Research Laboratories Report J214453-1, September 1970.

28. Shamroth, S. J. and McDonald, H.: Assessment of a Transitional Boundary Layer Theory at Low Hypersonic Mach Numbers. NASA CR-2131, November 1972.

29. Kreskovsky, J. P., Shamroth, S. J., and McDonald, H.: Parametric Study of Relaminarization of Turbulent Boundary Layers on Nozzle Walls. NASA CR-2370, 1974.

30. Hairston, D. E.: Survey and Analysis of Current Boundary Layer Transition Prediction Techniques. Preprint No. 71-985, AIAA, October 1971.

31. Peaceman, D. N. and Rachford, H. H.: The Numerical Solution of Parabolic and Elliptic Differential Equations. Journal of the Society of Industrial and Applied Mathematics, Vol. 3, No. 42, 1955, pp. 28-41.

32. McDonald, H. and Kreskovsky, J. P.: Effect of Free Stream Turbulence on the Turbulent Boundary Layer. United Aircraft Research Laboratories Report M110887-1, June 1973.

33. Carta, F. O., Commerford, G. L., Carlson, R. G., and Blackwell, R. H.: Investigation of Airfoil Dynamic Stall and Its Influence on Helicopter Control Loads. USAAMRDL Technical Report 72-51, 1972.

34. Lighthill, M. J.: The Response of Laminar Skin Friction and Heat Transfer to Fluctuations in the Stream Velocity. Proceedings of the Royal Society of London, Series A, Vol. 224, June 1954, pp. 1-23.

35. Rosenhead, L. and Simpson, J. H.: Note on the Velocity Distribution in the Wake Behind a Flat Plate Along the Streamline. Proceedings of the Cambridge Philosophical Society, Vol. 32, 1936.

36. Karlsson, S. K. F.: An Unsteady Turbulent Boundary Layer. Journal of Fluid Mechanics, Vol. 5, 1959, pp. 622-636.

37. McCroskey, W. J.: Inviscid Flow Field of an Unsteady Airfoil. AIAA Journal, Vol. 11, No. 8, August 1973, pp. 1130-1137.

38. Patay, S. A.: Leading Edge Separation on an Airfoil During Dynamic Stall. M.I.T. Aeroelastic and Structures Research Laboratory Report ASRL TR 156-1, 1969.

39. Velkoff, H. R., Blaser, D. A., and Jones, K. M.: Boundary Layer Discontinuity on a Helicopter Rotor Blade in Hovering. Journal of Aircraft, Vol. 8, 1971, pp. 101-107.

40. Isogai, K.: An Experimental Study of the Unsteady Behavior of a Short Bubble of an Airfoil During Dynamic Stall With Special Reference to the Mechanism of the Stall Overshoot Effect. M.I.T. ASRL TR-130-2, June 1970.

41. Liiva, J.: Unsteady Aerodynamic and Stall Effects on Helicopter Rotor Blade Airfoil Sections. Preprint No. 68-58, AIAA, 1968.

42. Halfman, R. L., Johnson, H. C., and Haley, S. M.: Evaluation of High Angle-of-Attack Aerodynamic Derivatives and Stall Flutter Prediction Techniques. NACA TN 2533, November 1951.

43. Rainey, A. G.: Measurements of Aerodynamic Forces for Various Mean Angles of Attack on an Airfoil Oscillating in Pitch and on Two Finite Span Wings Oscillating in Bending with Emphasis on Damping in Stall. NACA Report 1305, 1957.
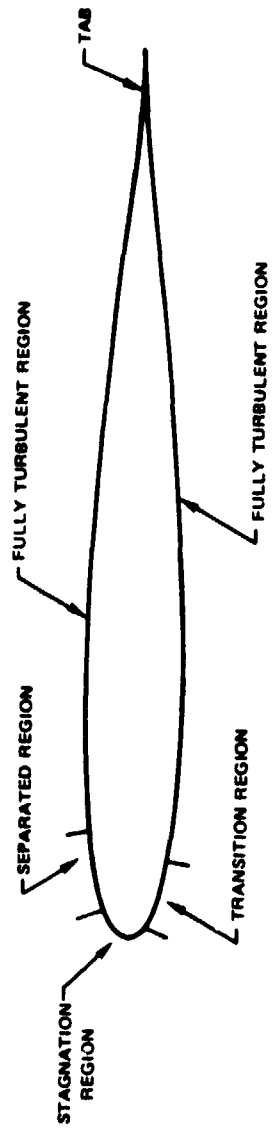
Figure 1. – Division of viscous flow regions.

THEORY OF GIESING (REF. 10)

EXPERIMENTAL DATA OF CARTA ET AL (REF. 33)

LIFT COEFFICIENT

MOMENT COEFFICIENT
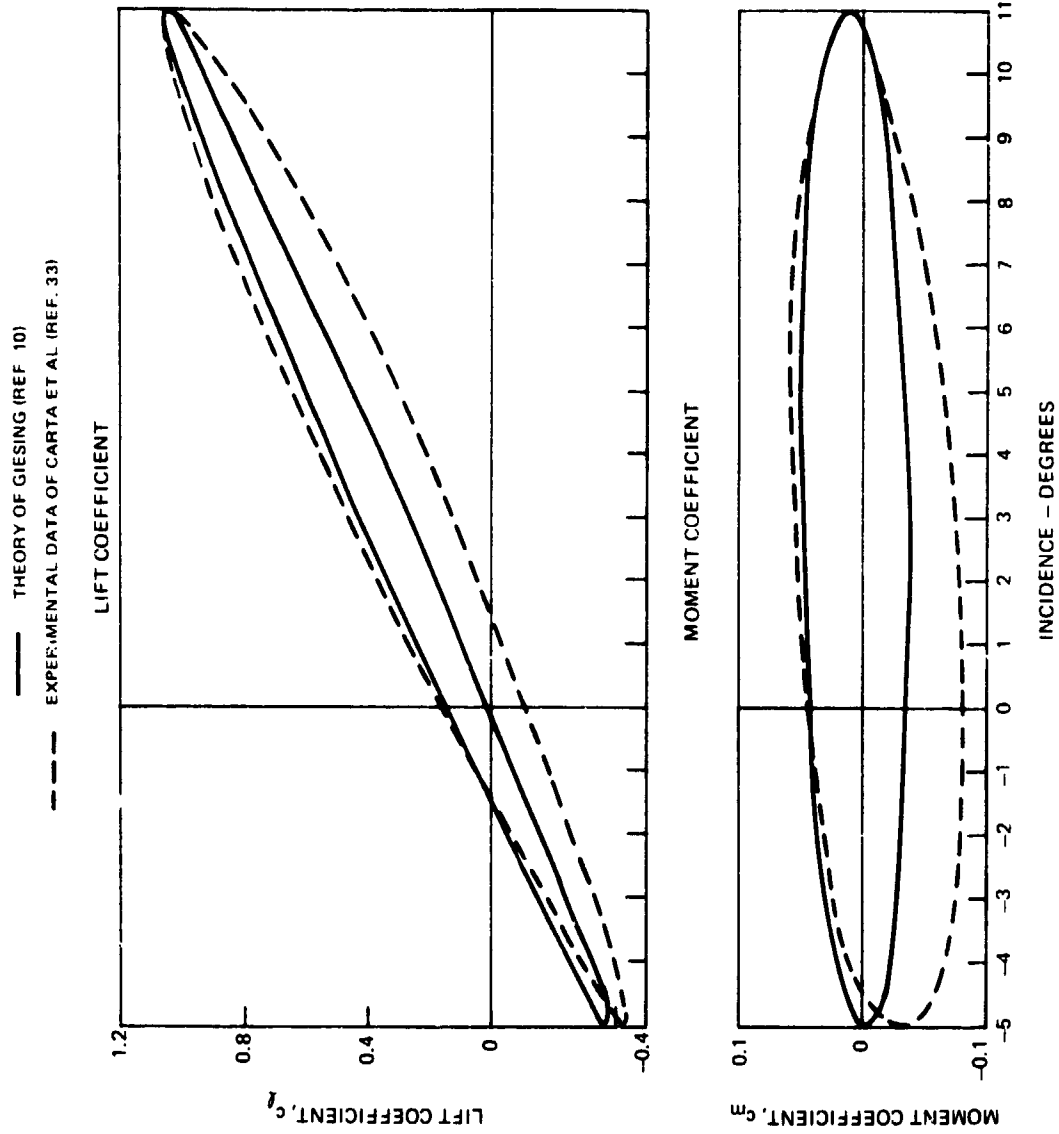
Figure 2. – Comparison between theoretically predicted and experimentally measured aerodynamic coefficients.

63

INVISCID FLOW FIELD GIVEN BY

$u = ax$

$v = -ay$

—— ANALYTICAL SOLUTION (REF 15)

O   NUMERICAL SOLUTION

Figure 3. — Comparison between numerical solution and analytical solution for Hiemenz flow.
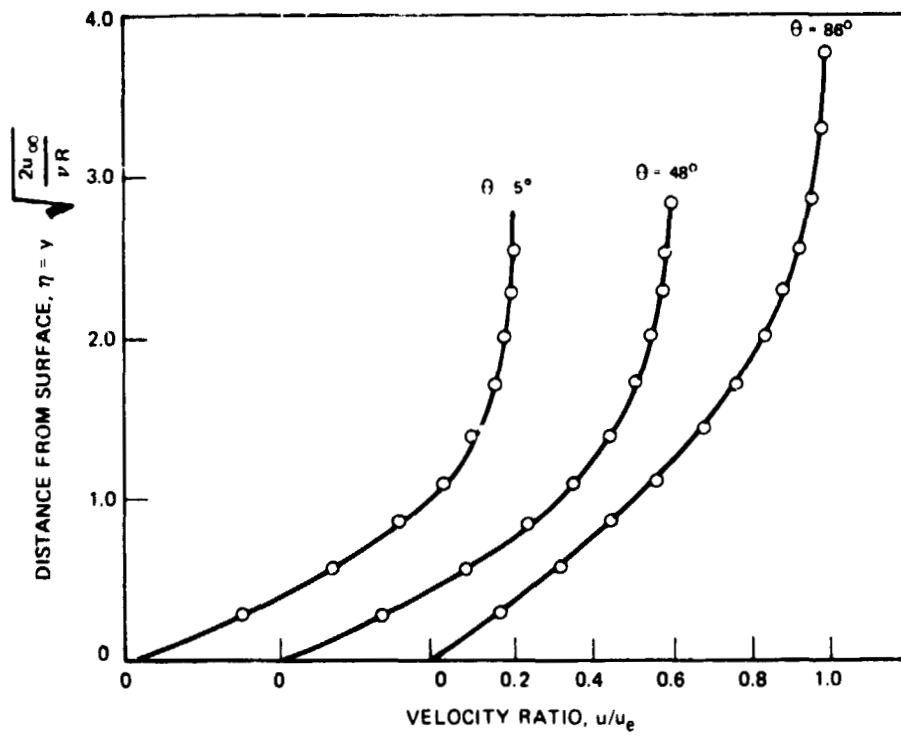
Figure 4. — Comparison between numerical solution and analytical solution for flow about circular cylinder.

VELOCITY PROFILES

INVISCID FLOW FIELD GIVEN BY

$u = u_0 \cos \omega t$

$u_0 = 3050 \text{ CM/SEC (100 FT/SEC)}$

$\omega = 100/\text{SEC}$

━━━━ ANALYTICAL SOLUTION (REF 15)

O   NUMERICAL SOLUTION

Figure 5. — Comparison between numerical solution and analytical solution for oscillating plate flow.

66

WALL VORTICITY

INVISCID FLOW FIELD GIVEN BY

$u = u_0 \cos \Omega t$

$u_0 - 3050$ CM SEC (100 FT SEC)

$\Omega = 100$/SEC

——— ANALYTICAL SOLUTION (REF 15)

NUMERICAL SOLUTION

○   n = 1

□   n = 2
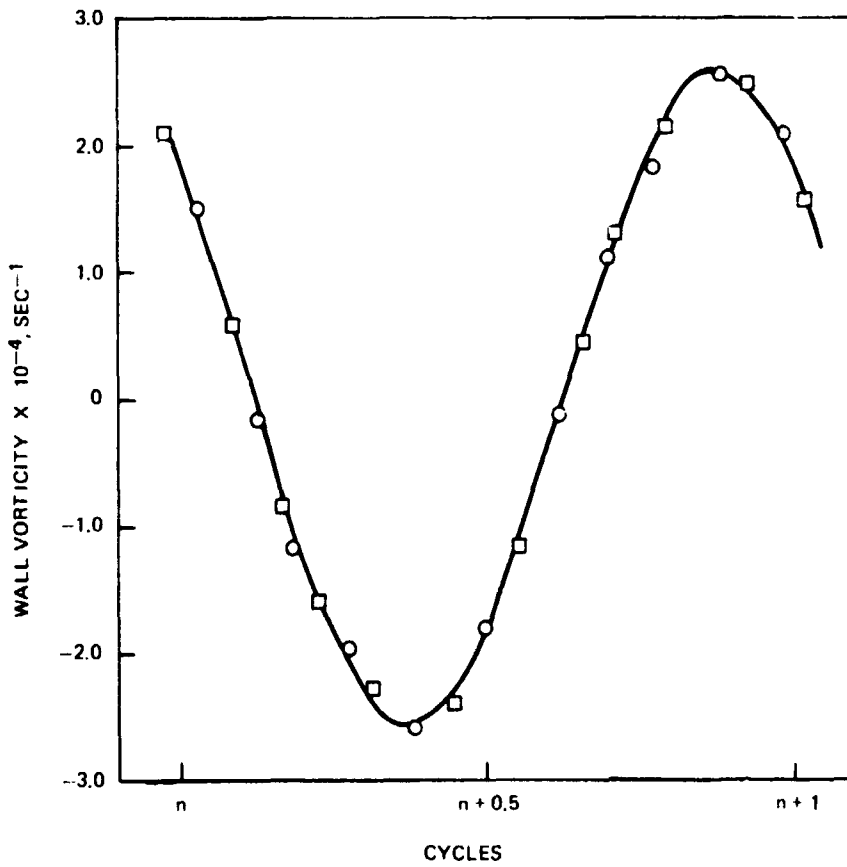
Figure 6. — Comparison between numerical solution and analytical solution for oscillating plate flow.
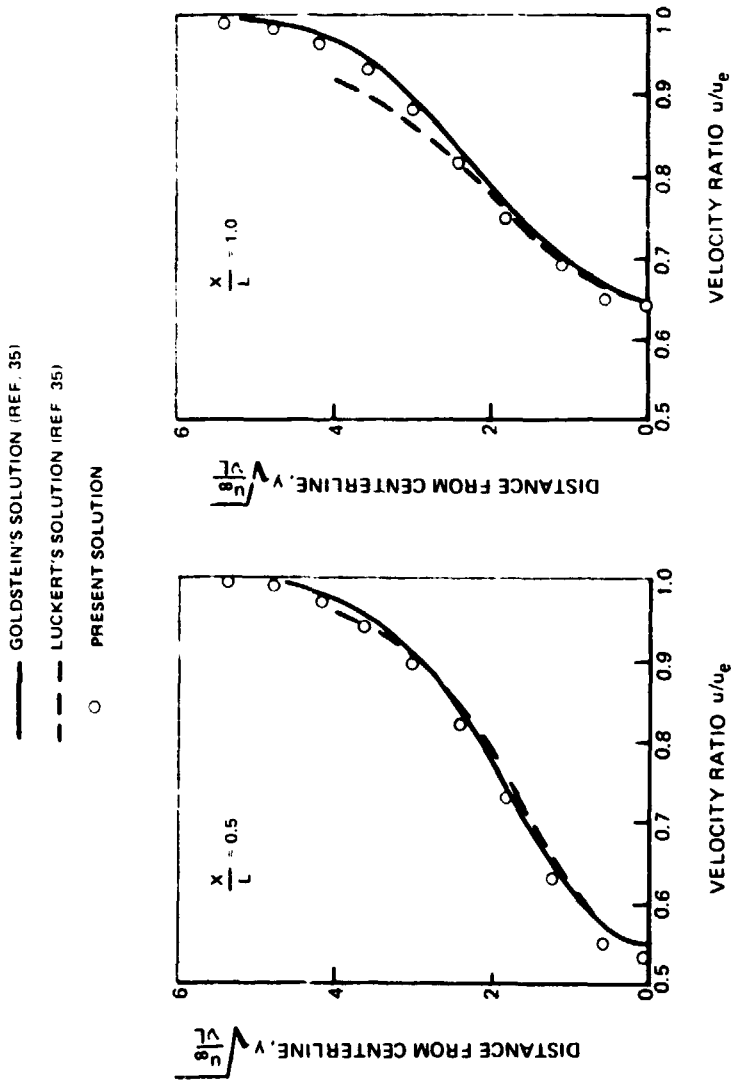
Figure 7. — Prediction of wake behind a flat plate.
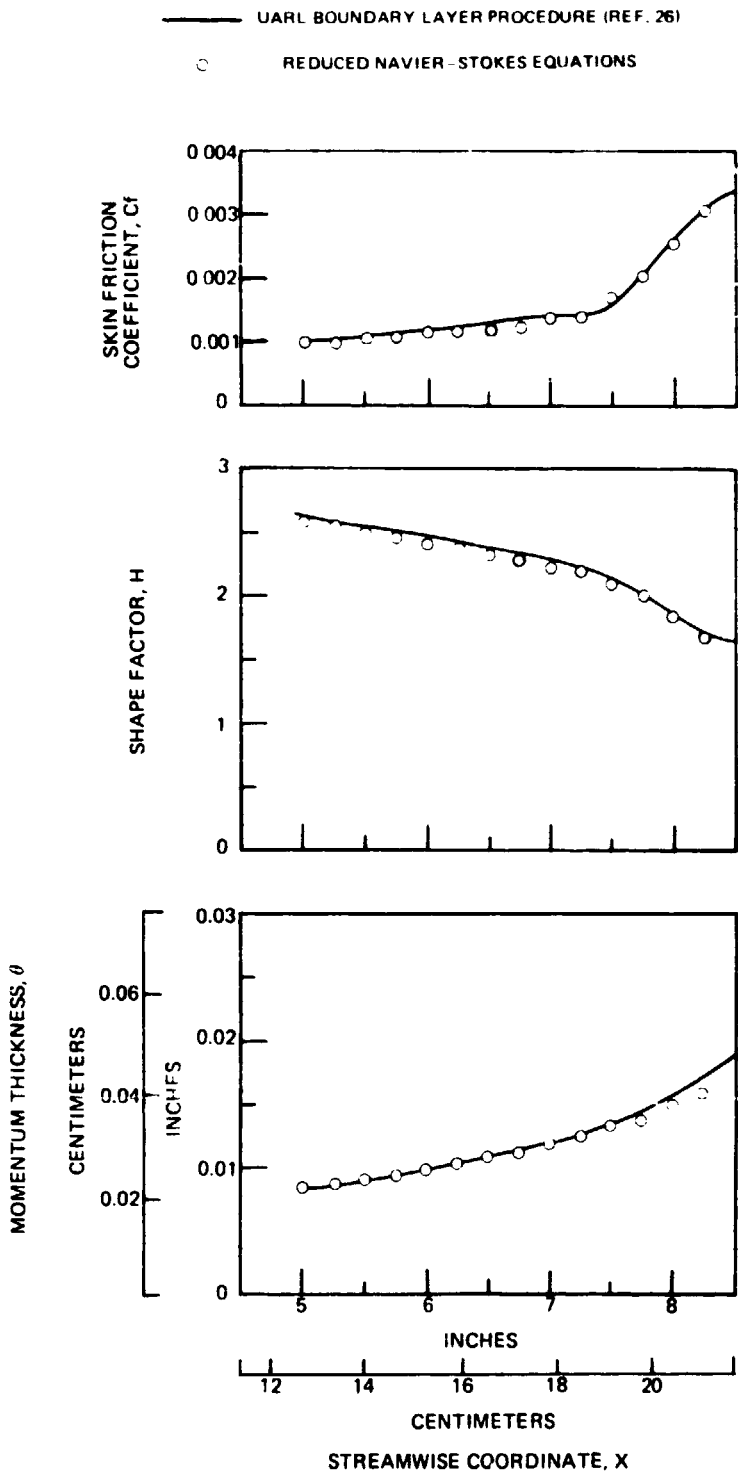
Figure 8. — Predictions of transitional boundary layer development.
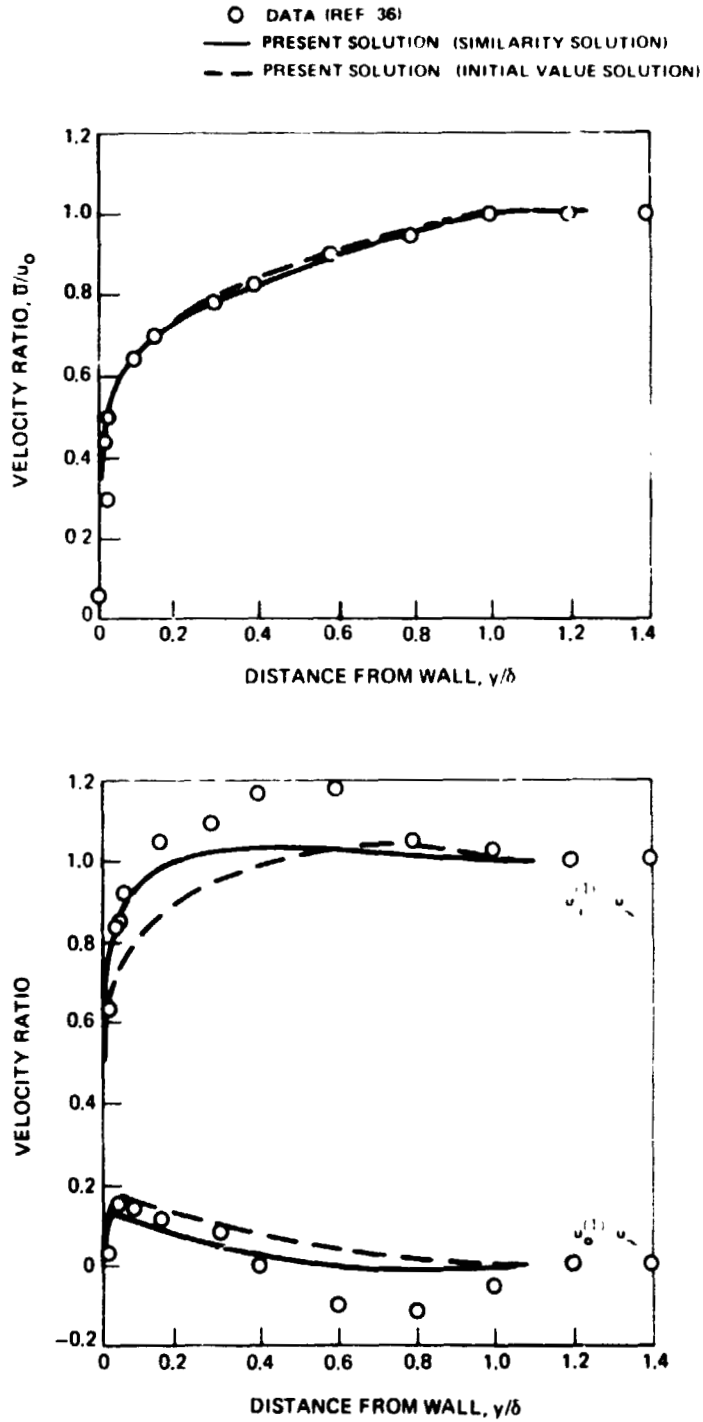
Figure 9. — Comparison between theoretical prediction and experimental data for oscillating turbulent boundary layer.

70
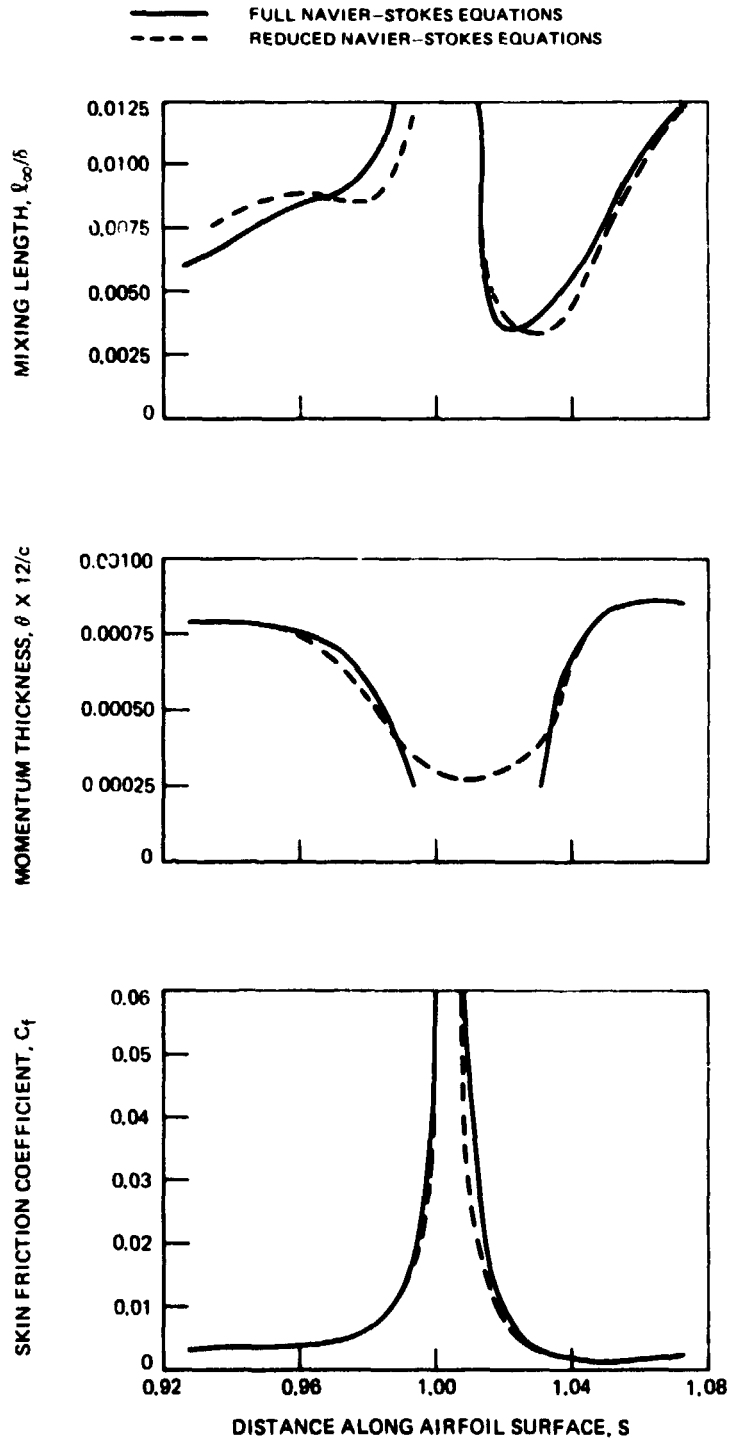
Figure 10. — Viscous layer development in vicinity of leading edge.

THEORY OF GIESING (REF 10)
--- EXPERIMENTAL DATA OF GRAY AND LIIVA (REF 3)
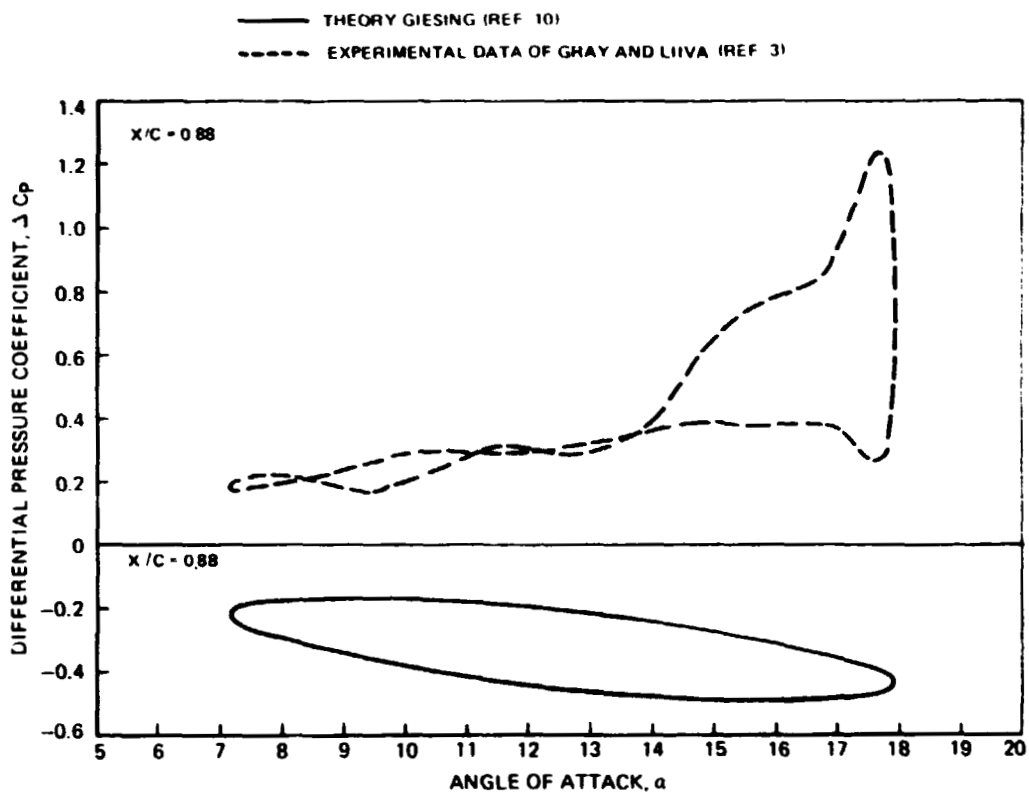
LIFT COEFFICIENT
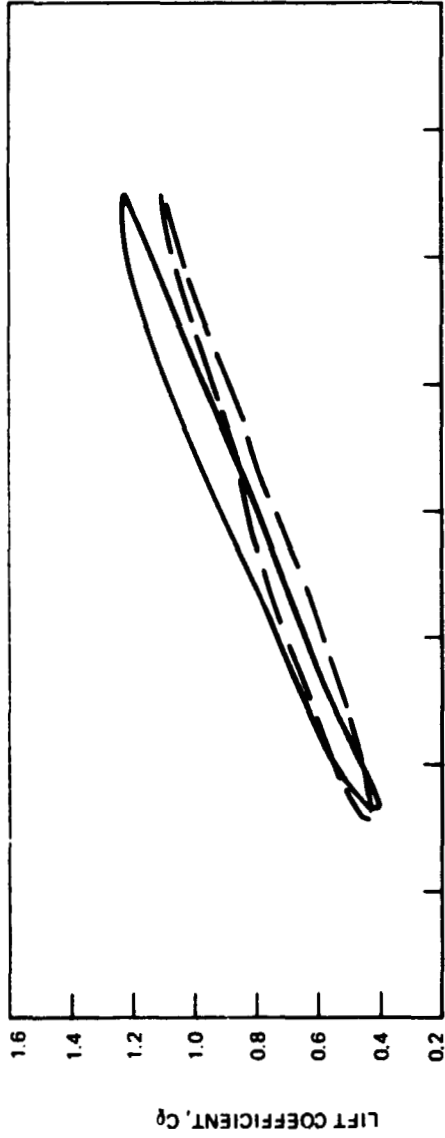
MOMENT COEFFICIENT
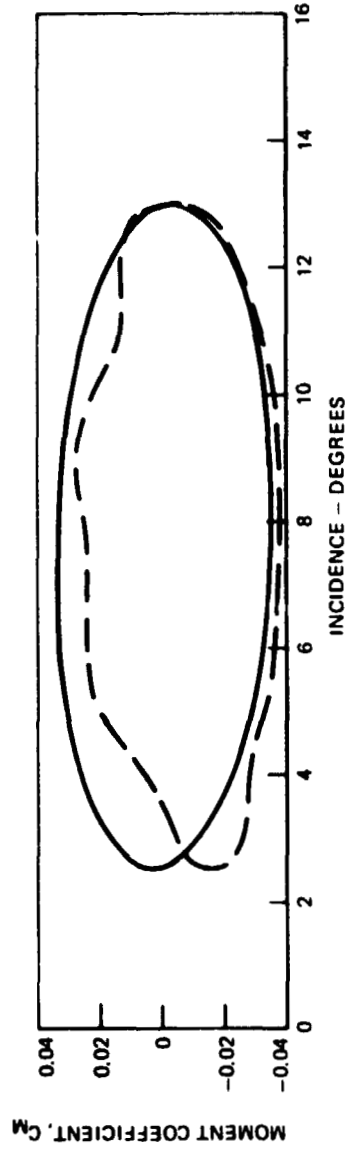
Figure 11 . — Comparison between theoretically predicted and experimentally measured aerodynamic coefficients for Case I.

72
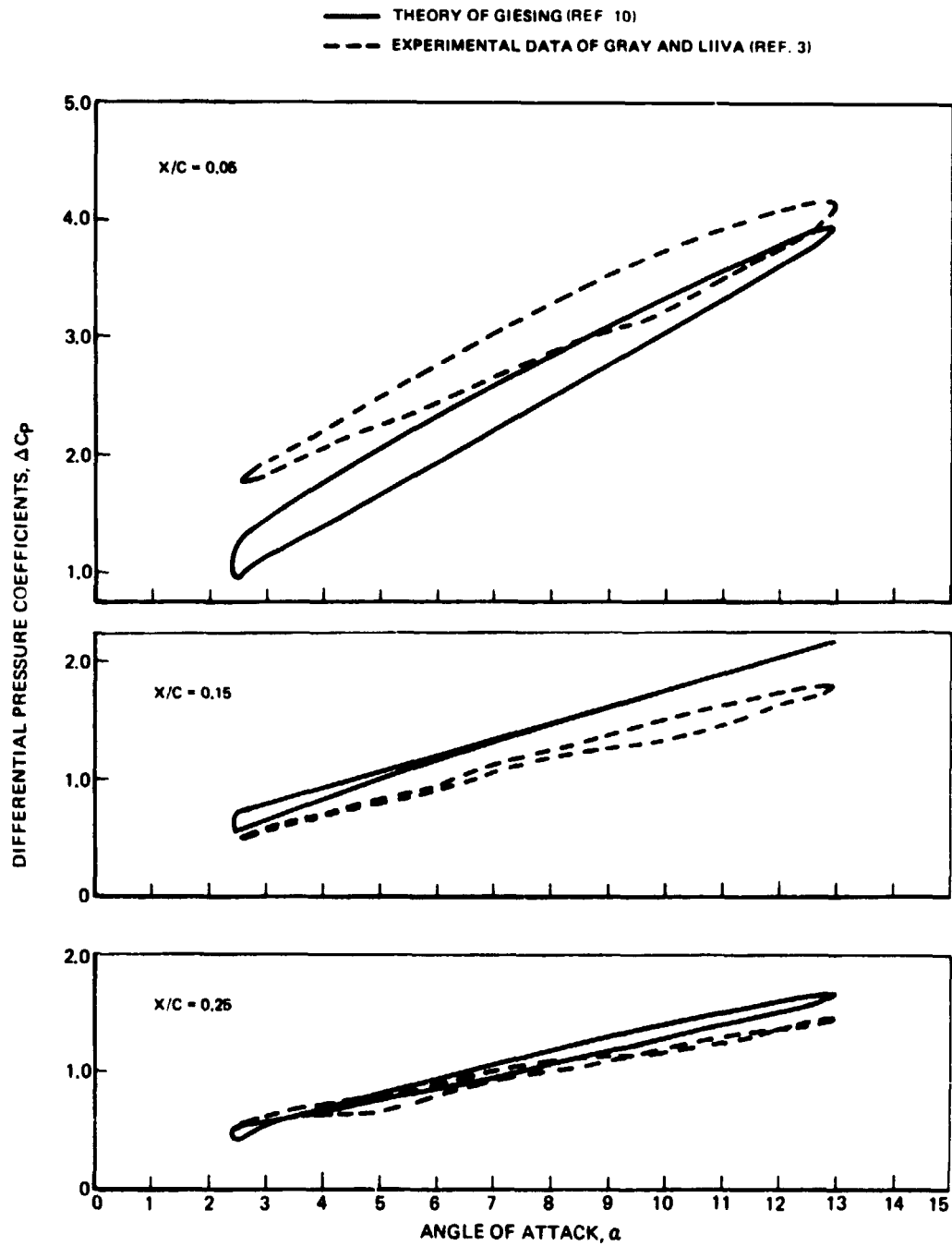
Figure 12. — Comparison between theoretically predicted and experimentally measured differential pressure coefficients for Case I .

73
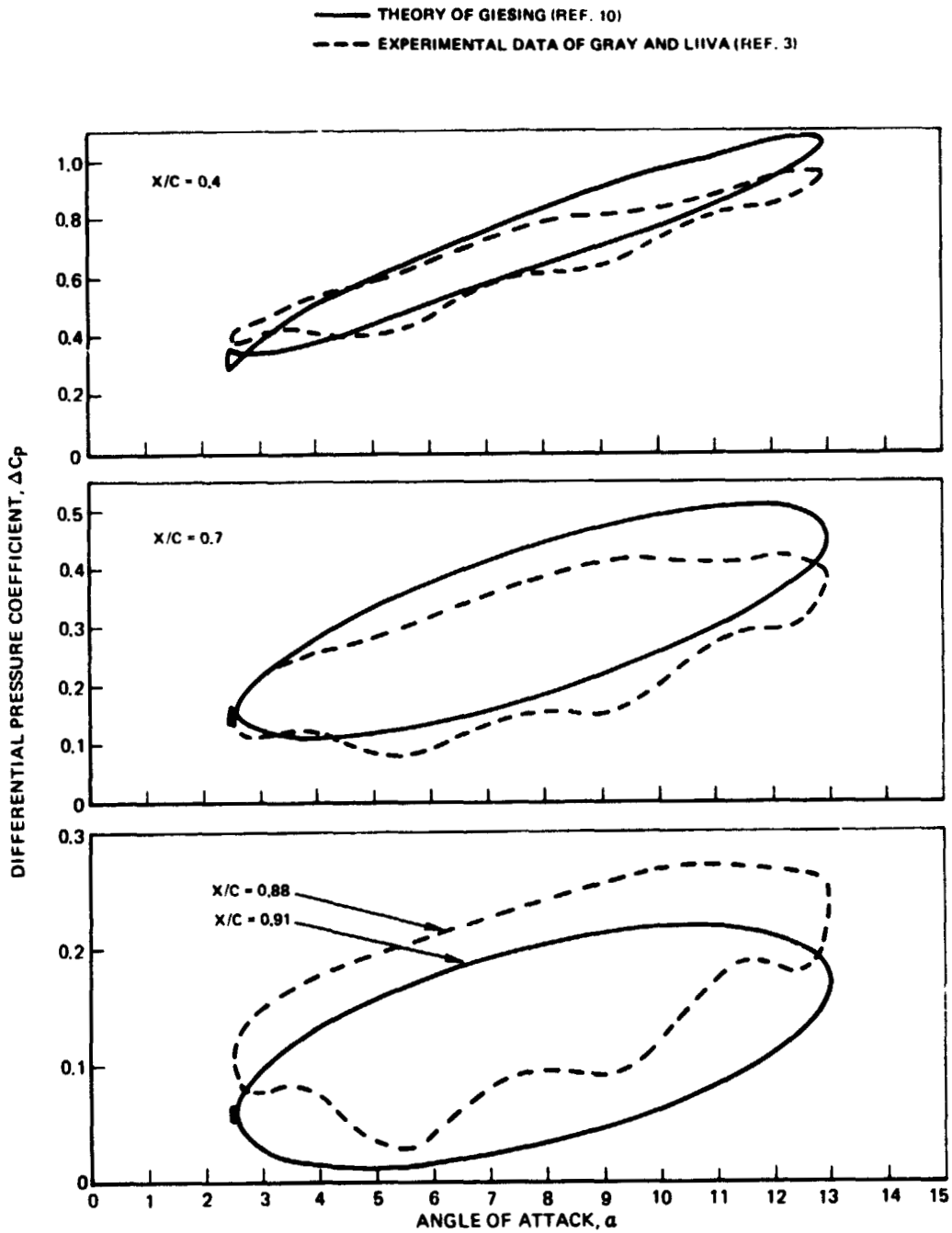
Figure 13. — Comparison between theoretically predicted and experimentally measured differential pressure coefficients for Case I .

74
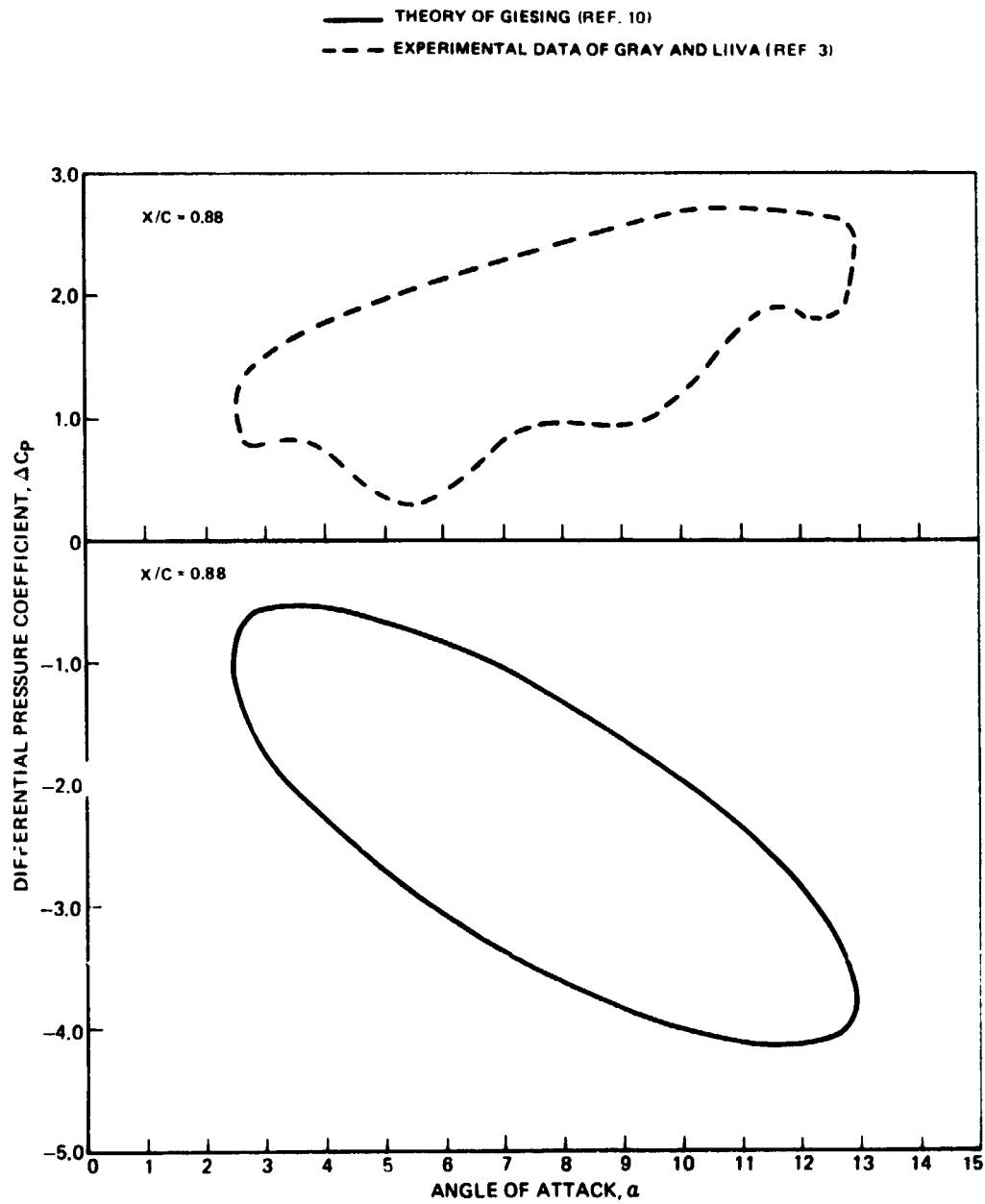
Figure 14. — Comparison between theoretically predicted and experimentally measured differential pressure coefficients for Case I.
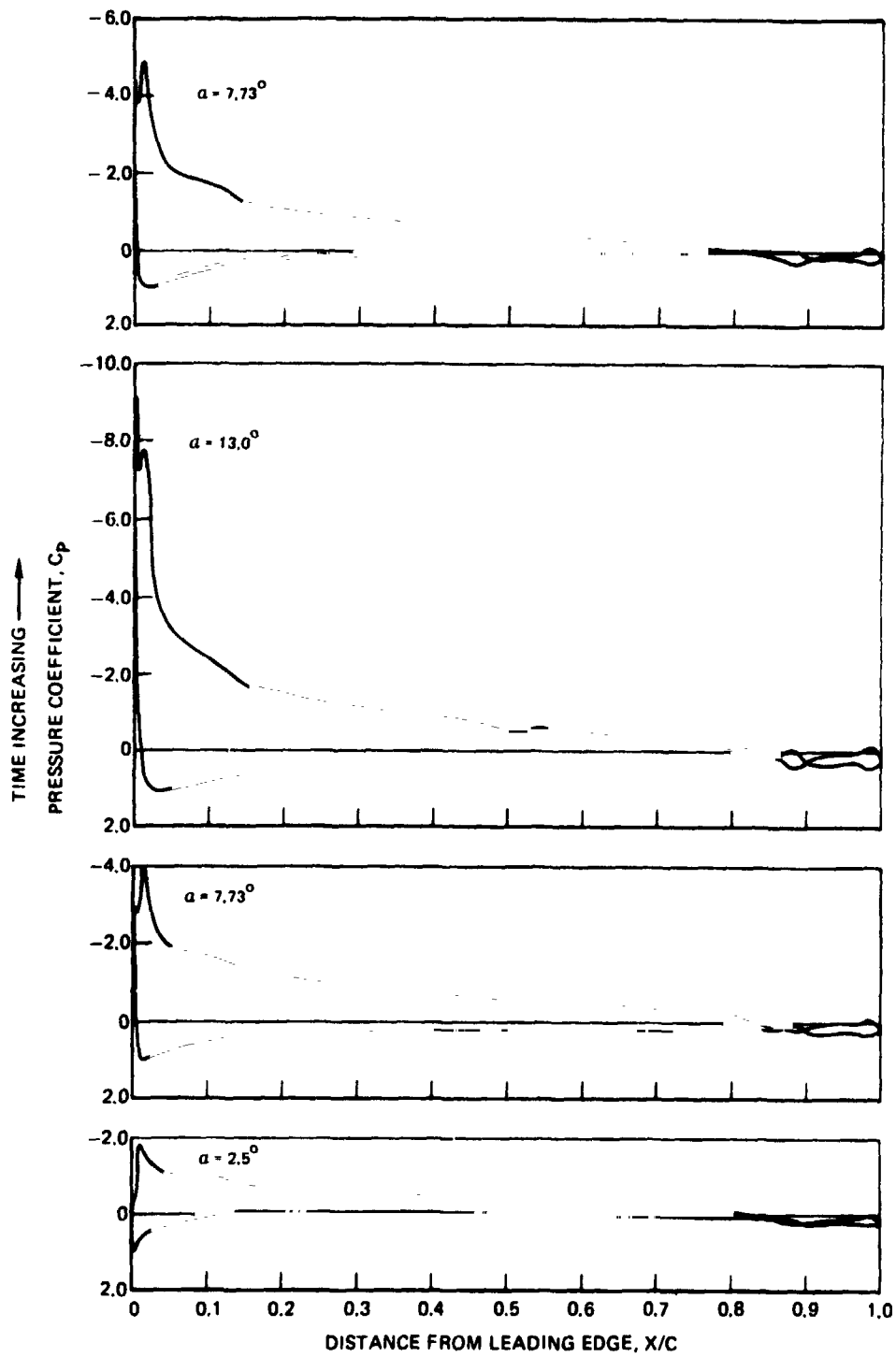
Figure 15 . — Variation of the pressure coefficient on the airfoil surface at various instantaneou..
angles of attack for Case I.
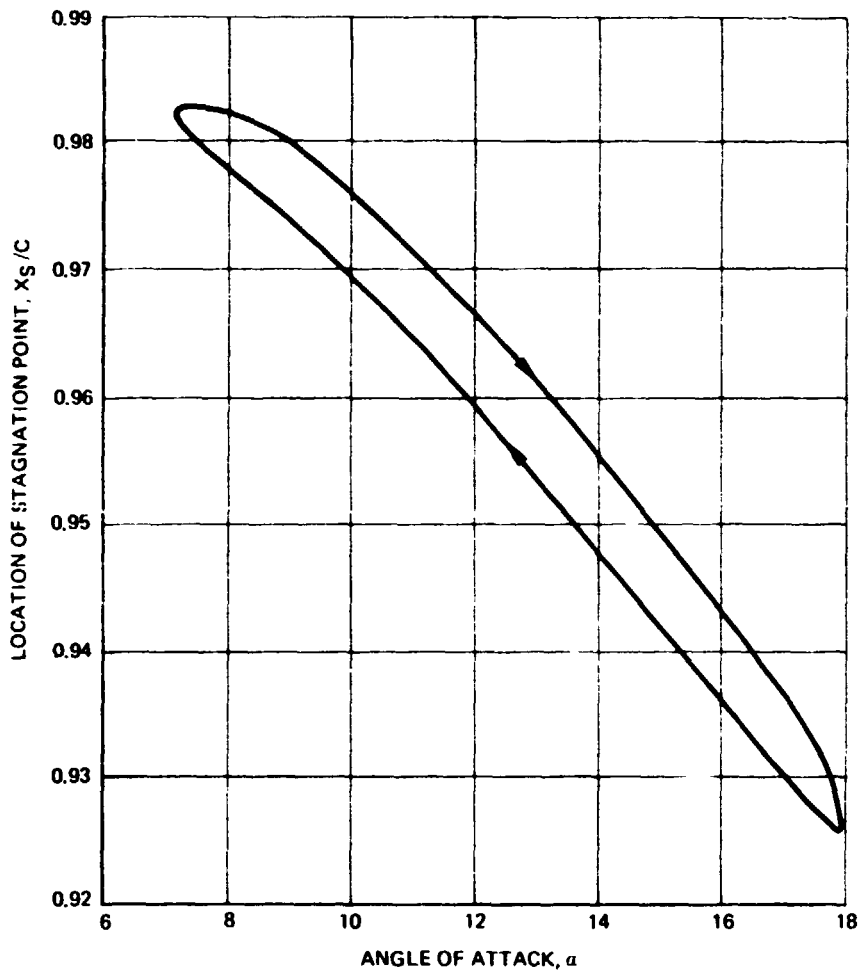
76

ARROW INDICATES DIRECTION OF INCREASING TIME
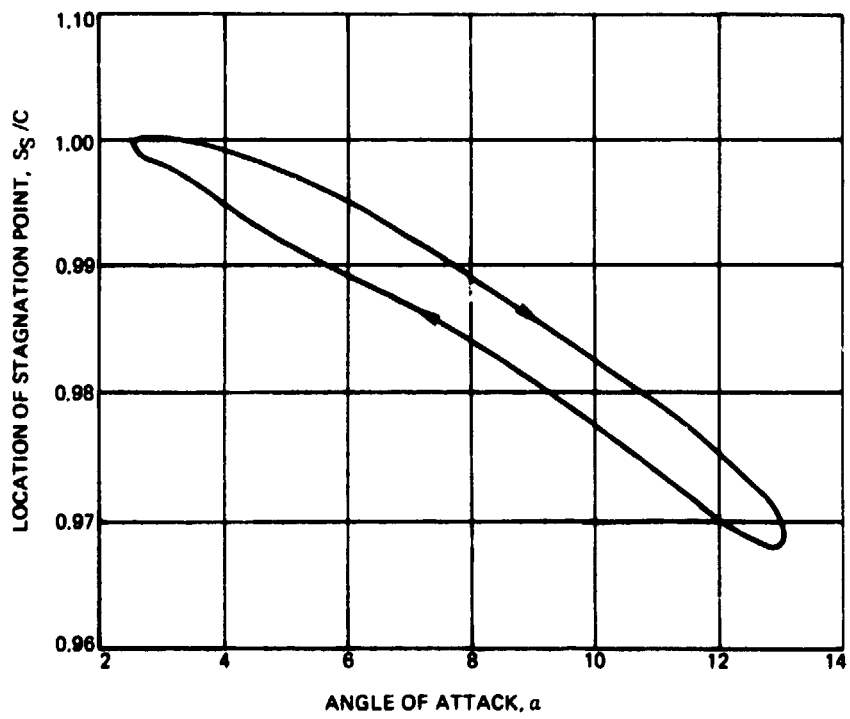
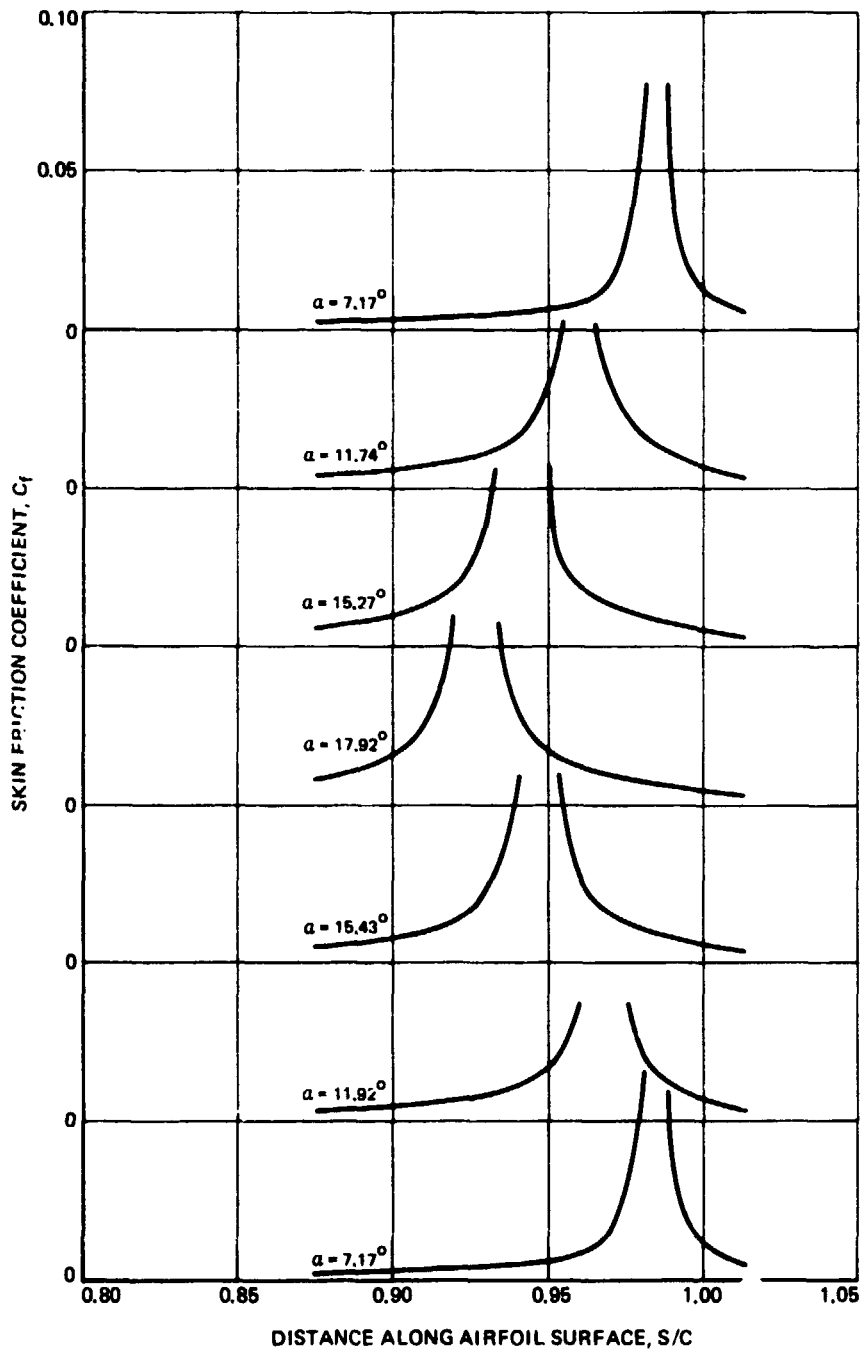Figure 16 . -- Location of stagnation point as a function of angle of attack
for Case I .
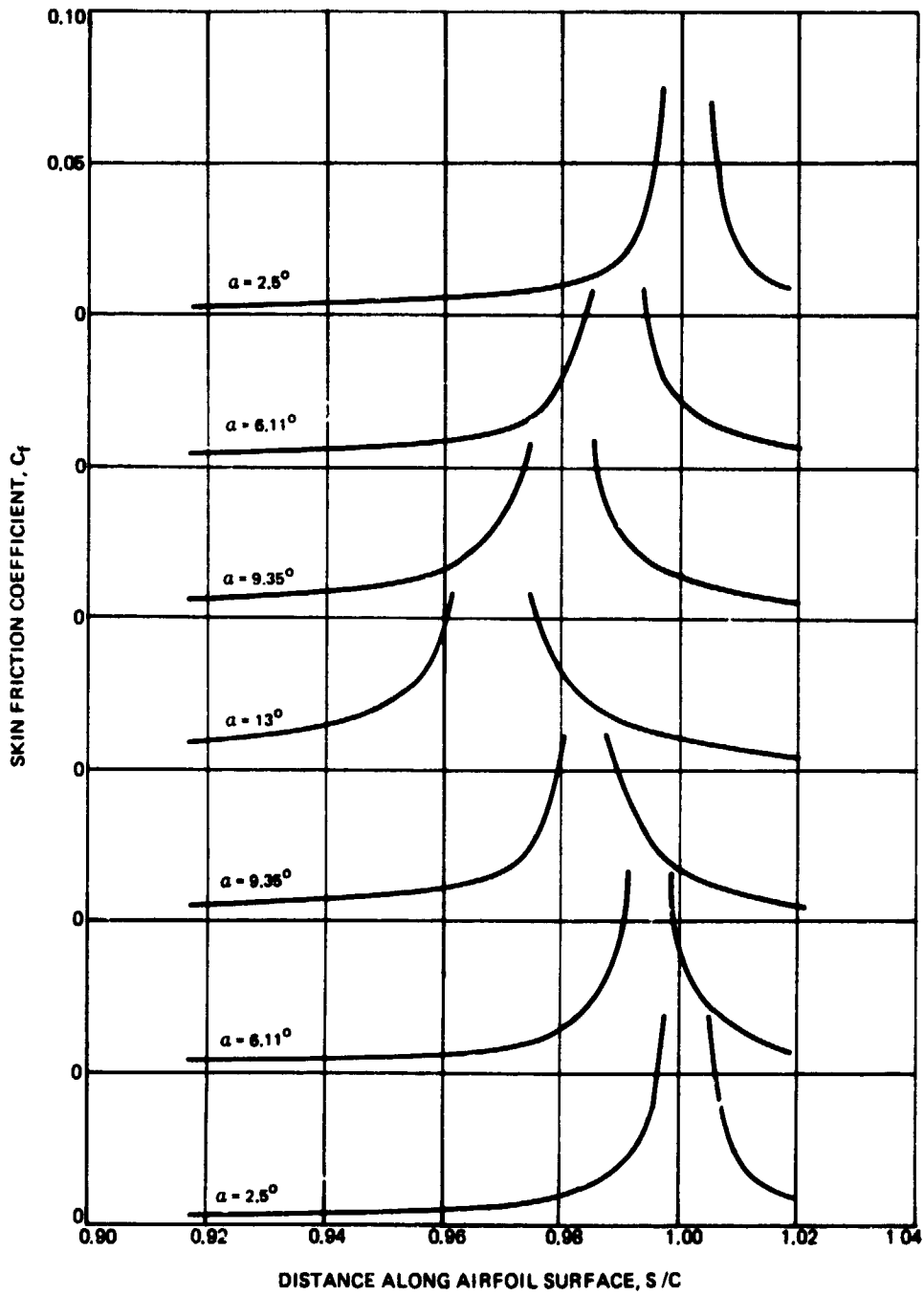
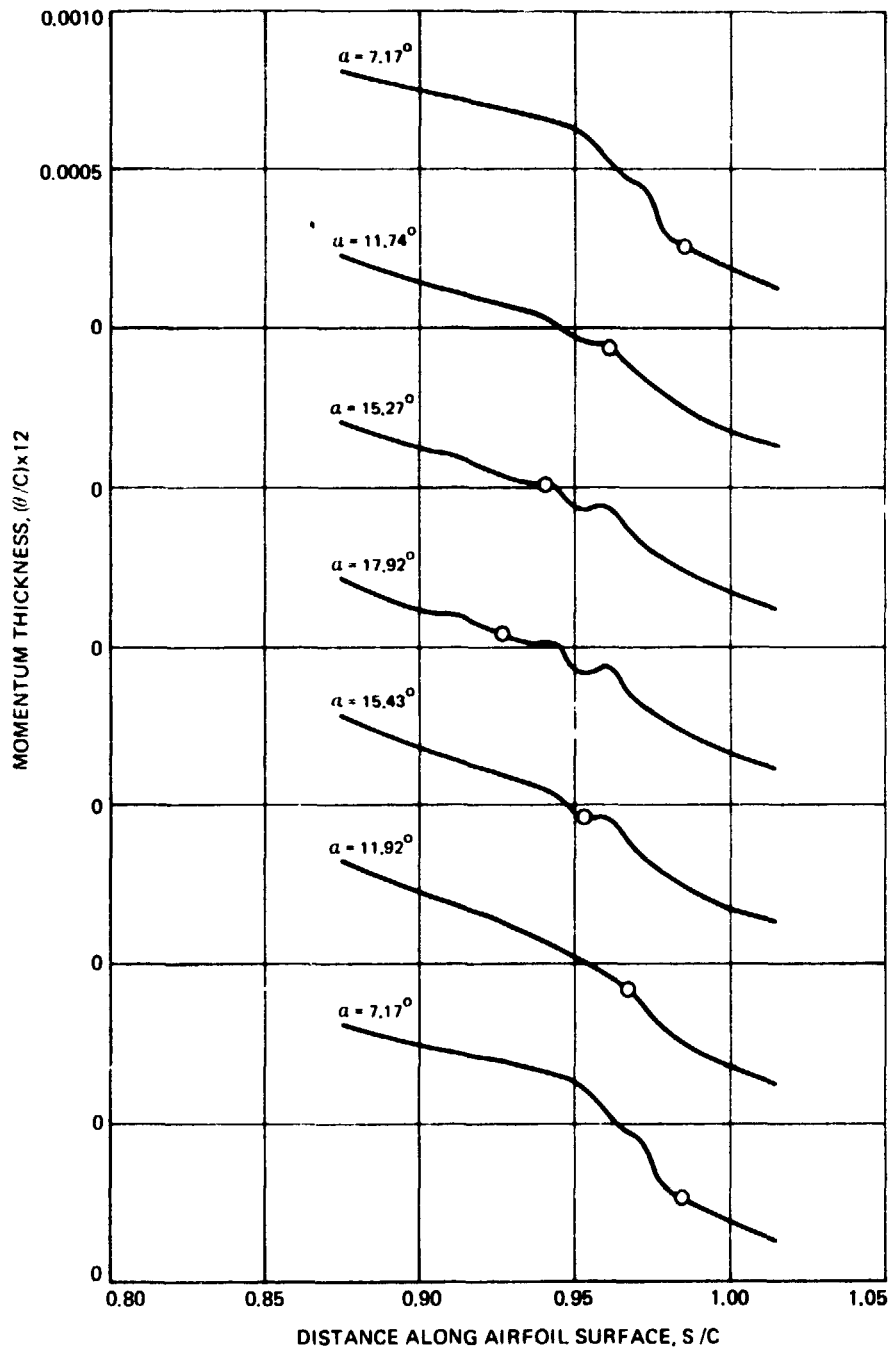Figure 17. — Variation of skin friction coefficient in the stagnation region at various instantaneous angles of attack for Case I.

78
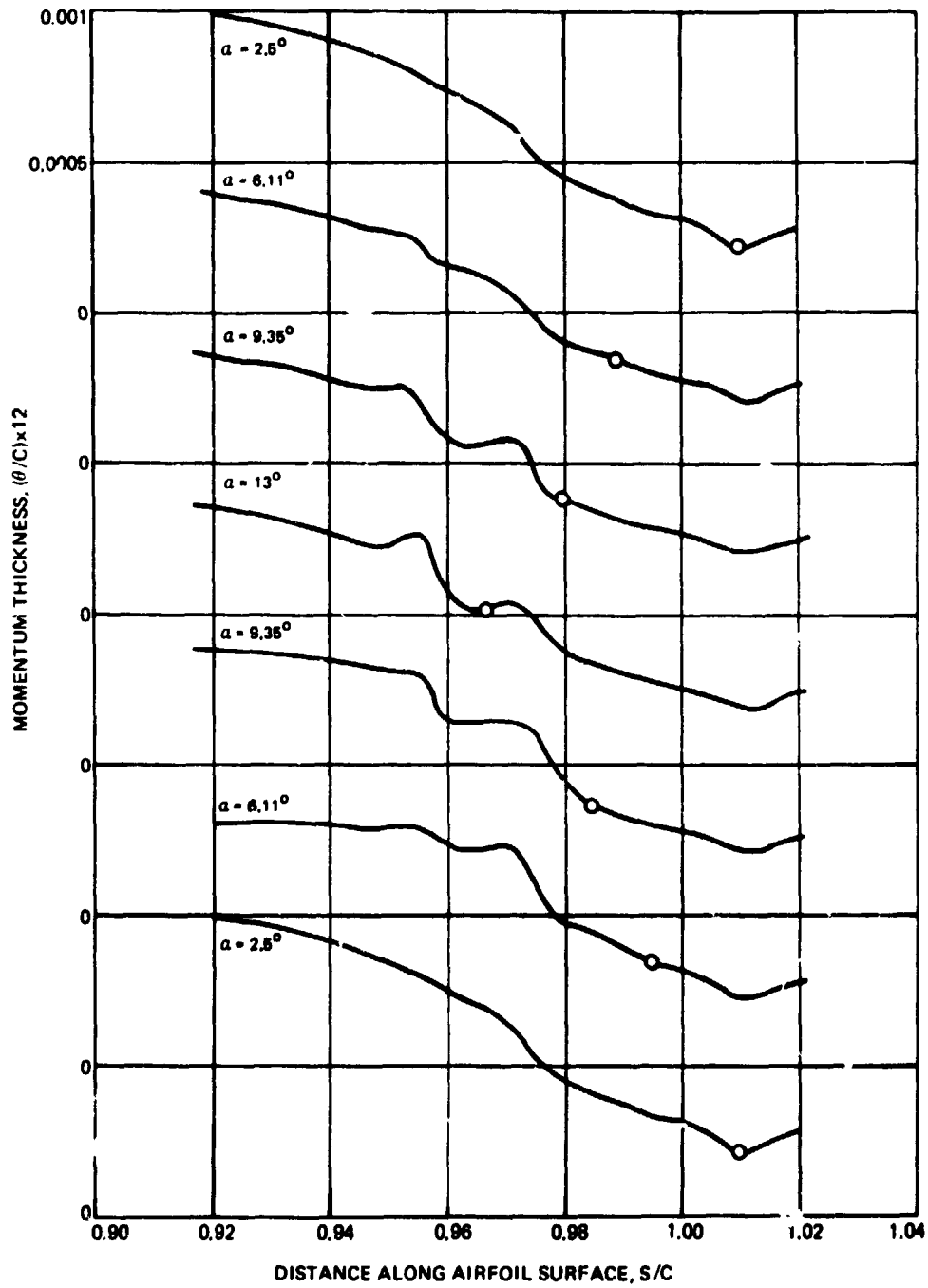
Figure 18. — Variation of momentum thickness in the stagnation region at various instantaneous angles of attack for Case I.
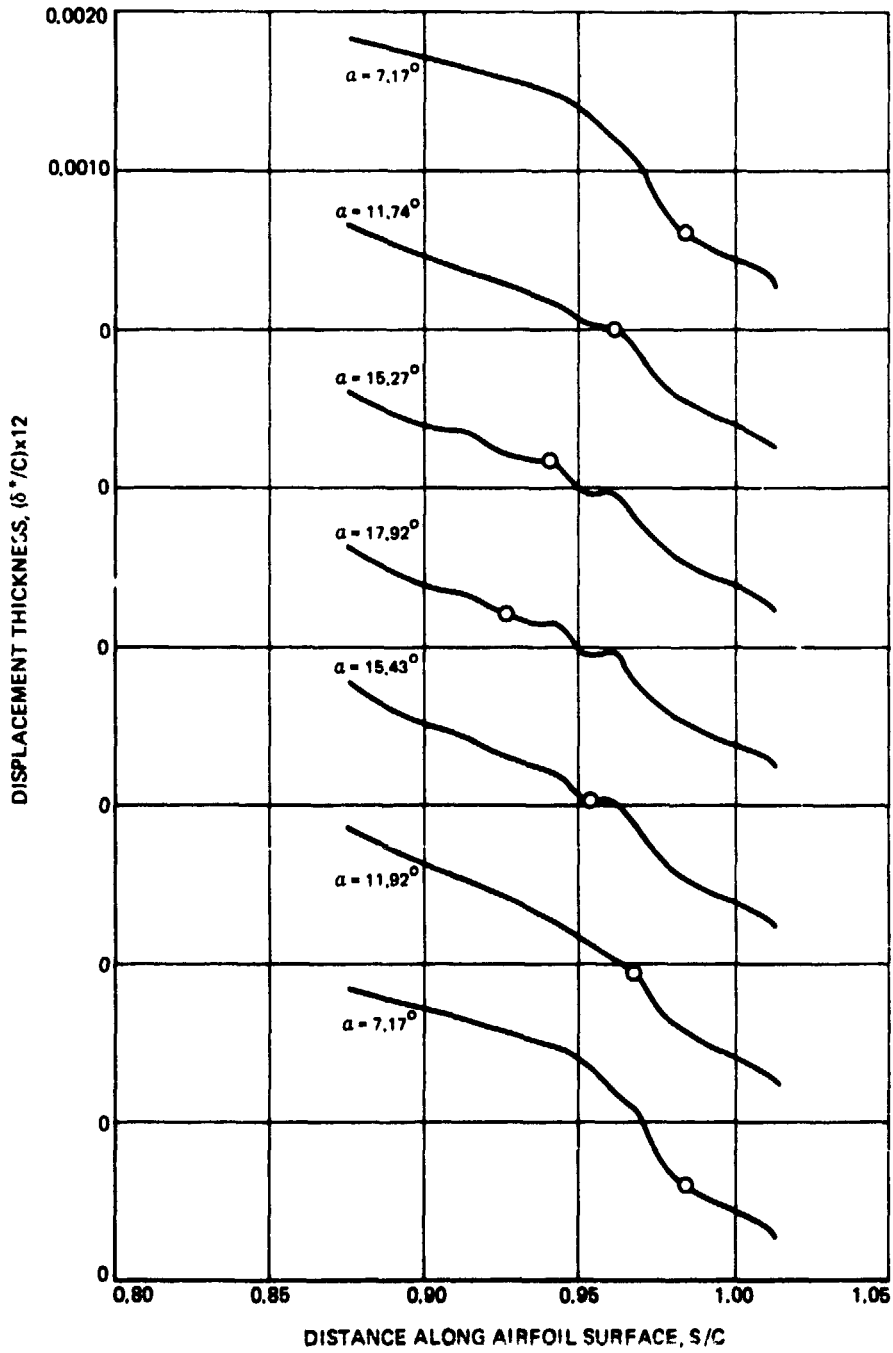
79
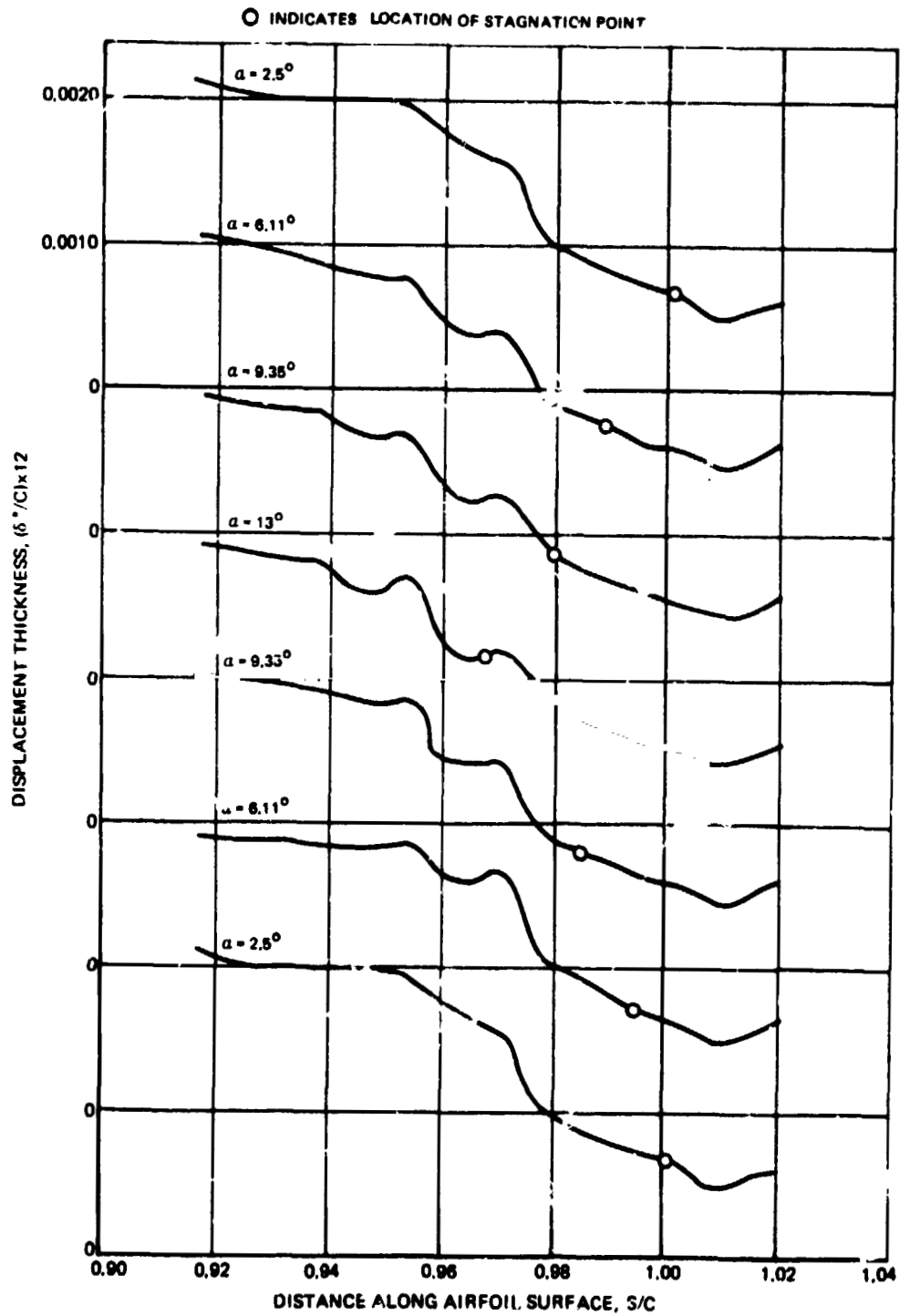
Figure 19. — Variation of displacement thickness in the stagnation region at various instantaneous angles of attack for Case I.
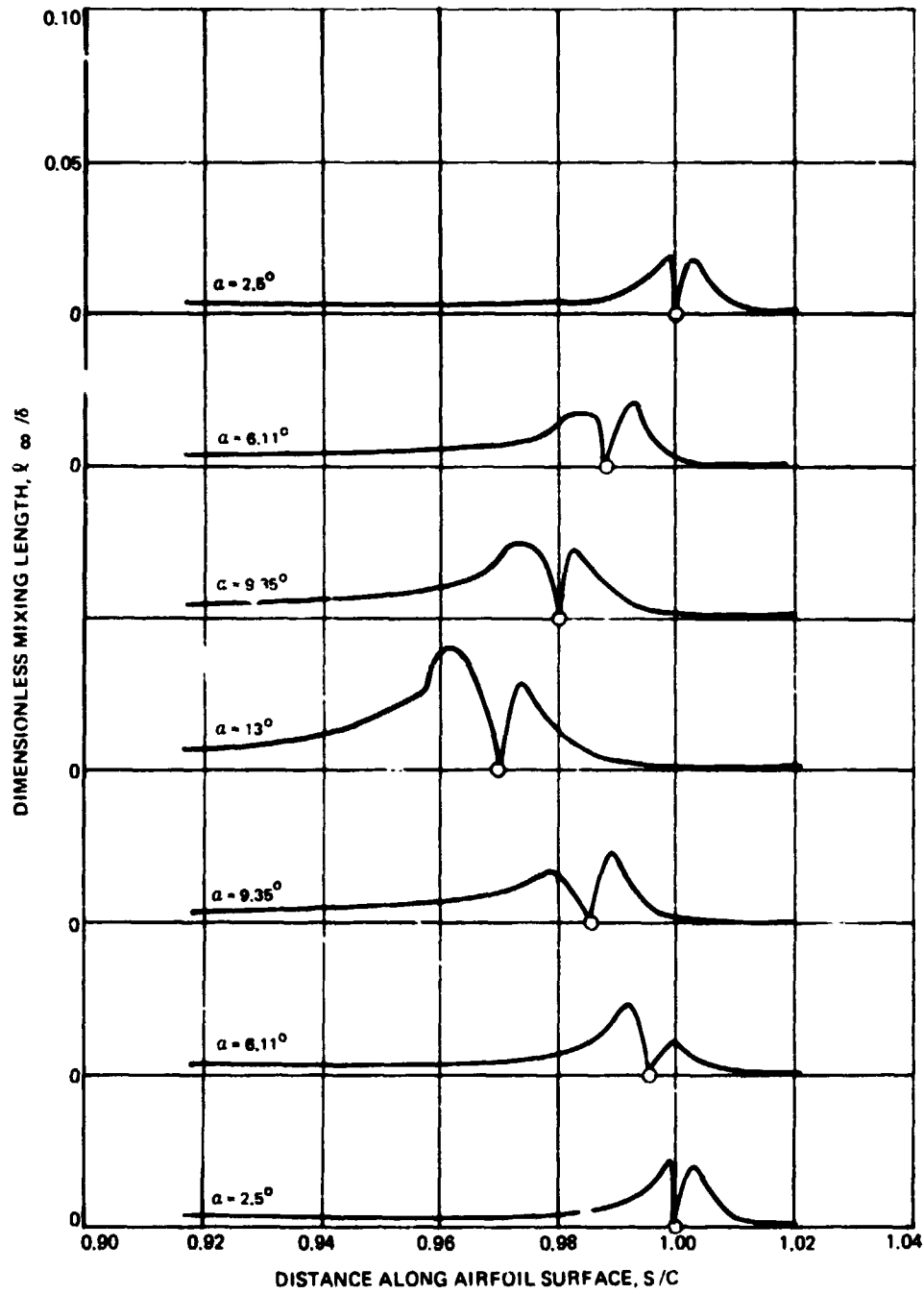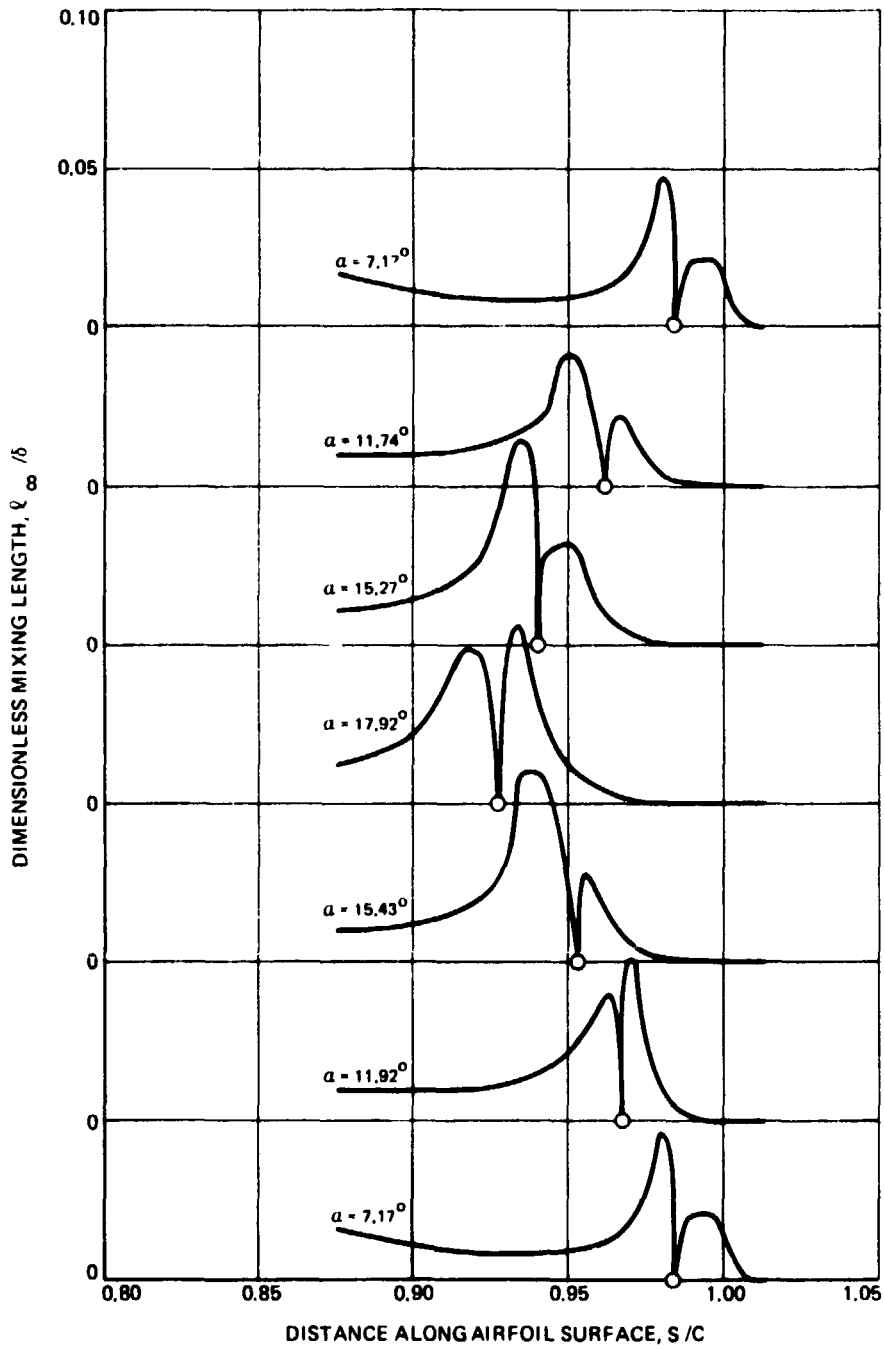
Figure 20. — Variation of dimensionless mixing length in the stagnation region at various instantaneous angles of attack for Case i .

81
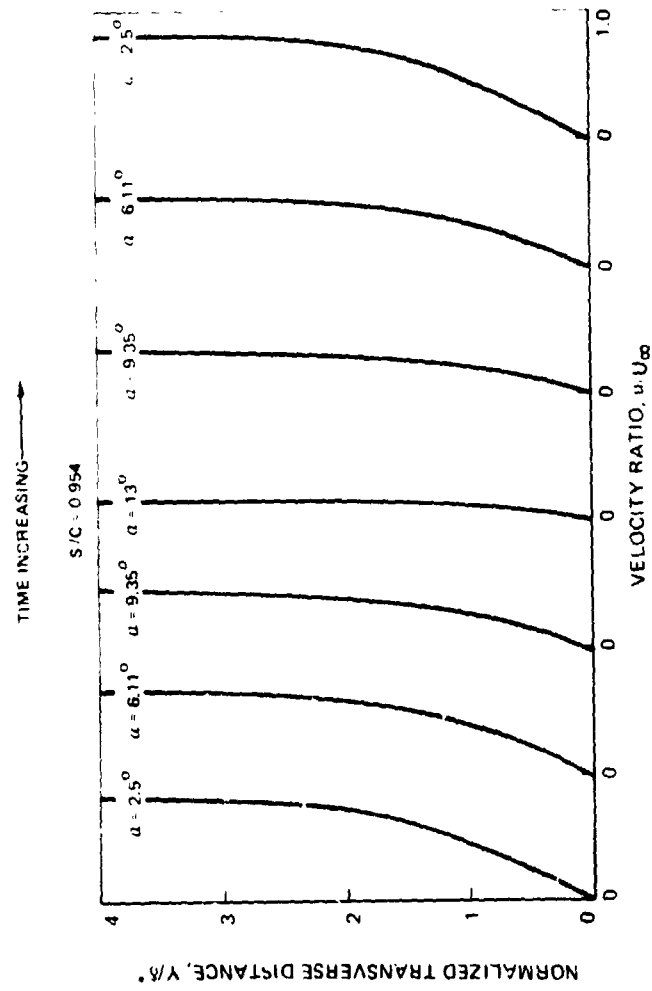
Figure 21. — Predicted instantaneous velocity profiles at a fixed streamwise location in the stagnation region pressure side for Case I.

NO1-167-1
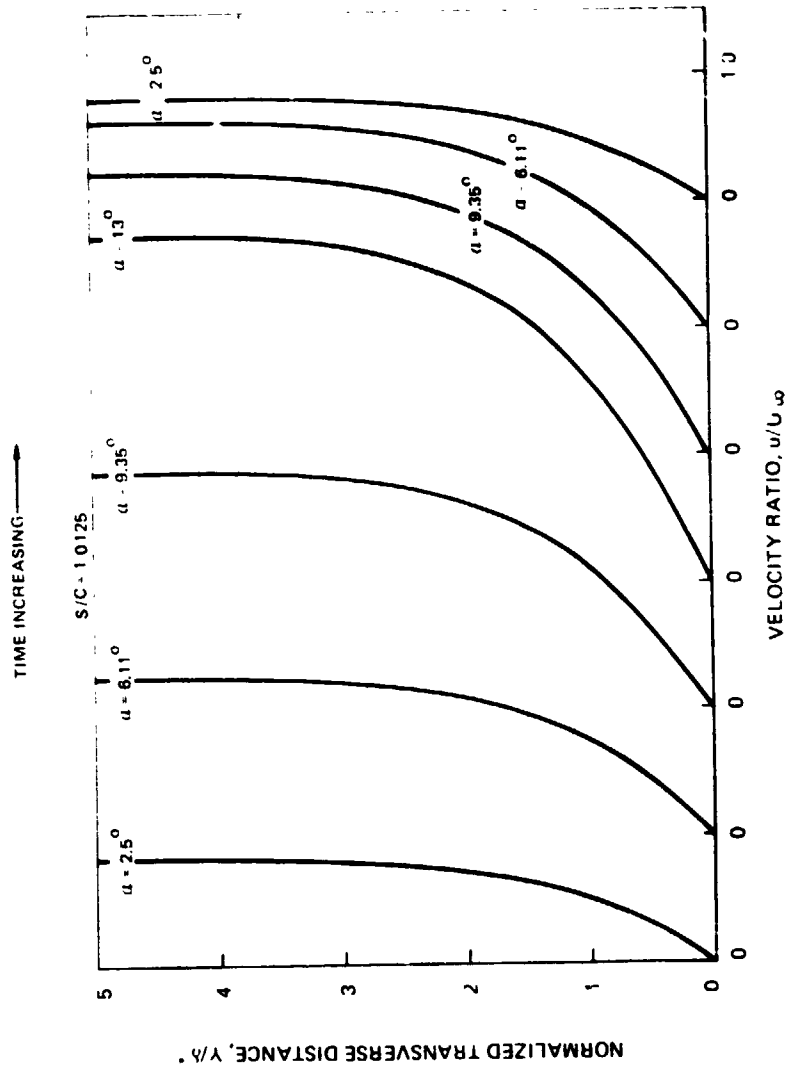
Figure 22. — Predicted instantaneous velocity profiles at a fixed streamwise location in the stagnation region suction side for Case I.
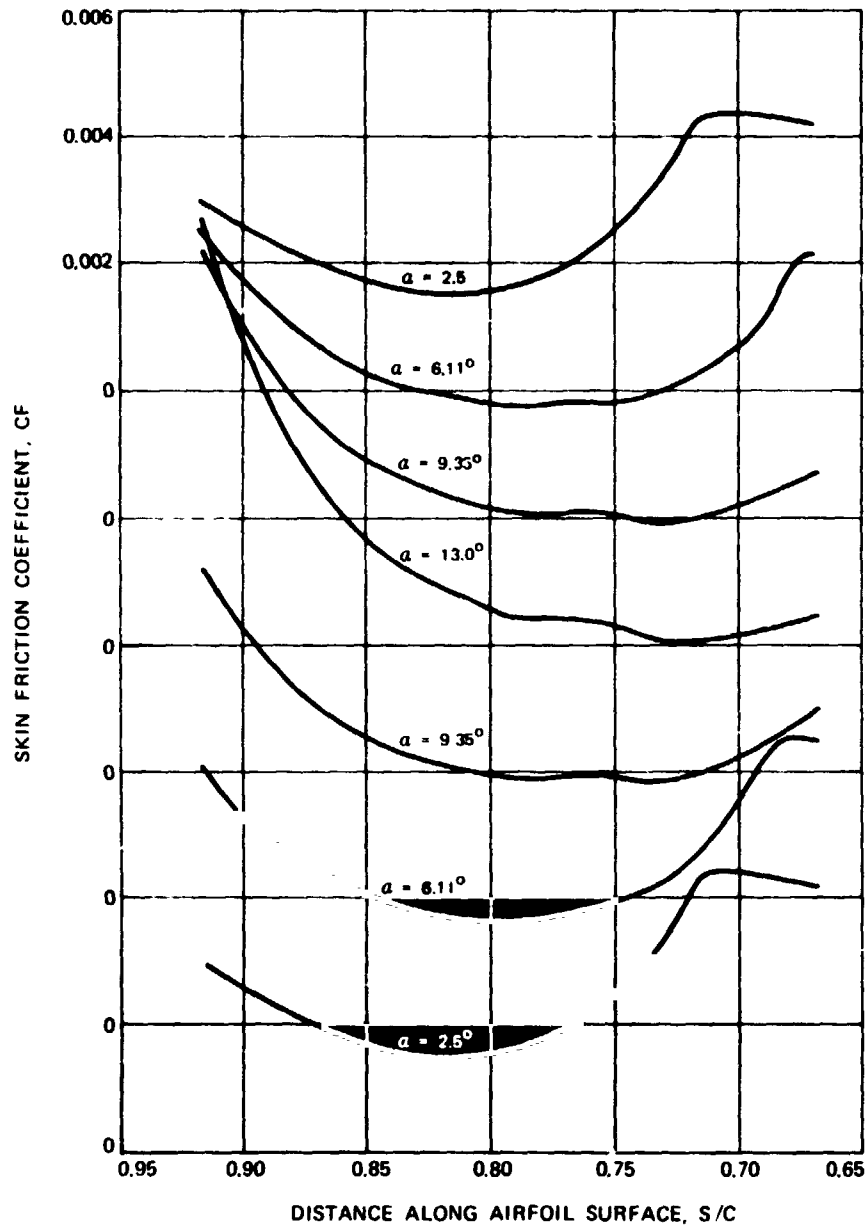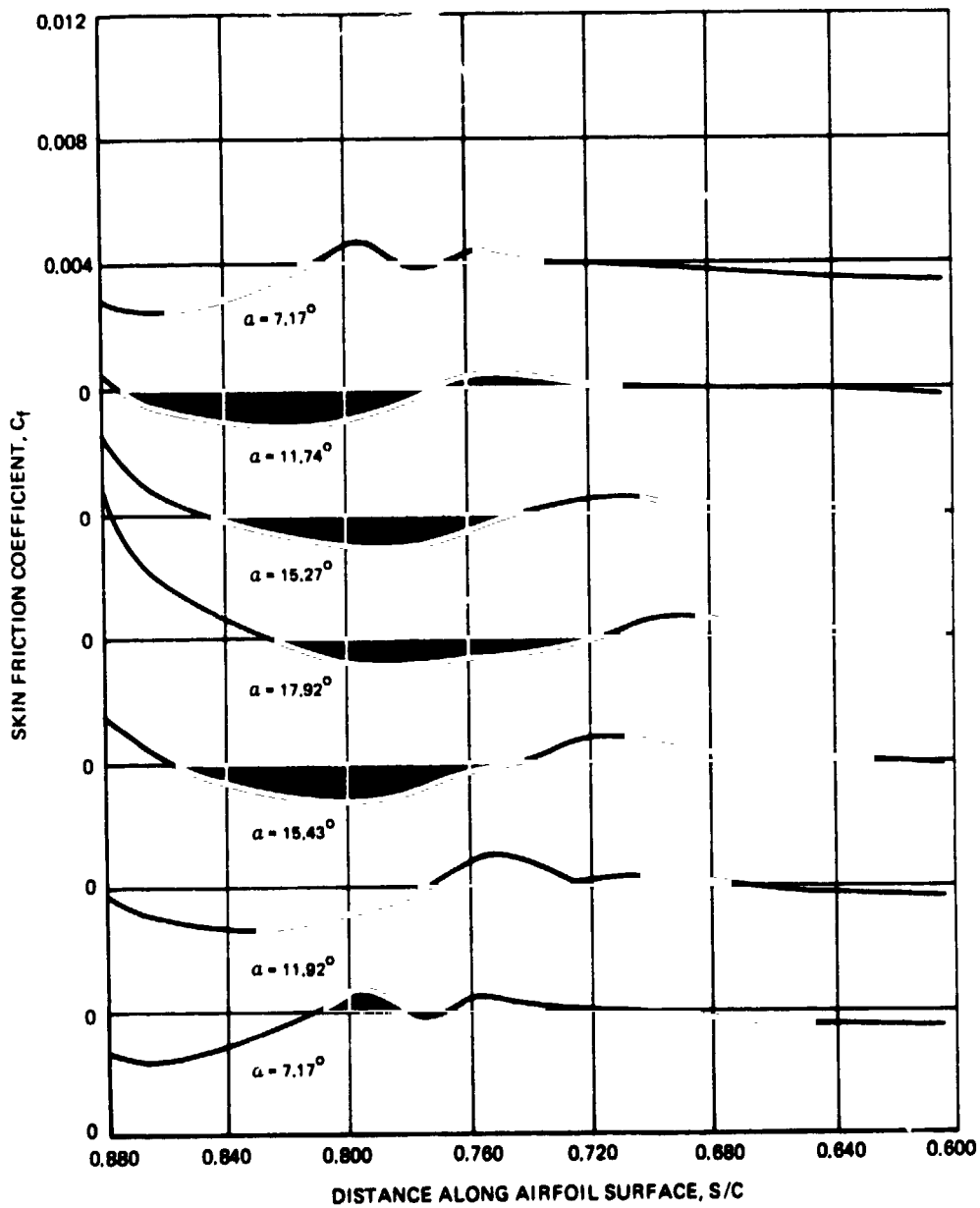
Figure 23.— Variation of skin friction coefficient along airfoil surface in the pressure side transition region at various instantaneous angles of attack for Case I.
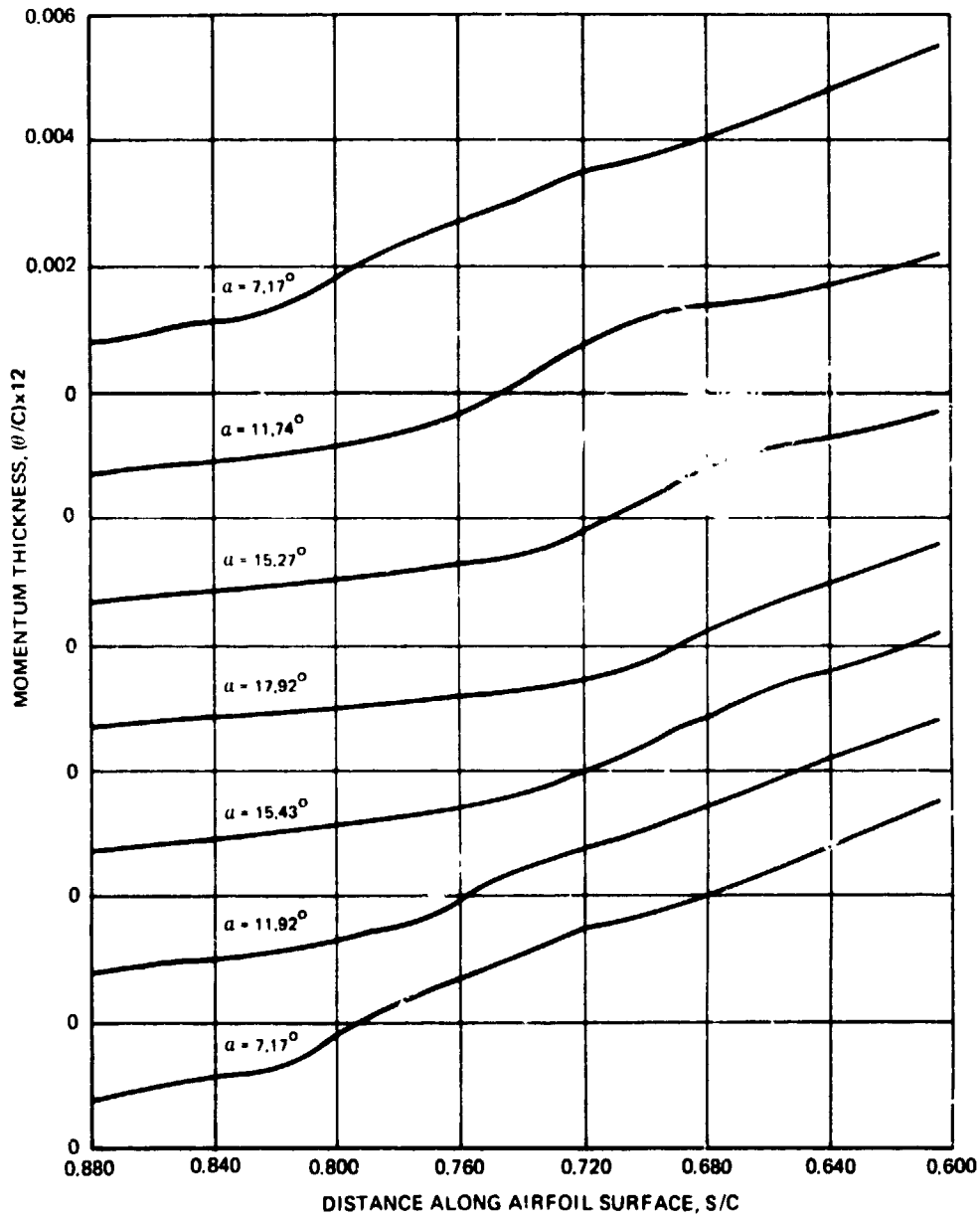
84
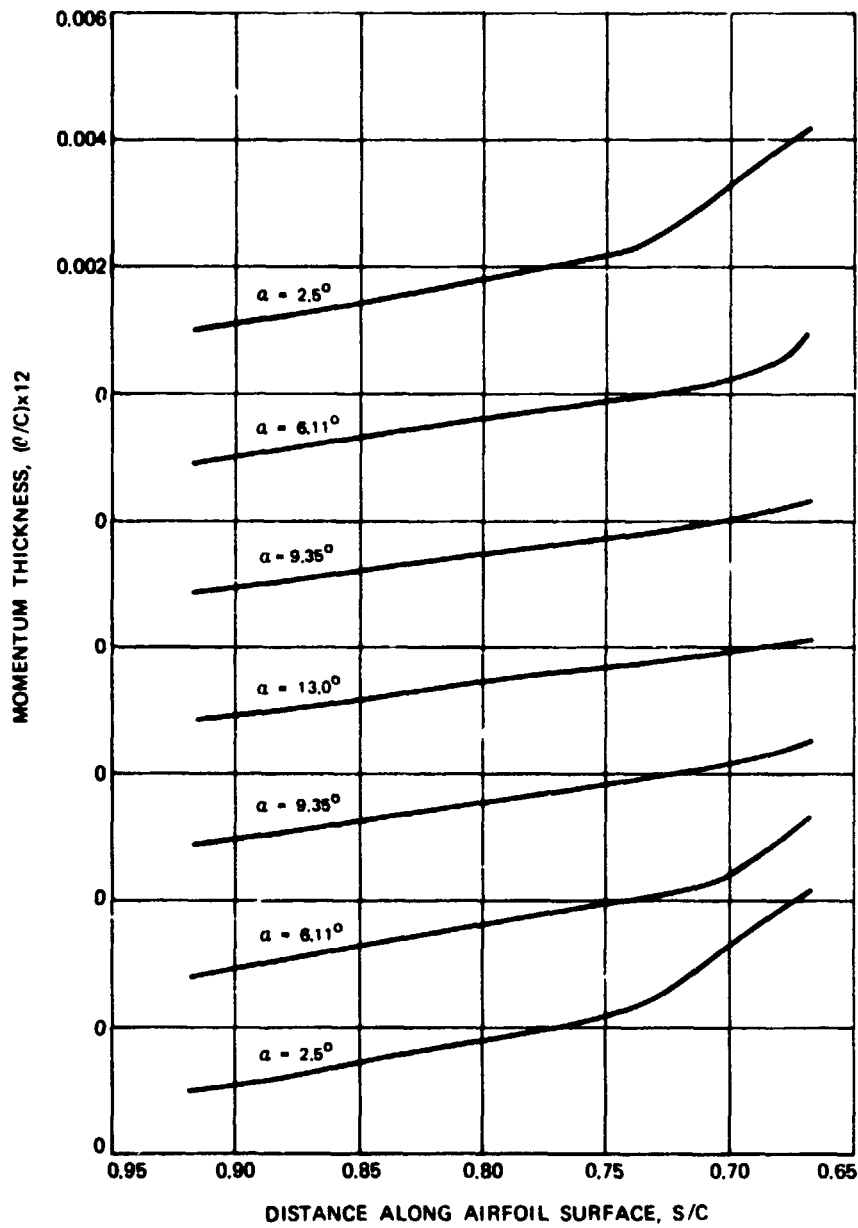
Figure 24. — Variation of momentum thickness along airfoil surface in the pressure side transition region at various instantaneous angles of attack for Case I.
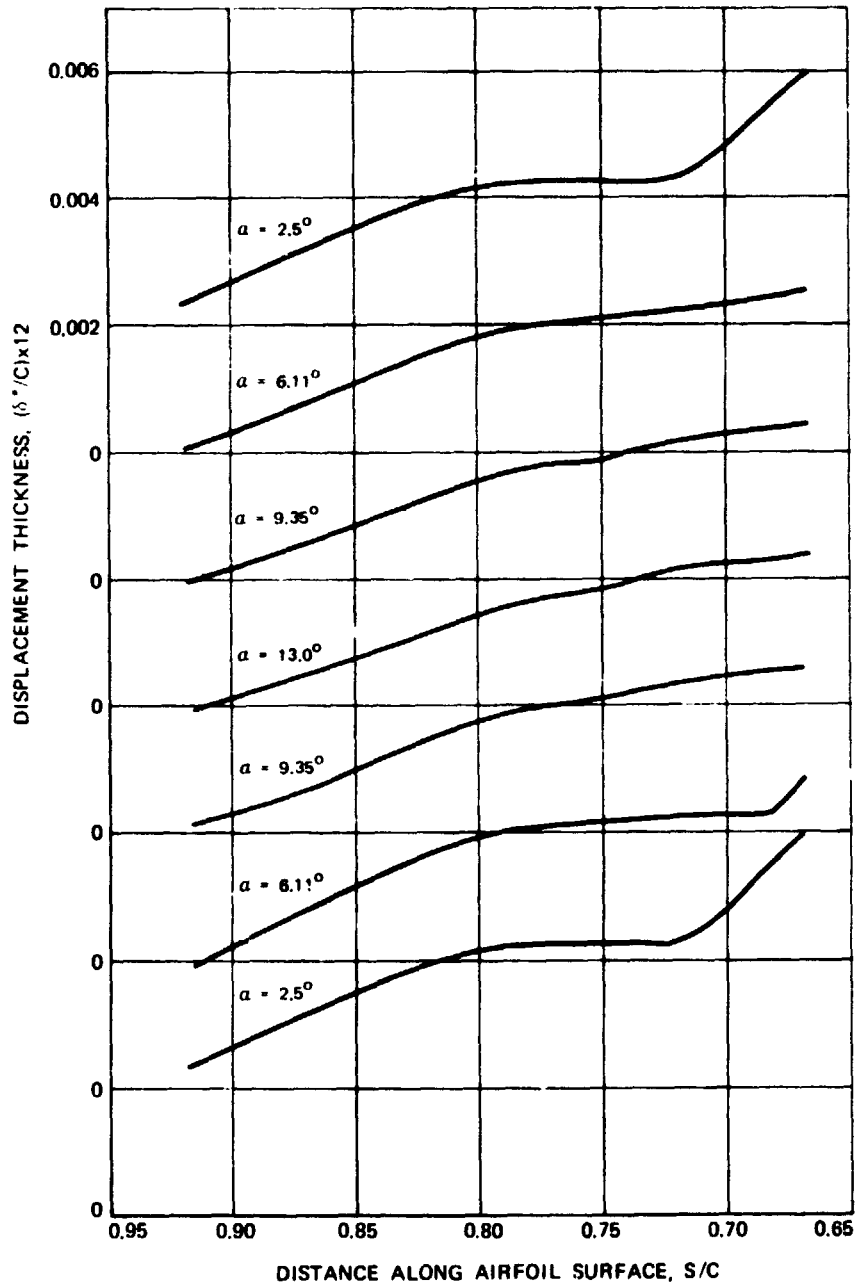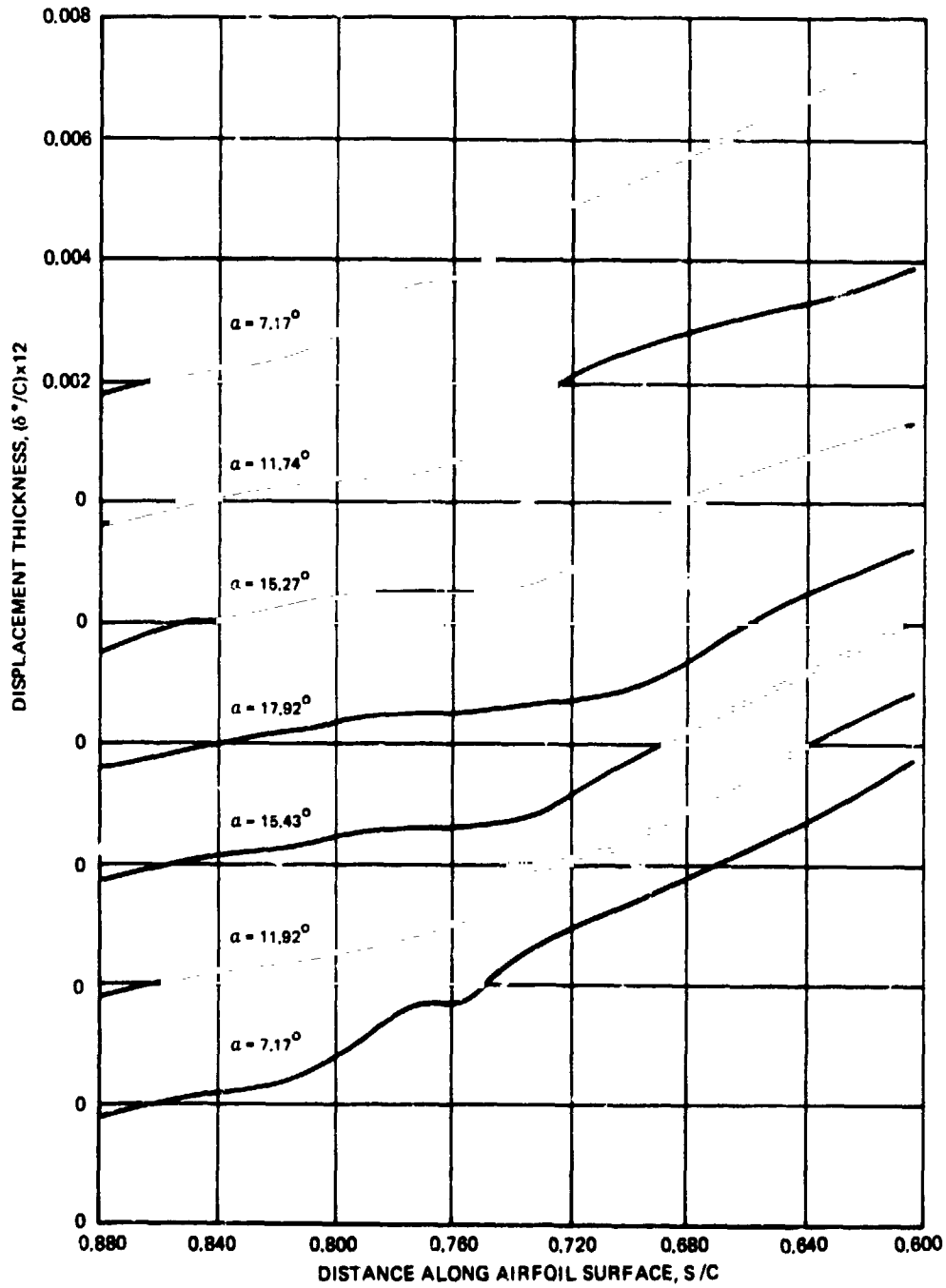
Figure 25. — Variation of displacement thickness along airfoil surface in the pressure side transition region at various instantaneous angles of attack for Case I.
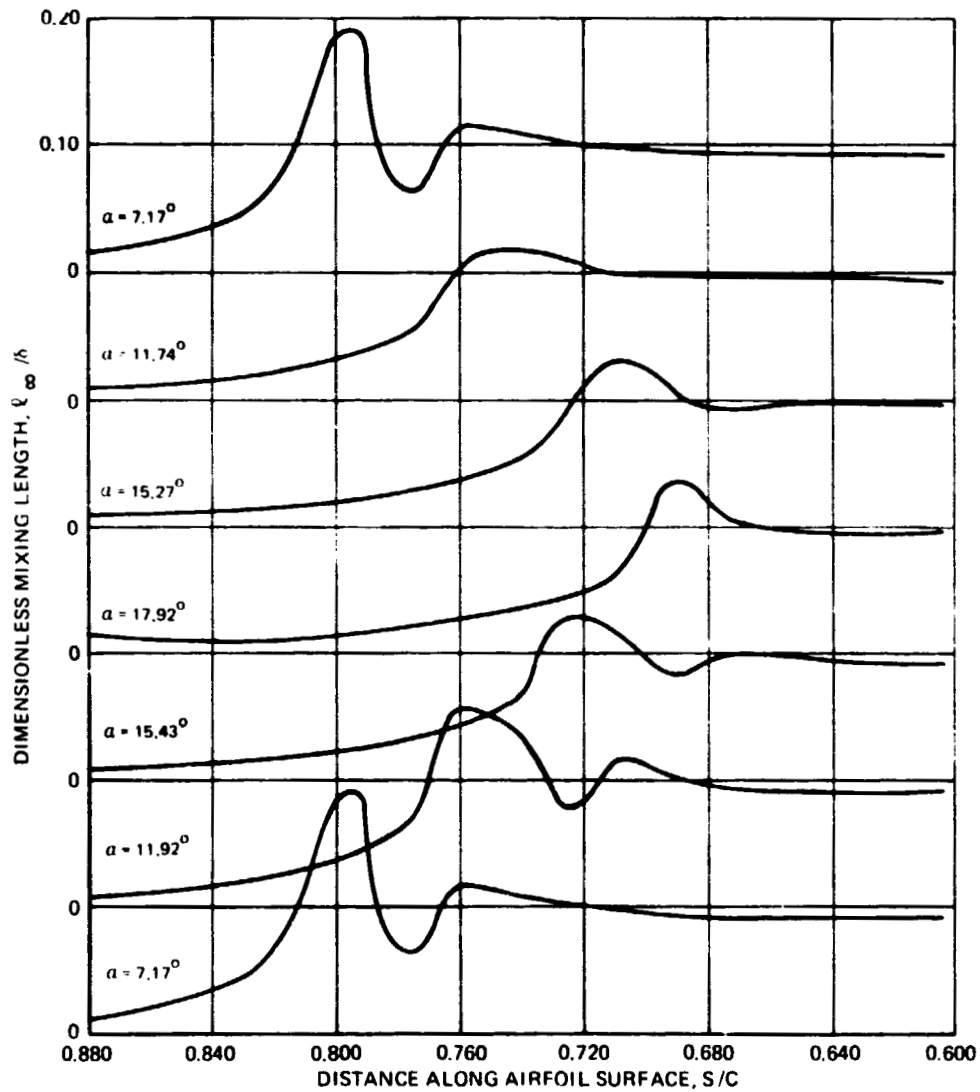
86

Figure 26. — Var'. tion of dimensionless mixing length along airfoil surace in the pressure side transition region at various instantaneous angles of attack for Case I.

87
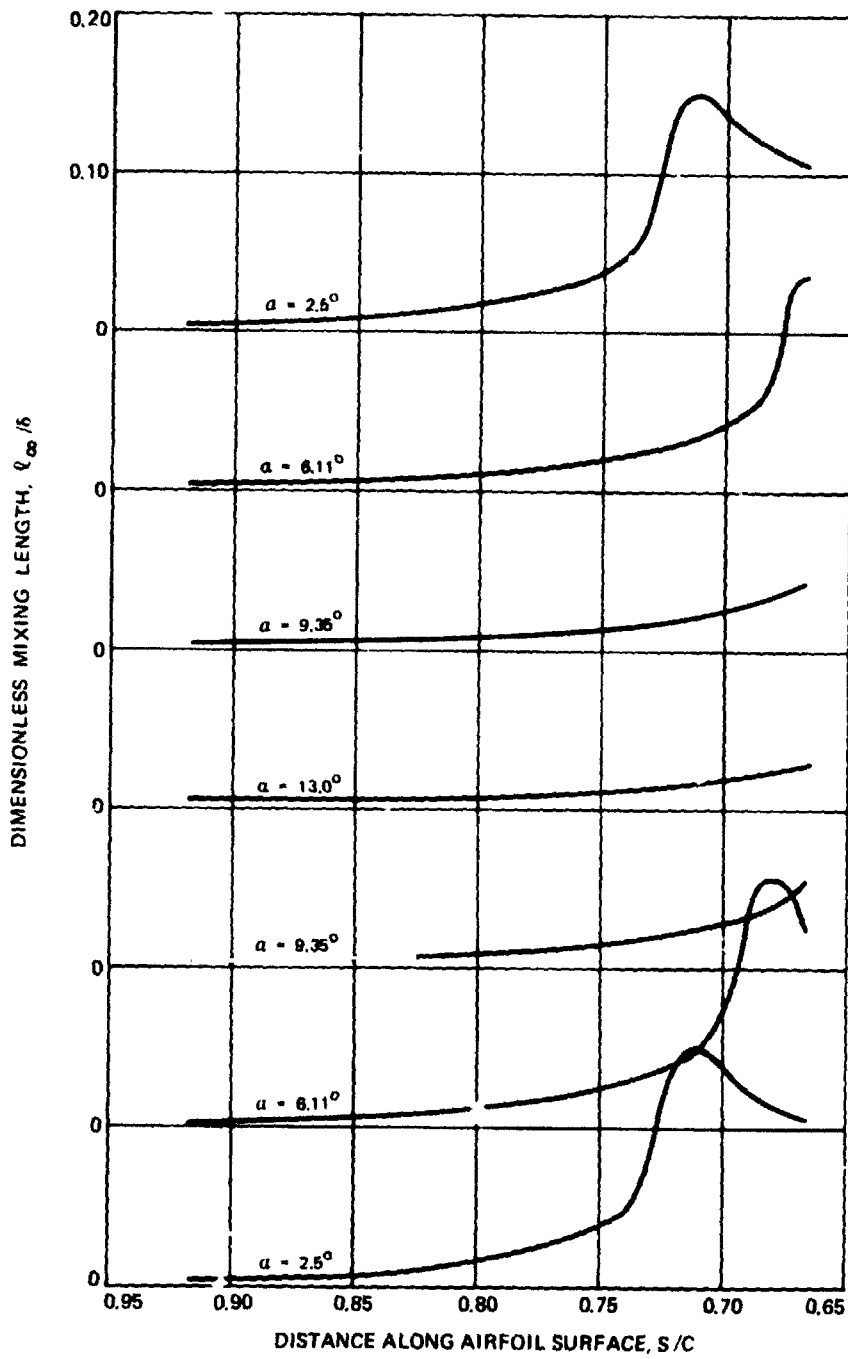
Figure 27. — Predicted instantaneous velocity profiles at a fixed streamwise location in the press ire side transition region for Case I .
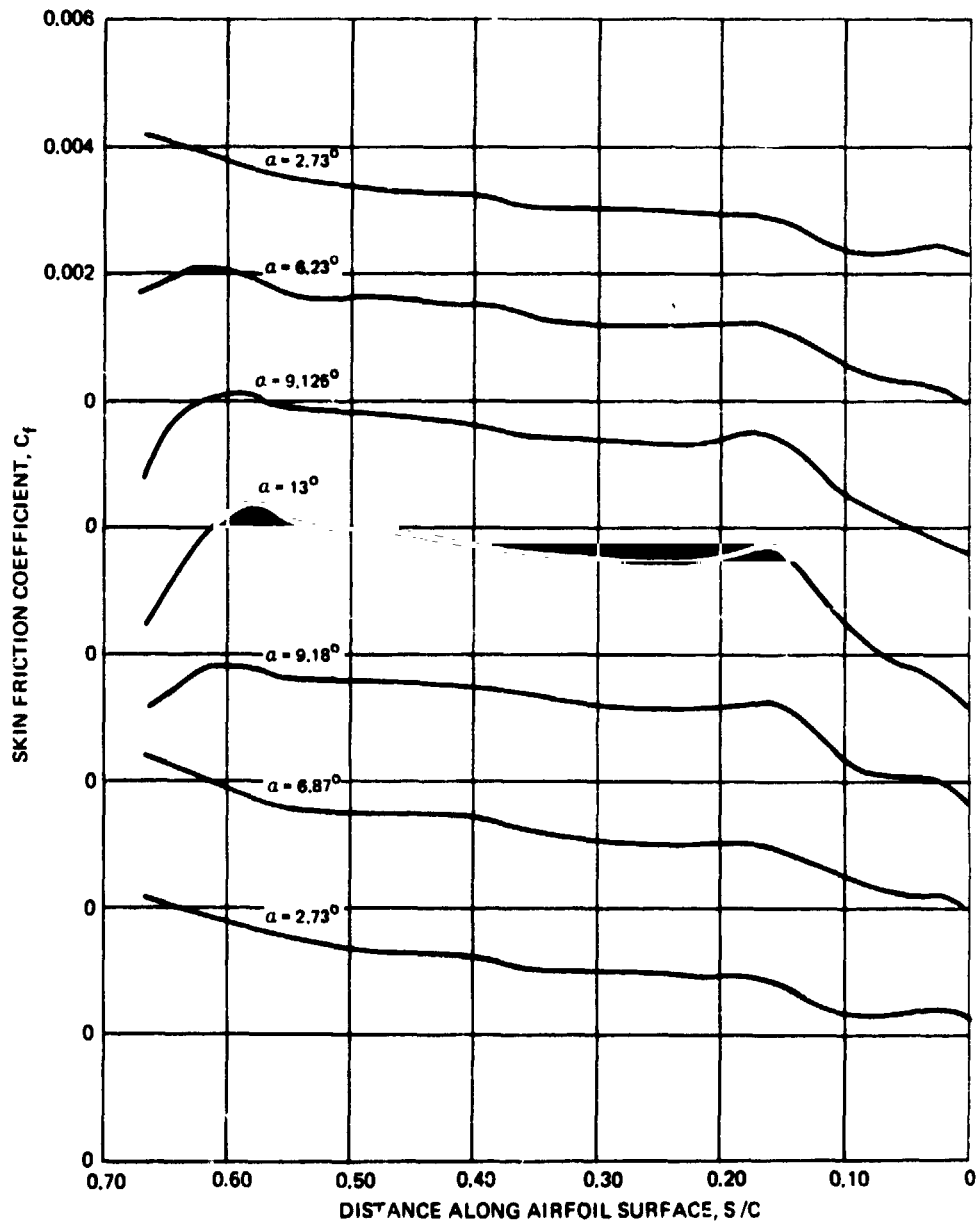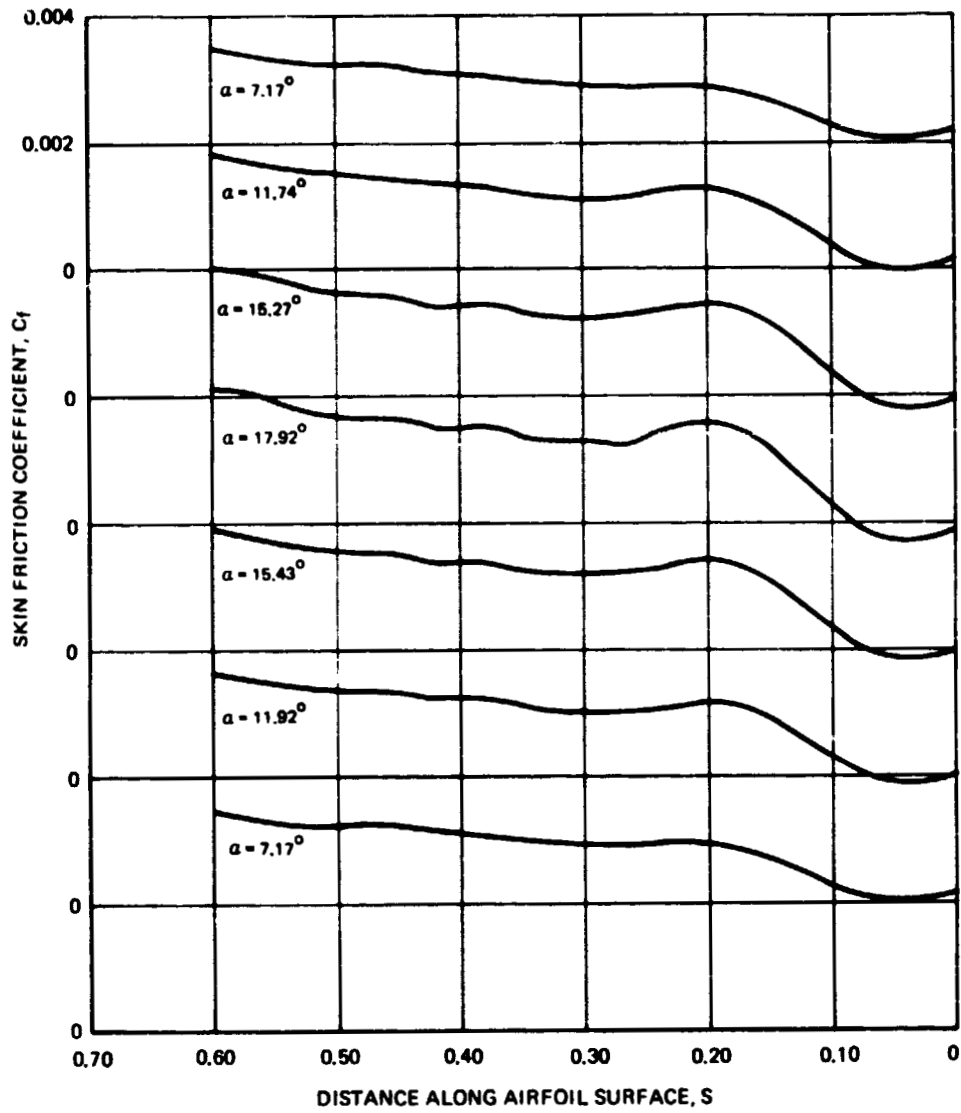
Figure 28. — Variation of skin friction coefficient alo..g airfoil surface in the pressure side fully turbulent region at various instantaneous angles of attack for Case I .

89

Figure 29 . — Variation of momentum thickness along airfoil surface in the pressure side fully turbulent region at various instantaneous angles of attack for Case I .
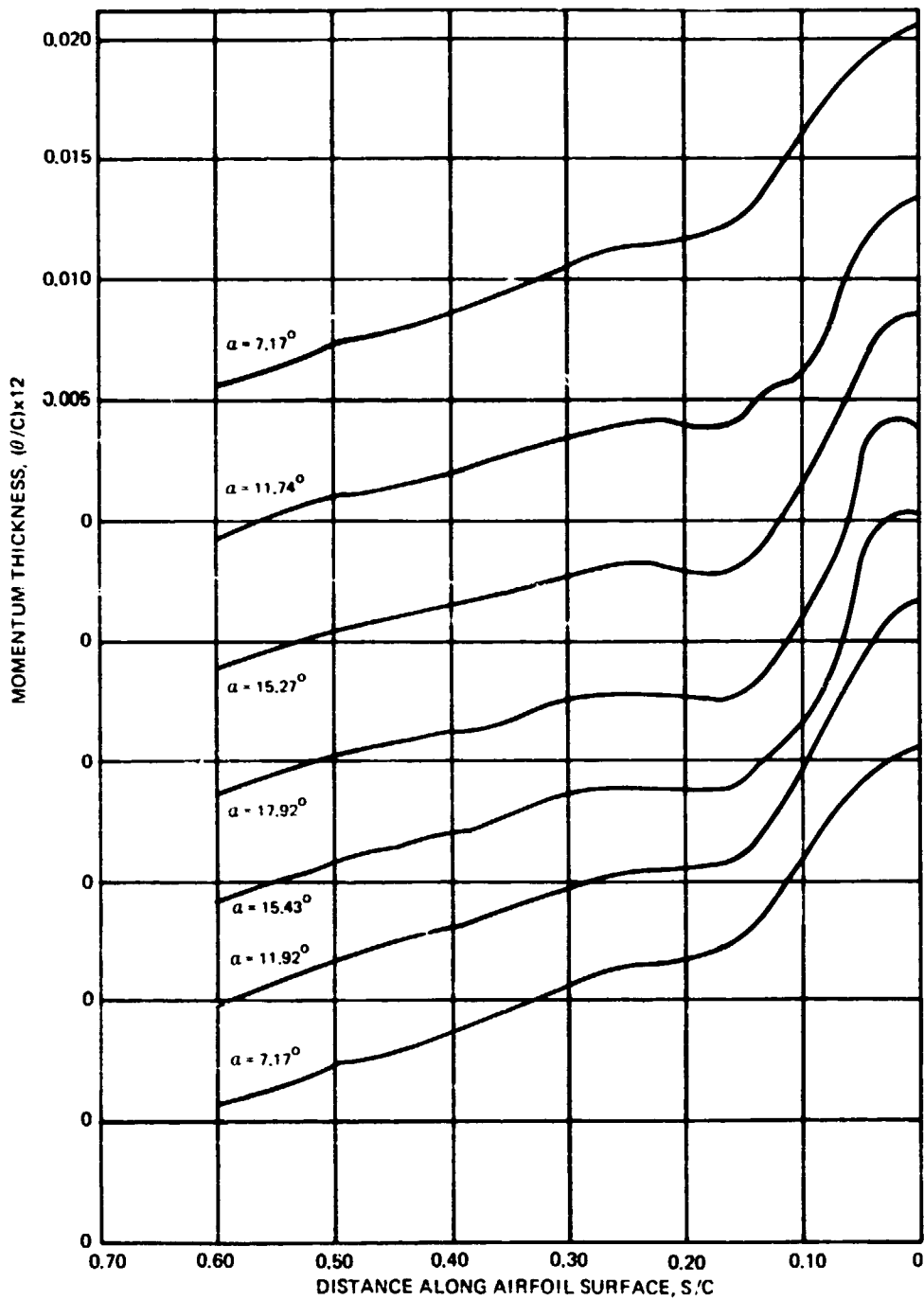
90
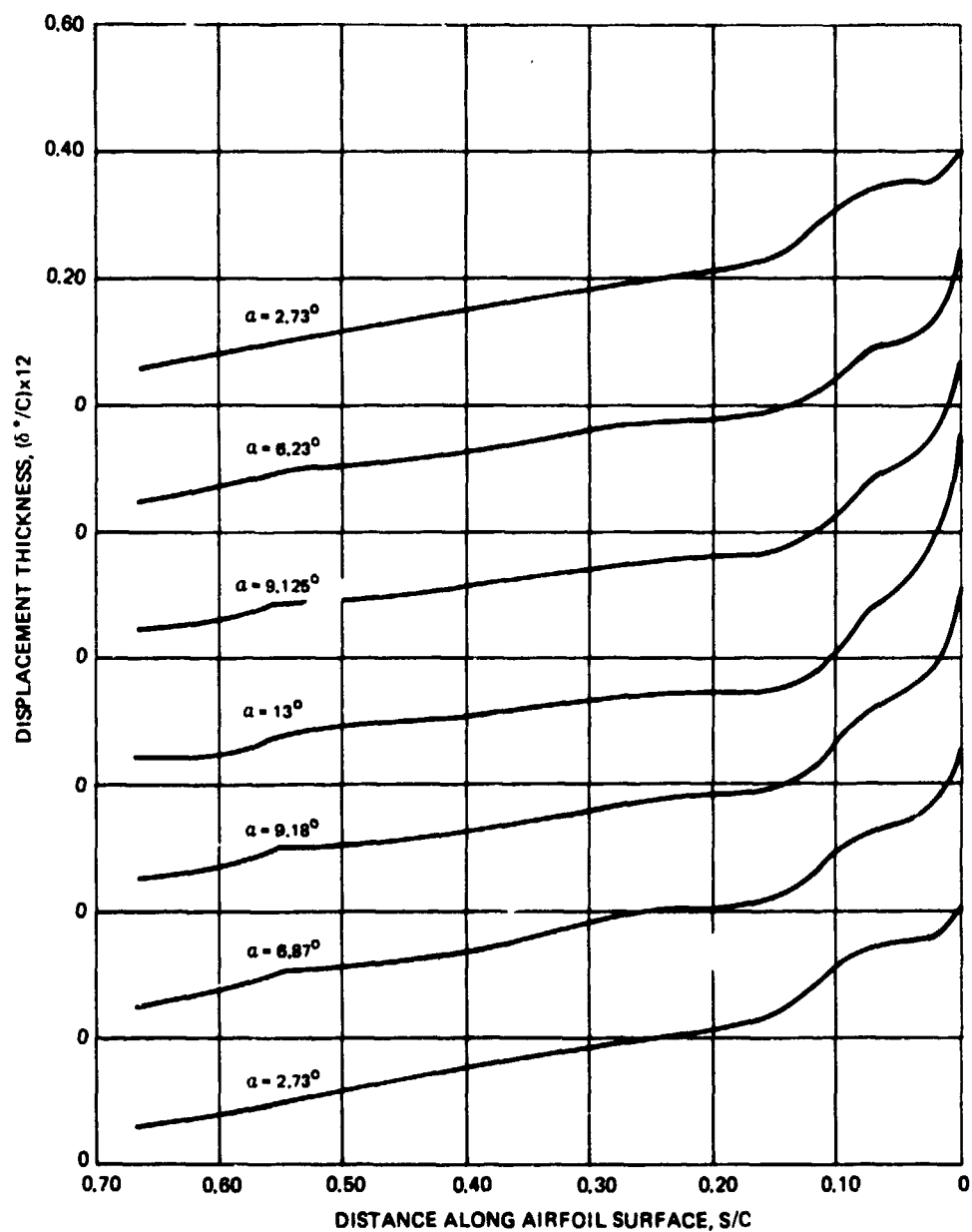
Figure 30. — Variation of displacement thickness along airfoil surface in the pressure side fully turbulent region at various instantaneous angles of attack for Case I.

91
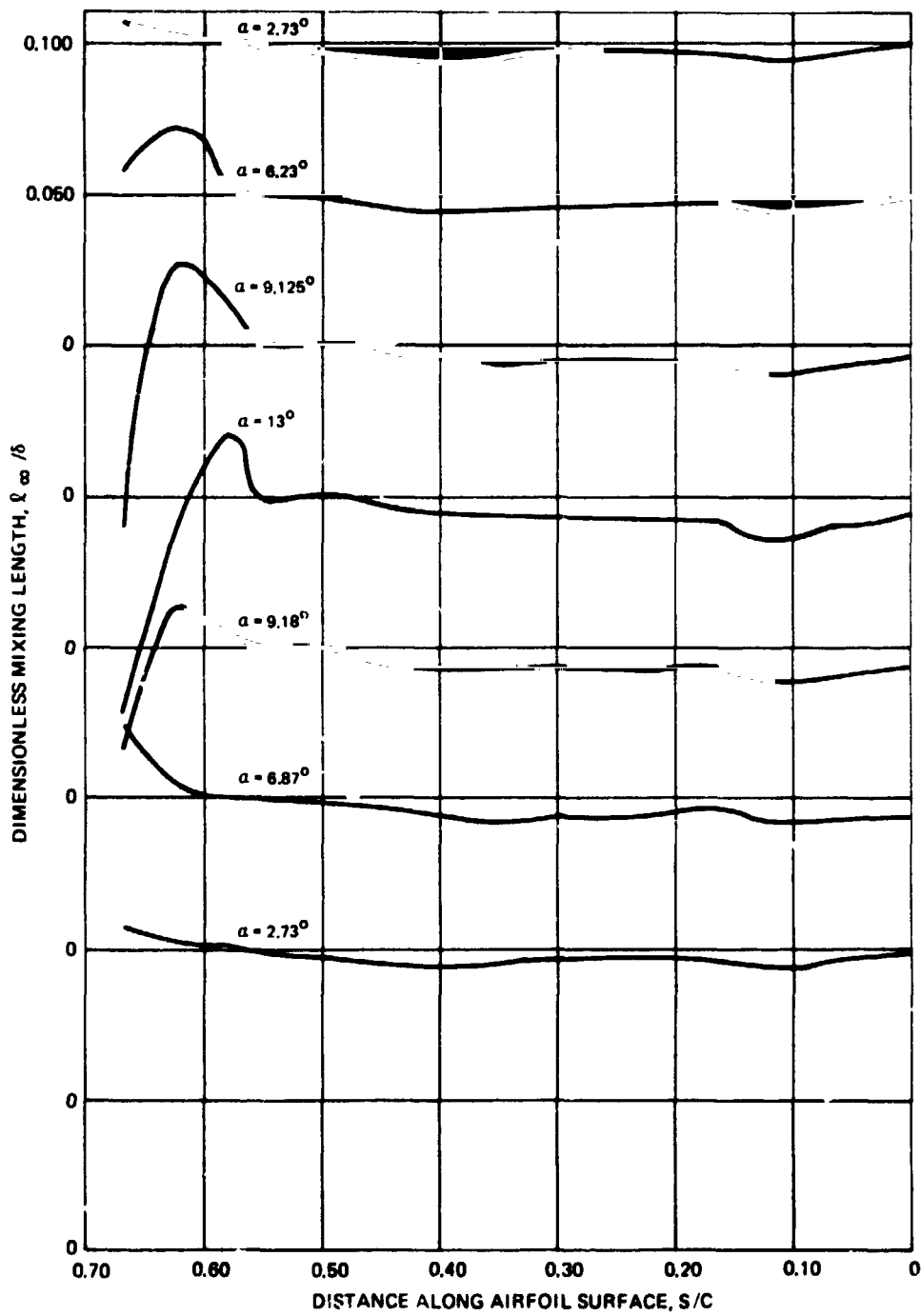
Figure 31. — Variation of dimensionless mixing length along airfoil surface in the pressure side fully turbulent region at various instantaneous angles of attack for Case I .

92
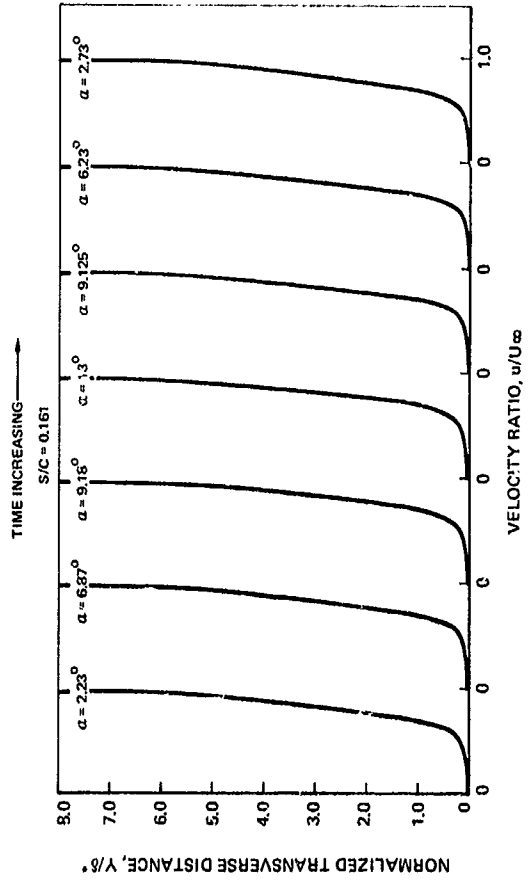
Figure 32. — Predicted instantaneous velocity profiles at a fixed streamwise location in the pressure side fully turbulent region for Case I .

93
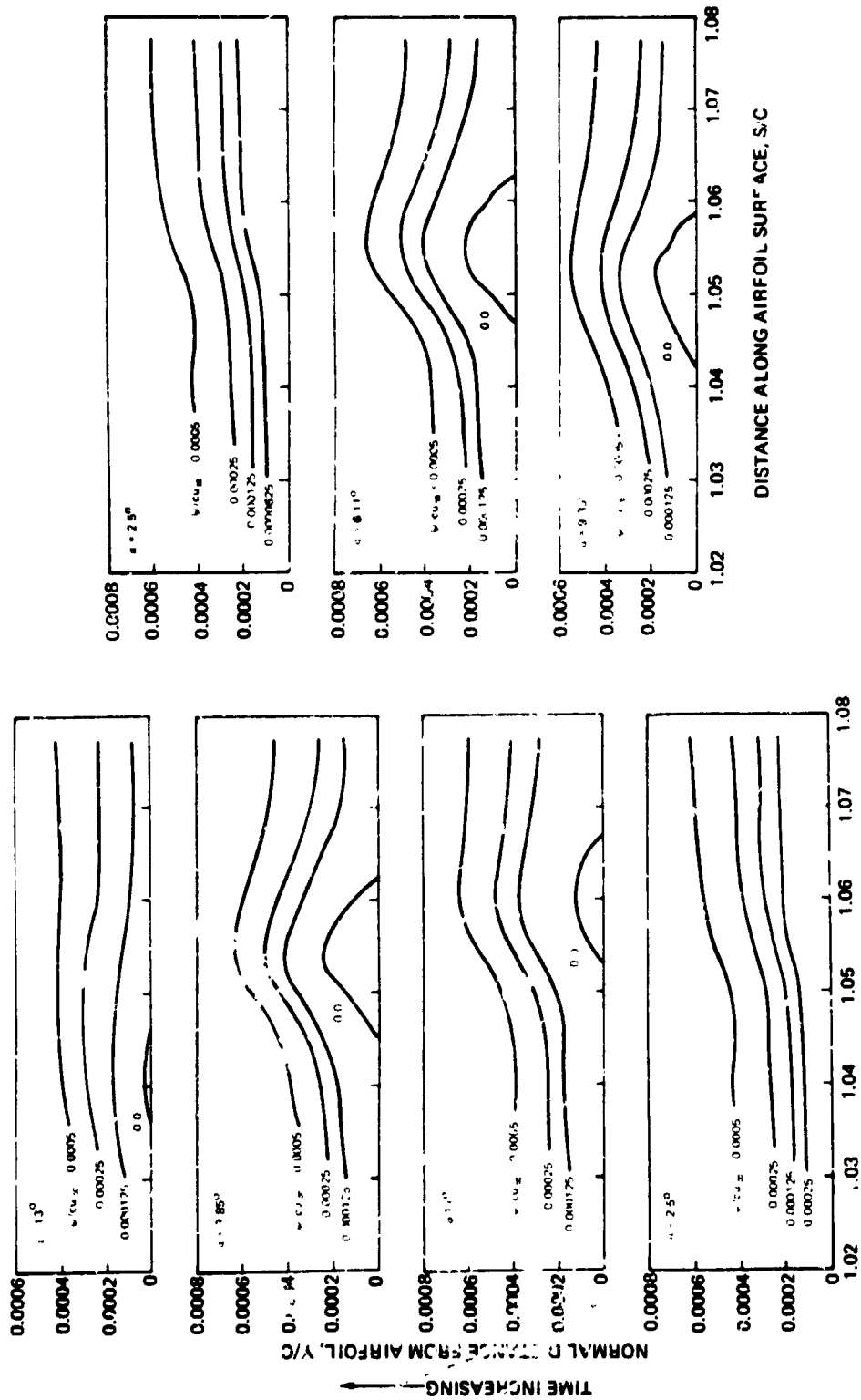
Figure 33. — Streamlines in the separated region of the airfoil suction side at various instantaneous angles of attack for Case I.
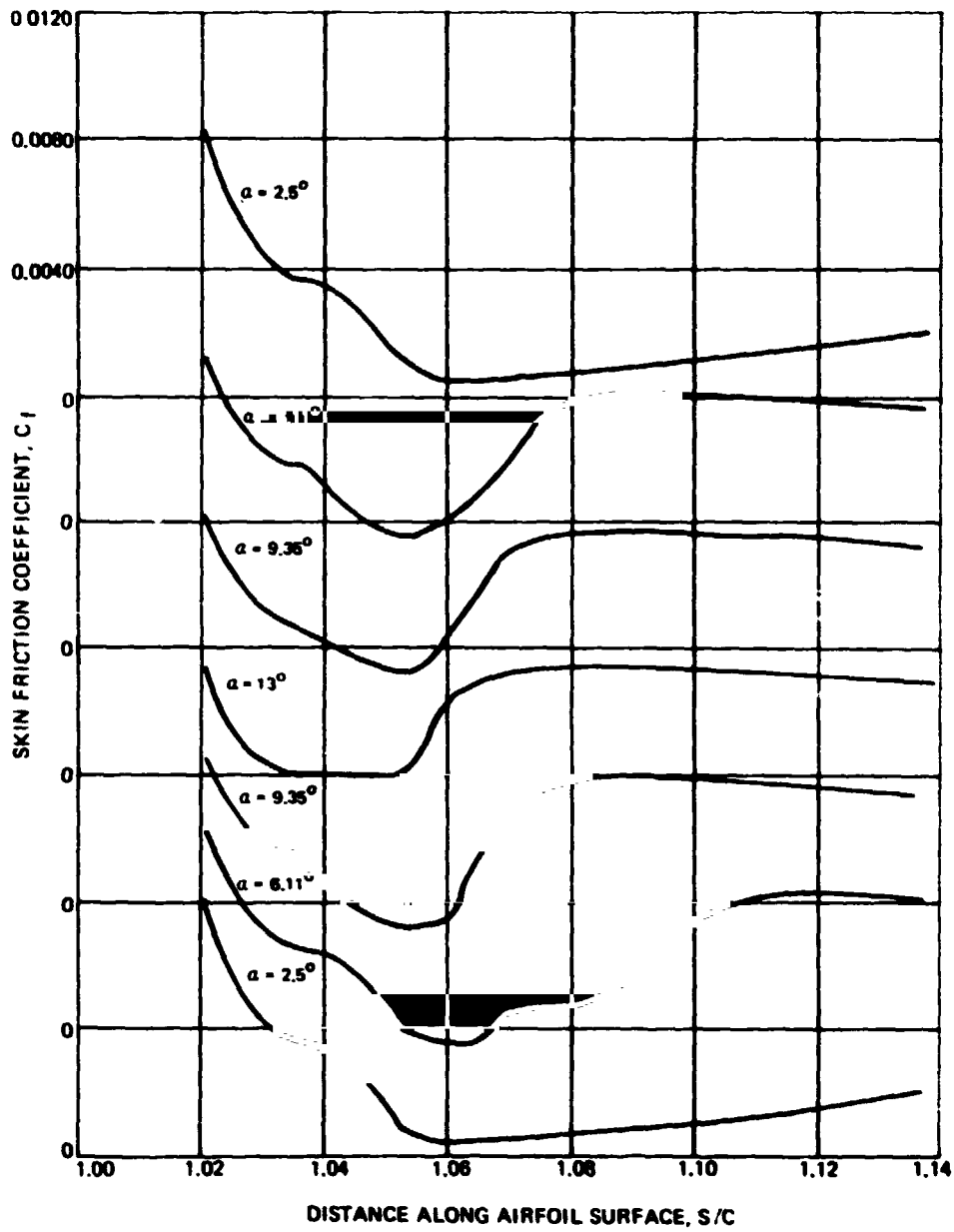
Figure 34.—Variation of skin friction coefficient in the separated region of the airfoil suction side at various instantaneous angles of attack for Case I.
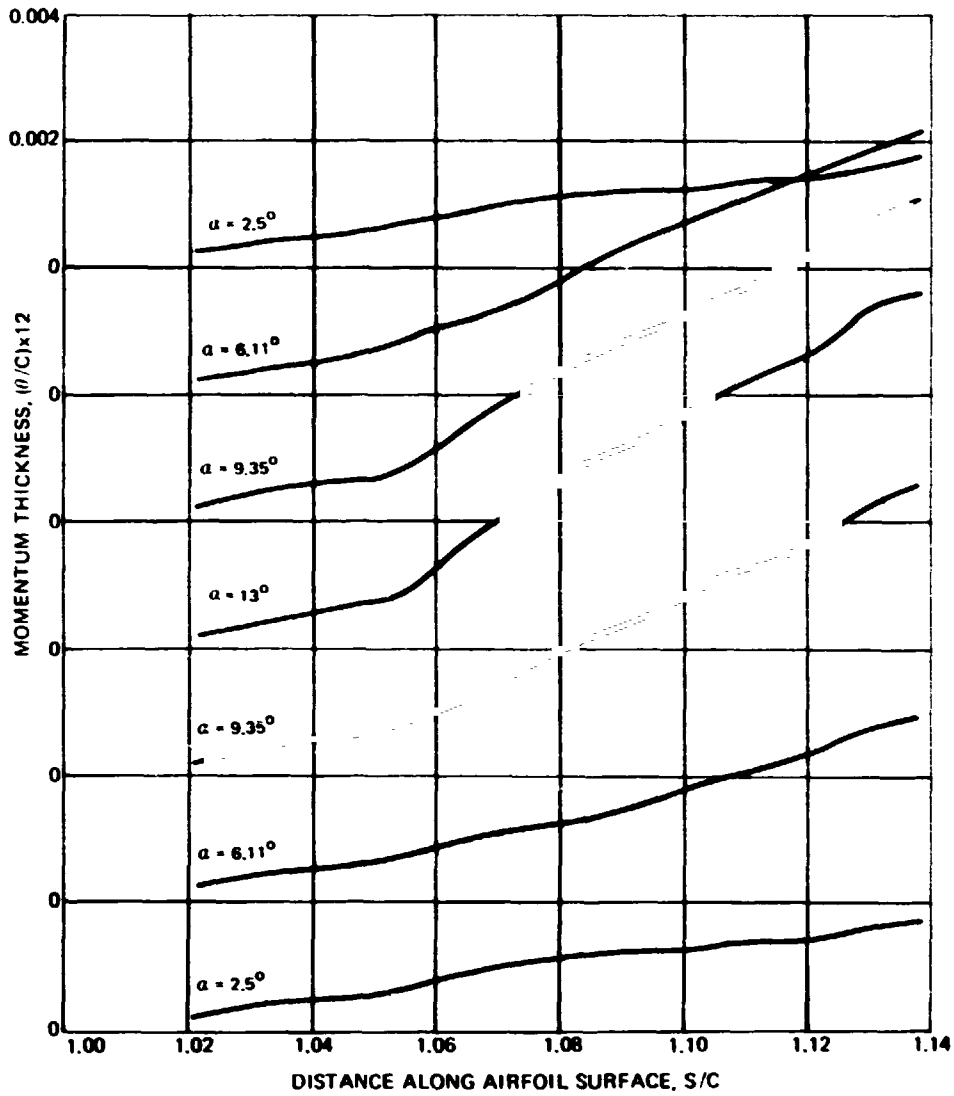
Figure 35. — Va. iation of momentum thickness in the separated region of the airfoil suction side at various instantaneous angles of attack for Case I.
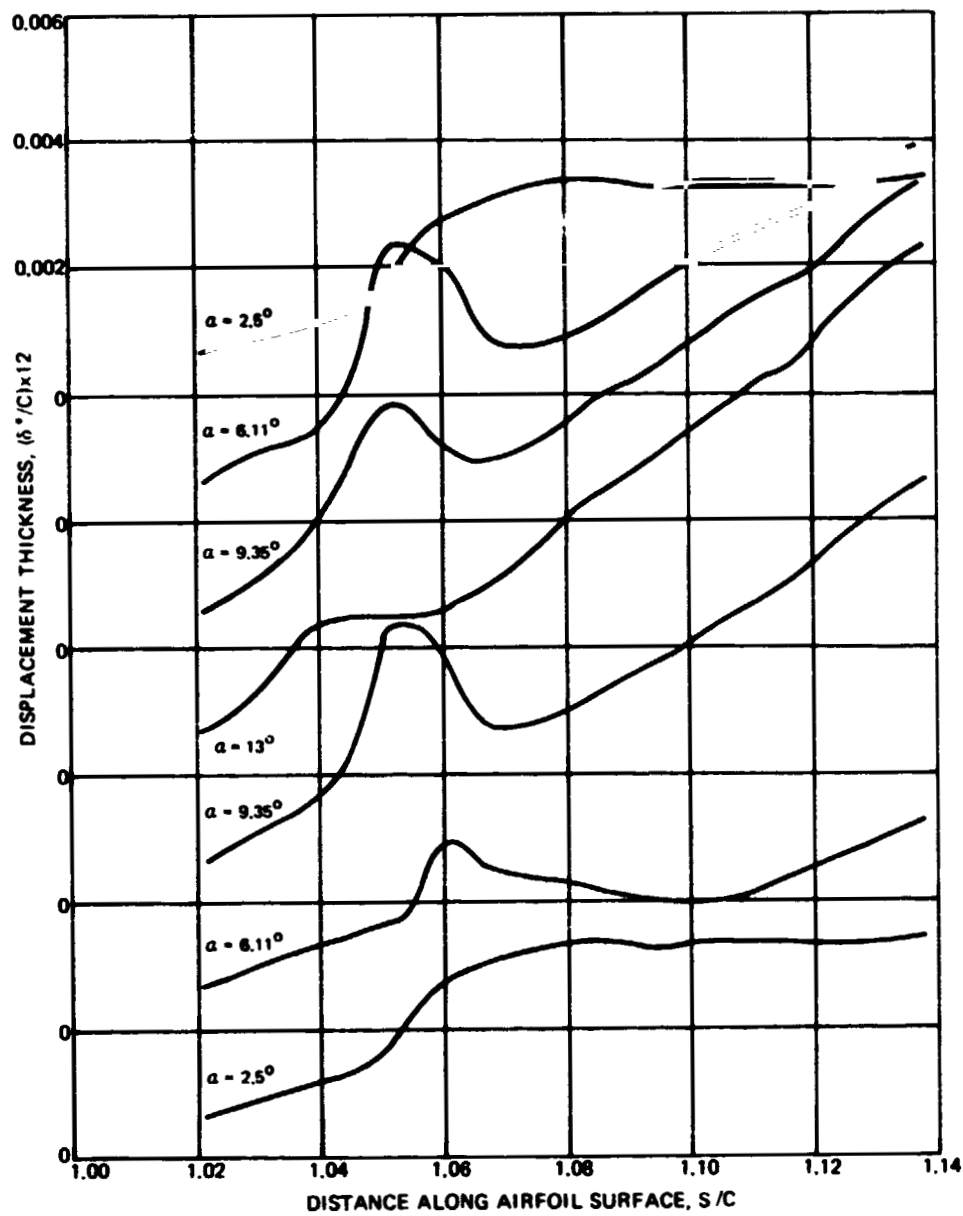
Figure 36.— Variation of displacement thickness in the separated region of the airfoil suction side at various instantaneous angles of attack for Case I .
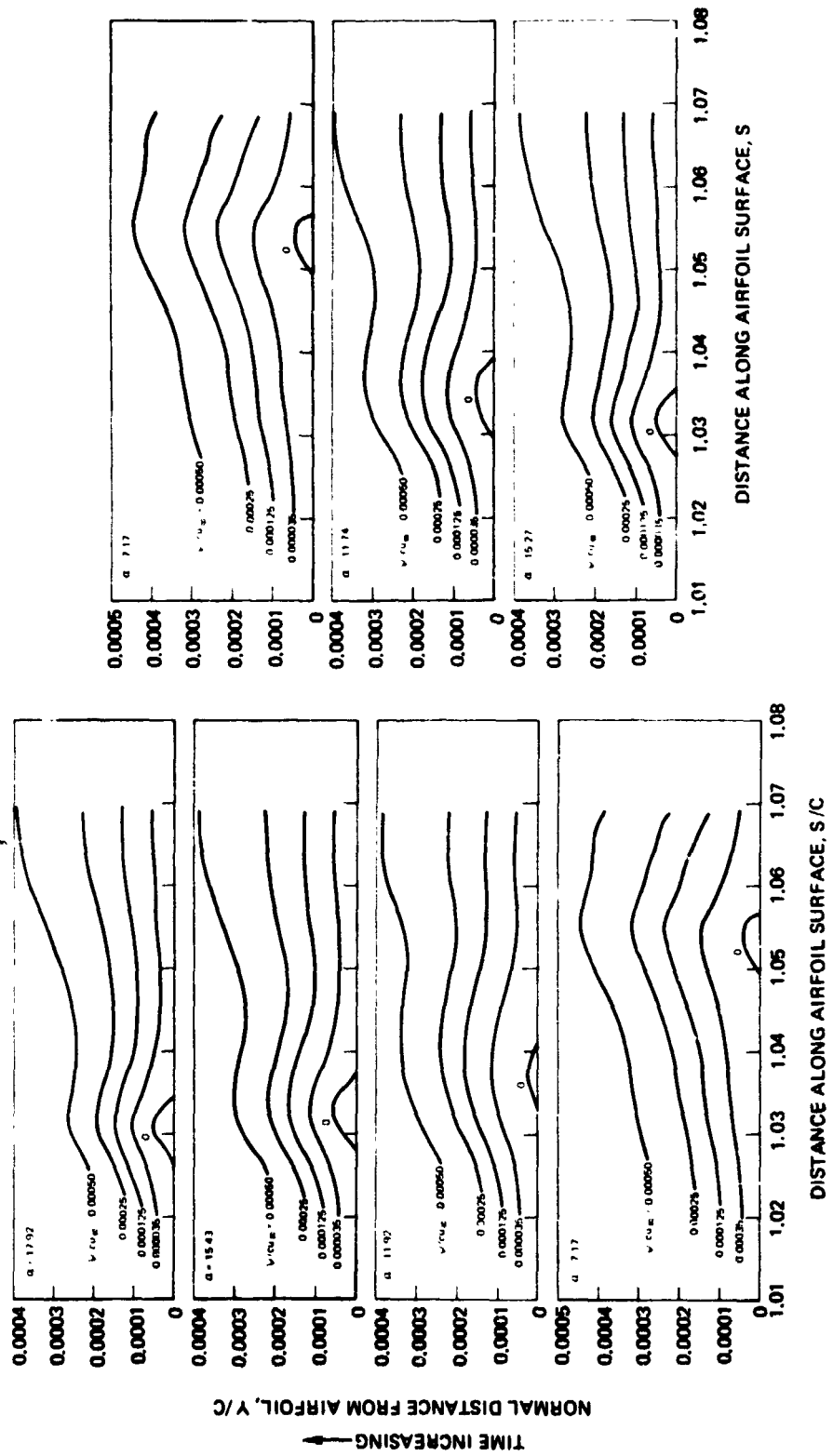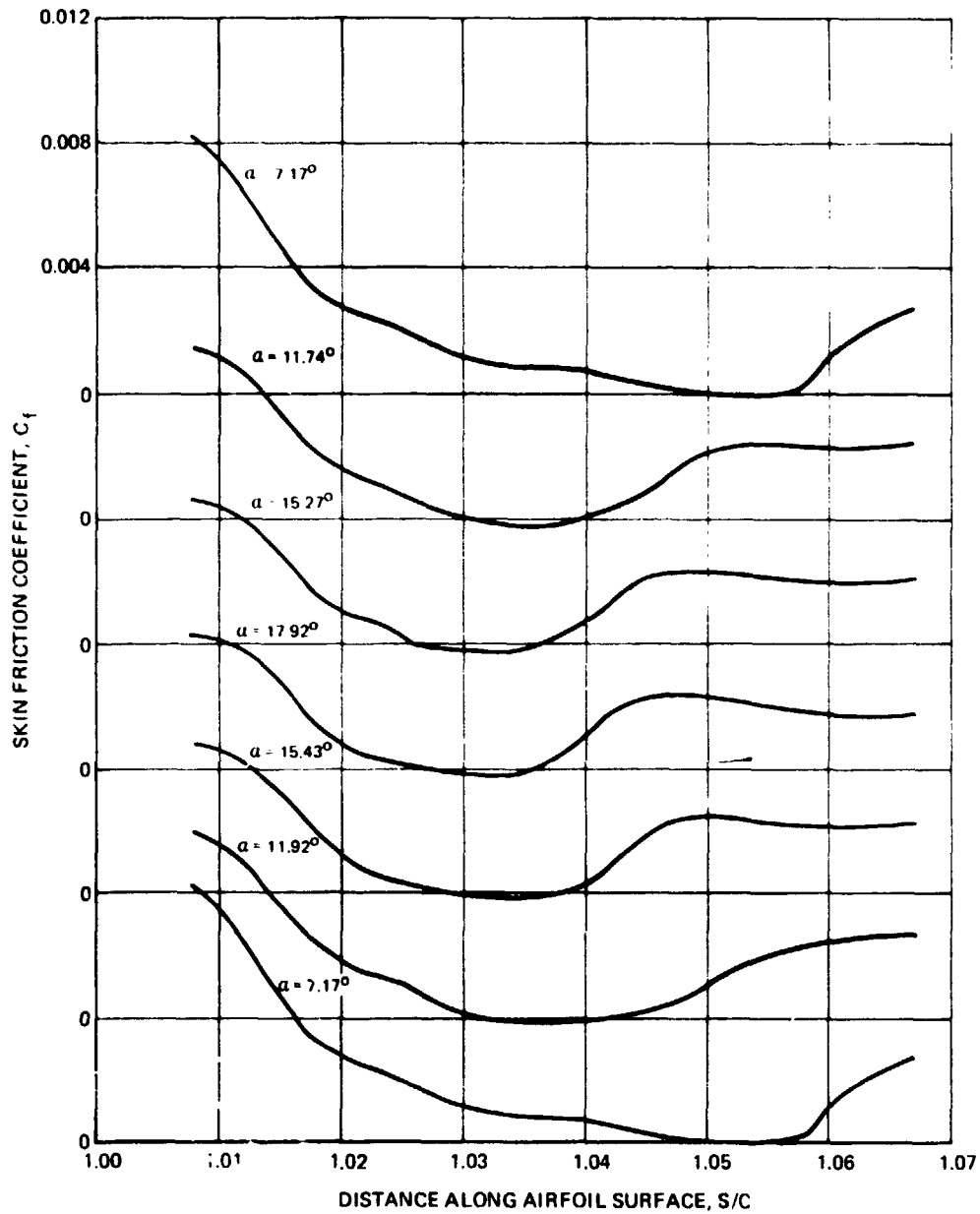
97
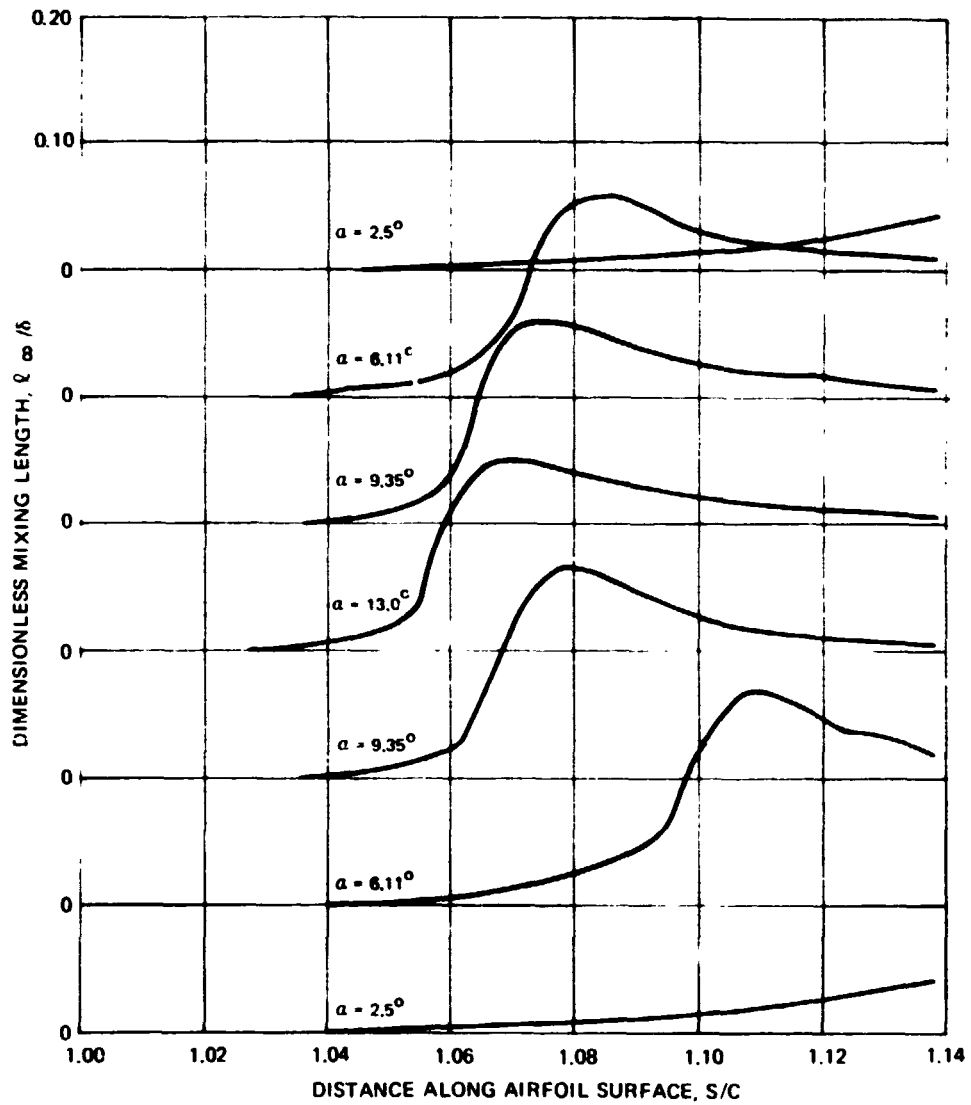
Figure 37. — Variation of dimensionless mixing length in the separated region of the airfoil suction side at various instantaneous angles of attack for Case I.

TIME INCREASING ———→

S / C = 1.057

NORMALIZED TRANSVERSE DISTANCE, Y/δ*

VELOCITY RATIO, u/U∞

$\alpha = 2.5°$ $\alpha = 6.11°$ $\alpha = 9.35°$ $\alpha = 13°$ $\alpha = 9.35°$ $\alpha = 6.11°$ $\alpha = 2.5°$
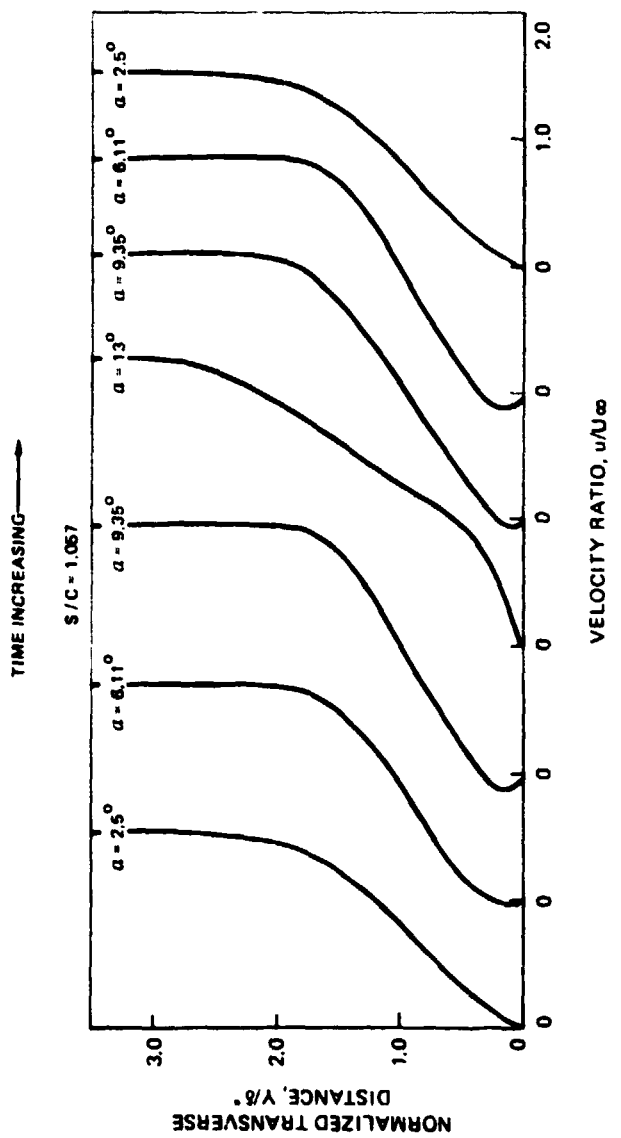
Figure 38. — Predicted instantaneous velocity profiles at a fixed streamwise location in the separated region for Case I.
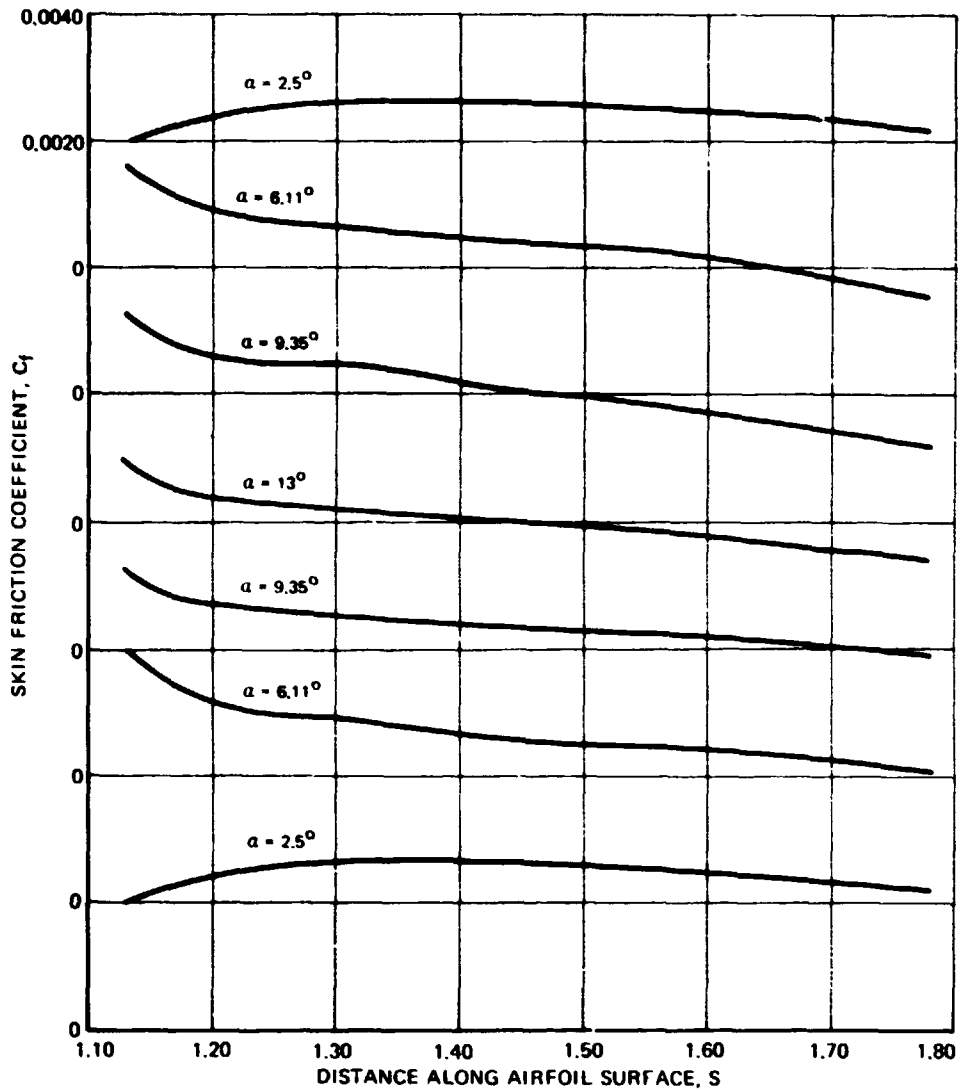
Figure 39.— Variation of skin friction coefficient along the airfoil surface in the suction side fully turbulent region at various instantaneous angles of attack for Case I.
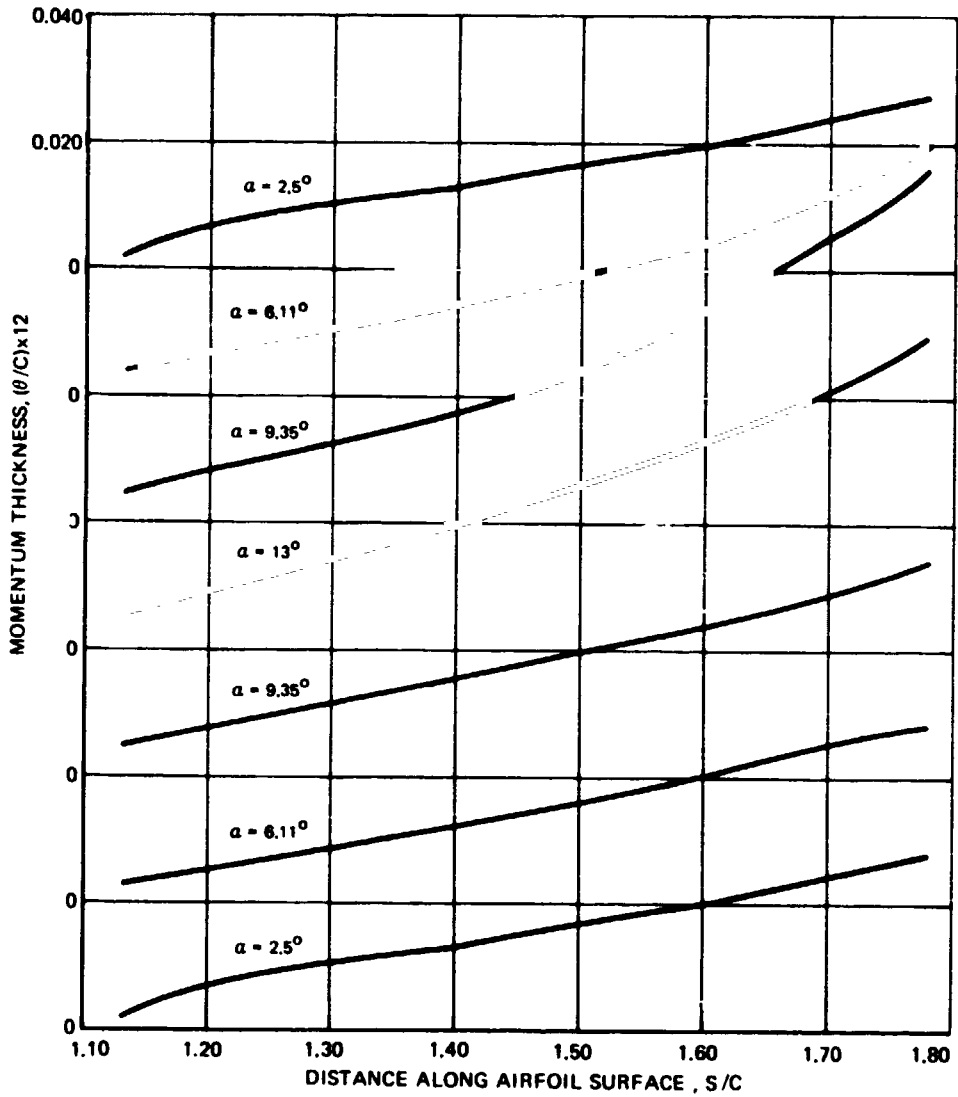
Figure 40. — Variation of momentum thickness along the airfoil surface in the suction side fully turbulent region at various instantaneous angles of attack for Case I.
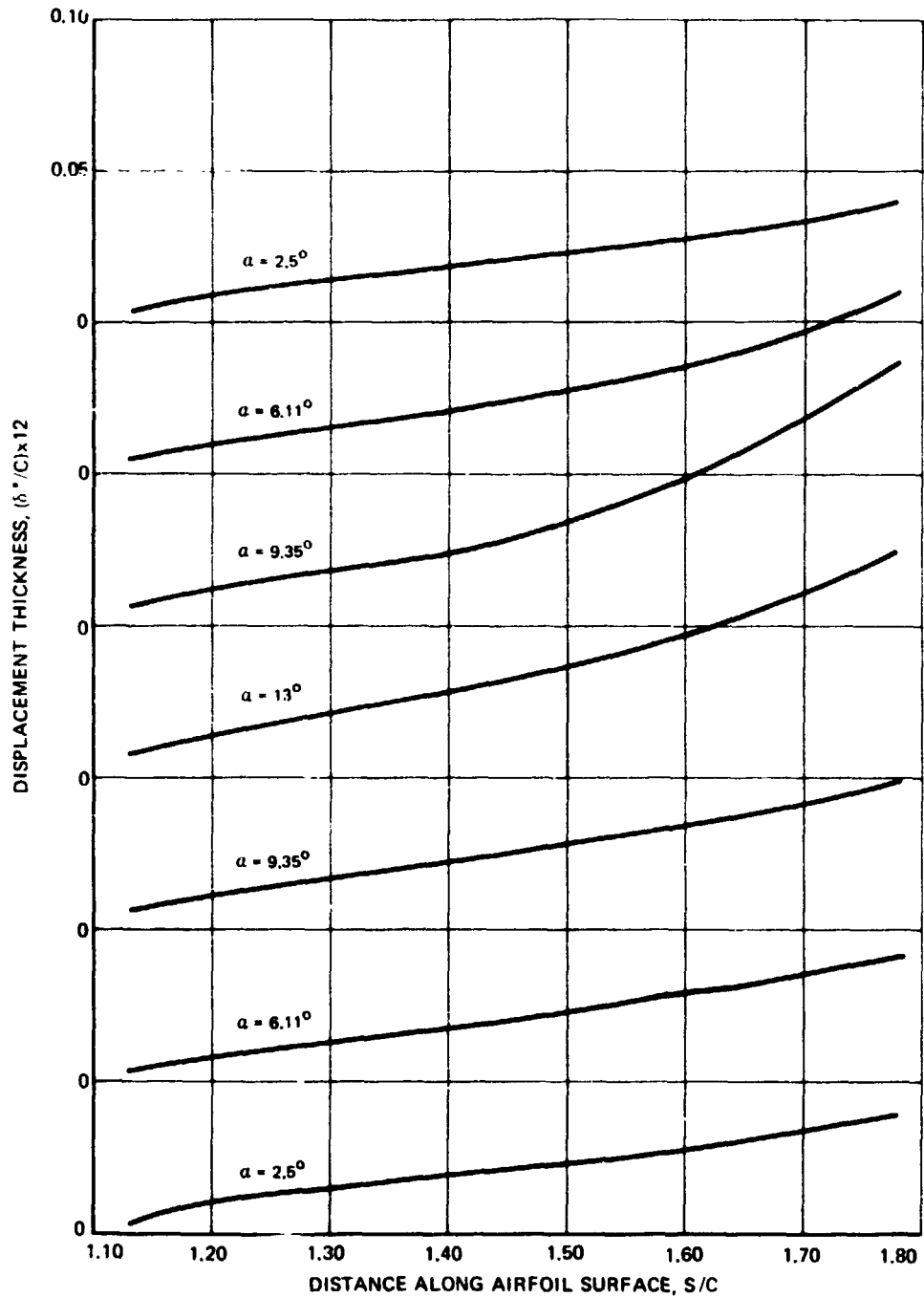
Figure 41. — Variation of displacement thickness along the airfoil surface in the suction side fully turbulent region at various instantaneous angles of attack for Case I.

102
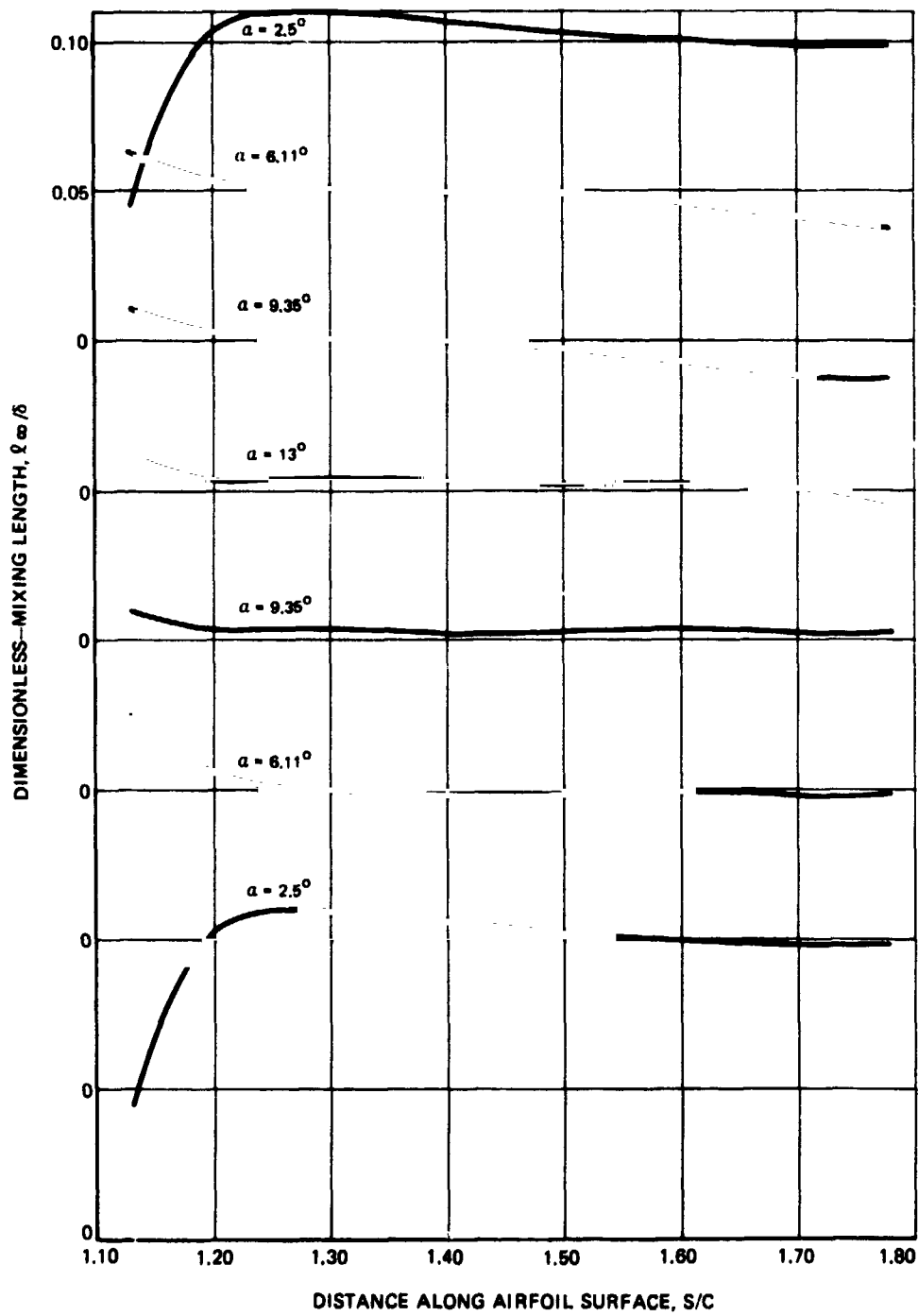
Figure 42. — Variation of dimensionless mixing length along the airfoil surface in the suction side fully turbulent region at various instantaneous angles of attack for Case I.
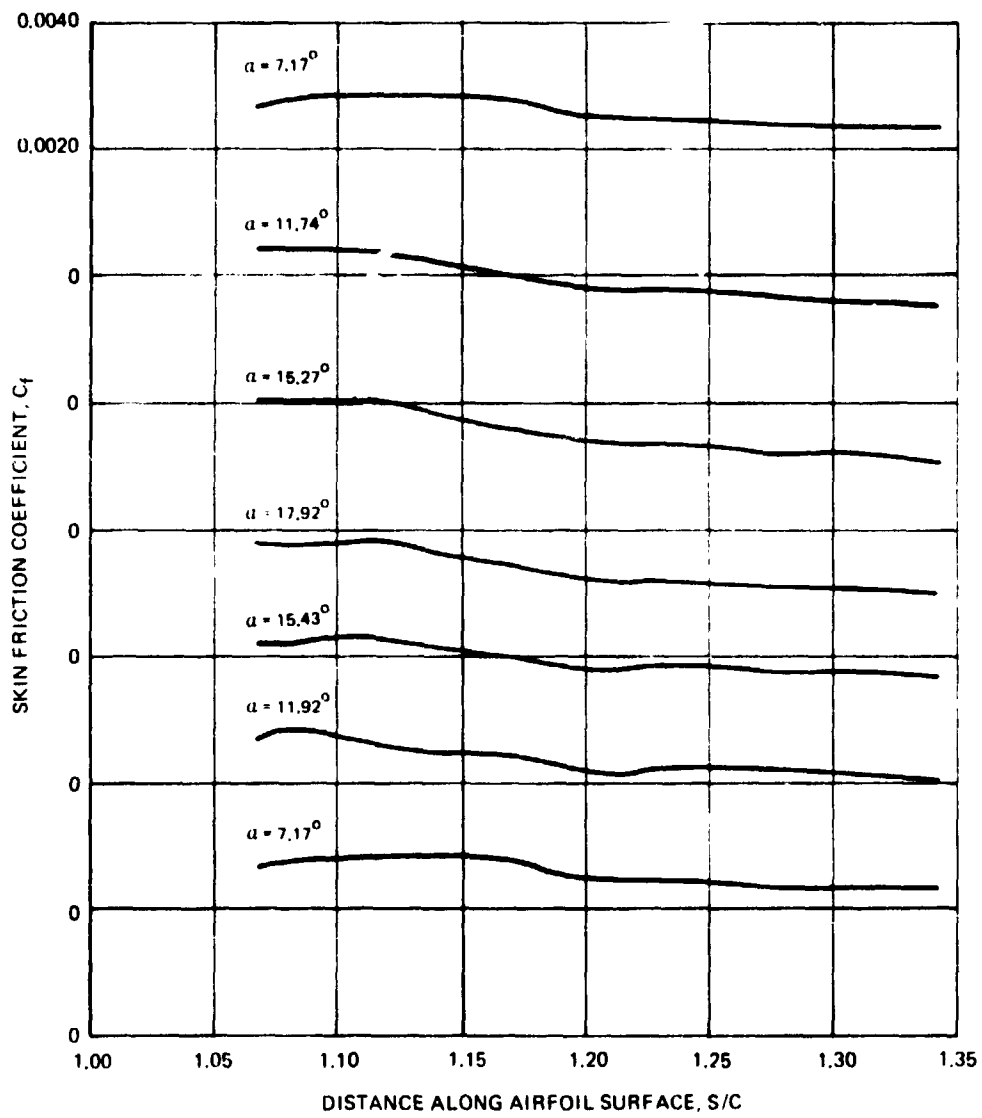
103
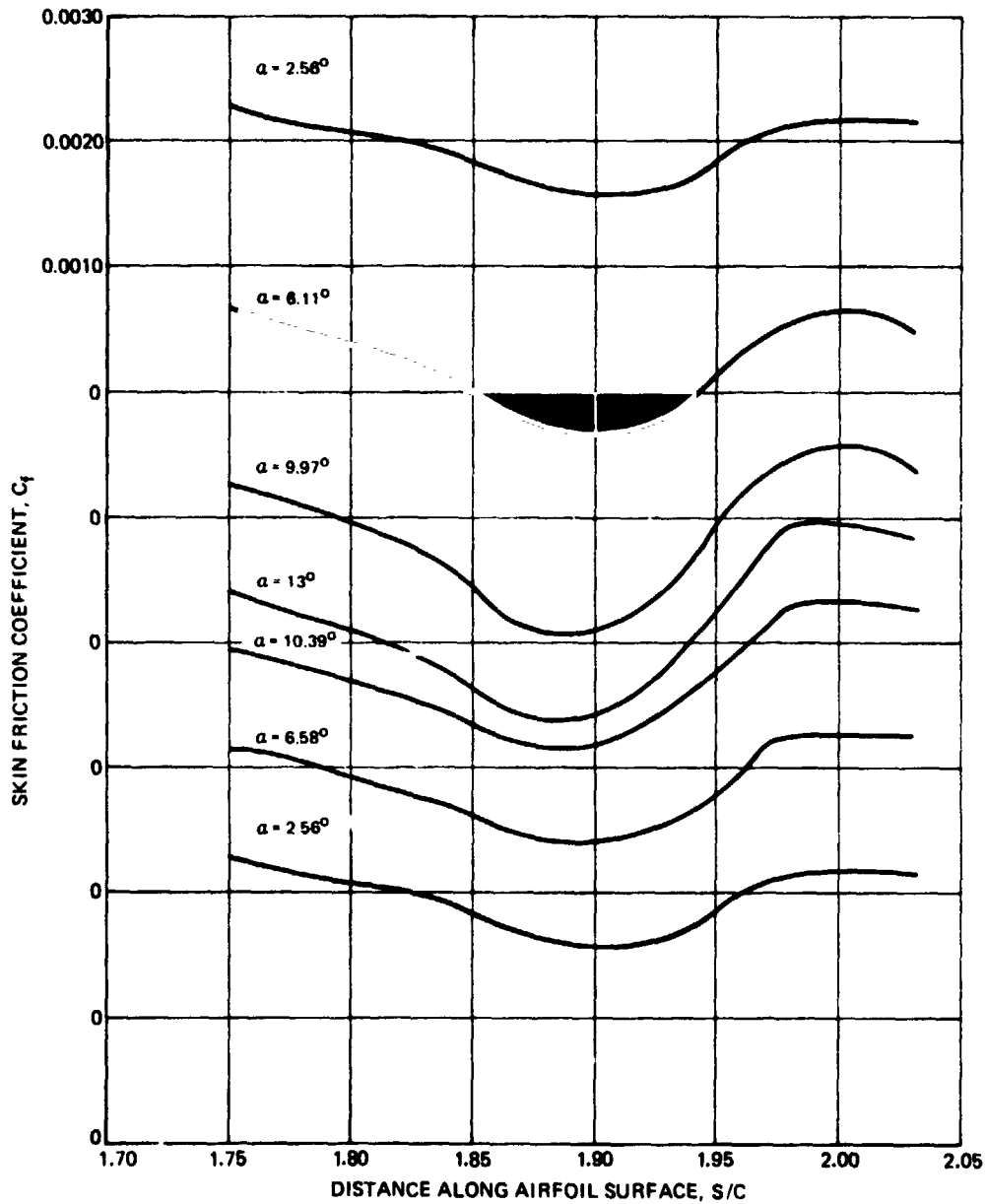
Figure 43. — Variation of skin friction coefficient along the airfoil surface in the suction side trailing edge fully turbulent region at various instantaneous angles of attack for Case I.
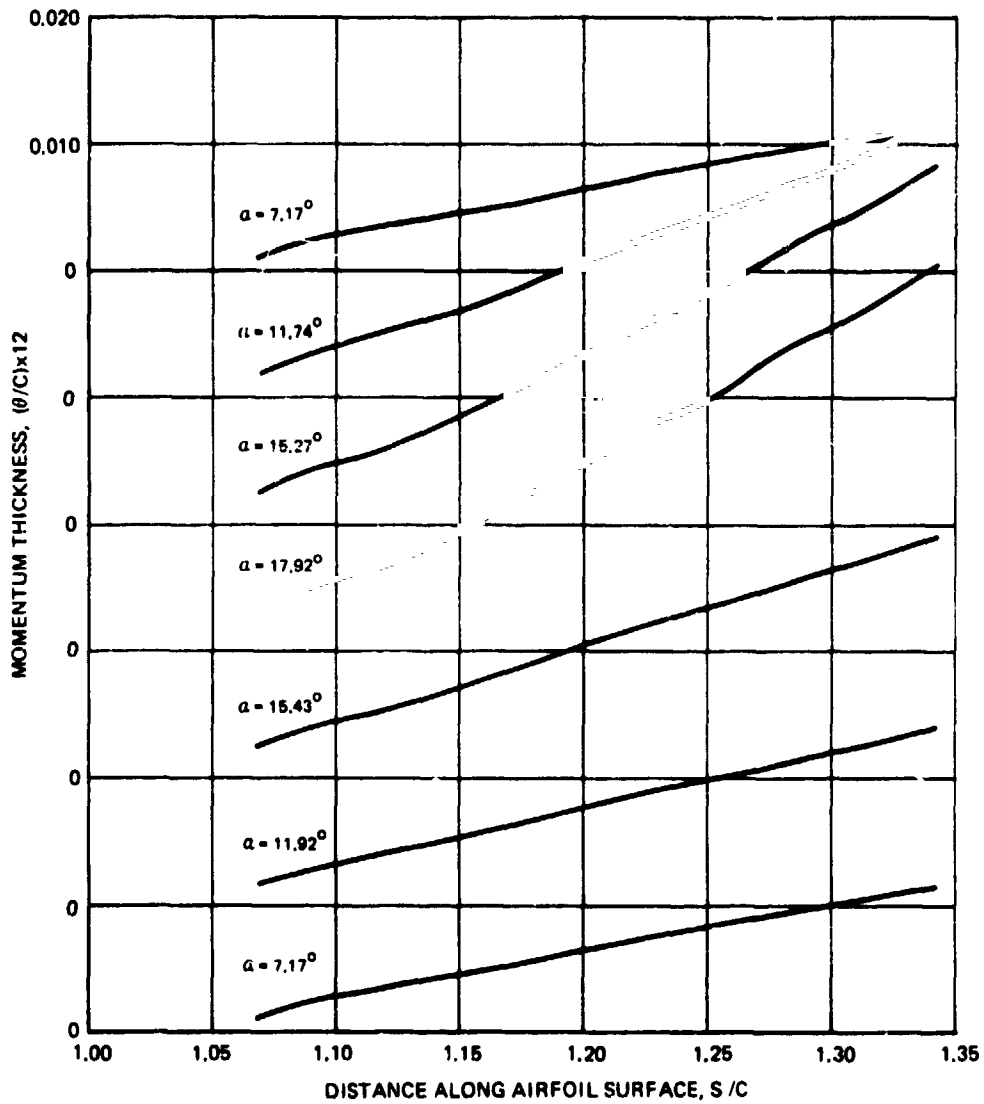
104
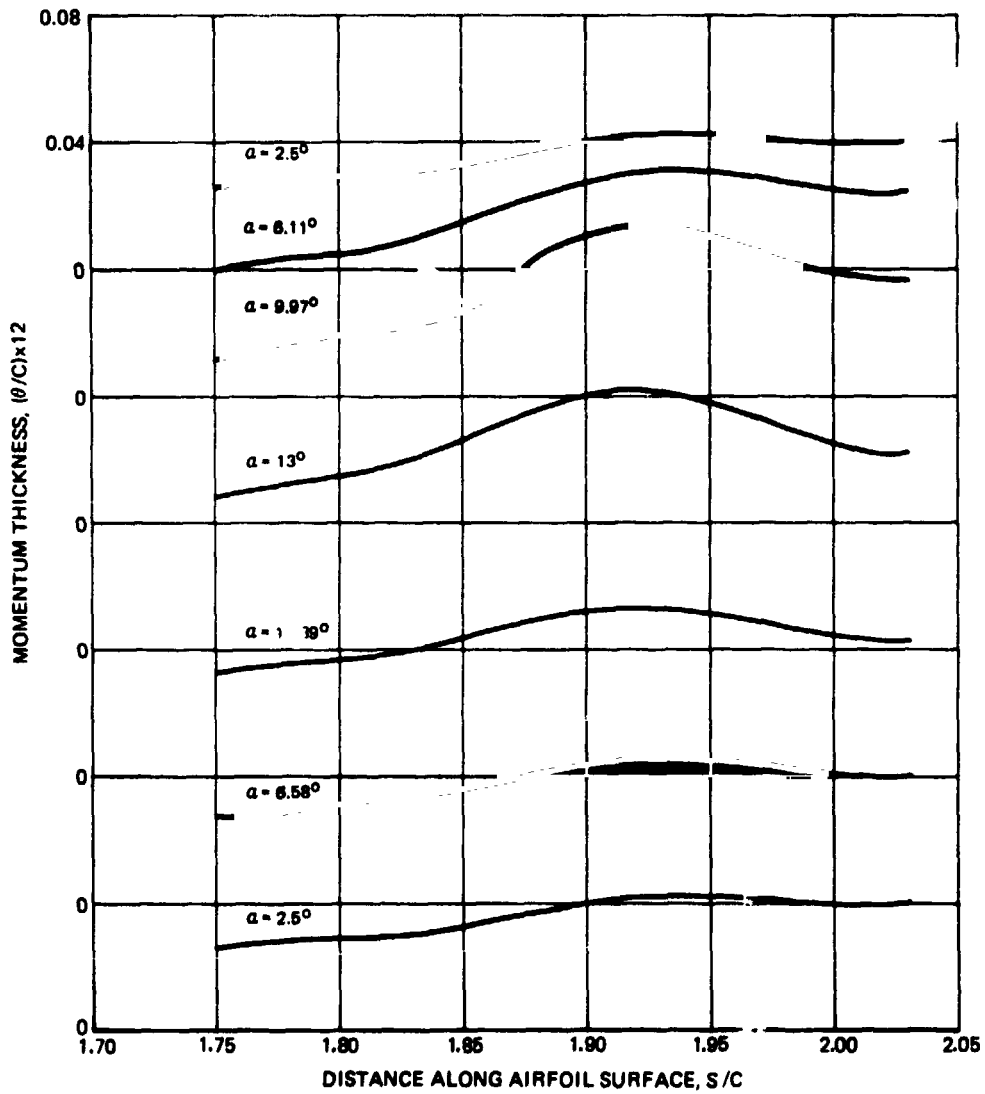
Figure 44. — Variation of momentum thickness along the airfoil surface in the suction side trailing edge fully turbulent region at various instantaneou. angles of attack for Case I .
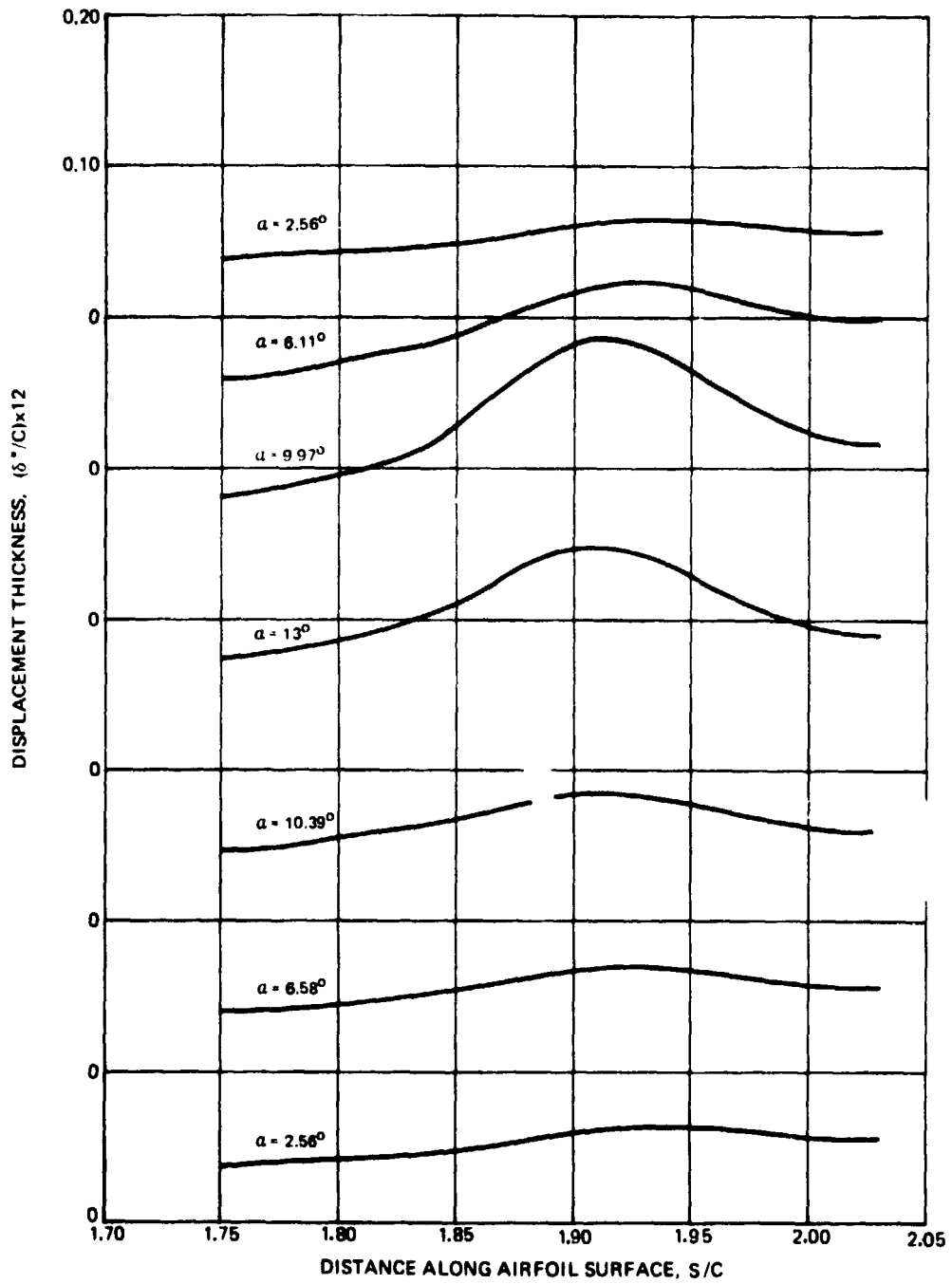
Figure 45. — Variation of displacement thickness along the airfoil surface in the suction side trailing edge fully turbulent region at various instantaneous angles of attack for Case I.
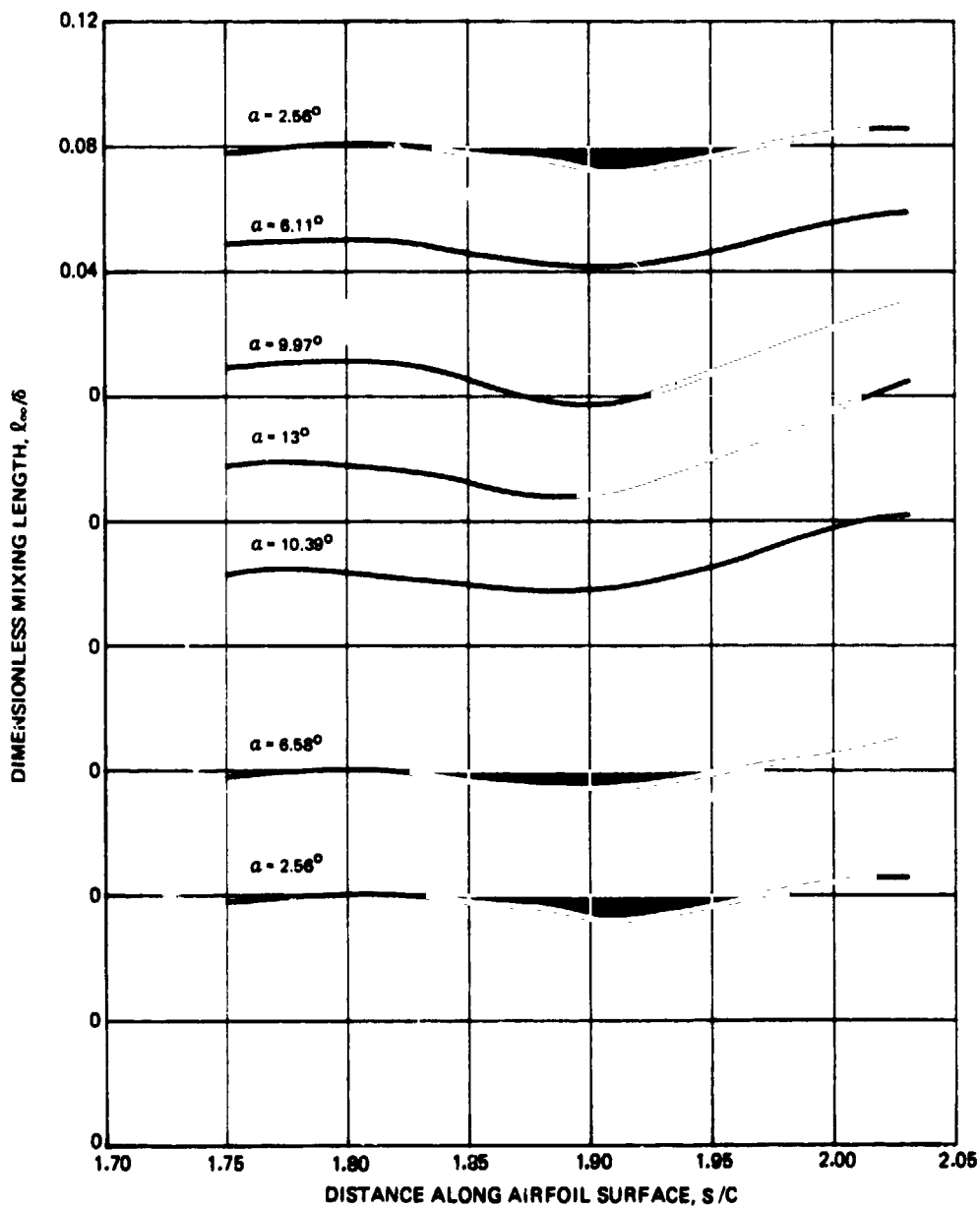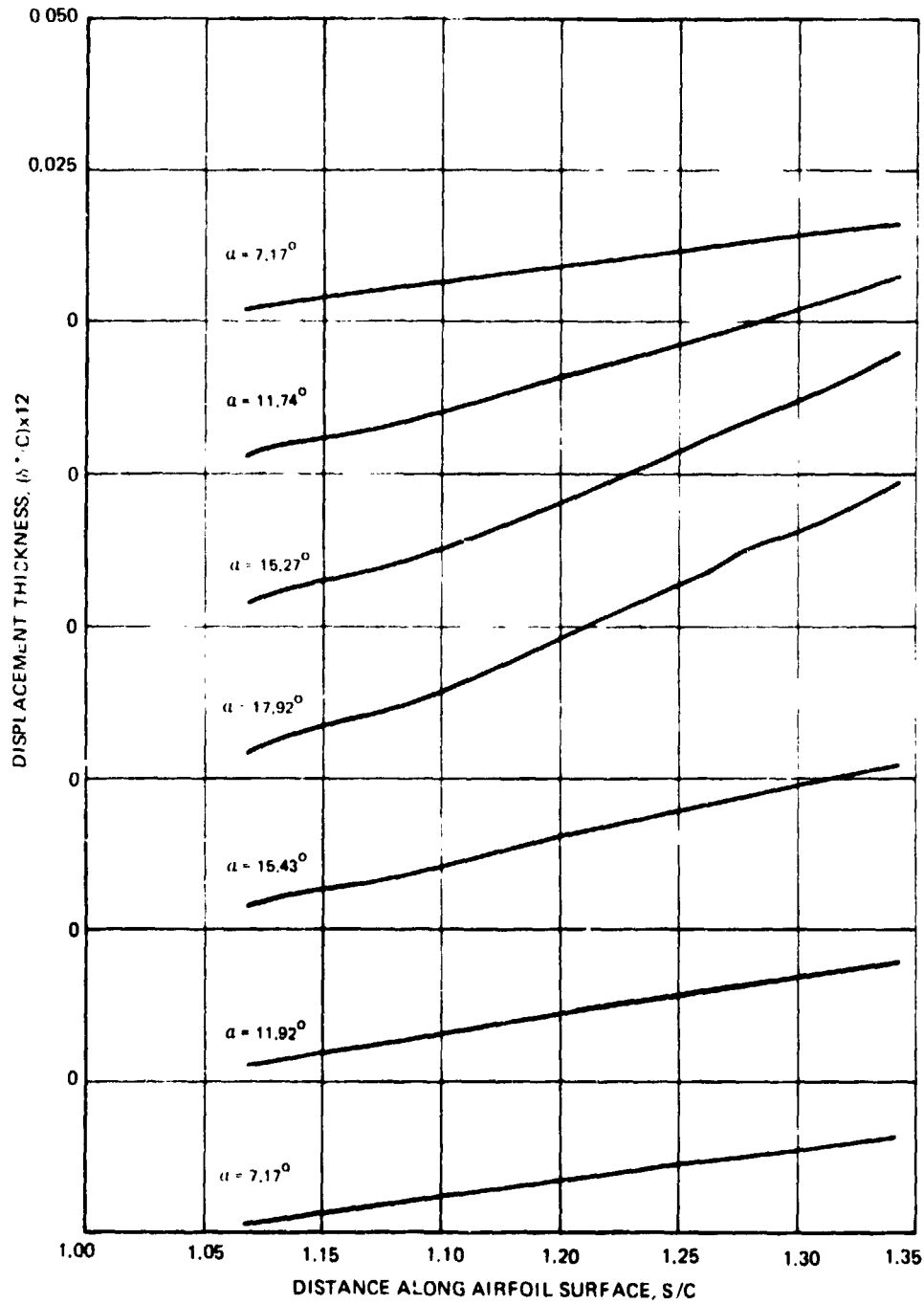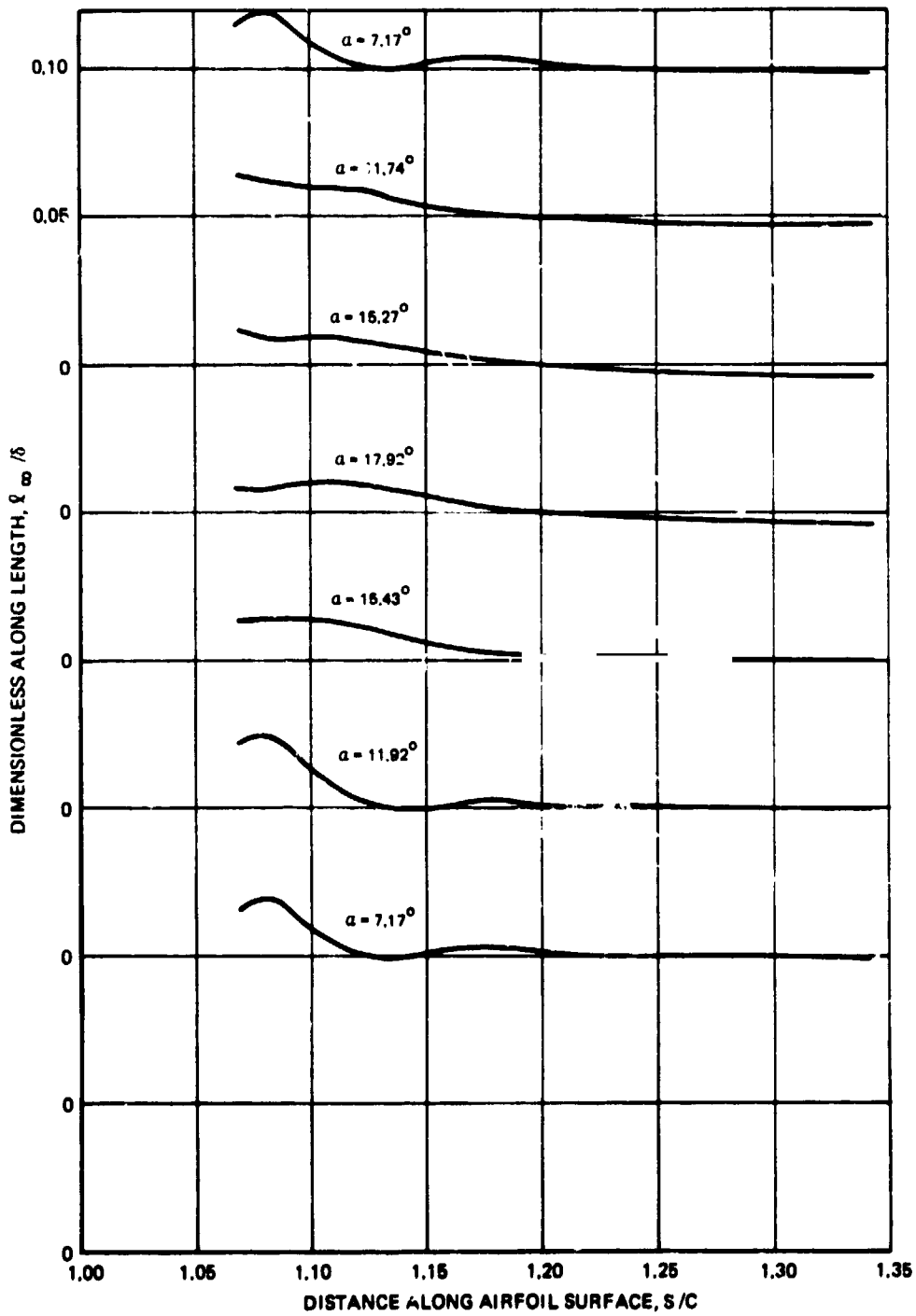
Figure 46. — Variation of dimensionless mixing length along the airfoil surface in the suction side trailing edge fully turbulent region at various insta...taneous angles of attack for Case I.

S/C = 1.44

$\alpha = 2.5^{\circ}$ $\alpha = 6.11^{\circ}$ $\alpha = 9.35^{\circ}$ $\alpha = 13^{\circ}$ $\alpha = 9.35^{\circ}$ $\alpha = 6.11^{\circ}$ $\alpha = 2.5^{\circ}$

NORMALIZED TRANSVERSE DISTANCE, Y/Δ^*

6.0
5.0
4.0
3.0
2.0
1.0
0

S/C = 1.88

$\alpha = 2.5^{\circ}$ $\alpha = 6.85^{\circ}$ $\alpha = 10.39^{\circ}$ $\alpha = 13^{\circ}$ $\alpha = 9.97^{\circ}$ $\alpha = 6.11^{\circ}$ $\alpha = 2.5^{\circ}$

NORMALIZED TRANSVERSE DISTANCE, Y/Δ^*

6.0
5.0
4.0
3.0
2.0
1.0
0

0   0   0   0   0   0   0   1.0

VELOCITY RATIO, u/u_{∞}
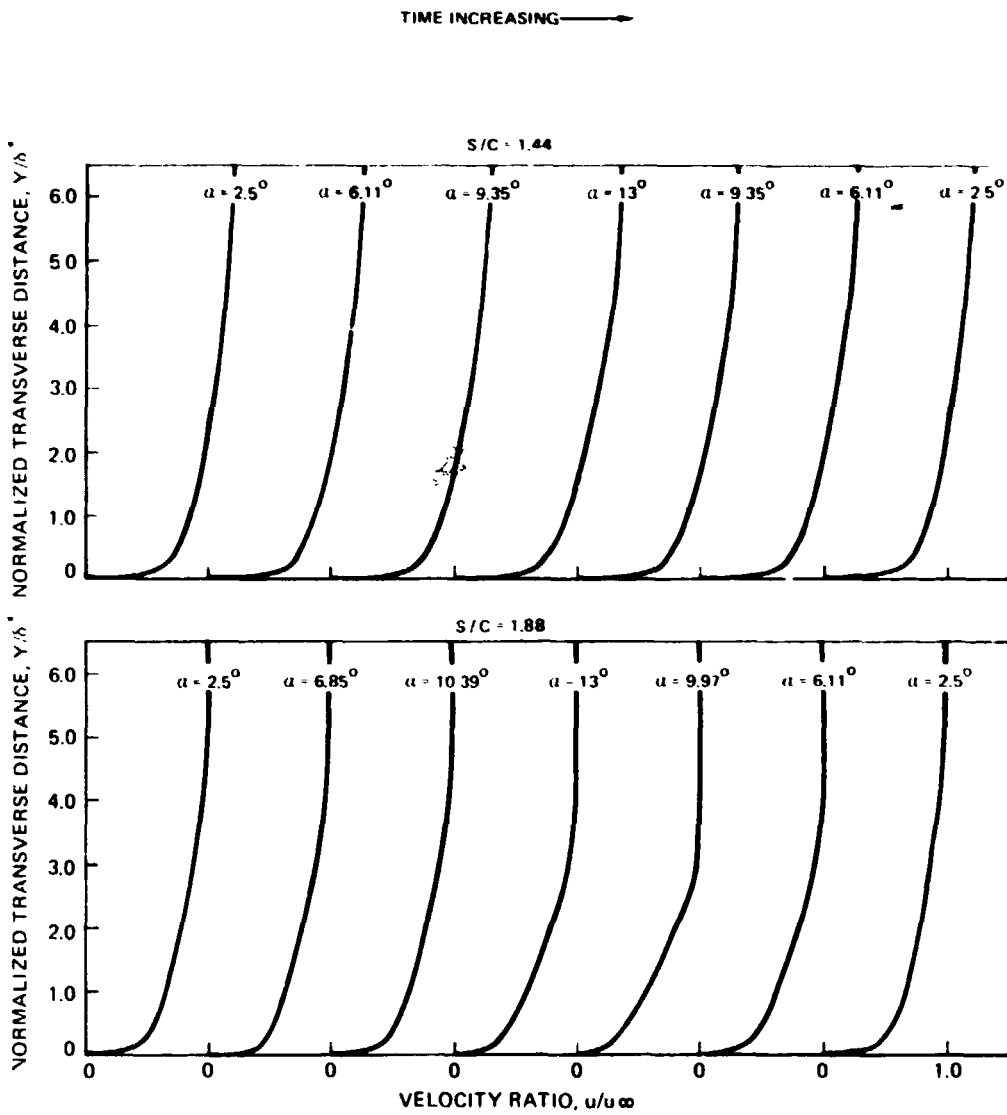
Figure 47. — Predicted instantaneous velocity profiles at a fixed streamwise location
in the suction side fully turbulent region for Case I .

N01-167-6
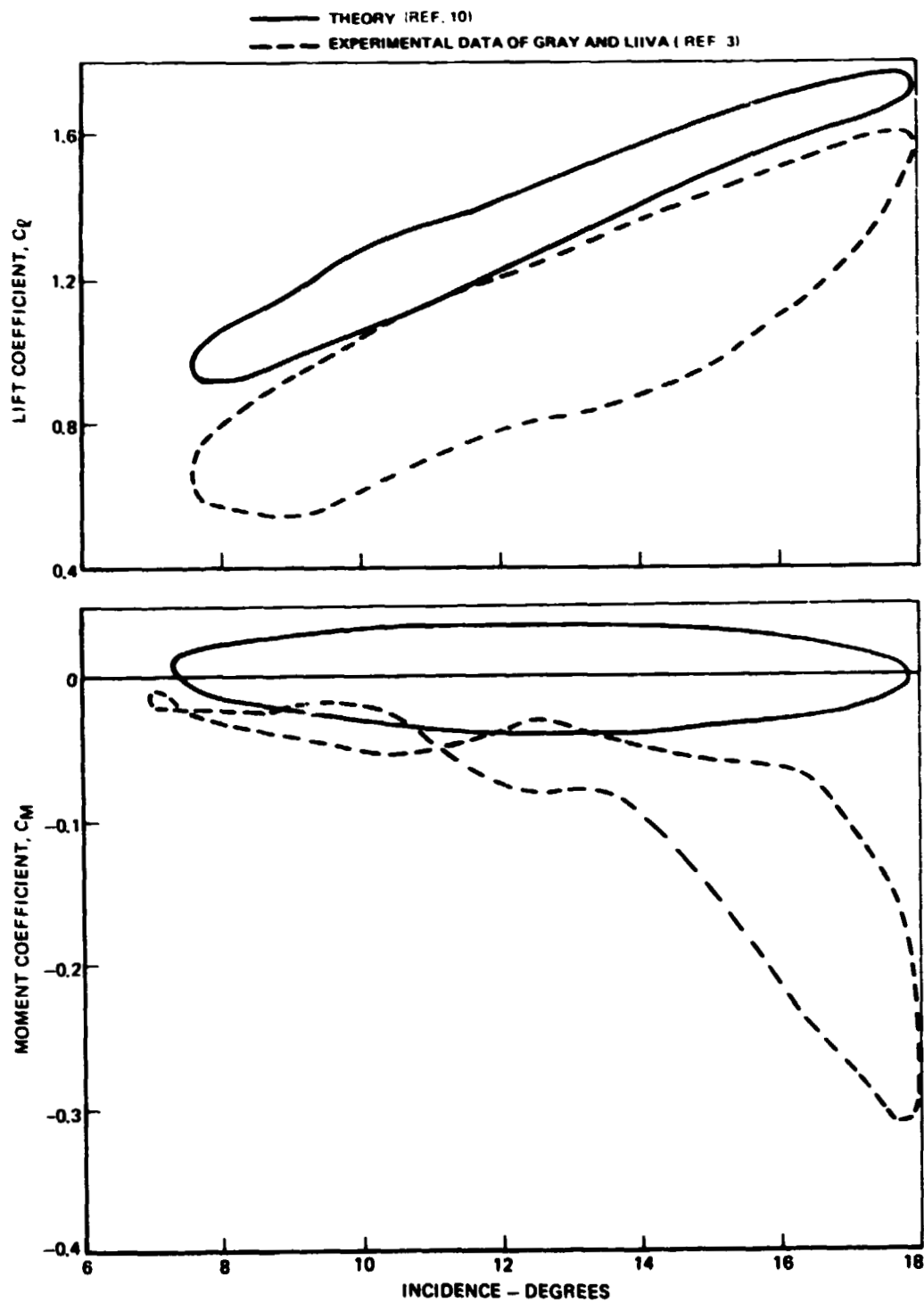
Figure 48. — Comparison between theoretically predicted and experimentally measured aerodynamic coefficients for Case II.
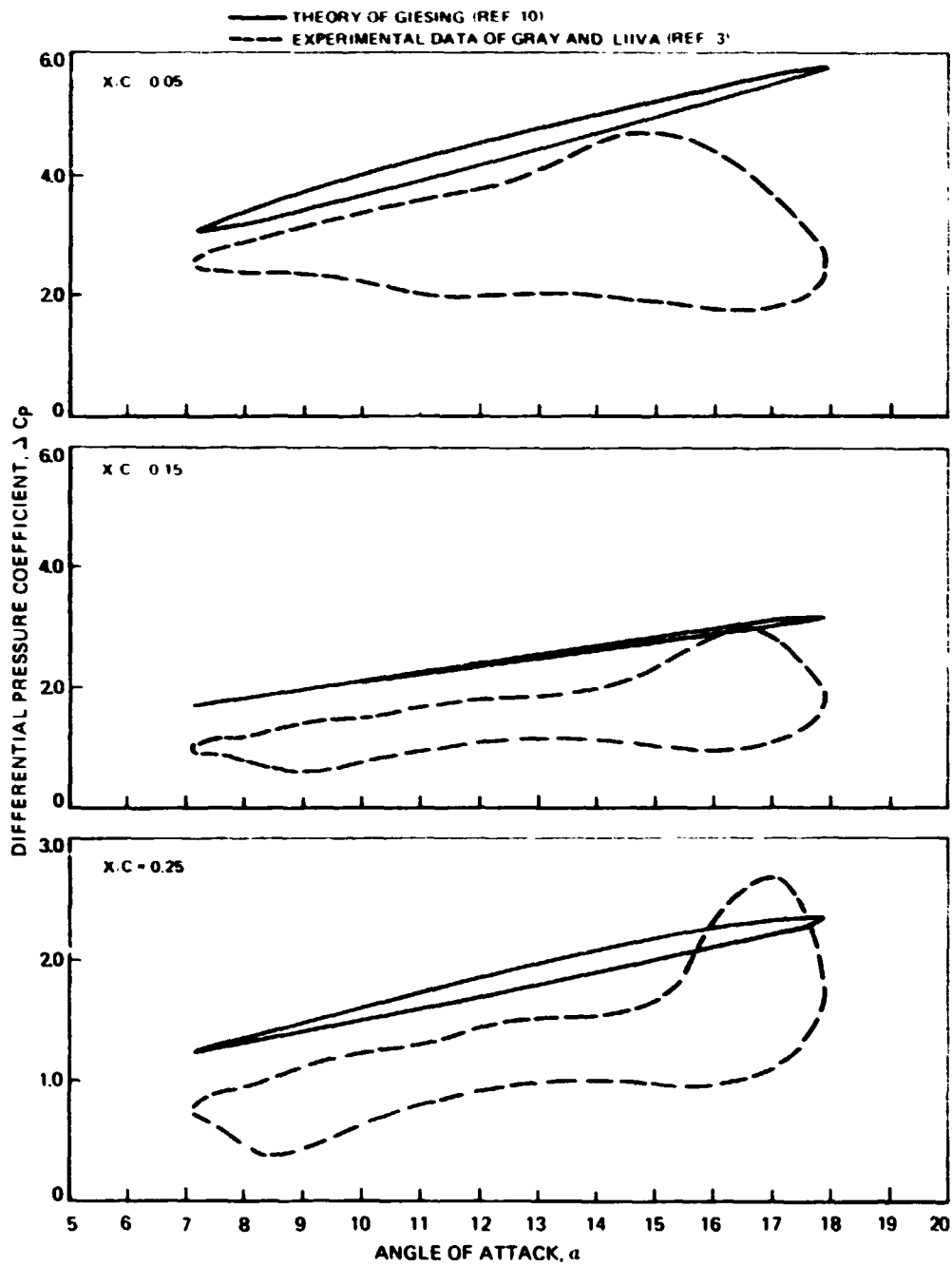
Figure 49 . — Comparison between theoretically predicted and experimentally measured differential pressure coefficients for Case II.
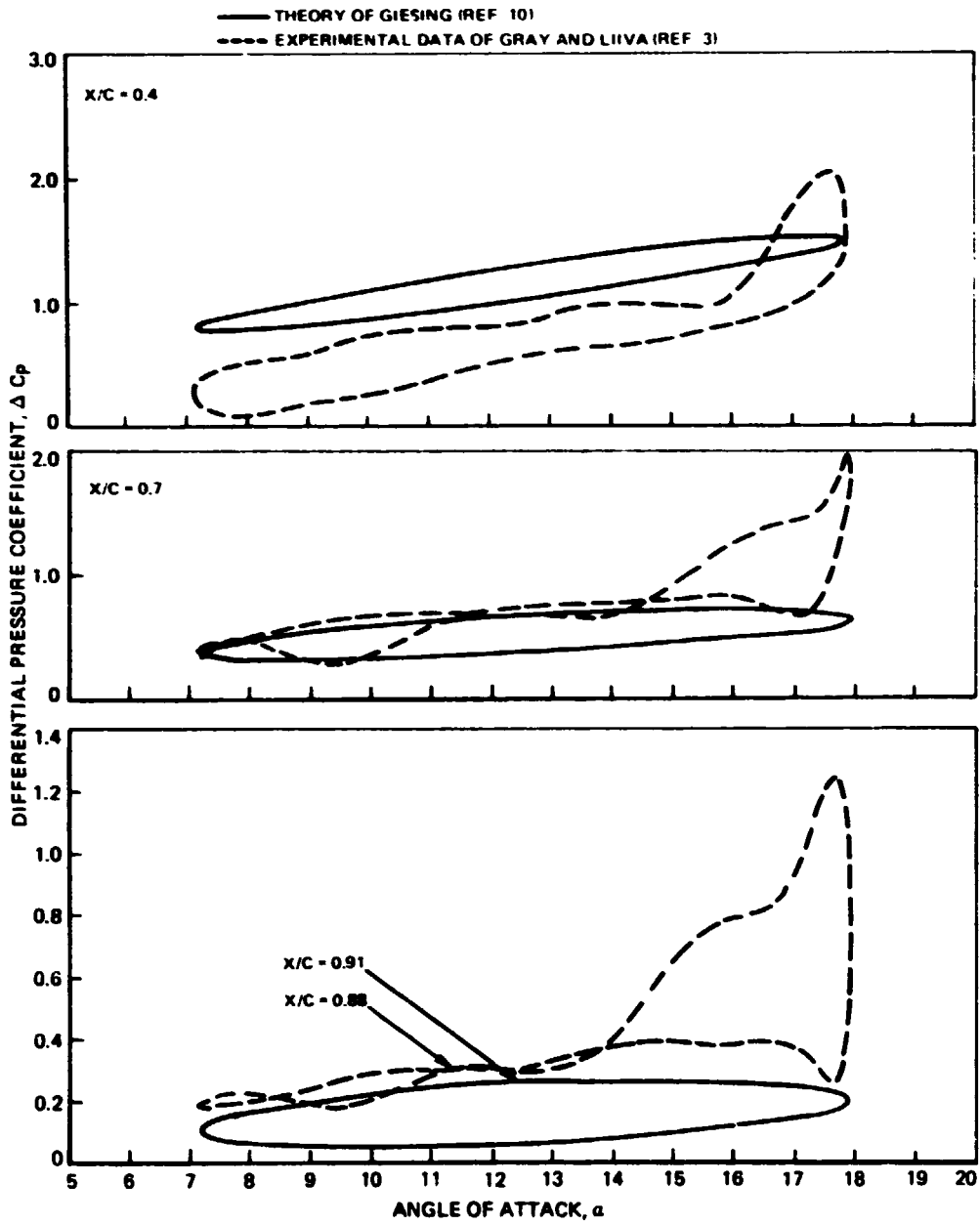
Figure 50. — Comparison between theoretically predicted and experimentally measured differential pressure coefficients for Case II.

111

Figure 51.— Comparison between theoretically predicted and experimentally measured differential pressure coefficients for Case II.
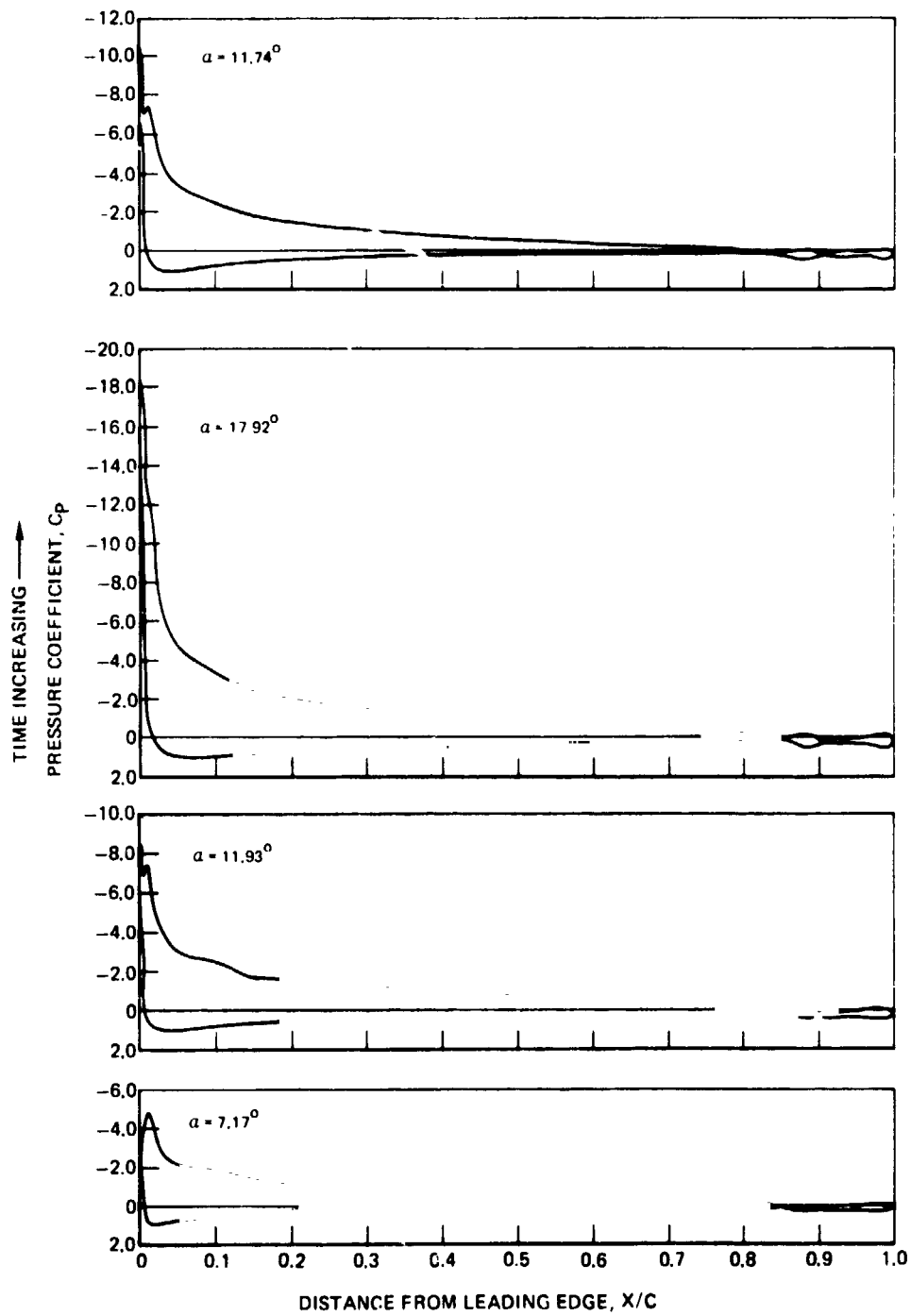
Figure 52. — Variation of the pressure coefficient on the airfoil surface at various instantaneous angles of attack for Case II.

ARROW INDICATES DIRECTION OF INCREASING TIME

Figure 53. — Location of stagnation point as a function of angle of attack
for Case II .

Figure 54. — Variation of skin friction coefficient in the stagnation region at various instantaneous angles of attack for Case II .

Figure 55. — Variation of momentum thickness in the stagnation region at various instantaneous angles of attack for Case II.

O INDICATES LOCATION OF STAGNATION POINT

Figure 56. — Variation of displacement thickness in the stagnation region at various instantaneous angles of attack for Case II.

117

Figure 57. — Variation of dimensionless mixing length in the stagnation region at various instantaneous angles of attack for Case II .

118

Figure 58. — Variation of skin friction coefficient along the airfoil surface in the pressure side transition region at various instantaneous angles of attack for Case II .

Figure 59. — Variation of momentum thickness along the airfoil surface in the pressure side transition region at various instantaneous angles of attack for Case II .

120

Figure 60. — Variation of displacement thickness along the airfoil surface in the pressure side transition region at various instantaneous angles of attack for Case II.

Figure 61. — Variation of dimensionless mixing length along the airfoil surface in the pressure side transition region at various instantaneous angles of attack for Case II.

122

Figure 62. — Variation of skin friction coefficient along the airfoil surface in the pressure side fully turbulent region at various instantaneous angles of attack for Case II .

123

Figure 63. — Variation of momentum thickness along the airfoil surface in the pressure side fully turbulent region at various instantaneous angles of attack for Case II .

124
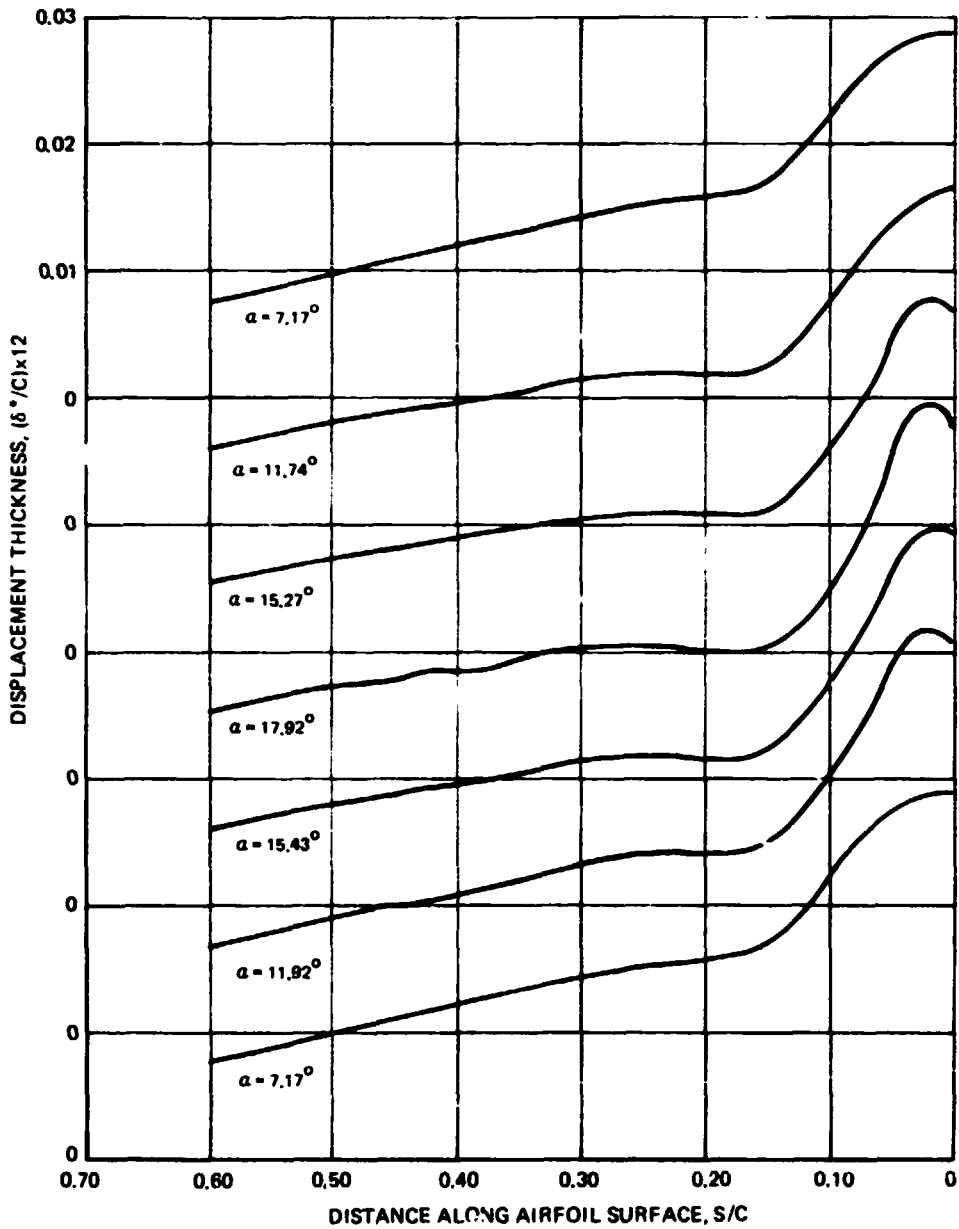
Figure 64. — Variation of displacement thickness along the airfoil surface in the pressure side
fully turbulent region at various angles of attack for Case II .

125
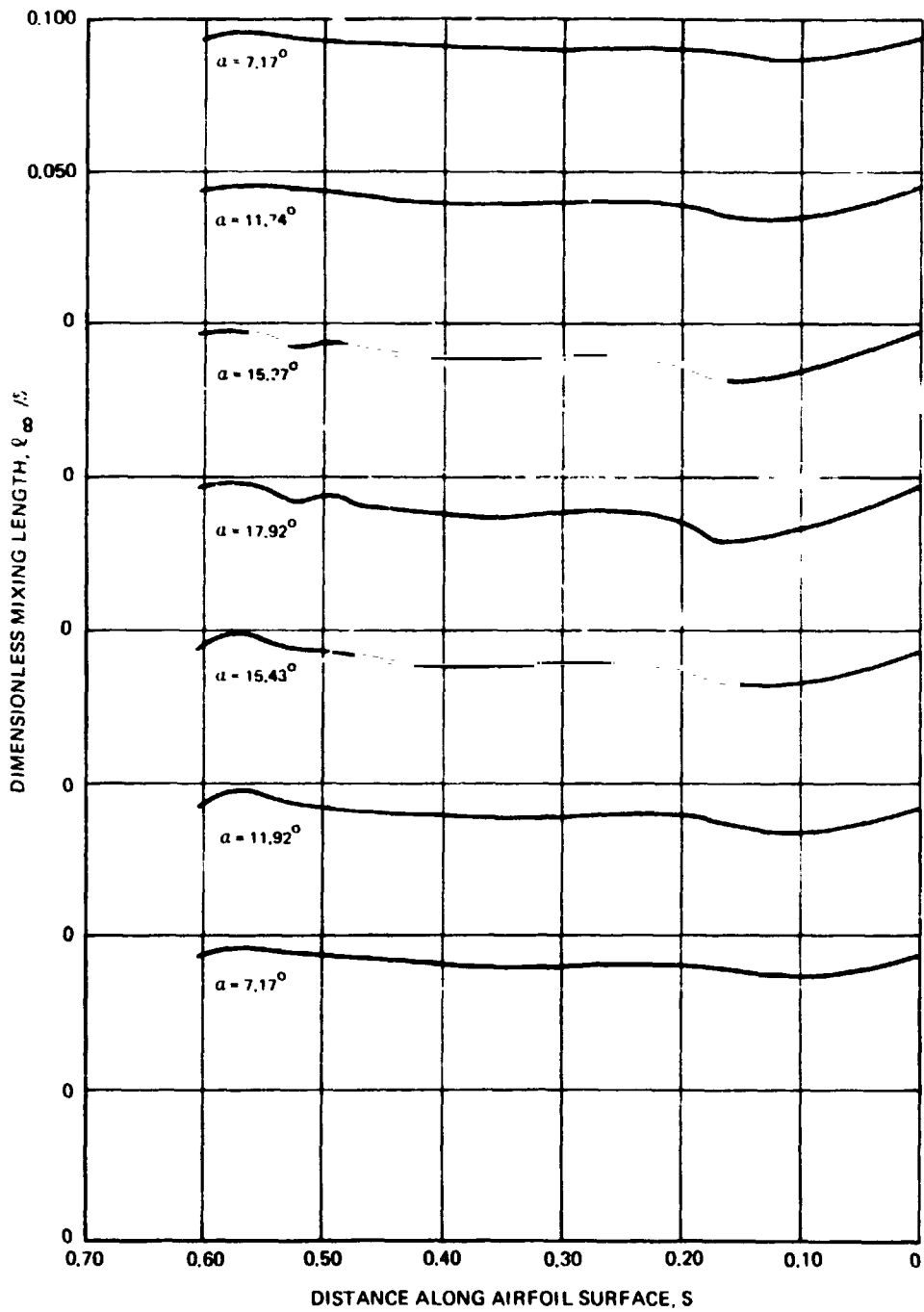
Figure 65. — Variation of dimensionless mixing length along the airfoil surface in the pressure side fully turbulent region at various instantaneous angles of attack for Case II .

126

Figure 66. -- Streamlines in the separated region of the airfoil suction side at various instantaneous angles of attack for Case II.

127

Figure 67. — Variation of skin friction coefficient in the separated region of the airfoil suction side at various instantaneous angles of attack for Case II .

128
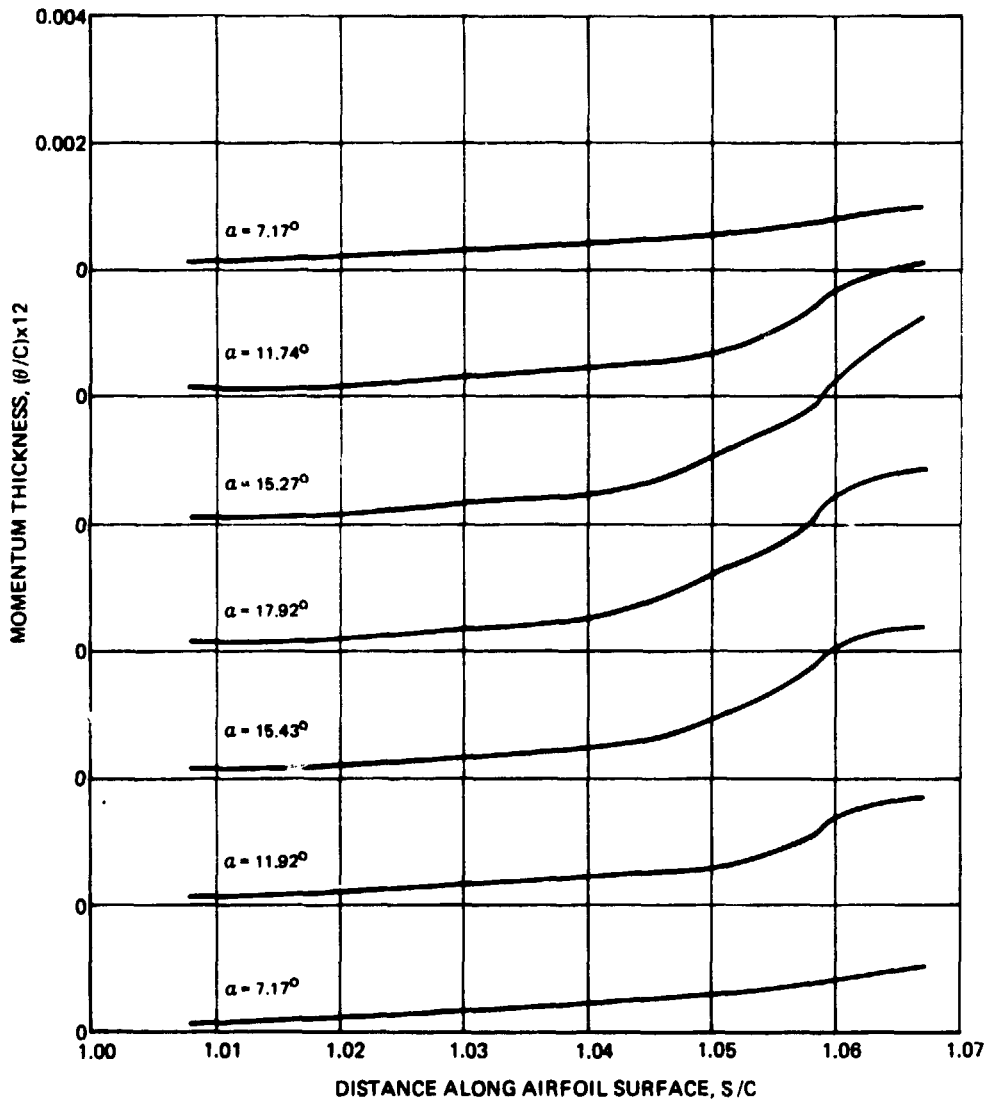
Figure 68. — Variation of momentum thickness in the separated region of the airfoil suction side at various instantaneous angles of attack for Case II.
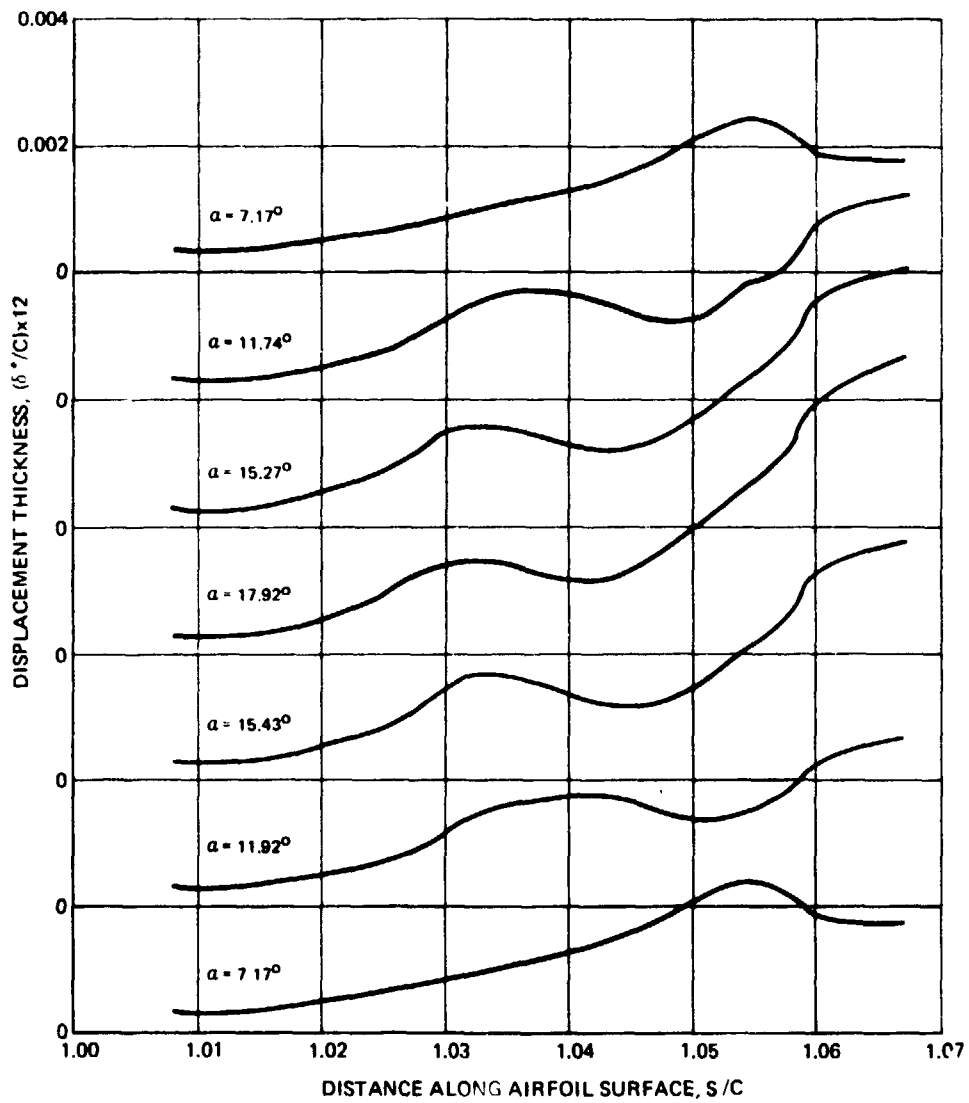
Figure 69. — Variation of displacement thickness in the separated region of the airfoil suction side at various instantaneous angles of attack for Case II .
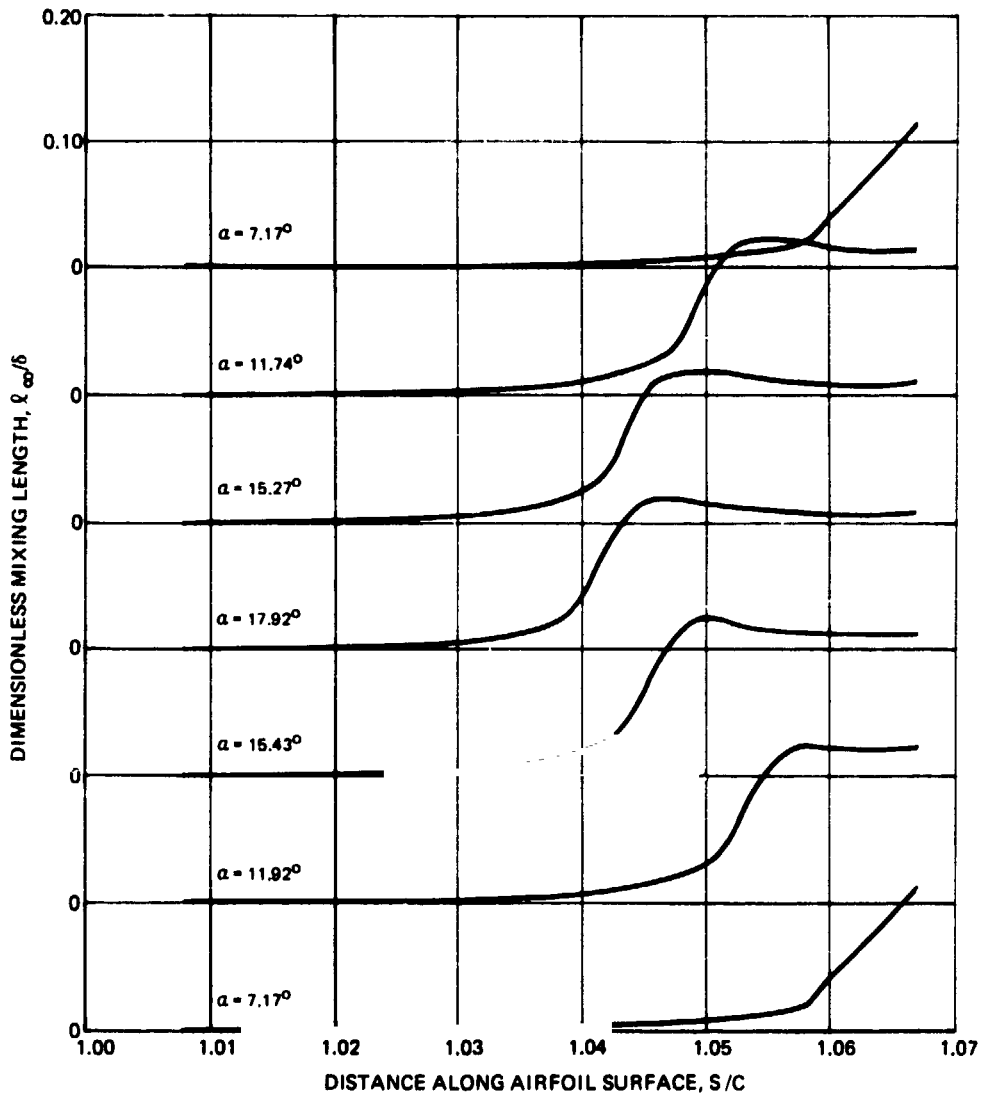
Figure 70. — Variation of dimensionless mixing length in the separated region of the airfoil suction side at vario   instantaneous angles of attack for Case II.

Figure 71. — Variation of skin friction coefficient along the airfoil surface in the suction side
fully turbulent region at various instantaneous angles of attack for Case II .

Figure 72. — Variation of momentum thickness along the airfoil surface in the suction side fully turbulent region at various instantaneous angles of attack for Case II .

Figure 73. — Variation of displacement thickness along the airfoil surface in the suction side fully turbulent region at various instantaneous angles of attack for Case II.

134

Figure 74. — Variation of dimensionless mixing length along the airfoil surface in the suction side
fully turbulent region at various instantaneous angles of attack for Case II.

135
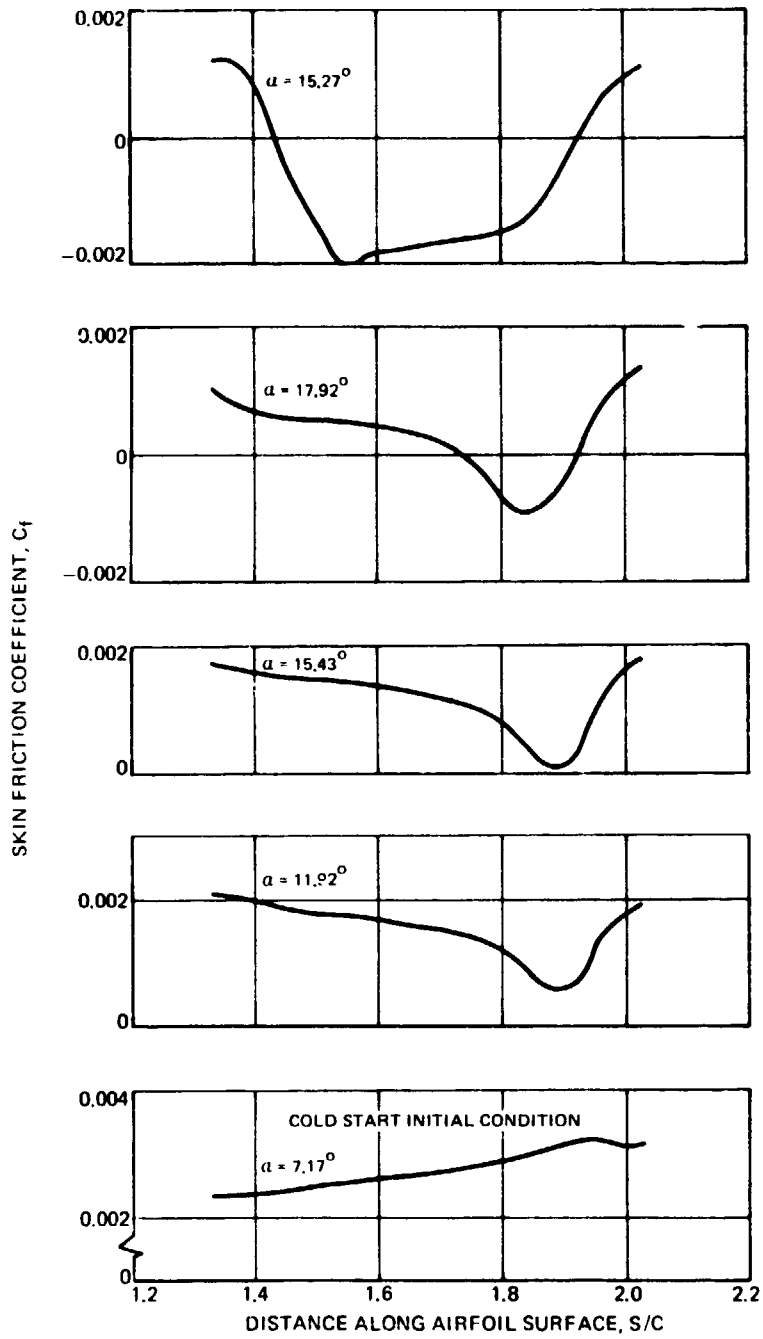
Figure 75. — Variation of skin friction coefficient along the airfoil surface
in the suction side trailing edge fully turbulent region
at various instantaneous angles of attack for Case I I.

136
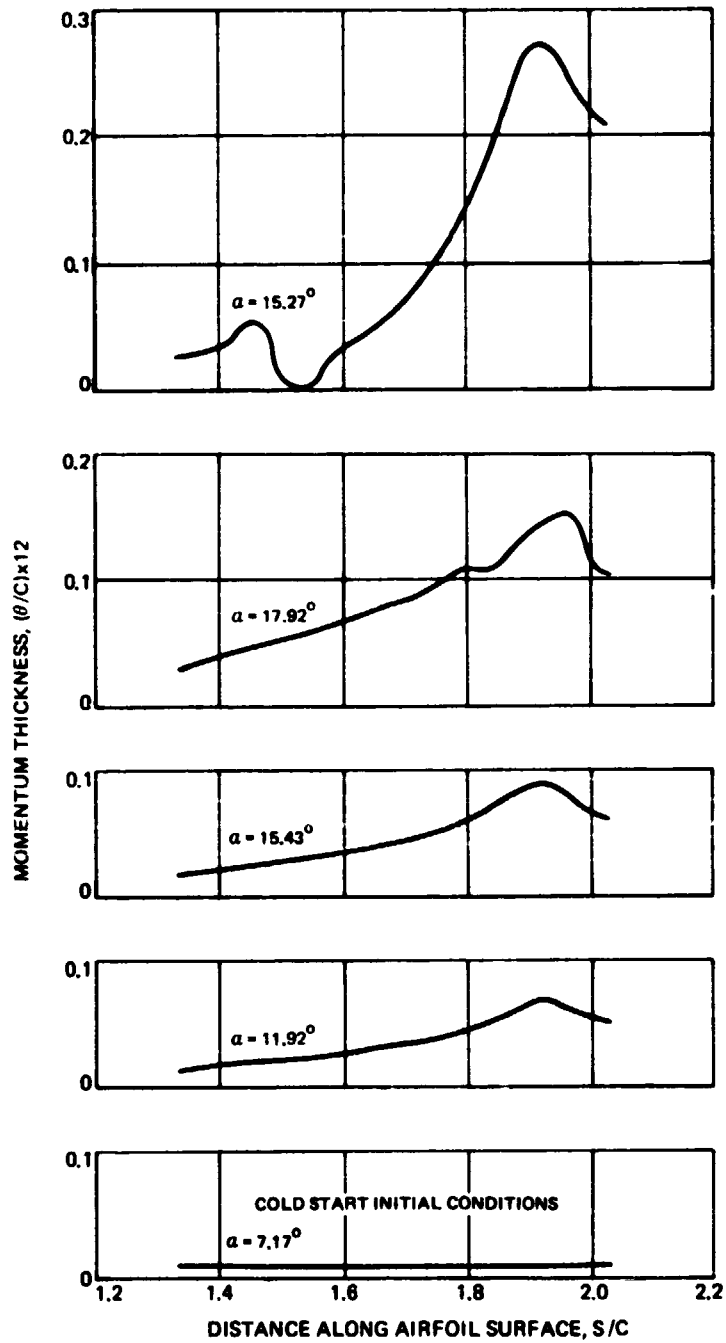
Figure 76. — Variation of momentum thickness along the airfoil surface in the suction side trailing edge fully turbulent region at various instantaneous angles of attack for Case I I.
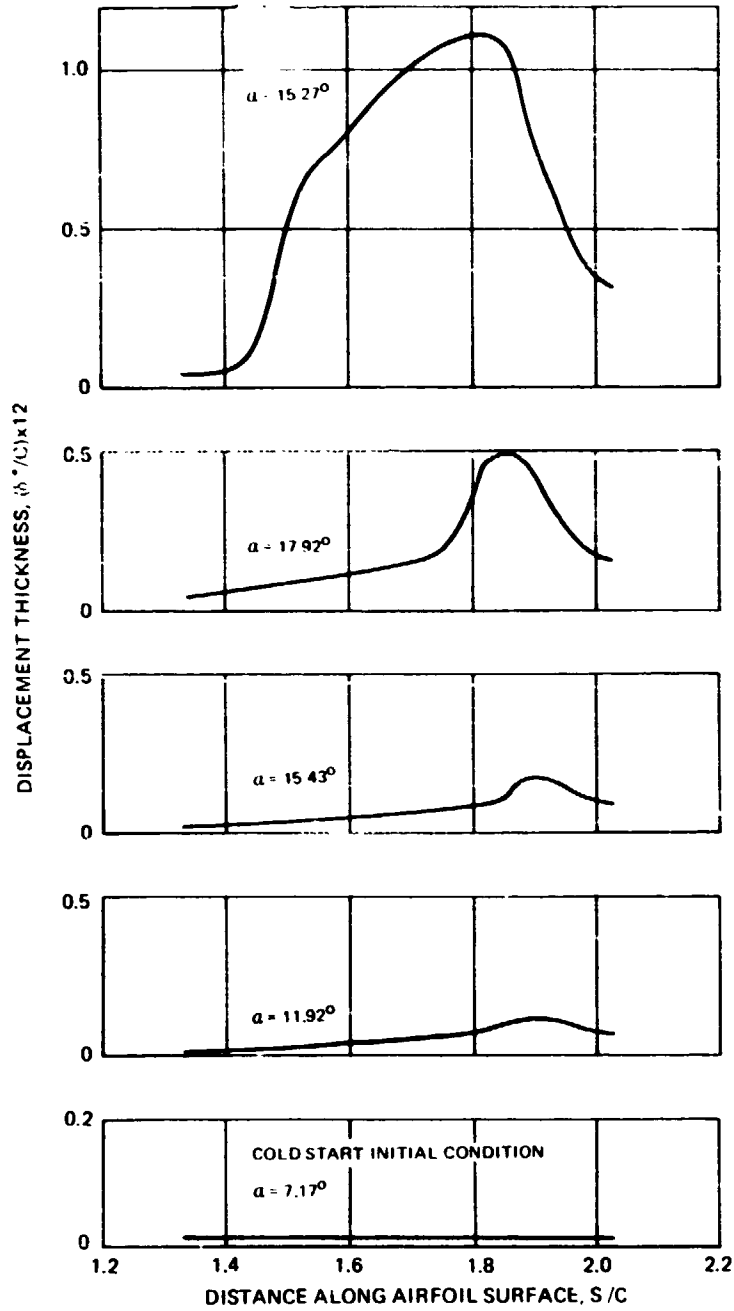
Figure 77. Variation of displacement thickness along the airfoil surface in the suction side trailing edge fully turbulent region at various instantaneous angles of attack for Case II.

138
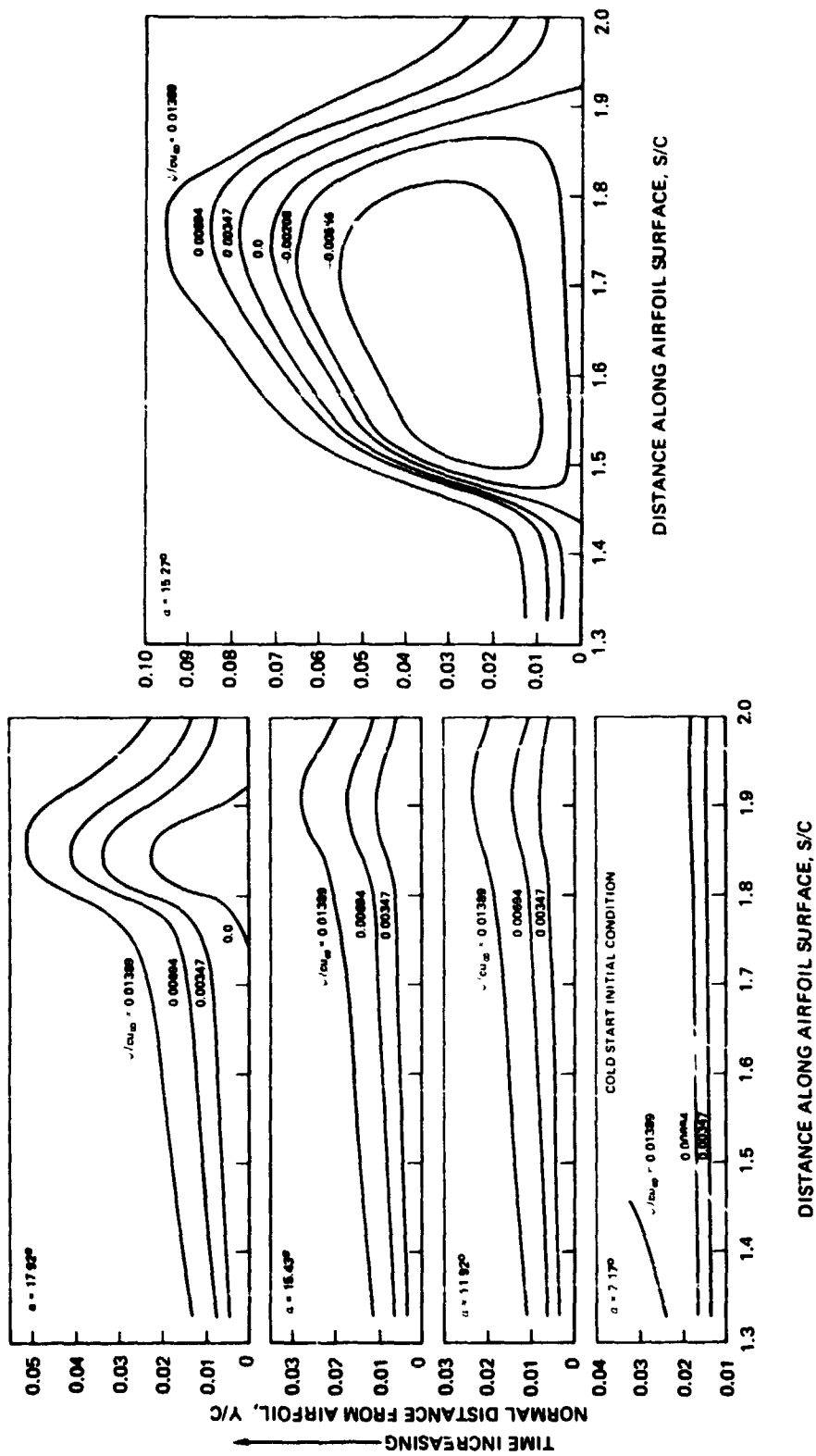
Figure 78 . Streamlines in the suction side trailing edge fully turbulent region at various instantaneous angles of attack for Case II .
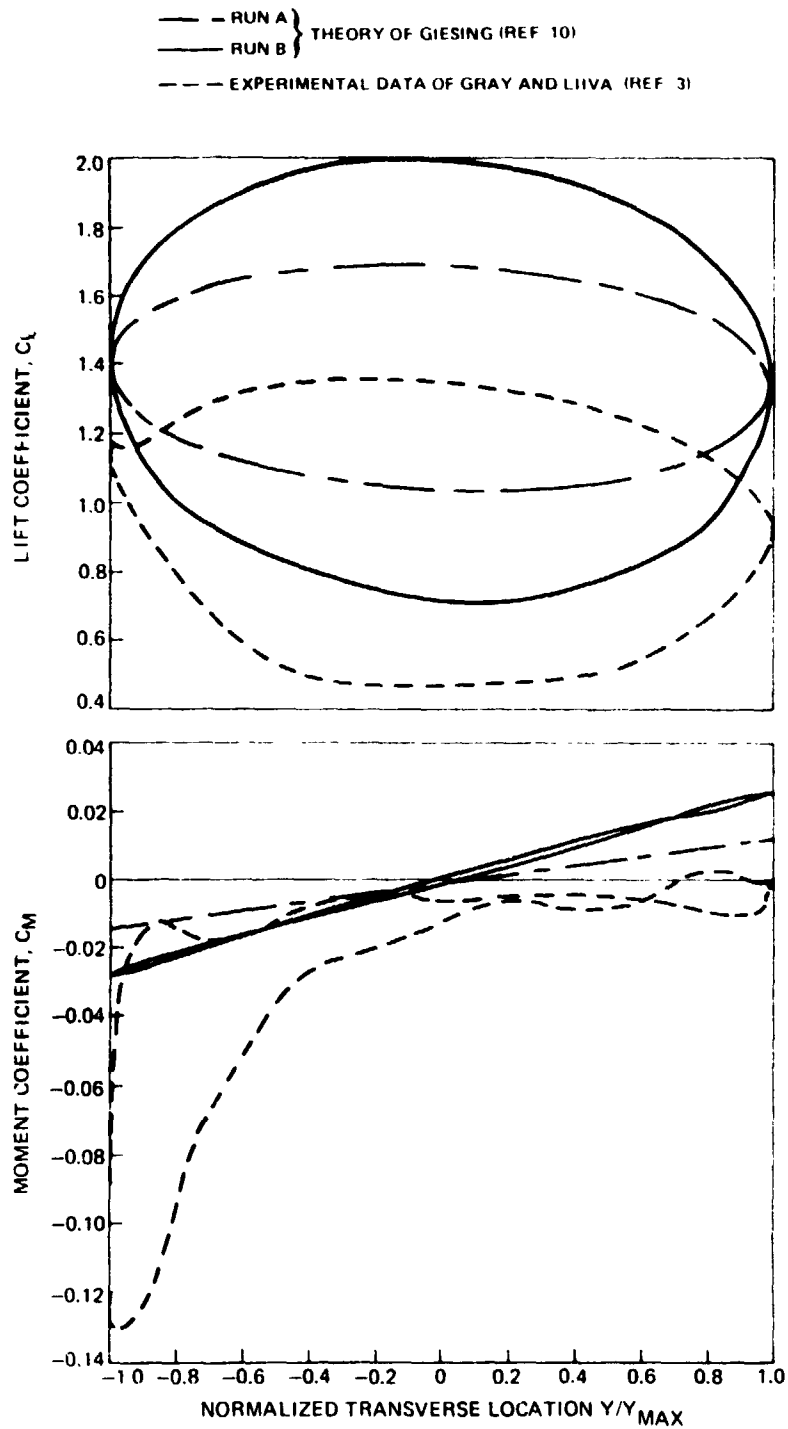
Figure 79. — Comparison between theoretically predicted and
experimentally measured aerodynamic coefficients
for Case III .

140
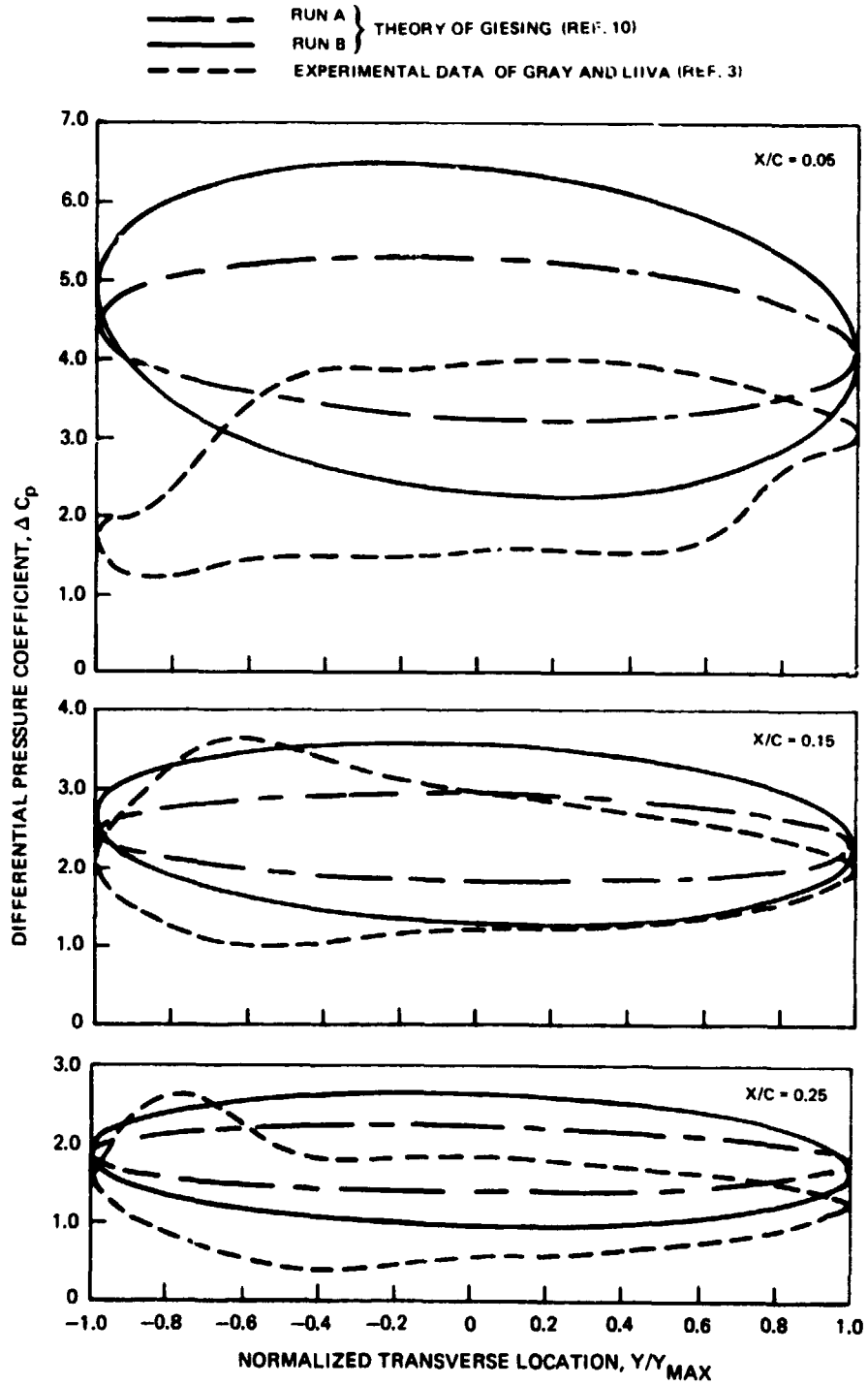
Figure 80. — Comparison between theoretically predicted and
experimentally measured aerodynamic coefficients
for Case III.
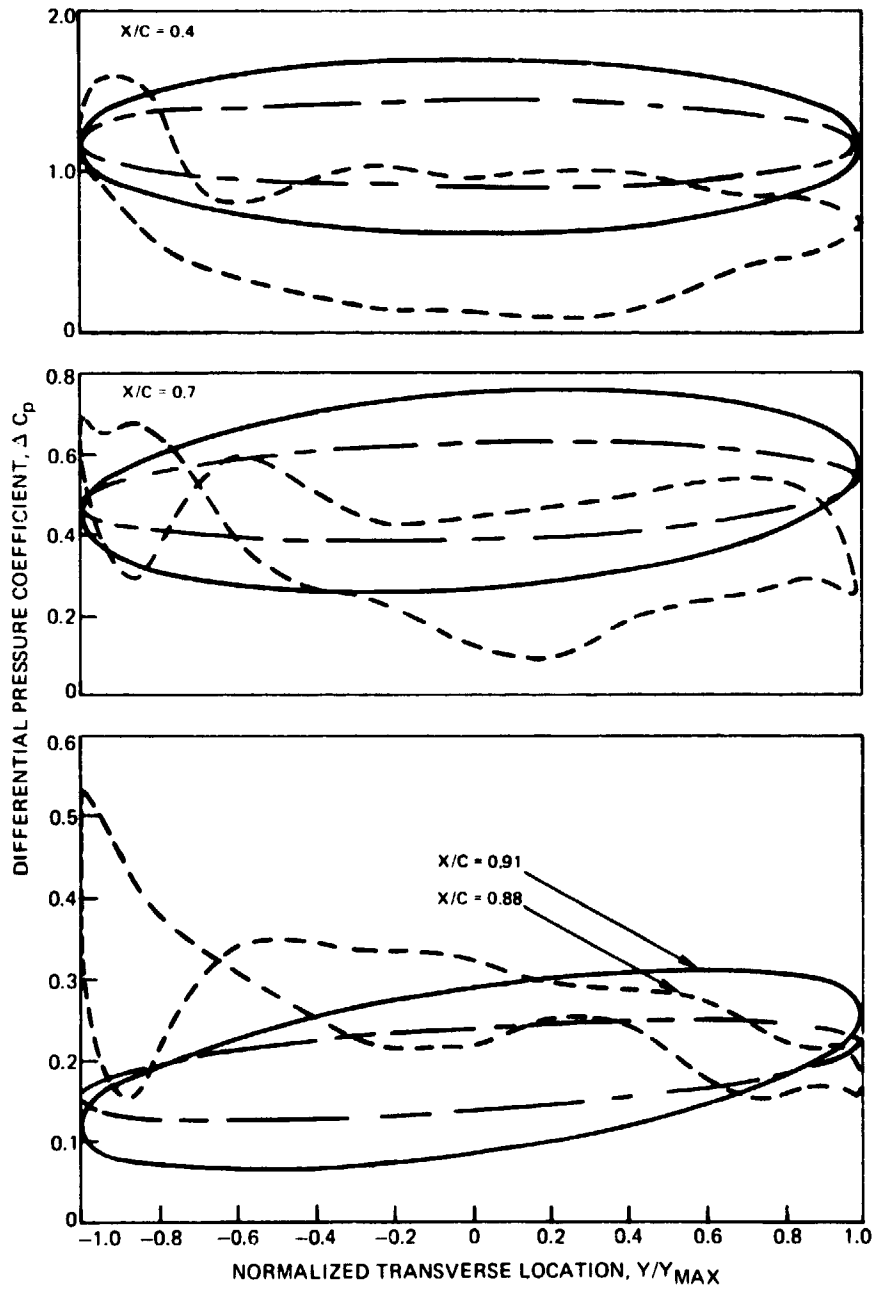
Figure 81. — Comparison between theoretically predicted and experimentally measured aerodynamic coefficients for Case III.

NO1-18-3
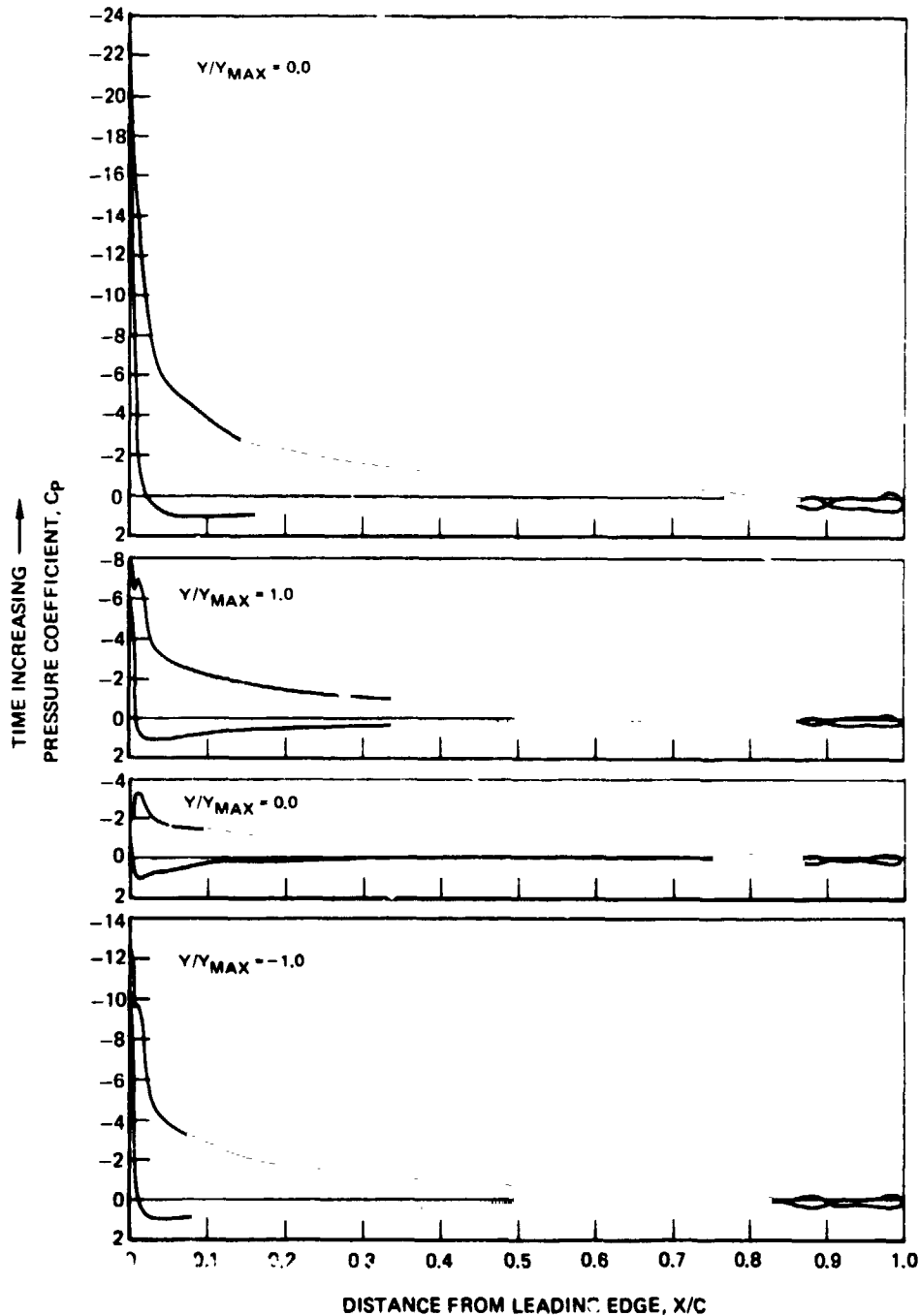
Figure 82. — Variation of the pressure coefficient on the airfoil surface at various instantaneous normalized transverse locations for Case III, Run B.
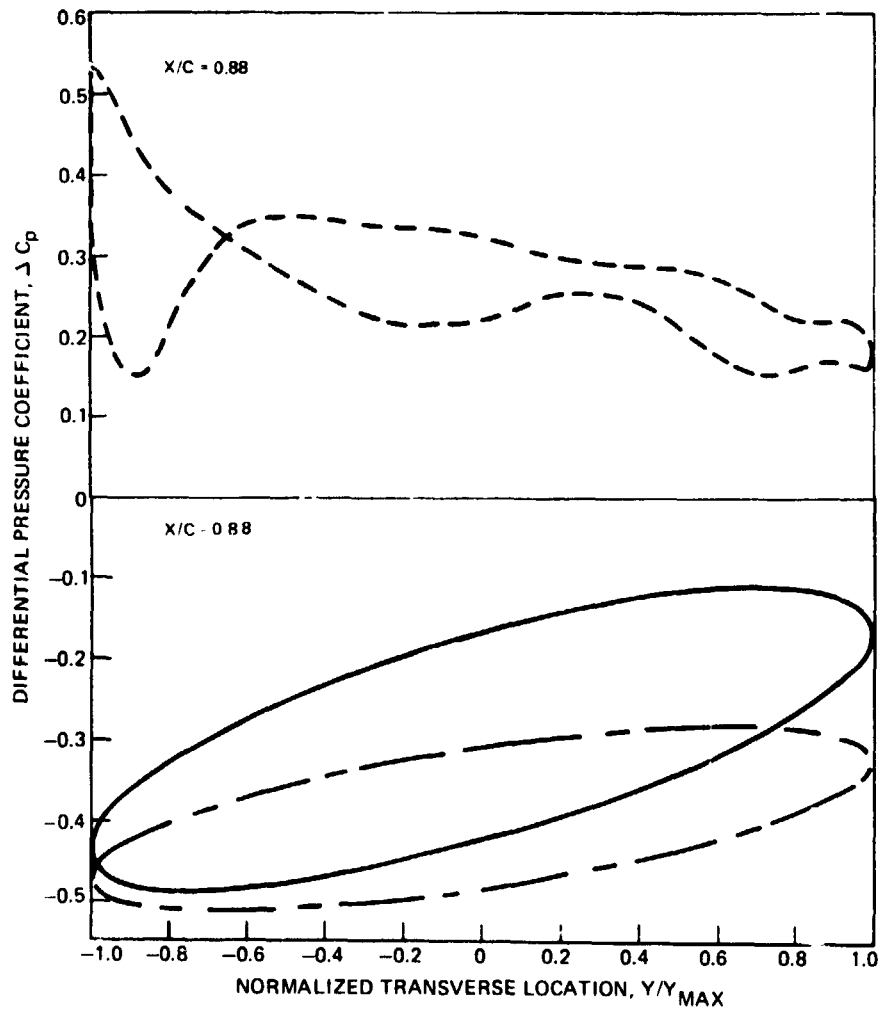
Figure 83. — Comparison between theoretically predicted and
experimentally measured aerodynamic coefficients
for Case III .

ARROW INDICATES DIRECTION OF INCREAS'NG TIME
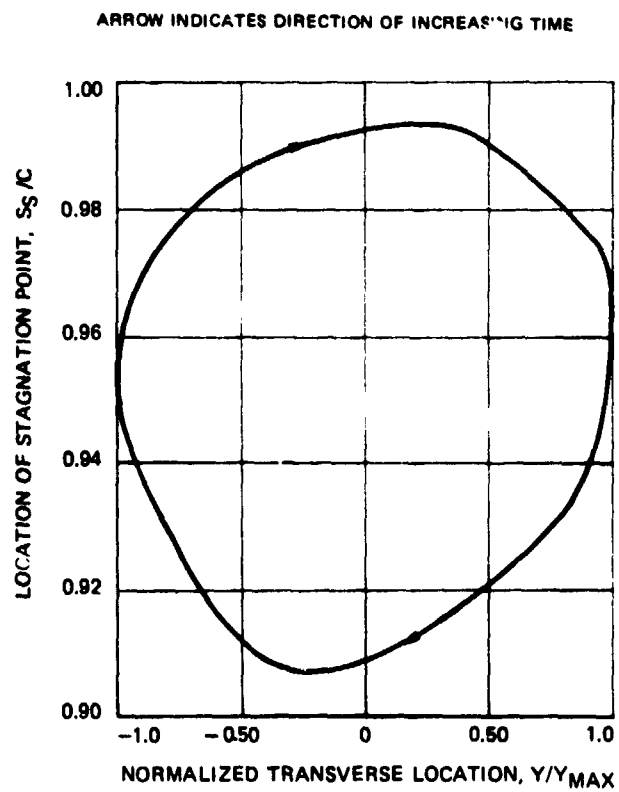
Figure 84. — Location of stagnation point as a function of normalized transverse location for Case III.
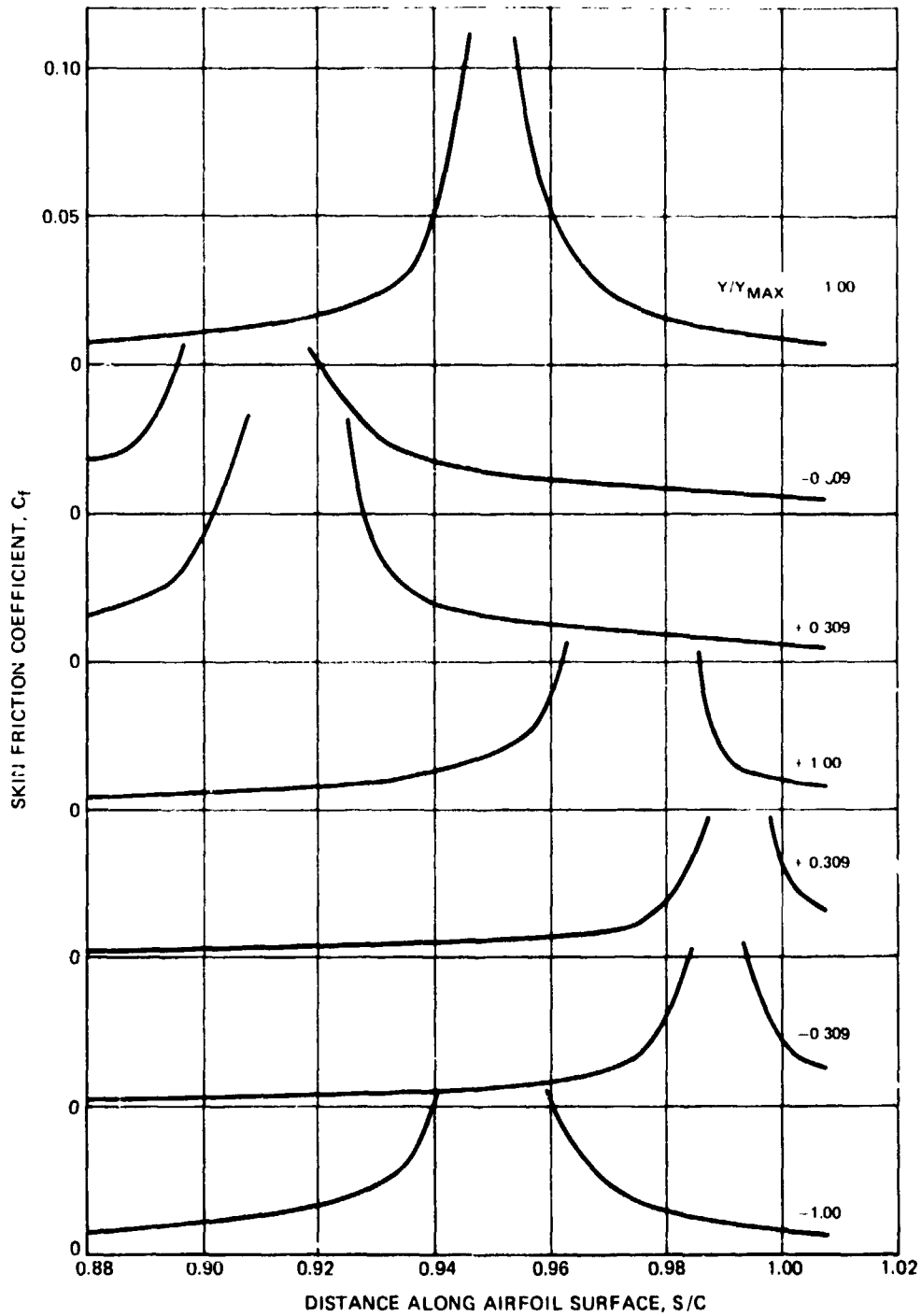
Figure 85. — Variation of skin friction coefficient in the stagnation region at various instantaneous normalized transverse locations for Case III.

N01–17–6

O INDICATES LOCATION OF STAGNATION POINT
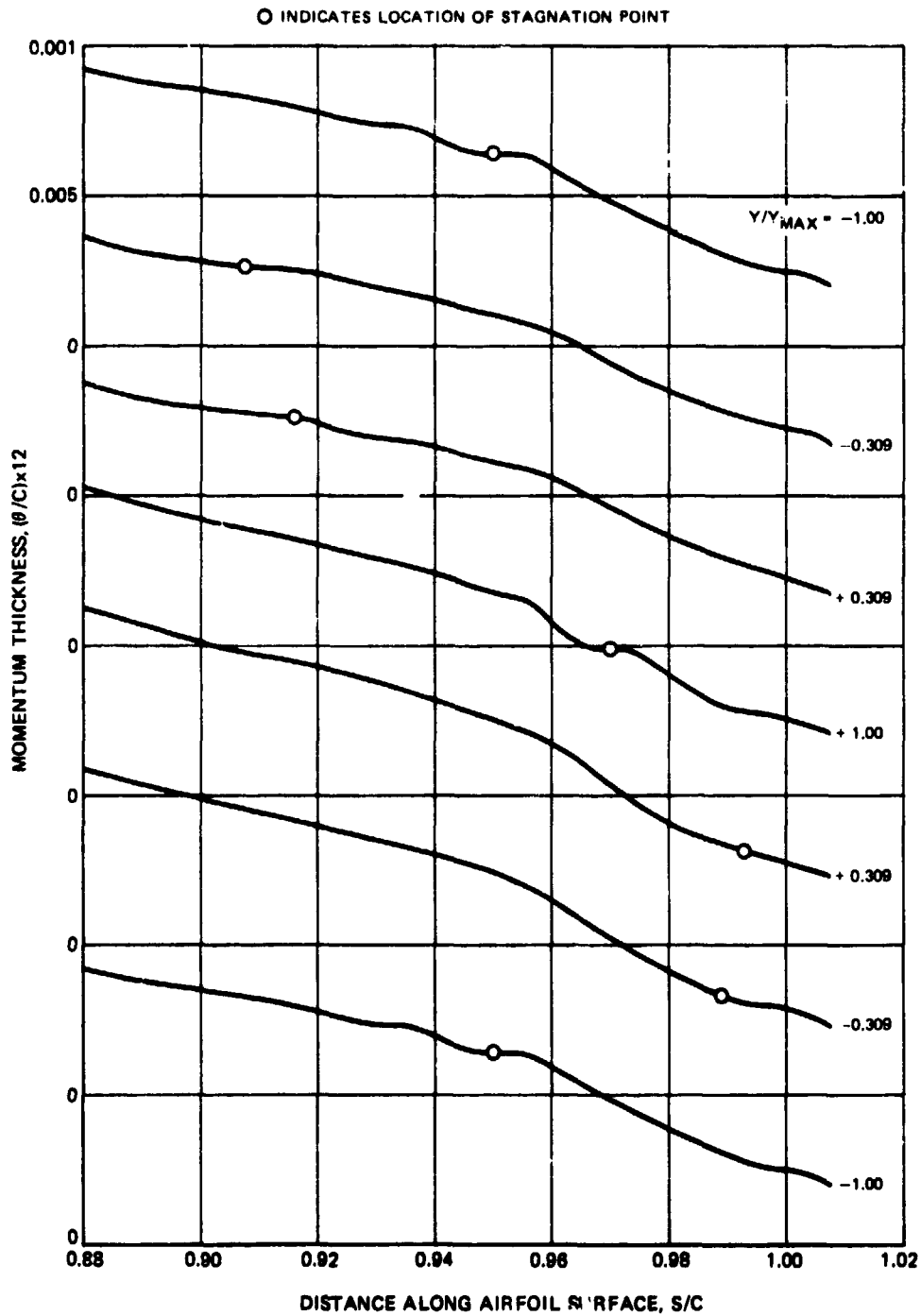
Figure 86. — Variation of momentum thickness in the stagnation region at various instantaneous normalized transverse locations for Case III.
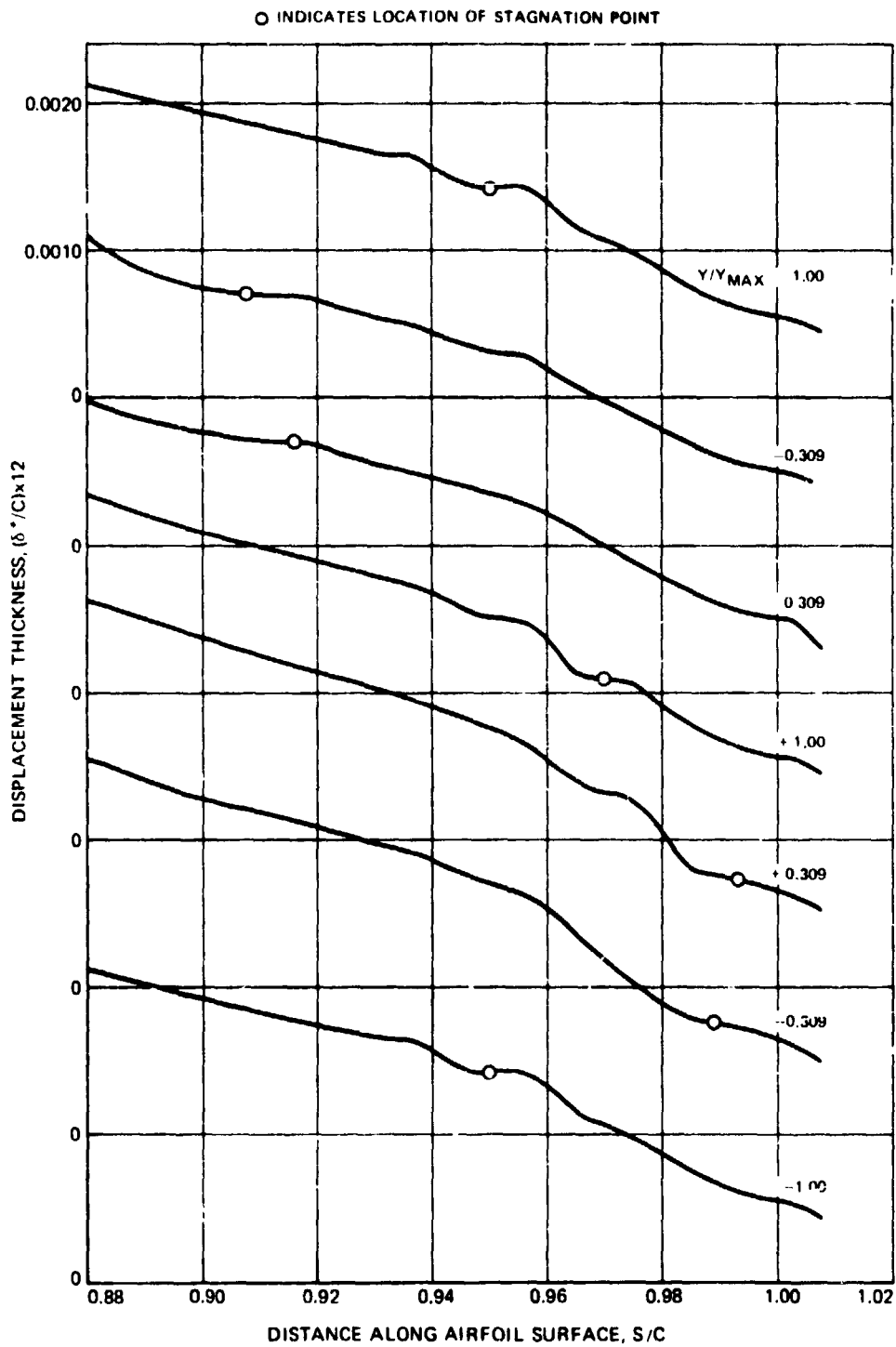
Figure 87. — Variation of displacement thickness in the stagnation region at various instantaneous normalized transverse locations for Case III .

148

N01-17 8
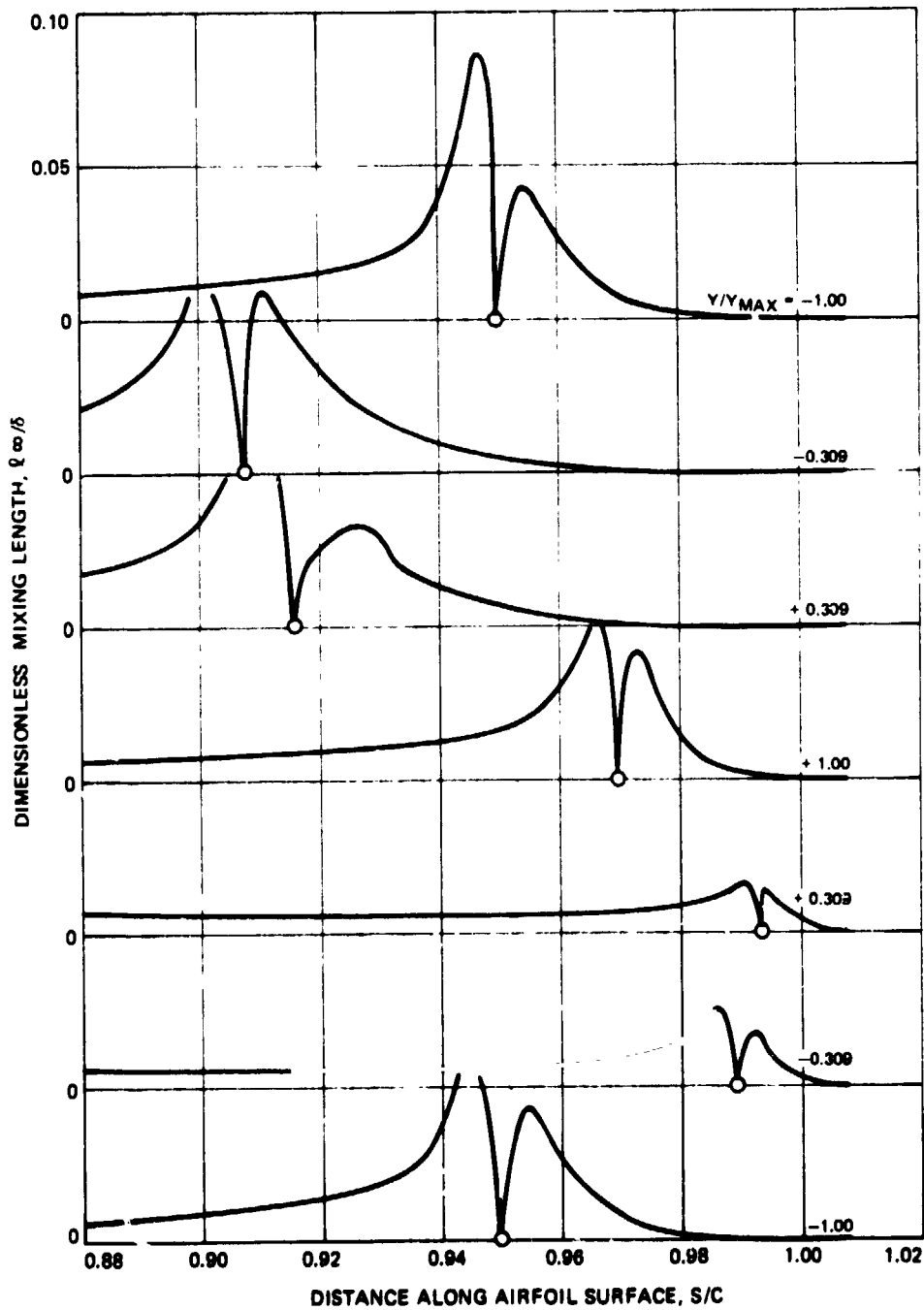
Figure 88. — Variation of dimensionless mixing length in the stagnation region at various instantaneous normalized transverse locations for Case III.
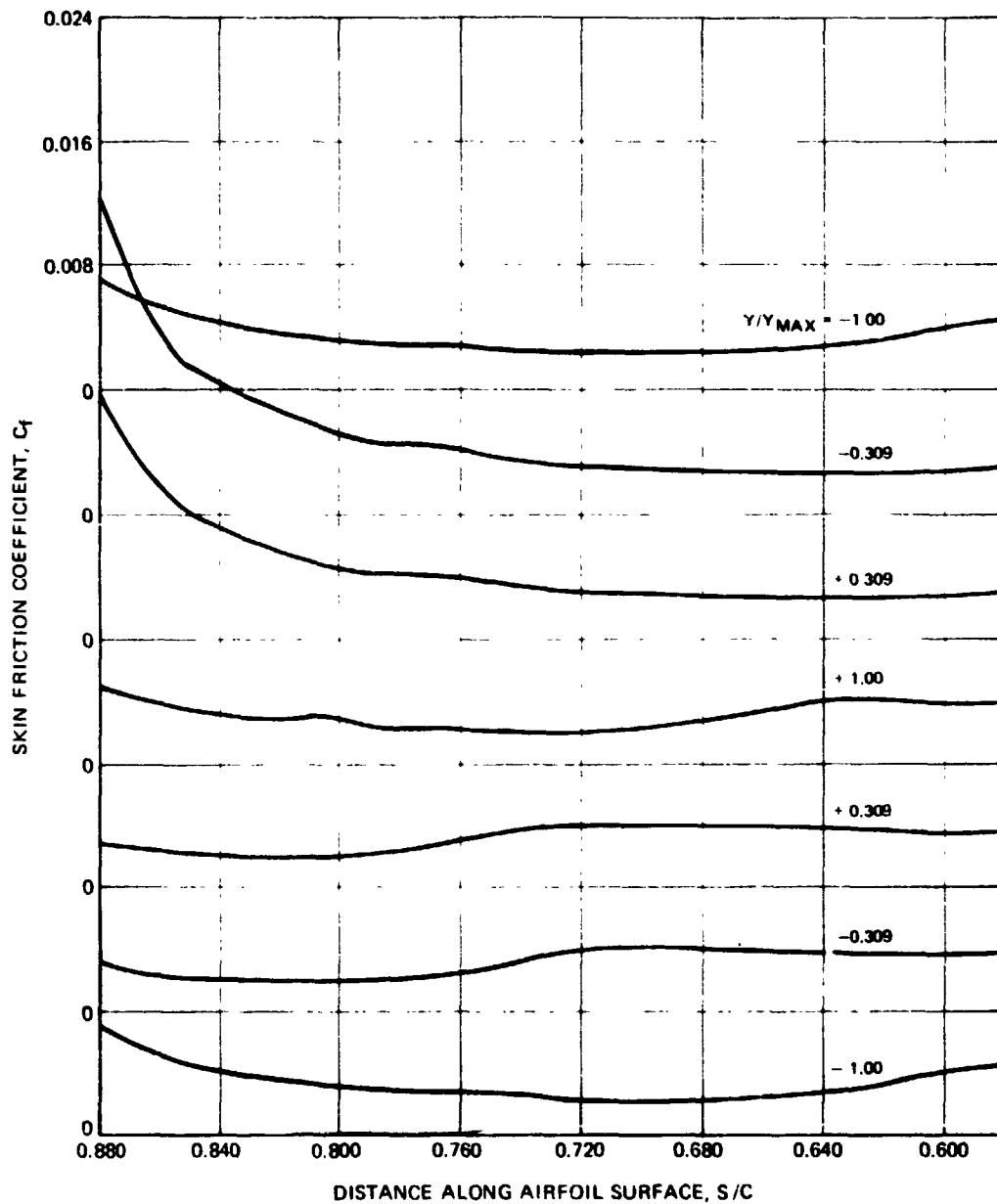
Figure 89. — Variation of skin friction coefficient along the airfoil surface in the pressure side transition region at various instantaneous normalized transverse locations for Case III .
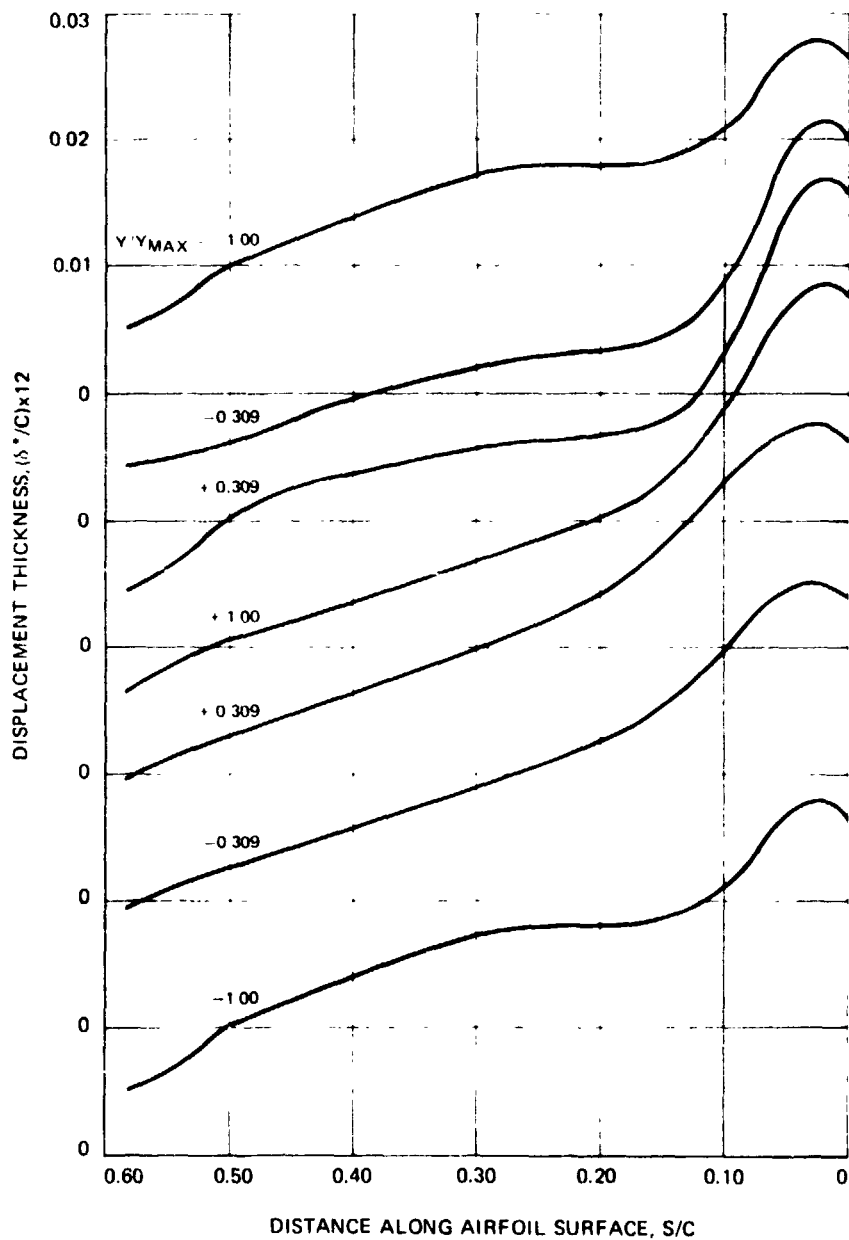
150
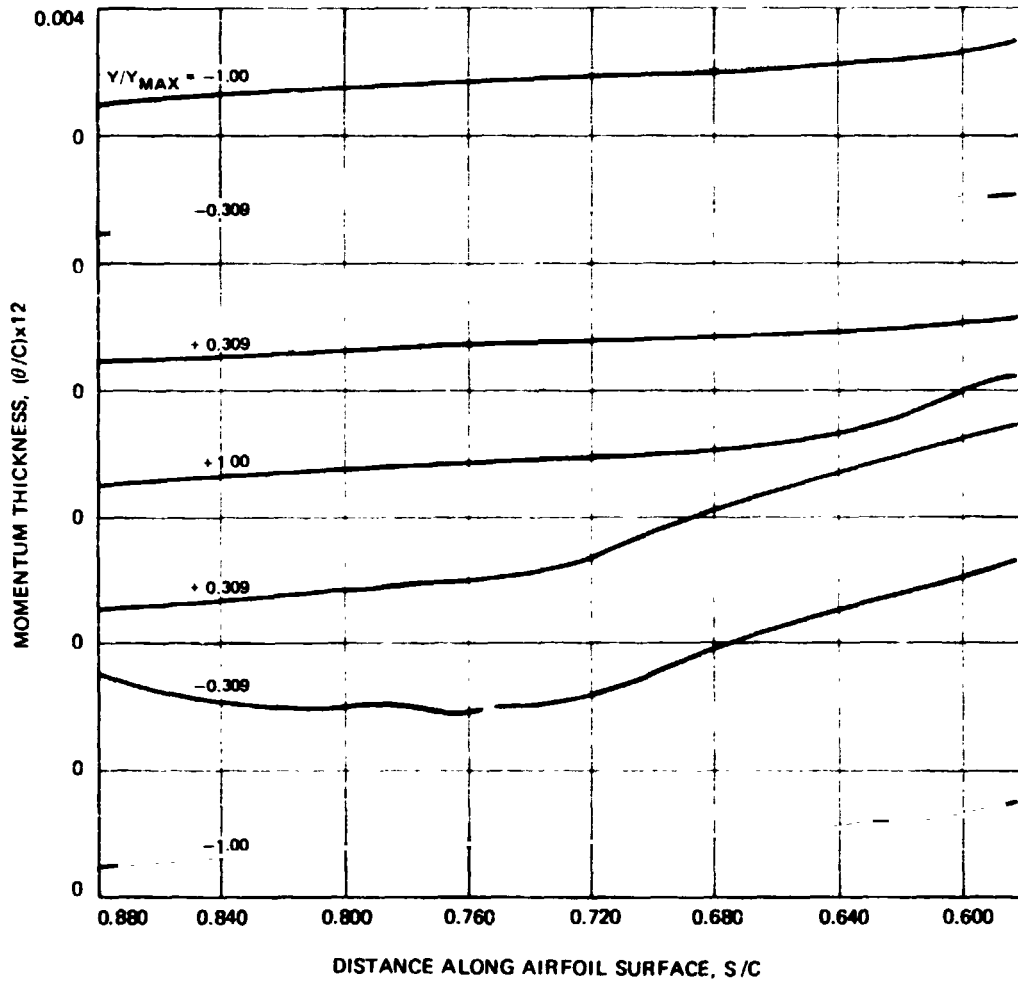
Figure 90. — Variation of momentum thickness along the airfoil surface in the pressure side
transition region at various instantaneous normalized transverse locations
for Case III.
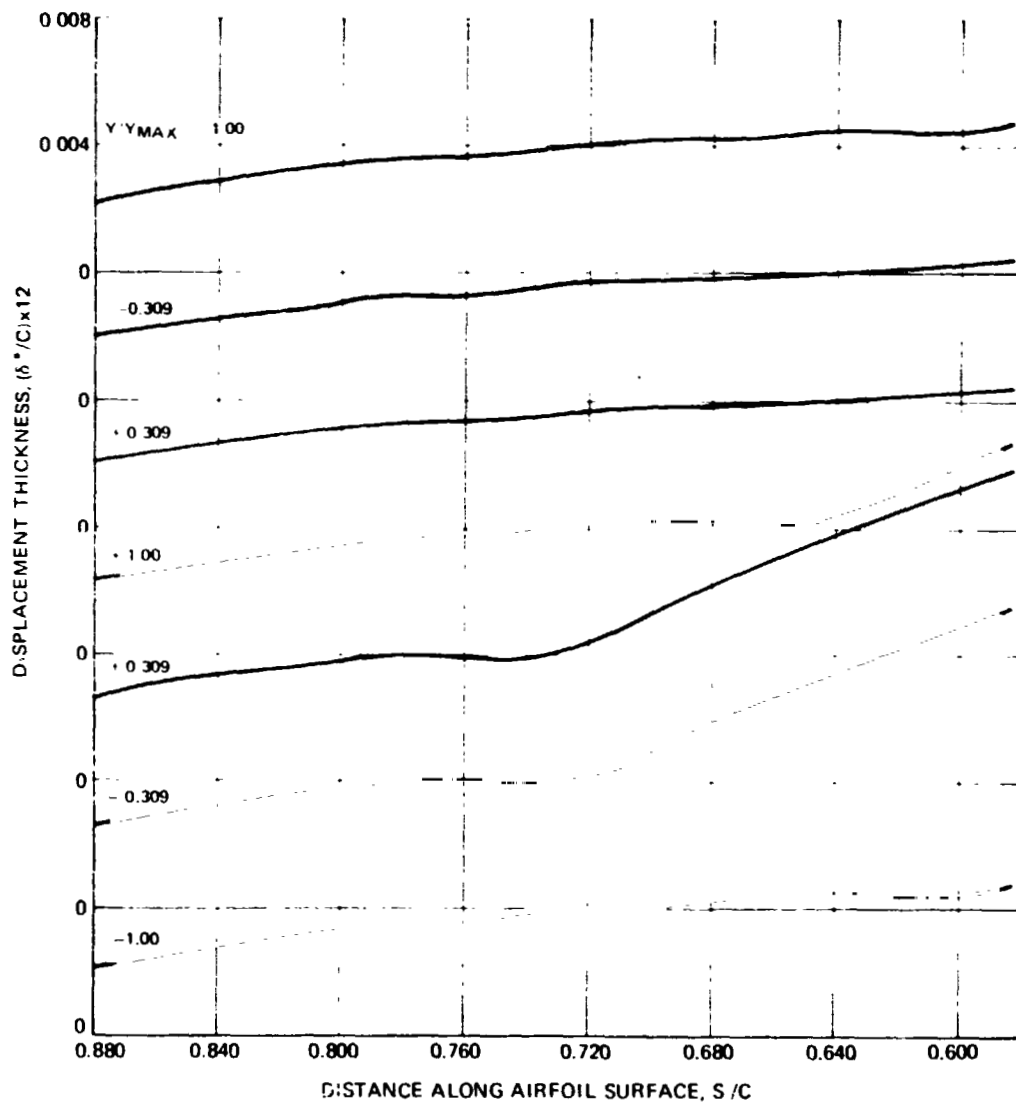
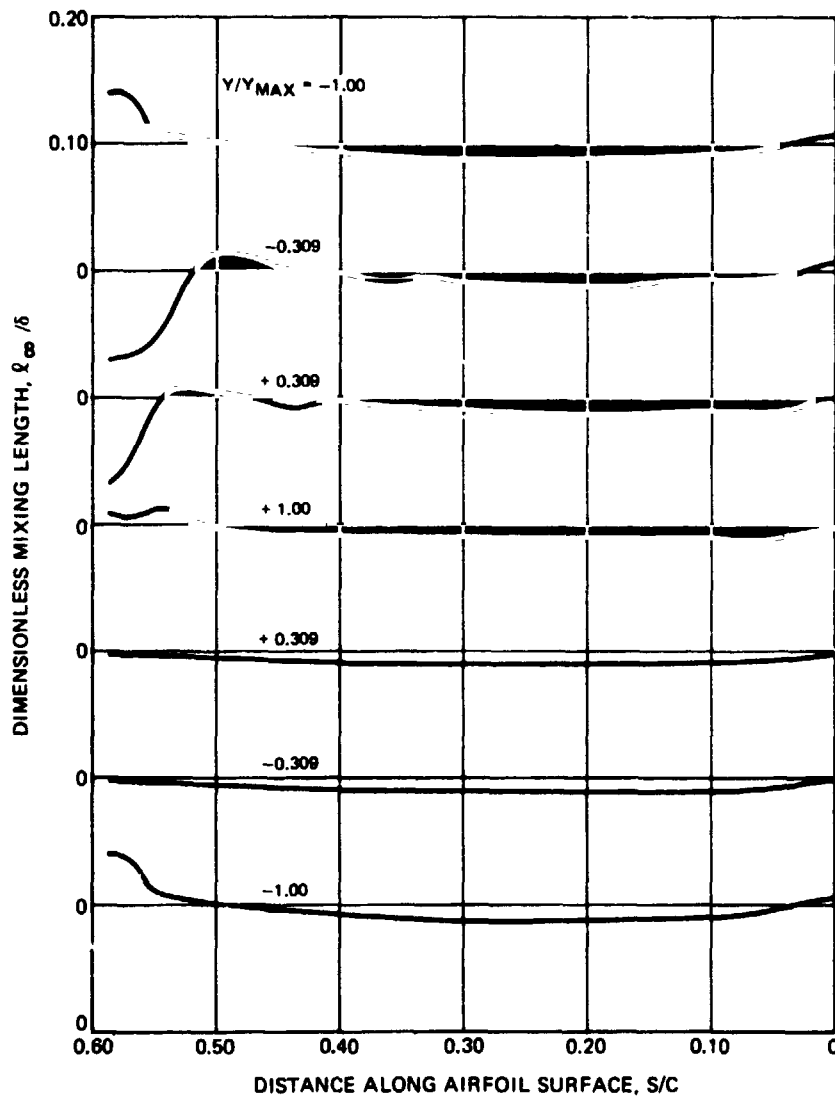Figure 91. — Variation of displacement thickness along the airfoil surface
in the pressure side transition region at various instantaneous
normalized transverse locations for Case III .

152
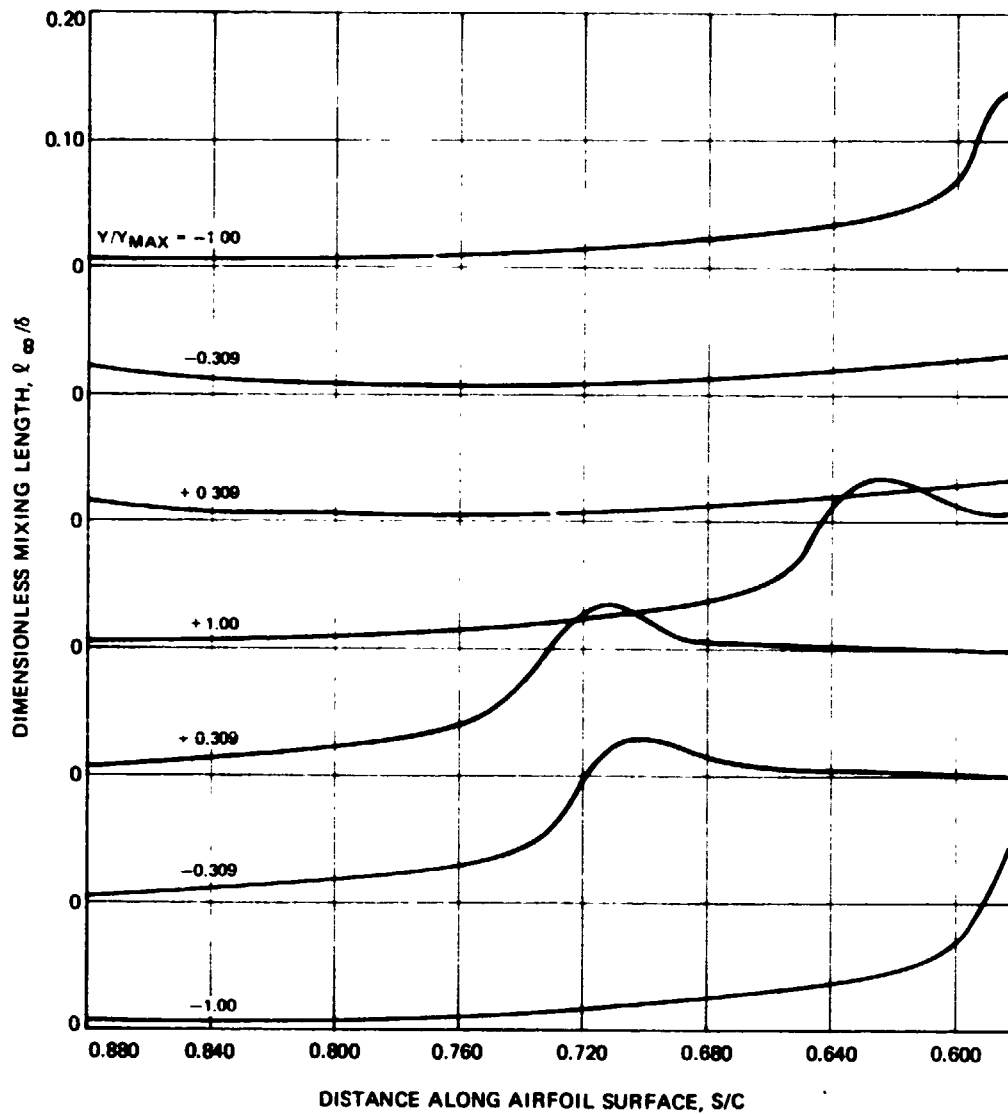
Figure 92. — Variation of dimensionless mixing length along the airfoil surface in the pressure side transition region at various instantaneous normalized transverse locations for Case III.
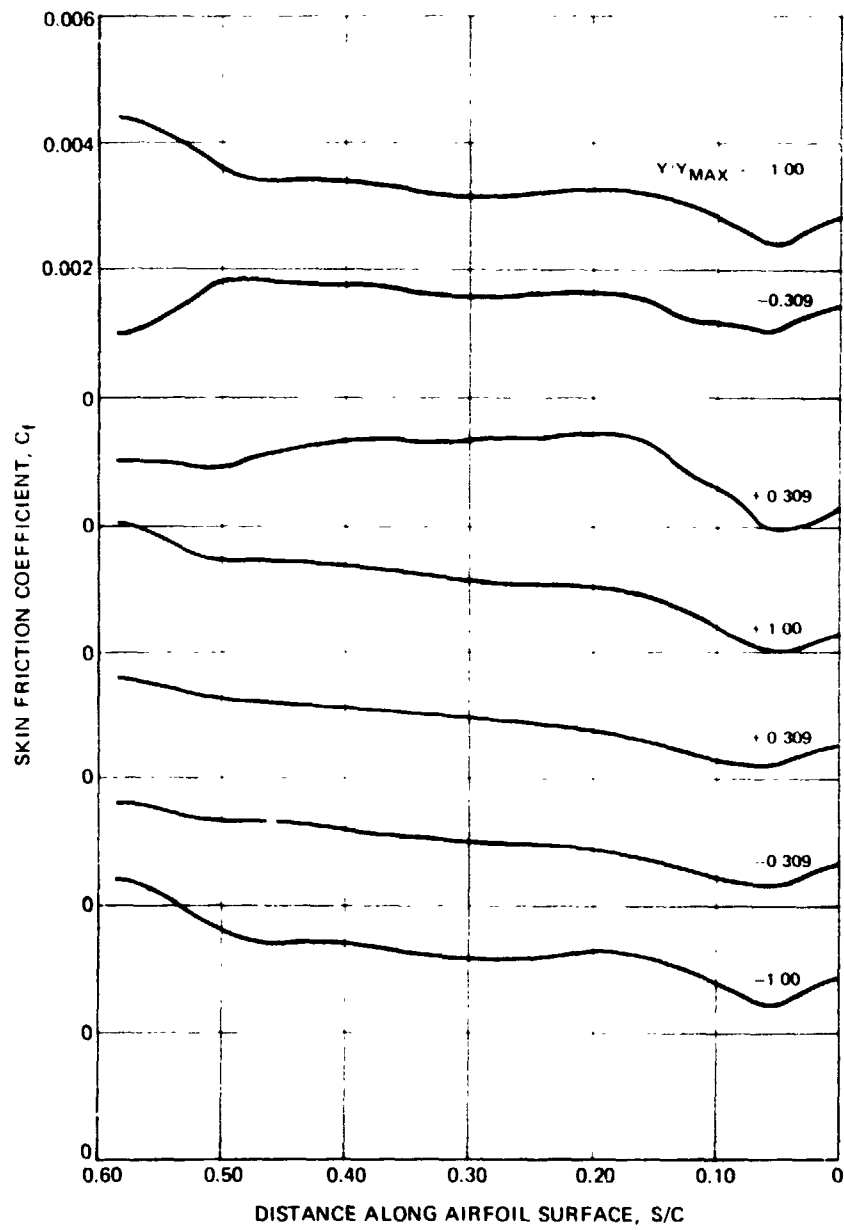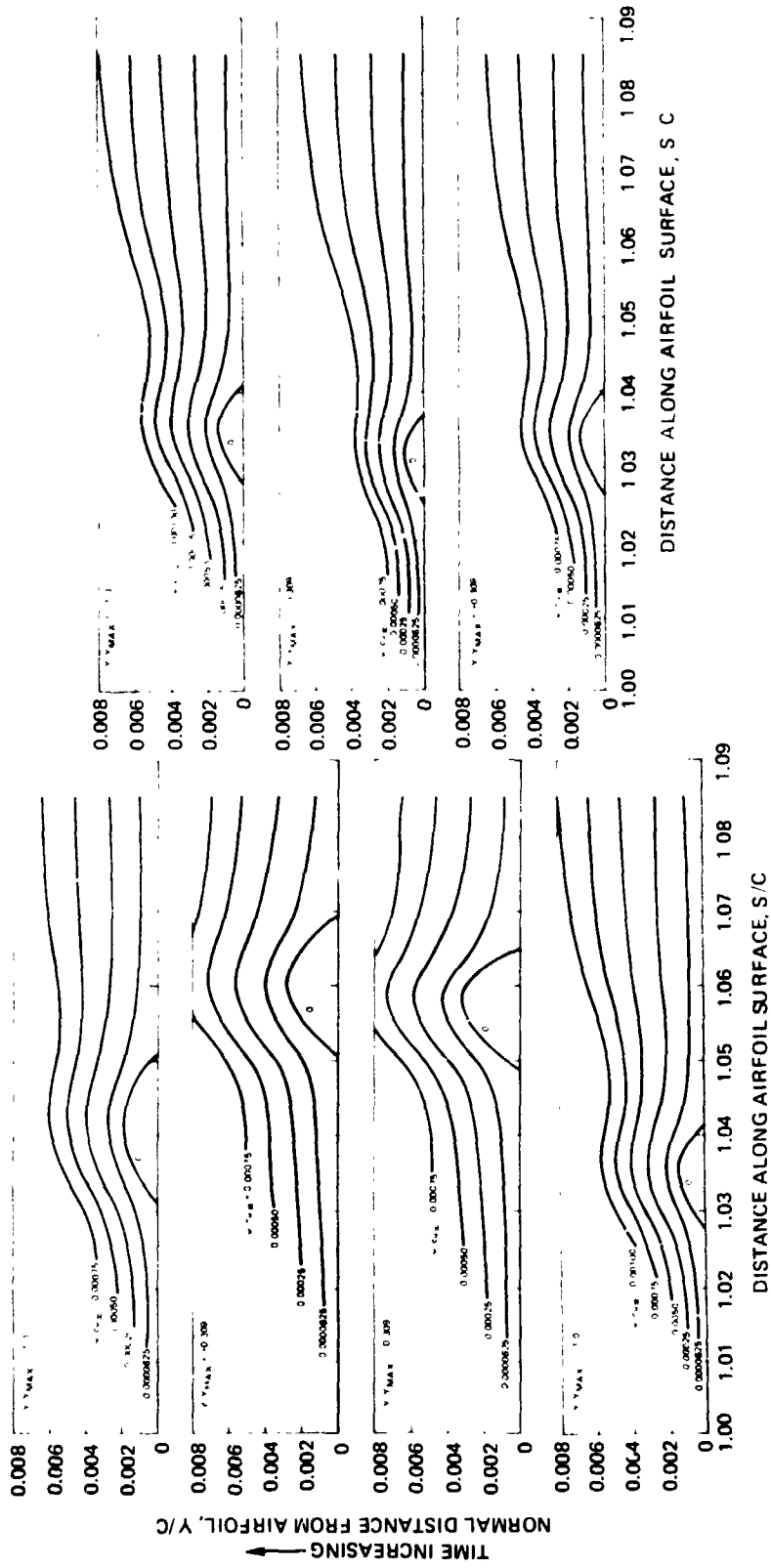
Figure 93. — Variation of skin friction coefficient along the airfoil surface
in the pressure side fully turbulent region at various
instantaneous normalized transverse locations for Case III .

N01-17-14
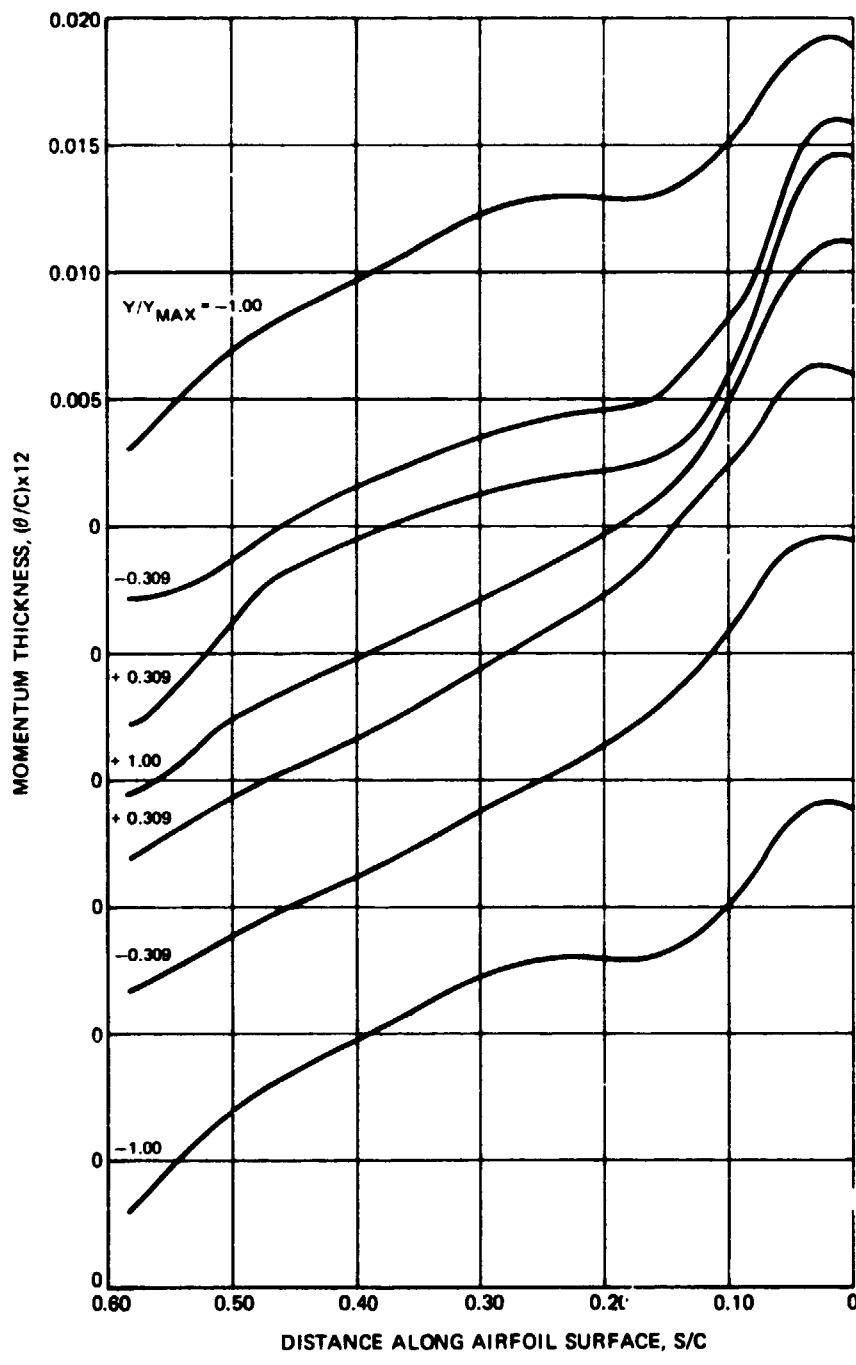
Figure 94. — Variation of momentum thickness along the airfoil surface in the pressure side
fully turbulent region at various instantaneous normalized transverse locations
for Case III.

Figure 95. — Variation of displacement thickness along the airfoil surface in the pressure side fully turbulent region at various instantaneous normalized transverse locations for Case III .

N01-17-16

Figure 96. — Variation of dimensionless mixing length along the airfoil surface in the pressure side fully turbulent region at various instantaneous normalized transverse locations for Case III .

Figure 97. Streamlines in the separated region at various instantaneous normalized transverse locations for Case III.
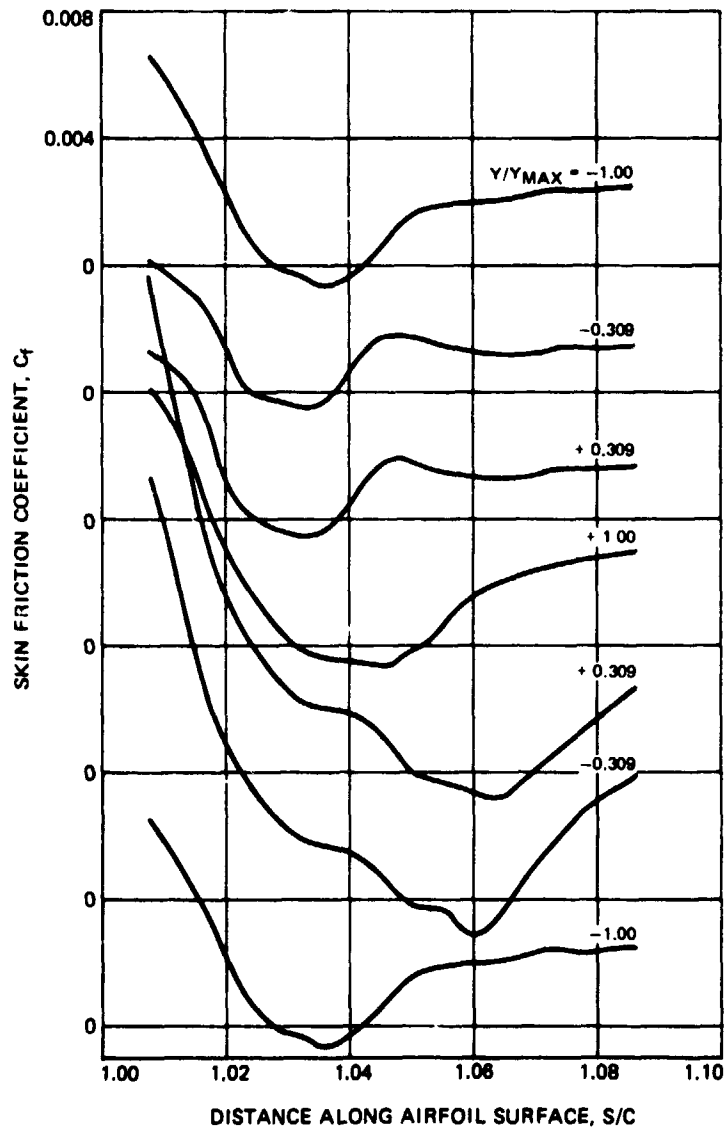
Figure 98. — Variation of skin friction coefficient in the separation region of the airfoil suction side at various instantaneous normalized transverse locations for Case III .
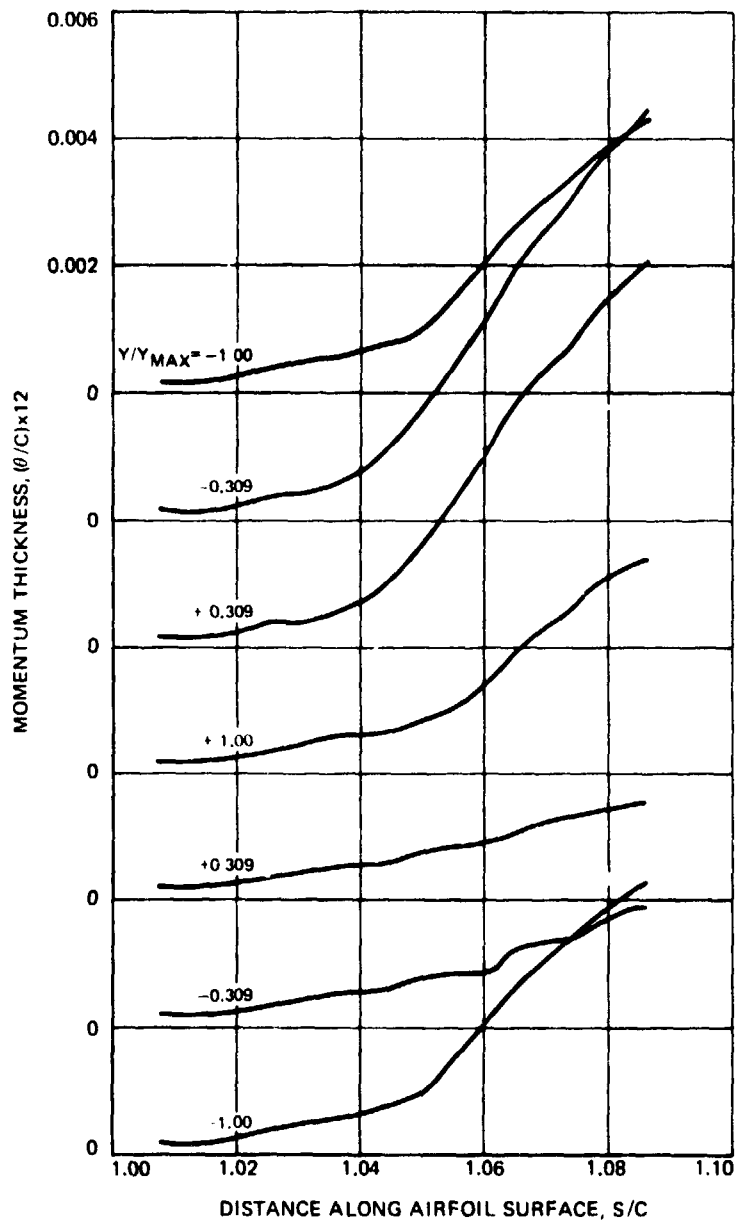
Figure 99. — Variation of momentum thickness in the separation region of the airfoil suction side at various instantaneous normalized transverse locations for Case III.
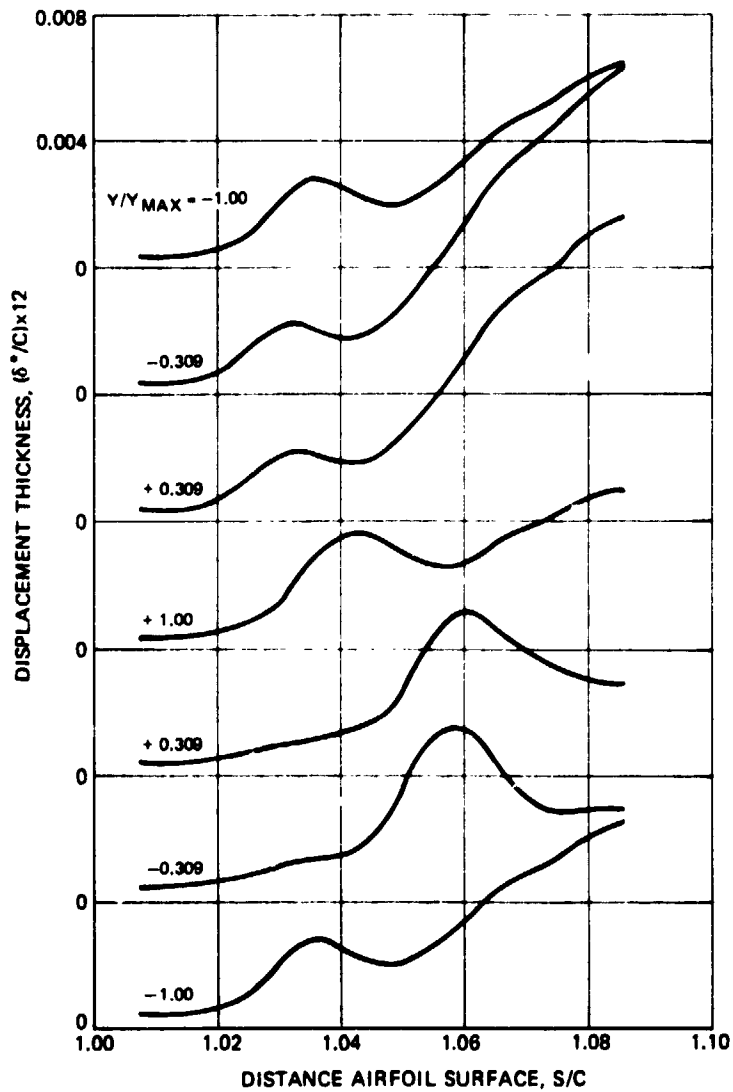
Figure 100. — Variation of displacement thickness in the separation region of the airfoil suction side at various instantaneous normalized transverse locations for Case III.
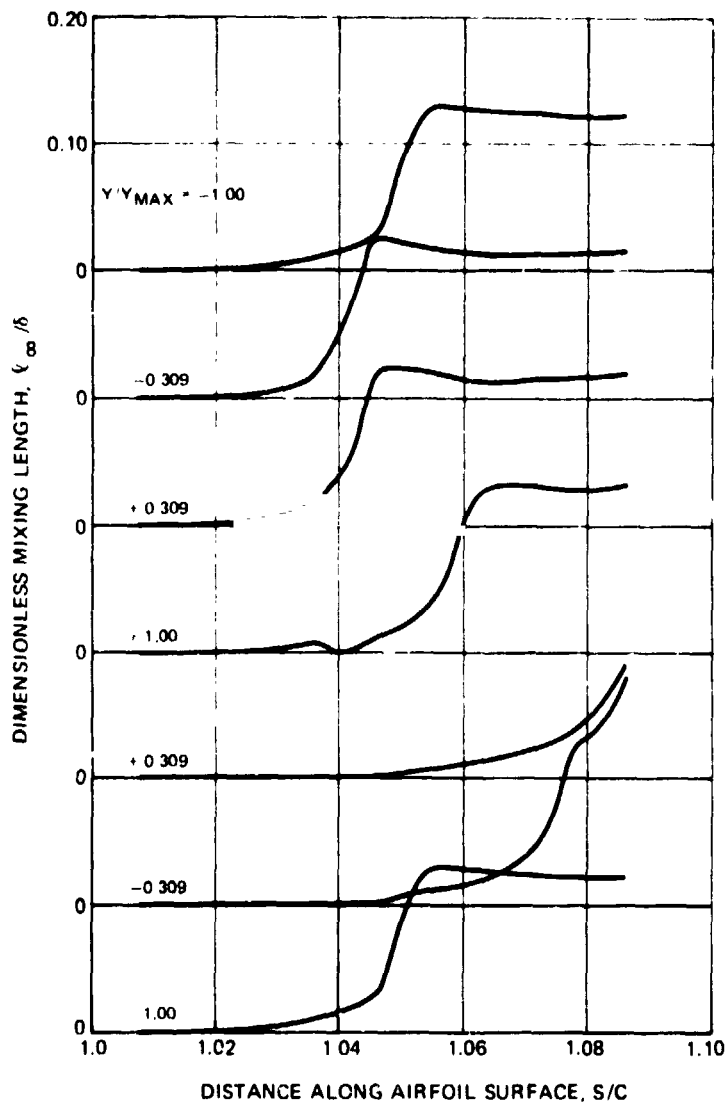
Figure 101. — Variation of dimensionless mixing length in the separation region of the airfoil suction side at various instantaneous normalized transverse locations for Case III .
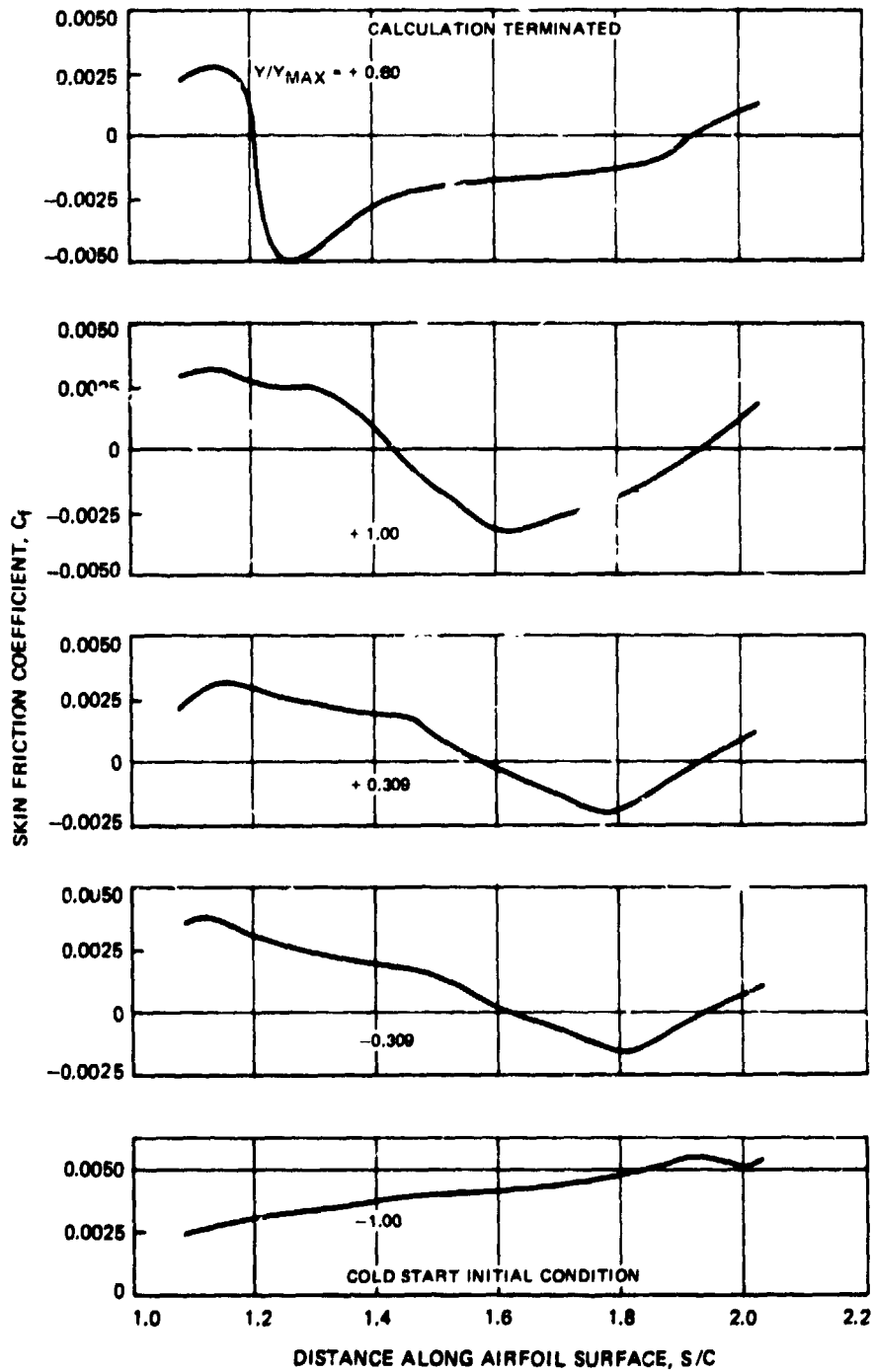
Figure 102. — Variation of skin friction coefficient along the airfoil surface in t:.3 suction side fully turbulent region at various instantaneous no. malized transverse locations for Case III.
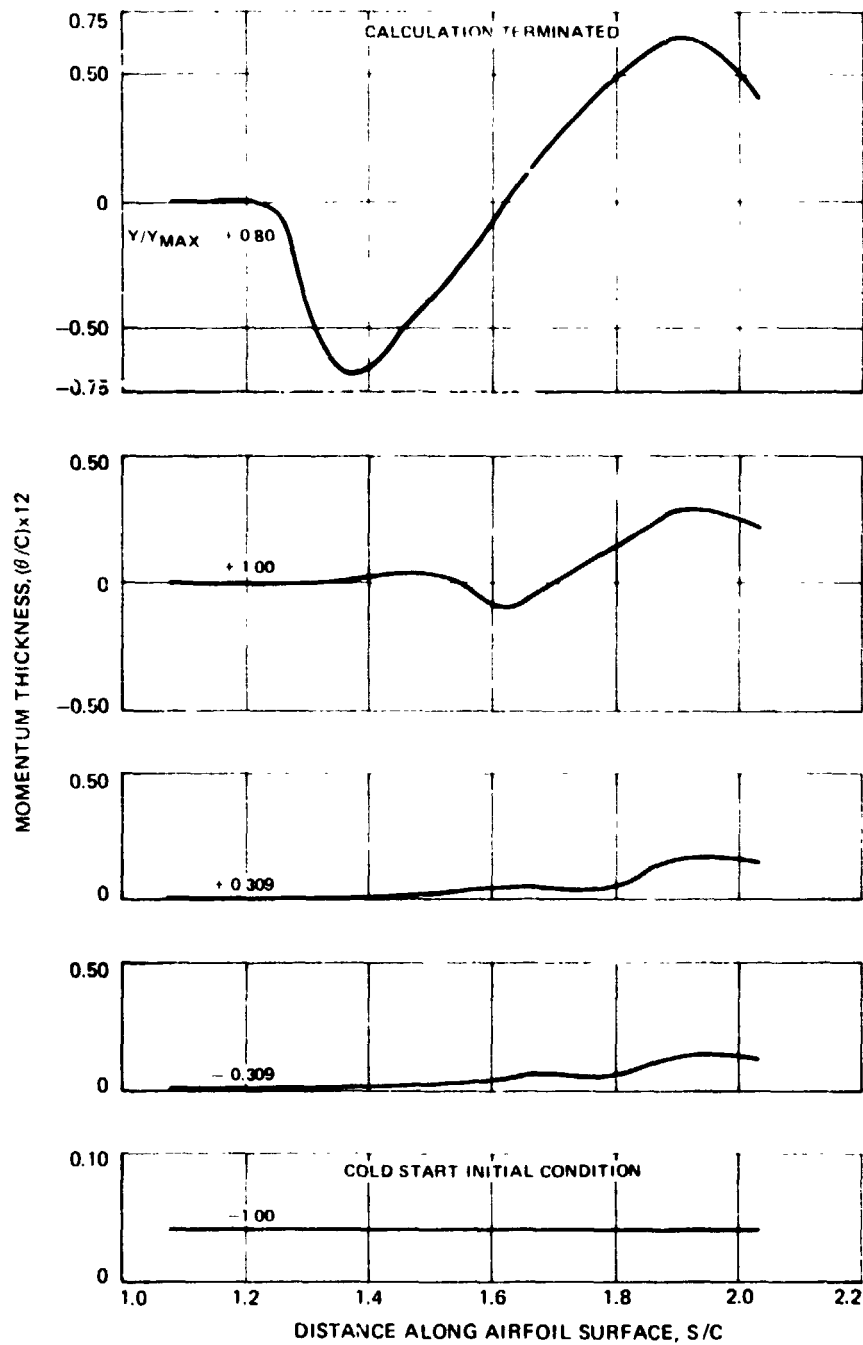
163

Figure 103. — Variation of momentum thickness along the airfoil surface in the suction side fully turbulent region at various instantaneous normalized transverse locations for Case III .
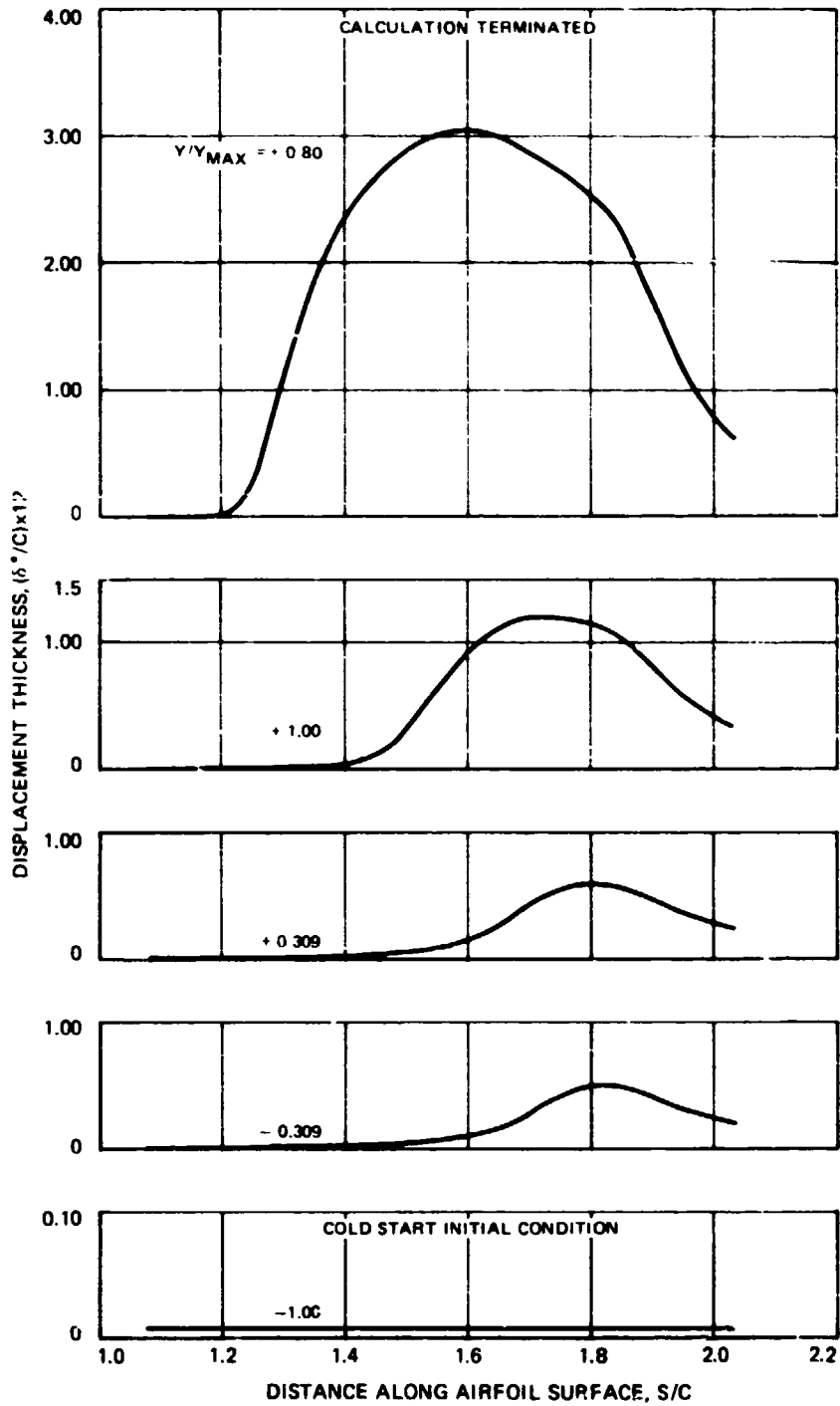
N01-17-24

Figure 104. — Variation of displacement thickness along the airfoil surface in the suction side fully turbulent region at various instantaneous normalized transverse locations for Case III.

N01—17—25